UNIVERSITÀ DEGLI STUDI DI
CASSINO E DEL LAZIO MERIDIONALE

Corso di Dottorato in
Metodi, Modelli e Tecnologie per l'Ingegneria
Curriculum: Ingegneria Elettrica
Ciclo XXXIII

Design and Prototyping of Battery Management Systems for Lithium-ion Battery Packs

SSD: ING/IND-32

Supervisor
Prof. Giuseppe Tomasso

Ph.D. Student
Francesco Porpora

Coordinator
Prof. Wilma Polini

January 2021

UNIVERSITÀ DEGLI STUDI DI CASSINO E DEL LAZIO MERIDIONALE

Date: **Gennaio 2021**

Author: **Francesco Porpora**

Title: **Design and Prototyping of Battery Management Systems for Lithium-ion Battery Packs**

Department: **Dipartimento di Ingegneria Elettrica e dell'Informazione "M. Scarano"**

Degree: **PHILOSOPHIAE DOCTOR**

Permission is herewith granted to university to circulate and to have copied for non-commercial purposes, at its discretion, the above title upon the request of individuals or institutions.

Signature of Author

THE AUTHOR RESERVES OTHER PUBLICATION RIGHTS, AND NEITHER THE THESIS NOR EXTENSIVE EXTRACTS FROM IT MAY BE PRINTED OR OTHERWISE REPRODUCED WITHOUT THE AUTHOR'S WRITTEN PERMISSION.

THE AUTHOR ATTESTS THAT PERMISSION HAS BEEN OBTAINED FOR THE USE OF ANY COPYRIGHTED MATERIAL APPEARING IN THIS THESIS (OTHER THAN BRIEF EXCERPTS REQUIRING ONLY PROPER ACKNOWLEDGEMENT IN SCHOLARLY WRITING) AND THAT ALL SUCH USE IS CLEARLY ACKNOWLEDGED.

Be the best of whatever you are.
Seek earnestly to discover what you are called to,
and then start doing it passionately.

Martin Luther King

Foremost, I would like to express my sincere gratitude to the team of the Laboratory of Industrial Automation of University of Cassino and Southern Lazio. A special mention to Prof. Giuseppe Tomasso, he has represented a precious guide for my Ph.D. study and research during these years, transmitting me knowledge and enthusiasm. Moreover, many thanks to Dr. Mauro Di Monaco for the help, the support and the encouragement he gave me.

My sincere thanks also goes to Prof. Giorgio Rizzoni and Prof. Marcello Canova, who gave me the opportunity to study at The Ohio State University - Center for Automotive Research. I wish to particularly thank Dr. Matilde D'Arpino for her support and guidance during my abroad experience in the USA as well as during this intense last year of my Ph.D path. Furthermore, I would like to thank the NASA ULI program 'Electric Propulsion: Challenges and Opportunities' for supporting the research contribute of this dissertation.

At the end of this challenging, but full of satisfaction, Ph.D path I wish to thank all those who have walked and are walking with me: my family and my friends.

Contents

Introduction

The research activity described in this dissertation is related to the design and prototyping of advanced battery management systems (BMSs) for maximizing the performance of lithium-ion battery packs while ensuring their safe operating conditions. In particular, this research activity consists of three main tasks. The first one deals with the development of optimized control algorithms that allow for extending the lifetime of the battery pack, correctly evaluating its state of charge (SoC) and state of health (SoH) as well as properly managing the cell equalization processes and the charging/discharging procedures. The second task includes the definition of design strategies for passive and active equalization circuits, taking into account for the real parameters of the components involved as well. On the other hand, the third task concerns the sizing and the implementation of modular architectures for BMSs that allow for managing high-voltage battery packs or hybrid systems, which are composed by different technologies of batteries (second life applications). Despite the presented technologies and devices can be adopted in all the fields of application that require battery storage systems, automotive applications have been considered as reference for the development of the BMSs due to the higher performance required in terms of charging/discharging currents, size, cost, reliability and modularity of the architecture.

Motivation

Over the last few decades, concerns over the dependence and price instability of limited fossil fuels as well as environmental pollution and global warming have encouraged researchers, scientists and engineers to conduct more proactive research activities on vehicles with alternative energy sources. Currently, electric vehicles (EV) represent an economical and technically sustainable driver for future transportation systems. The European Union (EU) and other public authorities worldwide are defining increasingly strong regulations in terms of greenhouse gas (GHG) and pollutant emissions, including the ambition of overcoming the dependence to fossil fuels as well as accelerating the adoption of renewable energy sources (RESs). In detail, the targets defined by the EU for 2030 include a 40% reduction in GHG emissions with respect to 1990 levels, a 27% integration of RESs and 27% improvement in energy efficiency.

However, according to the data from the International Energy Agency, it results that the transport system is responsible for approximate 20% of total CO_2 emissions from fossil-fuel combustion. Moreover, the majority of these emissions comes from road transportation. Therefore, relevant fuel economy improvements in road transportation sector are required to stabilize and reduce GHG and pollutant emissions.

In this context, vehicle electrification can significantly contribute to the decarbonisation and emission reduction of the road transport. However, taking into account the Energy Technology Perspective report illustrated by the International Energy Agency, a complete electrification of the road transport will be achieved only by 2070 in a Sustainable Development Scenario. Therefore, novel concepts and innovations need to be developed for making transportation systems more energy-efficient, reliable and safe with zero or reduced emissions at an affordable cost. This would allow for accelerating the decarbonisation of the road transport and a large-scale adoption of EVs.

Currently, considering the three main components of the electric propulsion system of an EV (battery pack, traction inverter and electric motor), the battery storage system is limiting the overall vehicle performance in terms of size, cost, weight and driving range. Hence, advanced battery technologies need to be developed for improving their energy and power densities, cycle life, operating temperatures and high charging/discharging currents capability. The performance increase of battery technologies leads to remarkable developments in Battery Management System (BMS) as well.

The main motivations of the research described in this dissertation regards the development of cost-effective BMS solutions for lithium-ion battery packs. These solutions have to be capable of increasing the efficiency, performance and lifetime of the battery pack while ensuring the operation within the safe voltage, current and temperature ranges. In addition, a cell voltage equalization circuit needs to be included in the BMS architecture in order to compensate the cell-to-cell parameter variations, which leads to voltage imbalance conditions in the battery pack, limiting its operability with a reduction of the usable capacity.

Original Contribute

High-performance equalization circuits have to satisfy different requirements, including modularity, scalability, weight and volume, reliability, cost, hardware and software complexity. Currently, the design targets are mainly focused on minimizing the equalization time and the overall size of the circuit. This also implies the definition of a proper thermal management for dissipating the heat generated due to the high balancing currents that may be needed.

However, literature and industry standards do not address the problem of the optimal sizing of the equalization circuits, which is strongly affected by the operating conditions of the battery pack as well as the parameter variations of the components adopted.

The original contribute proposed in this dissertation regards the definition of design methodologies for passive and active equalization circuits that take into account for relevant aspects of both battery pack and power electronics components. Firstly, the real operating conditions of both individual cells and the overall battery pack have been considered in terms of cell technology, temperature, model calibration and voltage imbalances among the cells. Secondly, the real behavior of the components used for the specific equalization circuit and their parameter variations have be taken into account. In this way, a proper evaluation of the performance of the equalization circuits can be achieved by considering their functionalities in real operating conditions. In particular, design strategies have been proposed for four BMS architectures, one for each main equalization type, including passive, capacitor-based, inductor-based and transformed-based solutions. Moreover, a novel architecture for an active equalization circuit has been developed for the transformer-based equalizer, which allows for achieving a cells-to-cells energy transfer.

Besides the development of design strategies for passive and active equalization circuits, real prototypes have been sized and implemented as well. In detail, a modular architecture for the passive equalizer of a 50HP electric kart and the novel active equalizer have been prototyped with the aim of validating their performance in real-world environments. These prototypes also allow for managing high-voltage battery packs or hybrid systems, which are composed by different technologies of batteries (second life applications). Moreover, a detailed comparison between the prototypes developed has been carried out in order to highlight their main features in different operating conditions, including charging, discharging and idle state.

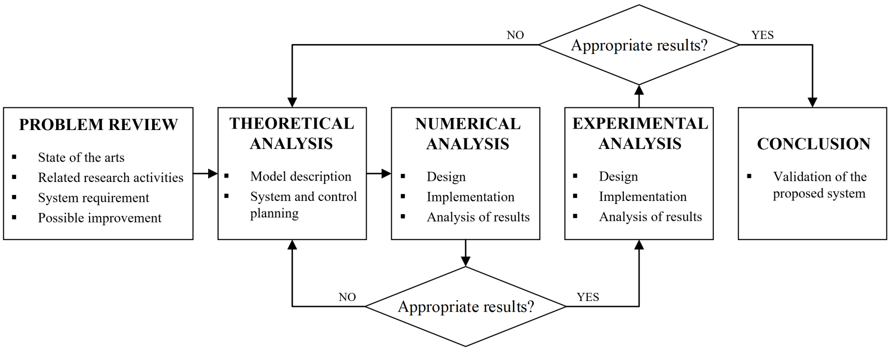

Figure 1: Flowchart of the methodological approach.

Methodological Approach

The methodology approach is crucial for the research activity to define a systematic procedure for a specific topic. According to the flowchart shown in figure 1, an experimental-research based model has been adopted in this dissertation, which consists of four main steps:

- *Problem Review*

  To gain familiarity with the specific topic,the state of the art and a bibliographic analysis of the background is needed. Therefore, all the functionalities of a BMS and the main architectures of the equalization circuits have been investigated. In addition, related research topics have been taken into account for extending the knowledge of the main research activity and thus further improving the overall performance of the BMS. These related research topics include the development of either battery models at both cell-level (electrical, thermal and aging) and pack-level (series-parallel and parallel-series architectures) or algorithms for estimating the SoC and SoH as well as the evaluation of hazard conditions for lithium-ion battery packs.

- *Theoretical Analysis*

  This represents an important step to provide an explanation of the system by means of mathematical models. The parameters of these models can be achieved mathematically or by experimental testing. A novel structure and/or control concept can be carried out by the state of art analysis matched with future improvement.

- *Numerical Analysis*

  This has been adopted for investigating the behavior of the equalization circuits and the related control algorithm as well as testing the proposed design methodologies. The numerical results can also demonstrate the no-accuracy of the models considered. Thus, an improvement of the proposed system can be necessary.

- *Experimental Analysis*

  In case of positive feedback from the numerical analysis, an experimental set-up is designed and implemented to fully validate the performance and the functionalities of the proposed prototypes of equalization circuits.

Summary

The dissertation is organized in five chapters. The first one reports the fundamentals of electric propulsion for road transportation, while the main features of lithium-ion battery packs are illustrated in the second one. The third chapter provides a detailed overview of the BMS functionality as well as all the architectures presented in literature for the equalization circuits. The last two chapters highlight the original contribute of the proposed research activity, including the design methodologies for different equalization circuits and the prototypes developed and implemented in real-world applications.
In detail, the dissertation is organized as following:

- **Chapter 1**: a detailed section regarding expectations, benefits and challenges for vehicle electrification as well as market trends is reported. Then, the main components of the electric propulsion system are illustrated, including energy storage systems, electric motors and power electronics converters. Moreover, different architectures for vehicle technology are discussed, highlighting advantages and disadvantages of each solution.

- **Chapter 2**: after an introduction related to the main battery terminology, the architecture and the operating principles of lithium-ion cells are illustrated, highlighting the most adopted materials and future trends. Then, major components of the battery pack architecture for automotive applications are discussed. A brief overview regarding the battery modeling approaches, safety and aging conditions is reported as well.

- **Chapter 3**: a description of the main BMS architectures, the requirements and functions are discussed, including details related to sensing and measurement, safety and protection, interface and communication, diagnostics and performance management. An overview of the SoC and SoH estimation methods is reported in the diagnostics section, while the main charging techniques are illustrated in the performance management section. Moreover, a wide description of the equalization circuits is discussed with the aim of evaluating and comparing the balancing performance of each architecture.
- **Chapter 4**: the design strategies for different balancing circuits are illustrated with the aim of achieving the desired performance in terms of equalization time, efficiency and maximum balancing current. In particular, four architectures have been considered, one for each main equalization type, including passive, capacitor-based, inductor-based and transformed-based solutions. A novel architecture for an active equalization circuit has been proposed for the transformer-based equalizer. The impact of parameter variations and the operating conditions of the battery pack on the overall performance of the BMS has been evaluated as well.
- **Chapter 5**: the details related to the development, sizing and implementation of real prototypes of equalization circuits are reported. In particular, a modular architecture for passive equalizer and the novel active equalizer have been prototyped with the aim of validating their performance in real-world environments. These prototypes also allow for managing high-voltage battery packs or hybrid systems, which are composed by different technologies of batteries (second life applications). Automotive applications have been considered as reference for the development of the BMSs due to the high performance required in terms of charging/discharging currents, size, cost, reliability and modularity of the architecture. Moreover, a detailed comparison between the prototypes developed has been carried out in order to highlight their main features in different operating conditions, including charging, discharging and idle state.

Chapter 1

Fundamentals of Electric Propulsion for Road Transportation

Decarbonisation and emission reduction from road transportation are the main drivers for the electrification of vehicles. However, electric propulsion systems require technological achievements and improvements for enabling a large-scale adoption of electric vehicles.
In this chapter, a detailed introduction regarding expectations, benefits and challenges for vehicle electrification as well as market trends is reported. Then, the main components of the electric propulsion system are illustrated, including energy storage systems, electric motors and power electronics converters. Moreover, different architectures for vehicle technology are discussed, highlighting advantages and disadvantages of each solution.

1.1 Motivations for Vehicle Electrification

Nowadays, electric vehicles (EV) represent an economical and technically sustainable driver for future transportation systems. The European Union (EU) and other public authorities worldwide are defining increasingly strong regulations in terms of greenhouse gas (GHG) and pollutant emissions, including the ambition of overcoming the dependence to fossil fuels as well as accelerating the adoption of renewable energy sources (RESs).

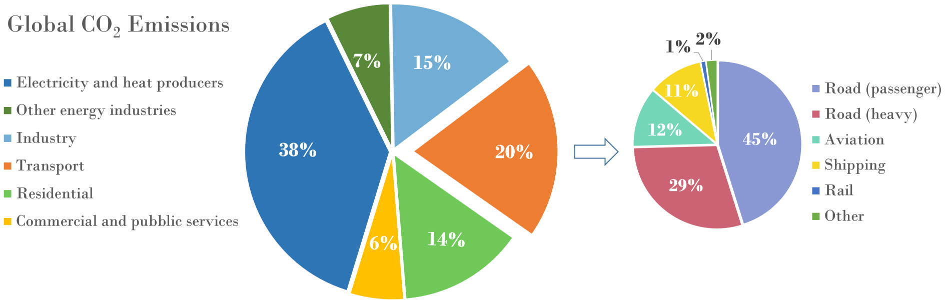

Figure 1.1: Global CO_2 emissions by sector, including a detailed distribution of the emissions for transport. *Data from International Energy Agency*

In detail, the targets defined by the EU for 2030 can be summarized as follows:

– 40% reduction in GHG emissions with respect to 1990 levels;
– 27% integration of RESs;
– 27% improvement in energy efficiency.

Figure 1.1 reports the CO_2 emissions worldwide divided by sector. It results that the transport system is responsible for approximate 20% of total CO_2 emissions from fossil-fuel combustion. Moreover, the majority of these emissions comes from road transportation. Indeed, passenger vehicles (cars and buses) and heavy vehicles (trucks and lorries) contribute 45% and 29%, respectively. While, the rest of the transport systems accounts for an overall 26%, including aviation, shipping, rail and transport for the movement of water, oil and gas via pipelines. As matter of fact, since the road transport impacts for three-quarters of transport emissions, it is responsible for 15% of total CO_2 emissions. In addition, considering that world population will increase from the existing 7.8 billion to around 10 billion in the next 30 years, an increase of the number of road vehicles is expected with further negative consequences in terms of CO_2 emissions. Therefore, relevant fuel economy improvements in road transportation sector are required to stabilize and reduce GHG and pollutant emissions.
Vehicle electrification can significantly contribute to the decarbonisation and emission reduction of the road transport. However, novel concepts and innovations need to be developed for making transportation systems more energy-efficient, reliable and safe with zero or reduced emissions at an affordable cost. This is reflected in the Energy Technology Perspective report illustrated by the International Energy

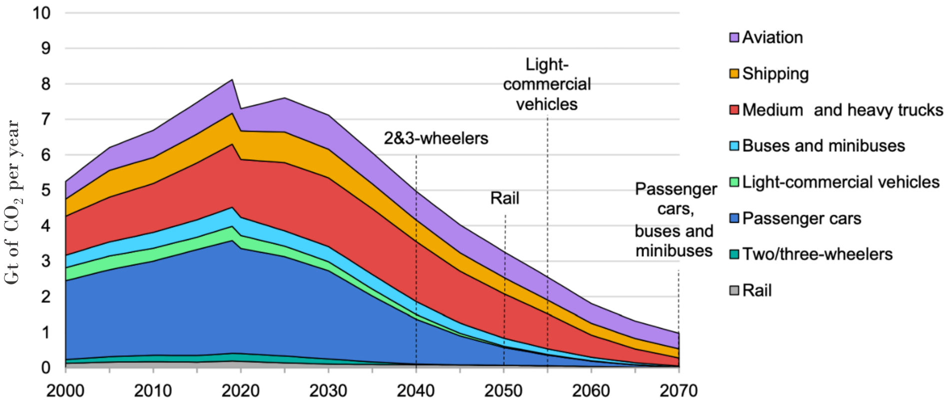

Figure 1.2: Global CO_2 emissions for the different transport modes in the Sustainable Development Scenario. *Source: International Energy Agency*

Agency. It shows a Sustainable Development Scenario for achieving net-zero CO_2 emissions from global energy by 2070. The results for the different transport modes in this optimistic scenario are reported in the figure 1.2. Dotted lines indicate the year in which various transport modes have stopped consuming fossil fuels and thus no longer contribute to CO_2 emissions. The Sustainable Development Scenario includes a roadmap for meeting international climate and energy targets and incorporates aspects of behavioral change alongside an intense transformation in energy system technology and infrastructure. As result, a complete electrification of the road transport will be achieved by 2070. While, it will be more difficult to decarbonize other transport modes, such as aviation and shipping. This scenario highlights the importance of a rapid deployment of low-carbon power generation as well as faster and consistent innovations in the vehicle electrification process in order to gain quicker progress towards net-zero emissions. Currently, there are different vehicle solutions that can be adopted for fully or partially replacing the conventional vehicles, which are based on internal combustion engine (ICE) and use petroleum products for propulsion:

- Battery electric vehicles (BEVs);
- Hybrid electric vehicles (HEVs);
- Plug-in hybrid electric vehicles (PHEVs);
- Fuel cell vehicles (FCVs).

Typically, BEVs and FCEVs are named as fully-electric vehicles. BEVs adopt electrochemical energy storage systems for providing the electric propulsion to the vehicle, whereas FCEVs use hydrogen as fuel. HEVs result as an integration between BEVs and ICE vehicles (ICEVs), since they include both electric motor and engine. The aim of this hybridization is to combine the advantages of both vehicle solutions. However, the additional electric and mechanical components make the HEVs more complex, bulkier and expensive. PHEVs represent a more electrified hybrid solution, which allow for extending the electric driving range of the vehicles and thus achieving higher efficiency and reduced emission. More details about architectures and features of these vehicle will be provided in section 1.2.

1.1.1 Expectations

Currently, EVs are considered as main competitor and sustainable alternative of conventional ICEVs. Efforts and substantial resources are directed to meet market requirements for high performance, energy-efficient, durable, safe and affordable electrified vehicles. The expectations of the consumers and fleet operators regarding EVs can be summarized as follows:

- Similar prices or total cost of ownership competitive to current ICEVs;
- Range, reliability, durability and re-sale value of EVs similar to conventional ones;
- Range adapted to specific use cases;
- Usage comfort as good as the state of the art ICEvs in terms of availability, refilling time and possibilities, passenger comfort and transport volume;
- Safe parking and infrastructure also for two-wheeler fleets;

It is important to highlight that the current state of the art of EVs does not allow for replacing conventional vehicles maintaining the same universality with driving ranges and refilling times less than 5 minutes. There are still several technological limitations that need to be accomodated for a large-scale adoption of EVs. These drawbacks can be compensate by additional advantages, including the access to zero-emission zones or preferential parking for EVs, ease of charging and driving comfort. Common EU legislation may accelerate market take up as well. Other advantages may also be achieved through synergies of the electrification with the connectivity and automation of vehicles. Connectivity would certainly provide particular benefits for the users in terms of easy access to charging infrastructure, optimization of driving routes and minimization of energy consumption. Whereas, the integration of automated EVs into sharing systems would allow to better match mobility supply and demand as well as manage the charging process.

Charging represents a crucial topic for the success of vehicle electrification. Regulatory efforts for the recharging of EVs have already been initiated. Indeed, the EU has made steps towards the creation of recharging infrastructures for EVs, providing an obligation on member state governments to expand the network of charging points, as the number of vehicles in service grows. National governments are responsible of ensuring a public networks of charging points suitable with respect to the EVs sales trends. In addition, it is expected that infrastructures combined with fast and high-power charging capabilities will represent an important solution for serving longer range needs.

The European Roadmap Electrification of Road Transport has published an interesting report in which the expected performance goals for different EV categories are illustrated [1].

Full Electric Vehicle

It is expected that relevant technological developments will impact on EVs by 2030, concerning:

- vehicle technologies, including battery, drivetrain components and energy management;
- industrialization (dedicated platforms, standardization, high volumes);
- charging infrastructures (availability, connectivity, high-power capabilities);
- additional features such as trip planning, car sharing and autonomous drive.

Table 1.1 shows the expected performance goals for EVs for 2020 and 2030. It is possible to divide the EVs marketed in two different types. The first one includes user friendly affordable EVs with more optimized range/cost solution. This category allows for enabling a better market penetration and thus an important impact on urban pollution and GHG reduction. The range of 250 km results suitable for

	EV 2020		EV 2030	
Hypothesis	User-friendly	High performance	User-friendly	High performance
Energy consumption (Wh/km)	130	135	115	120
Range (km)	250	500	250	700
Battery capacity (kWh)	33	68	29	84
Battery energy density (Wh/kg)	> 180	300	> 330	500

Table 1.1: Expected performance goals for EVs. [1]

urban/suburban use. Such vehicles would need to have an expected retail cost similar to ICEVs. The major challenge will be to achieve significant cost reduction of the battery and propulsion systems.

Plug-in Hybrid Electric Vehicle (PHEV)

PHEVs will represent a key solution for a more electrified road transportation thanks to their low fuel consumption and GHG emission. They can be considered as one of the market responses to potential city center driving bans. Furthermore, an increase of the full electric range up to 150 km and a further reduction of the fuel consumptions are expected by 2030, as shown in table 1.2. The reduction of retail extra cost of PHEVs will require massive progress in significantly reducing the cost of battery cells and systems as well.

Electrified L-Category Vehicles

L-category vehicles include two/three wheelers and light quadricycles, which are very suitable for electrification because of their small dimensions and lightweight, thus low energy consumption and lower battery cost. They can play an important role in urban areas in contributing to decongestion of traffic and relief for pressure on parking. Range and cost are main open issues for technology development and market penetration. Even if real autonomy is less important in urban area usage, customers are more inclined to EVs that do not need to be

	PHEV 2020	**PHEV 2030**
All electric range (km)	Up to 100	Up to 150
Dynamic performance in EV mode	Urban/suburban	Full
Retail extra cost (€)	∼3000 to 6000	∼2000 to 3000
Consumption under standard procedure (L/100 km)	0.8 to 1.0	0.45 to 0.65
CO_2 emission under standard procedure (g/100 km)	25 to25	10 to 20
Battery capacity (kWh)	∼15	∼20

Table 1.2: Expected performance goals for PHEVs. [1]

constantly recharged. However, battery sizes adopted specifically for urban or private use cases can lead to attractive total cost of ownership values. Therefore, the goal is to increase the attractiveness of L-category vehicles by reducing costs and improving the functionality in terms of appropriate range and shorter recharging time.

Electrified Commercial Vehicles

Commercial vehicles are typically custom-built to meet specific needs concerning load and operation, leading to a large variety and low production volume of different vehicle configurations. Plug-in hybrids and full electric vehicles can be adopted for urban and regional operation, where charging and dynamic power transfer infrastructures can be developed to an integrated transport system. On the other hand, longer distance and heavier transports are more suitable for conventional hybrids, plug-in hybrids and possibly dynamic power transfer due to the physical limitations of on-board electric energy storage.

In detail, commercial vehicles can be classified in four categories:

- *Trucks and vans for urban transport*

  These vehicles are characterized by transient loads with high-power peaks for acceleration with low loads in slow traffic and at standstill. The electric urban trucks will contribute to energy efficient, emission free and low-noise goods transport solution through full electric drive. The size of the battery pack will be dependent on both the size of the vehicle and the charging strategy, ranging from overnight charging to opportunity charging at logistic centers. While, plug-in distribution trucks will include both an electric energy storage and ICE, thus less dependence on charging infrastructure and lower charging time. They will provide higher energy efficiency compared with conventional distribution trucks and the possibility of limited emission free and low-noise transport through partially full electric drive. Moreover, higher voltage (up to 1500 V) on-board vehicle power networks may provide advantages to fulfill the requirements on these vehicles in terms of low-speed torque and efficiency.

- *Trucks for long-haul transport*

  Heavy trucks for long-haul transport (40 tons, 80 km/h) are characterized mainly by steady-state operation for longer periods combined with peak power demand during acceleration and uphill with low-speed operation through urban areas, in terminals and in highway congestion situations. The introduction of electric hybrids could strongly reduce the impact of these vehicles in terms of CO_2 and pollutant emissions. However, although battery technology holds great promise for passenger cars and light vehicles, additional improvements need to be achieved for a full electrification of long-haul transports. Hence, the target is to adopt hybrid vehicles and then also PHEVs using static fast charging and/or dynamic power transfer. Indeed, these solutions have the potential to shift energy supply, energy efficiency and decrease emissions for long-haul road transport. In addition, research activities in the area of heavy-duty vehicle powertrains will need to tackle the challenge of demonstrating electrification solutions in combination with range-extending technologies that show achievable improvements in cost and efficiency without significantly increasing packing dimensions or the weight of the overall powertrain.

- *City buses*

  Bus fleets are ideal for electrification since buses are normally in operation up to 18 h/day and energy charging infrastructure can be installed in a very cost-efficient way in existing bus depots or at dedicated bus stops. The operation is characterized by many stops and relatively low average speeds, resulting in transient loads with high power peaks for low-speed acceleration and wide use of breaking energy recovery. The electric bus will contribute to energy-efficient, emission-free and low-noise passenger transport solution through full electric drive. The size of battery pack will be dependent on the charging strategy, ranging from large storage for only overnight charging up to small storage when charging is performed at end stations, bus stops or by dynamic charging.

- *Inter-urban buses*

  These vehicles are characterized by few stops at a constant average speed higher than city buses. Full electric solutions are suitable considering a larger energy storage if the charging is performed at the end station or a smaller one in case of charging at bus stops and and/or dynamic power transfer. Hybrid solutions can be adopted as well, providing higher energy efficiency compared with conventional buses and the possibility of limited emission-free and low-noise passenger transport through partially full electric drive.

1.1.2 Benefits and Challenges

Beyond the global warming and climate change issues, one of the most important driver for electric mobility is the ability to operate locally emissions free, contributing to the air quality in cities and with less noise. However, there are different challenges that need to be matched for speeding up the electrification process of road transport.

Emissions and Integration of Renewable Energy Sources

It is necessary to point out that a real climate benefit from BEVs can be achieved only by increasing the use of RESs. Indeed, GHG emissions need to be evaluated in three different stages: production, utilization and end-of-life of vehicles. Figure 1.3 shows all causes of GHG

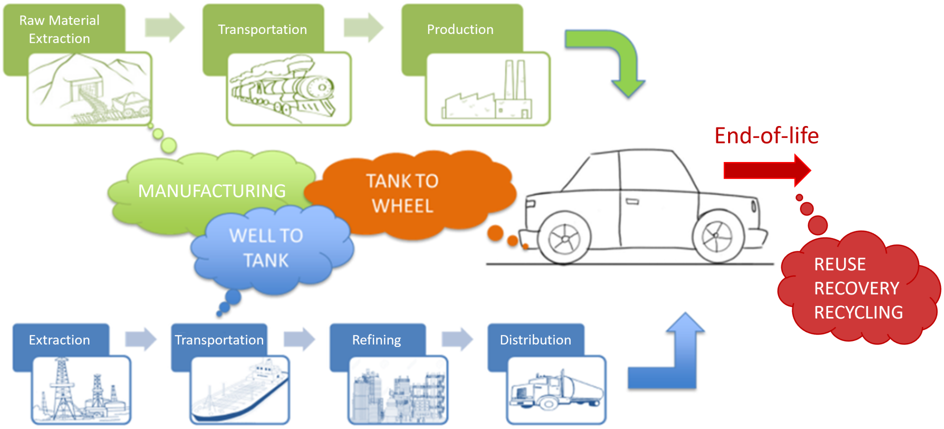

Figure 1.3: All causes of GHG emissions during the vehicle life stages.

emissions during the vehicle life stages. The emissions related to the vehicle production include those involved in raw material extraction and transportation. From a life cycle perspective, GHG and air pollutant emissions from BEVs production are generally higher than those from ICEVs production. This is largely due to the energy-intensive process of battery manufacture. Therefore, the impacts vary according to the battery chemistry and size, and the energy mix used in the production processes. Indeed, the negative environmental impacts of vehicle production can be minimized by increasing the adoption of RESs in providing energy for BEVs production.

On the other hand, the end-of-life stage is related to the possibility to recycle, recovery or reuse any vehicle component that results no longer able to meet the performance requirements. The end-of-life stage has the smallest impact in terms of total life cycle emissions. However, the reuse of lithium-ion batteries adopted for road transportation systems is becoming a relevant task for limiting the environmental impact of their end-of-life stages, leading to the second-life batteries. They can be used for stationary applications, where lower performance are required with respect to automotive standards.

For what concerns the utilization stage, the environmental impacts are typically described in terms of well-to-tank (WTT), tank-to-wheel (TTW) and well-to-wheel (WTW), in order to correctly compare impacts occurring from different stages of the fuel cycle. In detail, considering ICEVs, WTT refers to the processes needed to transform crude oil from wells into the fuel tank as useable petrol or diesel, and TTW refers to combustion in the engine. Whereas, considering BEVs,

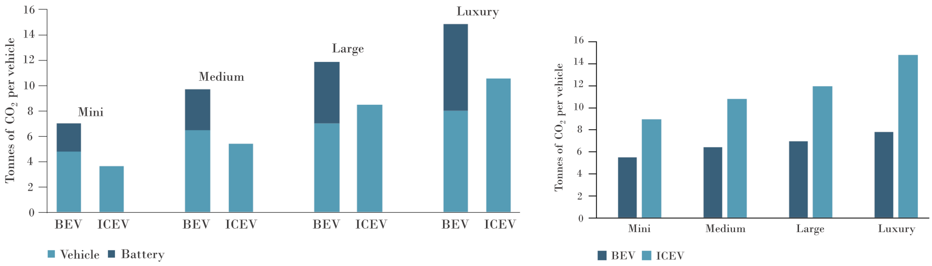

(a) (b)

Figure 1.4: CO_2 emissions for both BEVs and ICEVs during the production (a) and utilization (b) stages, including different car segments. [2]

WTT is related to any impacts from electricity production occurring upstream of vehicle charging, and TTW refers to the direct impacts of driving the vehicle. In the utilization stage, WTW emissions of GHG for BEVs tend to be lower than those for ICEVs. In addition, an intensive exploitation of RESs may strongly improve the environmental impacts in the utilization stage as well. Figure 1.4 shows the amount of CO_2 emissions for both BEVs and ICEVs during the production and utilization stages. These results provided by the European Environment Agency also include different car segments (mini, medium, large, luxury) depending on either the battery pack weight for BEVs or the total vehicle weight for ICEVs and BEVs [2]. Impacts are evaluated over a lifetime mileage of 180 000 km. As previously mentioned, the emissions due to BEVs production are higher with respect to ICEVs, especially for the contribution of battery manufacturers. While, BEVs allow for achieving lower environmental impacts than ICEVs thanks to their zero-emission TTW stage. Hence, it results clear that RESs can significantly help in reducing the CO_2 emissions in both production and WTT stages.

This is also confirmed by evaluating the WTW efficiency, which includes fuel production, distribution, retail and vehicle efficiencies, as illustrated in figure 1.5. The comparison is performed starting to different primary sources and fuels and by considering three vehicle categories (ICEV, BEV and FCEV). It results that higher WTW efficiencies can be achieved with the adoption of BEVs for all primary sources. However, only the integration of the RESs in the total life cycle of BEVs provides the highest WTW efficiency.

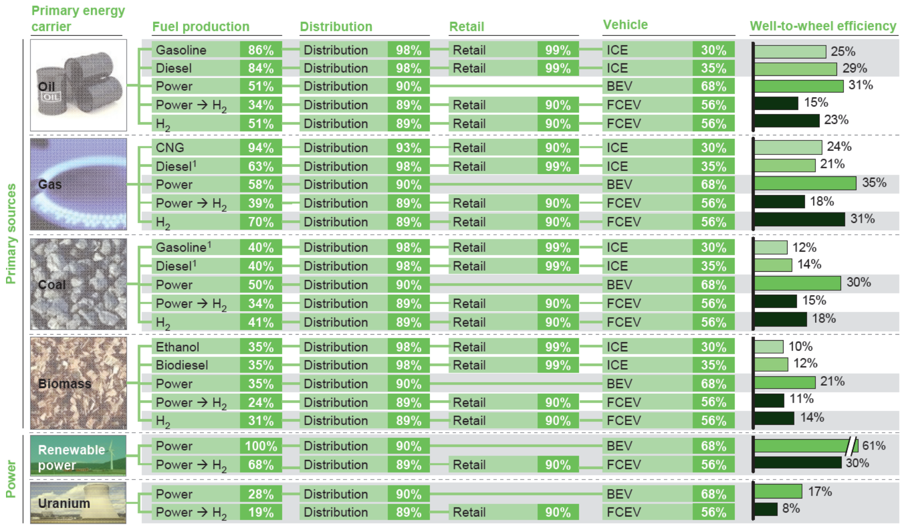

Figure 1.5: WTW efficiency starting to different primary sources and fuels and by considering three vehicle categories (ICEV, BEV and FCEV) [3].

Range and Cost

In order to increase consumer acceptance and enable a large-scale vehicle electrification, range capability improvements are fundamental for EVs. This will strongly depend on technological achievements in electro-chemical energy storage systems. Currently, the driving range for EVs can be extended only by increasing the energy capacity of the battery pack, leading to an increase of cost, size and weight as well. Efforts in improving the overall efficiency of the electric powertrain would also contribute to extend the range capability. However, considering the high efficiency already achieved from the current enhancements in EVs, an additional improvement would require much more effort to make modest increases in the driving range. On the other hand, battery cost is expected to fall in the next year, with increasing production numbers according to scale economies. These savings may be used by vehicle manufacturers for two different strategies: extending the range capability (higher performance EVs) or reducing cost of the vehicle, maintaining the existing driving range (user-friendly EVs).
Therefore, there are three points that need to be evaluated for matching the current range and cost issues of EVs:

- maintaining the driving range low may slow market uptake but it results an effective solution for lowering the costs;

- lower range could be compensated by improving charging comfort;
- vehicle manufactures may be forced by the market pressure to favor increases in driving range.

Charging Technology and Infrastructure

Improvements in charging technology and infrastructure represent one of the most important challenge for ensuring convenient and reliable recharging to urban dwellers and thus increasing the consumer acceptance of EVs. In particular, the following aspects are of particular interest from the user's perspective:

- *Wireless charging*

  Unlike ICEVs in which refueling can be operated typically once a week, EVs may require charging more frequently. Therefore, since there could be the possibility of picking up a little bit of a charge whenever the vehicle is not used, the charging infrastructures need to be as convenient as possible. Wireless charging is a promising complementary charge solution to be added to the conventional conductive one. It allows for recharging EVs easily thanks to the possibility to transfer energy without physical connection between charger and vehicle. The energy can also be transferred dynamically, with advantages in extending driving range and/or reducing the size of the battery pack. Moreover, wireless charging represents an ideal solution for urban transportation, where a high number of short stops are required. However, high control complexity and manufacturing cost is limiting the widespread of this technology for charging infrastructures.

- *Fast charging*

  High-power charging infrastructures represent an important solution for reducing the refilling time and thus partially overcoming driving range issues for EVs. Currently, these infrastructures include AC charging up to a 43 kW and DC connection for power levels up to 300 kW. Nevertheless, there are still several disadvantages that need to be better investigated. Firstly, considering the high power levels, a proper standardization of cables and connectors involved is required. Secondly, impact on the vehicle electrical architecture would have to be considered as well as the effects on battery pack lifetime. In addition, assuming a large-scale adoption of fast charging infrastructures, a major revision of the current electric grid needs to be operated for avoiding issues due to the peak power requested from simultaneous EVs in charging.

- *Vehicle-to-Grid*

  An interesting solution that has the potential to support the widespread use of standard low-power connecting points to the grid includes the vehicle-to-grid (V2G) technology. The idea is to share the energy stored in the battery packs of EVs connected to CP with the aim of providing locally grid support. V2G is very attractive for smart grid applications, since it can strongly contribute to the integration of RESs. It may suit long stay car parks at workplace or at transport hubs, such as airports and train stations. However, there are different barriers that limit the development of this technology. It is unclear how power would be monitored to allow accurate billing and power management. Indeed, charging and discharging processes impact on the battery pack lifetime. Therefore, the degradation cost of V2G service needs to be taken into account as well, depending on the number of cycles and power levels requested. In addition, the charging and discharging process is characterized by low efficiency due to the presence of two power converters: AC-DC for charging the battery pack and DC-AC for providing energy to the grid. There are also uncertainties related to the availability of a proper number of EVs when the peak power is required from the grid. High costs for the management and commissioning of V2G processes need to be considered as well.

1.1.3 Milestones for Electrified Road Transport

On the basis of the expectations, challenges and potential benefits of electric mobility previously described, the following ambitious milestones can be set for a more electrified road transport:

- mass production of passenger cars and scaling up of high duty vehicles electrification by 2020;
- fully revised EVs concept by 2025, including innovative zero

emission powertrain systems integrated with improved energy recovery and batteries as well as V2G and fast charging capabilities;

- redesigned electrified road transport meeting the requirements of the future connected and automated society by 2030.

The success and the rate of market penetration of EVs will strongly depend on the degree of usage of these vehicles in urban areas. Several cities have launched programs towards zero emission passenger cars and commercial vehicles. Despite the final target results a full pure electric inner city transport, a ramp-up phase is needed and meaningful. This could be achieved through HEVs with rather limited electric range and PHEVs, which could already cover most of electric driving range requirements towards BEVs or FCEVs. Easy-to-handle charging technology will certainly contribute to the electrification process, including high-power charging and V2G capabilities. Moreover, a relevant increase of acceptance of EVs can only be achieved by reducing significantly cost and eliminating or limiting driving range issues compared to ICEVs. Hence, major research efforts are needed in battery technology with the aim of improving the performance in terms of energy and power densities. Improvements of all other components of electric powertrains are also important for achievement of high market penetrations.

1.1.4 Market Trends

The future market penetration of EVs and PHEVs depends on a multitude of factors including technological developments, policy support, deployment of charging infrastructures, production capacity, future customer needs for mobility and their acceptance of new technologies, and economic parameters (vehicle production cost, vehicle total cost of ownership and energy prices). Bloomberg has provided a long-term forecast of how electrification, shared mobility and autonomous driving will impact road transport up to 2040 in [4]. Figure 1.6 reports a summary of the main interesting results, including EVs market trends from different perspectives.

Automakers are accelerating their EV launch plans, partly to comply with increasingly stringent regulations in Europe and China. COVID-19 will impact on the original timeline, leading to delays in production. However, it is still expected that there will be over 500 different EV models available globally by 2022.

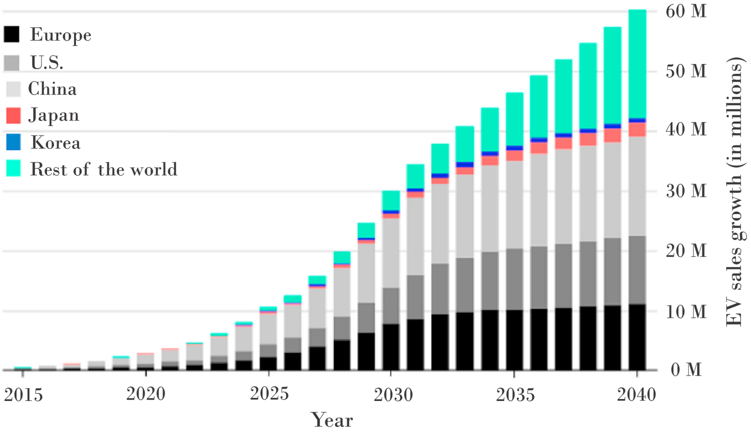

Figure 1.6: Market trends for passenger EVs in different countries. [4]

Passenger EVs sales will continue to rise up to 54 million units by 2040 as battery prices fall, energy density improves, more charging infrastructures are built, and sales spread to new markets. Moreover, despite the electric share of total vehicle sales is still small, it is estimated that over half of all passenger vehicles sold will be electric by 2040. Markets like China and parts of Europe achieve much higher penetrations, but lower adoption in emerging markets reduces the global average. Indeed, China will account for the largest share of global EV sales as it looks to reduce energy imports, clean up urban air quality, build its domestic auto industry, and attract manufacturing investment.
For what concern other road transportation categories, table 1.3 shows the expected electric share for two-wheeled vehicles (scooters, mopeds, motorcycles), urban buses and light commercial vehicles as well. Urban buses and two-wheelers result to be the most electrified vehicles. Heavy trucks are not included because they represent a more difficult category to be electrified, as highlighted in the previous sections.

	2020	**2030**
Urban buses	33%	58%
Two wheelers	30%	40%
Light commercial vehicles	2%	28%
Passenger vehicles	2.7%	28 %

Table 1.3: Expected electric share for different road transportation categories by 2030. [4]

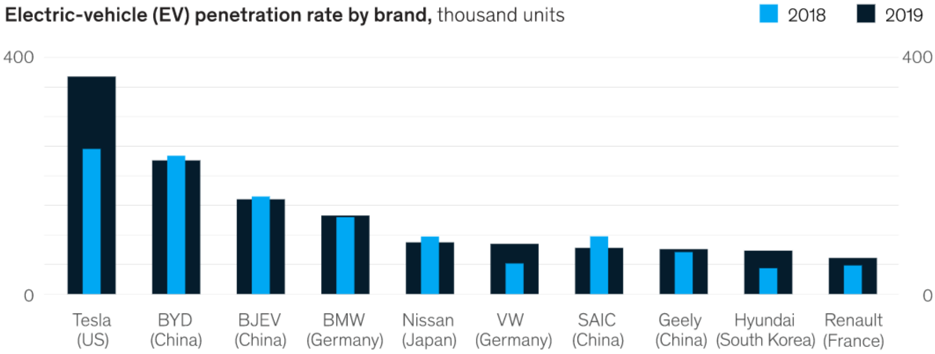

Figure 1.7: EVs penetration rate by considering market brands. [5]

In conclusion, it is important to mention the current key players operating in the EVs market. In particular, Tesla, BMW Group, Nissan Motor Corporation, Toyota Motor Corporation, Volkswagen AG, General Motors, Daimler AG, Energica Motor Company S.p.A, BYD Company Motors, and Ford Motor Company account for a major electric vehicle market share. However, Tesla results to be currently the market leader among EVs manufacturers, as illustrated in figure 1.7.

1.2 Vehicle Technology Architecture

As previously mentioned, depending on the architecture and the energy sources adopted, vehicles can be divided in conventional ICEVs, BEVs, HEVs, PHEVs and FCEVs. Each vehicle has its own capability and limitation in terms of emission rate, energy/power density, performance, fuel efficiency, size, weight, cost and safety. More details related to the architectures and operating modes are illustrated in the following sections.

1.2.1 Internal Combustion Engine Vehicle

Conventional ICEVs produce power by burning a petroleum fuel (gasoline/diesel) in their combustion chamber to propel the vehicle by means of mechanical transmission. Figure 1.8 shows the main components of ICEVs architecture. It consists of a fuel tank that provides the onboard energy source, the internal combustion engine and a mechanical transmission to transfer power from engine to wheels. Advantages of ICEVs include higher driving range due to the high en-

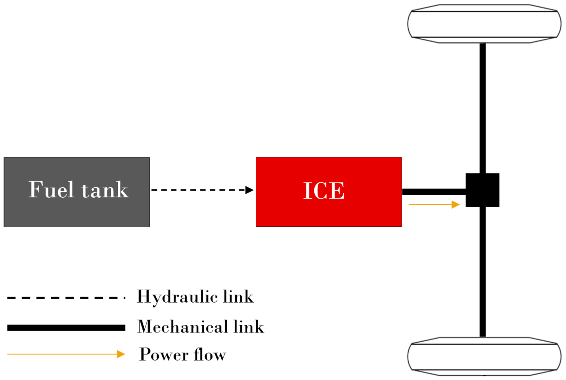

Figure 1.8: Architecture and main components of ICEV.

ergy density of liquid hydrocarbon fuels and lower refueling time with respect to EVs. The main drawbacks are low efficiency to convert the fuels into useful power and excessive tailpipe emission, which produces relevant impact on the environment in terms of GHG and pollutant emissions. The inefficiency of ICEVs strongly depends on the mismatch of engine power characteristic with the real load characteristic of the vehicles (high torque required at low speed). The impact of mechanical transmission efficiency and the waste of kinetic energy during braking contribute to further reduce the efficiency of ICEVs as well. Currently, improvements for ICEVs are focused on increasing energy efficiency and adopting more eco-friendly fuels [6], such as biodiesel and alcohol fuels (methanol and ethanol).

1.2.2 Battery Electric Vehicle

The architecture of BEV includes three main components: electric motor, power electronic converter and a battery pack as energy storage system. It is characterized by zero emission, high efficiency, independence of petroleum fuels, low noise pollutant, safe and smooth operation. Moreover, BEVs have the capability to recover the waste energy through regenerative braking. Disadvantages include high charging time and limited driving range. Therefore, advanced battery technology and intelligent energy management system are needed for strongly improving BEVs performance.

From what concerns the powertrain architecture of BEVs, figure 1.9 reports different configuration that can be selected depending on size, applications and cost constraints. The architectures shown in figures

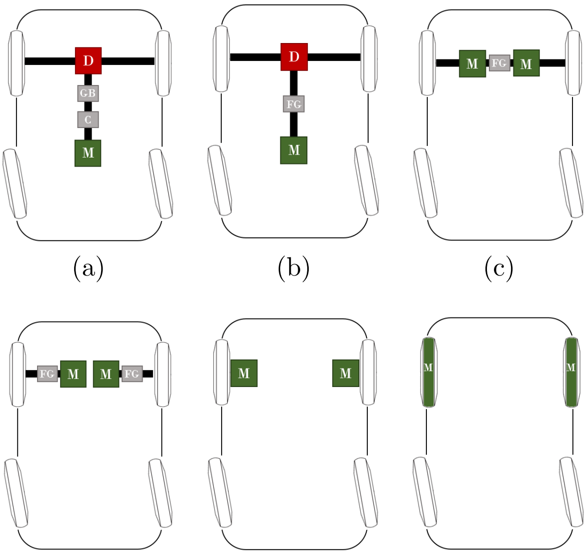

(a) (b) (c)

(d) (e) (f)

Figure 1.9: Different configuration for the powertrain architecture of BEV (C: clutch; D: differential; FG: fixed gear; GB: gearbox; M: electric motor).

1.9a, 1.9b and 1.9c adopt a mechanical differential, whereas those in figures 1.9d, 1.9e and 1.9f implement the electrical differential. In standard vehicles, the differential is a mechanical structure used during the cornering to transmit different speeds to the wheels. Indeed, the outer wheels need a higher speed to tread the curve compared to the inner ones. Figure 1.9a represents the typical solution implemented in a ICEV and used for replacing the engine with an electrical motor in an BEV. This topology of BEV has been adopted in the past years to maximize the utilization of the existing mechanical structures. Both wheels are connected to the same electric motor by means of a wide and heavy mechanical section (clutch, gearbox and differential). As result, this configuration has a huge mechanical transmission and it needs maintenance as for ICEVs.

However, considering the wide torque-speed range of an electric motor, the mechanical transmission of BEVs can be reduced by replacing clutch and gearbox with a fixed-gear, as illustrated in figure 1.9b. Moreover, including the differential in the fixed-gear transmission and using a double-motor architecture, it is possible to obtain the solution reported in figure 1.9c, which is usually adopted in modern BEVs.

Hence, the differential action can be provided using a double-motor structure with independent axis. In particular, electric motors can be connected to the wheels by means of a fixed-gear or directly, as shown in figures 1.9d and 1.9e, respectively. Gearless architecture (figure 1.9f) can also be considered for motor-wheels by adopting low-speed electrical motors. These architectures allows for maximizing the advantages of BEVs with respect to ICEVs in terms of cost, maintenance and efficiency. Indeed, they have a very poor mechanical transmission, leading to mechanical losses reduction.

1.2.3 Hybrid Electric Vehicle

An HEV aims to combine BEV and ICEV characteristics in order to achieve a sustainable solution in terms of driving range, cost, size, weight, GHG and pollutant emissions. It adopts two different energy sources to propel the vehicle, including a fuel (gasoline, diesel or hydrogen) and a stored energy (battery, ultracapacitor and flywheel). Hence, both electric motor and engine are needed.

The major advantages of HEVs are extended electric driving range, good fuel economy and sufficient onboard energy and power to meet the vehicle requirements in all driving profiles. Moreover, the presence of both electric motor and engine allows for achieving higher efficiency than ICEVs thanks to the possibility for the engine to operate at the minimum consumption operating point. The main concern is related to the management and control of power flows to properly coordinate the dynamics of the energy systems without compromising the vehicle performance. Indeed, combining BEV and ICEV technologies adds complexity in controls and makes the system heavier and costly. In addition, it is important to point out that the power flows from the fuel tank are unidirectional, while those from the energy storage system can be bidirectional. In particular, considering gasoline as fuel and battery as energy storage system, the following operating modes can be performed for a HEV:

1. Only gasoline provides to propel the vehicle (ICEV mode).
2. Only battery provides to propel the vehicle (BEV mode).
3. Both energy sources provide to propel the vehicle (HEV mode).
4. Gasoline supplies power to the battery.
5. Battery draws power from vehicle during regenerative braking.

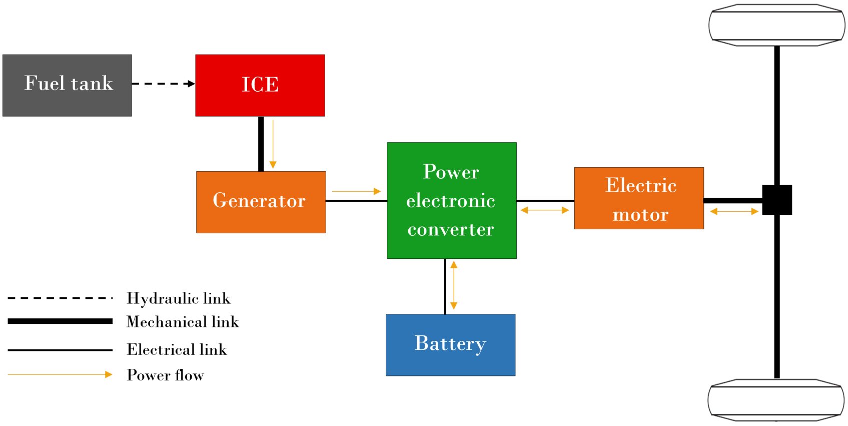

Figure 1.10: Architecture and main components of S-HEV.

6. Gasoline supplies power to both vehicle and battery.
7. Battery draws power from both vehicle and gasoline.
8. Gasoline supplies power to the battery, which provides to propel the vehicle.

Depending on the usage of the energy sources, HEVs can be classified into five categories: series, parallel, series-parallel, complex and plug-in configurations. Moreover, a hybridization factor is typically defined for HEVs, which represents the ratio between the rated power of the electric motor and the overall rated power of the vehicle. Based on this factor, two additional categories can be identified: Micro-HEV and Mild-HEV. The hybridization factor is very low for these two solutions. Micro-HEV is equipped with an electric motor with a rated power up to 2 kW, only for enabling the start-and-stop operation during a temporary stop of the vehicle. While, Mild-HEV also allows for the energy recovery during regenerative braking thanks to the integration of a low-capacity battery pack.

1.2.3.1 Series Configuration

A series hybrid electric vehicle (S-HEV) represent the simplest architecture for HEVs. It uses the two energy sources for empowering the electric motor, which provides to propel the vehicle. The ICE is mechanically coupled with an electric generator that is connected to both electric motor and battery pack through a power electronic converter, as illustrated in figure 1.10. Therefore, S-HEVs can also be considered as an ICEV without direct mechanical link between ICE and wheels.

All possible operating modes (1-8) of the two energy sources are applicable for S-HEVs. The operation of the ICE is controlled on the basis of the state of charge (SoC) of the battery. In particular, when the battery reaches the minimum SoC allowable, the ICE starts in order to charge the battery. While, the ICE stops when the battery reaches a desirable maximum SoC, which should be maintained in the range of 65%-75% of full charge in order to allow the battery to recovery energy during regenerative braking. In addition, a suitable control algorithm can be considered for ensuring the optimal operation of the engine, having high efficiency and low fuel consumption.

However, power flows from energy sources to wheels include two stages of power conversion (mechanical to electric and electric to mechanical), leading to increased energy losses and reduction in overall efficiency of the vehicle. The mechanical decoupling between the engine and wheels increases the degree of flexibility and reduces the complexity of the S-HEVs architecture. Moreover, since the electric motor provides a wide torque-speed range, multi-gear mechanical transmission system can be eliminated.

The main advantages include simplified construction, easy control strategy and reduced costs. While, the major concerns are related to the sizing of ICE, generator and electric motor due to weight and performance constraints. Reliability and versatility of this architecture also represent additional limitations due to the possibility to propel the vehicle only by the electric motor. The S-HEVs are suitable for city driving applications, where frequent starts and stops occur.

1.2.3.2 Parallel Configuration

In a parallel hybrid electric vehicle (PA-HEV), ICE and electric motor are connected in parallel to deliver power to the wheels, as illustrated in figure 1.11. The power split is operated by means of mechanical coupling, which increases the complexity of the control algorithm for PA-HEVs. All operating modes can be performed for better utilization of energy sources and reliable operation, except modes 7 and 8. Typically, the control strategy for PA-HEVs is based on enabling only the electric motor at low speed and only the ICE at high speed. In this way, ICE can operate at most efficient point, leading to better fuel consumption and reduced tailpipe emission. In case of

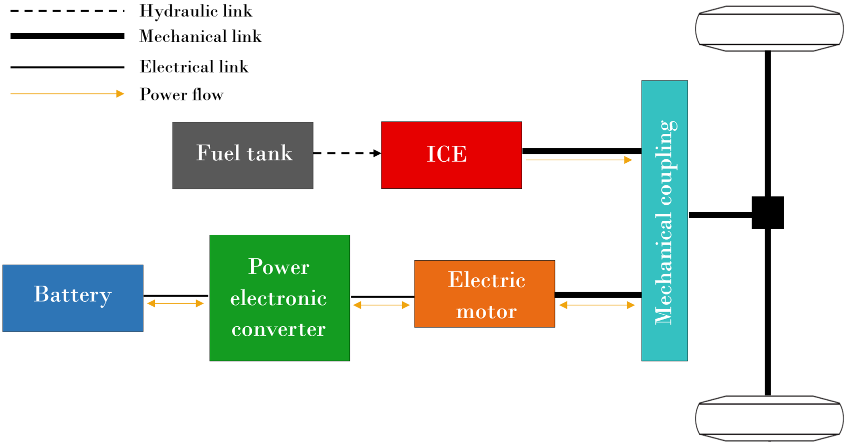

Figure 1.11: Architecture and main components of PA-HEV.

acceleration or hill climbing, both the power sources are activated to fulfill the desired power demand. The electric motor can operate as a generator to charge the battery when only ICE is enabled or in case of regenerative braking.
As compared with S-HEVs, a single-stage power conversion is needed for PA-HEVs. This increases the efficiency and reduces the weight and cost of the vehicle. Moreover, the possibility to split the power requested among ICE and electric motor allows for reducing their size. The main concern includes the optimal management of the mechanical coupling in order to achieve the best performance of the vehicle.

1.2.3.3 Series-Parallel Configuration

Series-parallel hybrid electric vehicle (SP-HEV) is an integration of the S-HEV and P-HEV. This configuration introduces an additional mechanical link with respect to the S-HEV and an additional generator with respect to the P-HEV, as shown in figure 1.12. SP-HEVs can be divided in electric-intensive and engine-intensive if the major contribution to the vehicle propulsion is provided by the electric motor and the ICE, respectively. Therefore, depending on the entity of this contribution, all the electric and mechanical components can be properly sized. The operating modes of both configurations are usually performed in the same way, including start, acceleration, deceleration, braking and battery charging. On the other hand, regarding the normal driving mode, the aim is to operate the engine at its most effi-

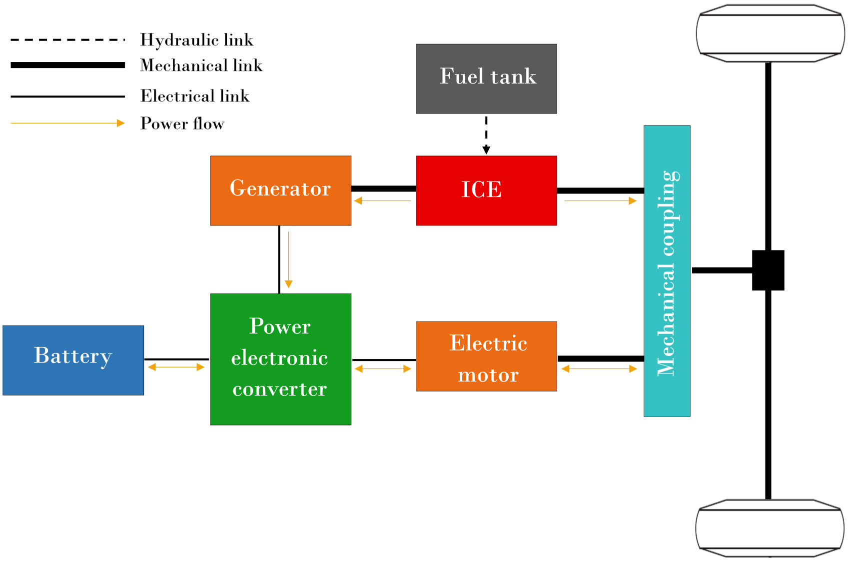

Figure 1.12: Architecture and main components of SP-HEV.

cient point. Despite the SP-HEV incorporates the advantages of both S-HEV and P-HEV, the adoption of additional electric and mechanical components (generator and planetary gear arrangement) increases complexity, weight and costs of this architecture.

1.2.3.4 Other Configuration

All the configurations previously discussed implement a single-axle propulsion for both front and rear wheels. However, complex hybrid electric vehicle (C-HEV) can also be adopted for implementing a dual-axle propulsion, as shown in figure 1.13.
In this way, both front and rear wheels contribute to propel the vehicle. Front-wheel and rear-wheel axles are decoupled from each other and there is no mechanical link between them. Therefore, both the axles are driven independently.
Unlike the SP-HEV in which the electric generator provides only an unidirectional power flow, C-HEV also allows for a bidirectional one, leading to additional flexibility and reliability. Both power flow configurations involve ICE, electric motor and generator to propel the vehicle. In particular, front wheels and can be propelled by hybrid propulsion system and rear wheels by electric propulsion system or vice-versa. A planetary gear arrangement is adopted for coupling ICE,

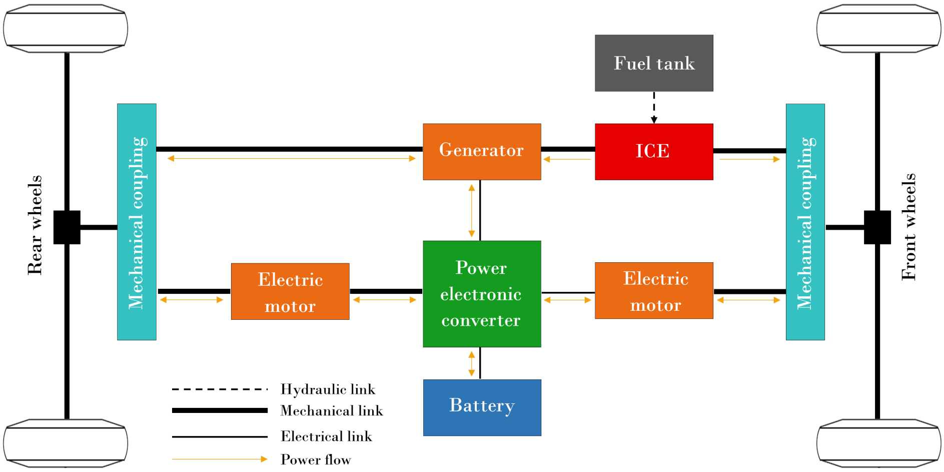

Figure 1.13: Architecture and main components of C-HEV.

front electric motor and front axle. The main advantage of C-HEVs includes the possibility to achieve an independent control of front and rear wheels, providing smooth vehicle operation and flexibility. Moreover, This, regenerative braking in all four wheels can significantly improve the overall efficiency of the system and thus fuel economy. Nevertheless, the large number of component needed strongly increases complexity, costs and weight of C-HEV.

1.2.4 Plug-in Hybrid Electric Vehicle

Plug-in hybrid electric vehicle (PHEV) is a transitional technology between BEVs and HEVs. Basically, PHEV is a HEV with large battery pack that can be recharged from an external source, such as the utility grid or RES, to extend the electric driving range of the vehicle. Therefore, all the configurations previously described for HEVs can be also adopted for PHEVs by integrating a recharging system, which includes a plug and eventually an on-board charger. More details about recharging systems for EVs will be provided in section 1.3.3.1.
PHEVs are also named as extended-range electric vehicles (E-REVs) because of their typical operation, reported in figure 1.14. In particular, there are three different operating modes. The first one is the electric-vehicle mode, also known as charge depletion phase, in which only the battery contribute to propel the vehicle. The battery is partly recharged with each regenerative braking event. Then, when the bat-

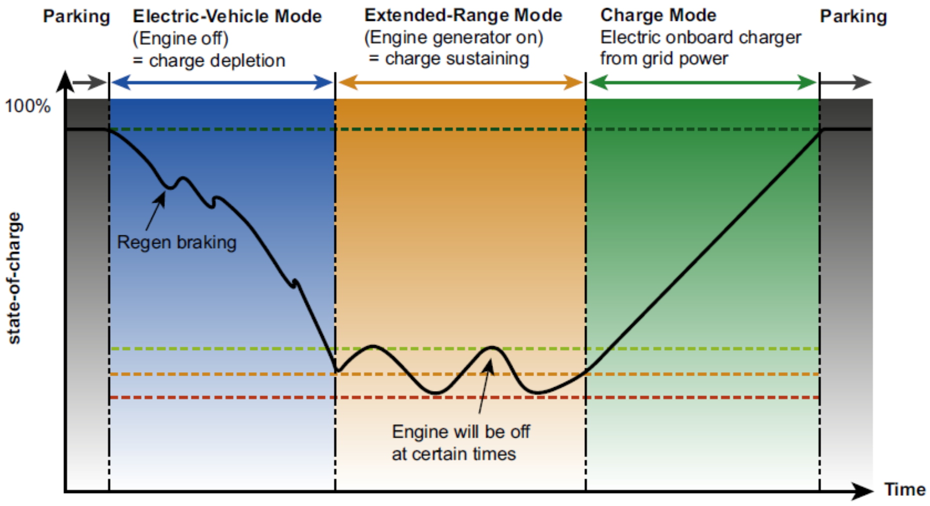

Figure 1.14: Battery SoC during the typical operation of a PHEV. [7]

tery is depleted to a defined minimum SoC, the vehicle switches to extended-range mode. Hence, the ICE is switched on with the aim of maintaining the battery within the SoC range marked by the green and red dashed lines in figure 1.14. After this phase named charge sustaining, the battery pack is recharged by means of the external source. In this way, PHEVs allows for extending the driving range of the vehicle while reducing the environmental impact. Furthermore, PHEVs represent an important solution for effectively enabling the V2G technology.

1.2.5 Fuel Cell Vehicle

Fuel cell vehicle (FCV) represents an alternative solution to EVs for meeting the requirements in terms of GHG and pollutant emissions. Indeed, unlike ICE, a fuel cell directly converts chemical energy into electric energy without internal combustion and pollution. On the other hand, unlike the battery, it can only generate electric energy and thus continue to supply energy as long as fuel is fed.
FCVs can be fueled with pure hydrogen gas stored on board in high-pressure tanks. They can also be fueled with hydrogen-rich fuels including methanol, natural gas, or even gasoline. In this case, an onboard component, named reformer, is needed to convert these fuels into hydrogen gas, leading to an increase of cost, complexity and

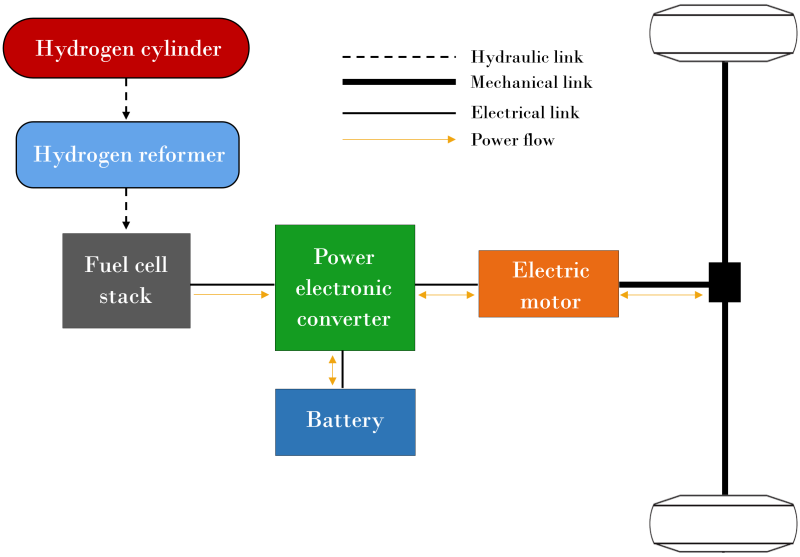

Figure 1.15: Architecture and main components of FCV.

weight of the vehicle. Moreover, zero emission can be achieved by considering FCVs fueled with pure hydrogen, only water and heat are produced as result of the fuel cell reactions. While, using hydrogen-rich fuels and a reformer, a small amounts of air pollutants is produced. Figure 1.15 shows the architecture of FCVs. The pure hydrogen coming from the reformer is fed to fuel cell stack where a chemical reaction occurs directly with the oxygen of the atmosphere, producing electric energy. In addition, since the power flow from the fuel cell to propulsion unit is unidirectional, low-capacity battery pack or ultracapacitor can be included in the architecture in order to allow energy recovery from regenerative braking. In this way, the energy stored can be provided to propulsion system during acceleration to assist the fuel cells. All the configurations and advantages of HEVs can be utilized by integrating ICE and battery pack with fuel-cell system. Furthermore, enabling bidirectional power flows between the battery pack and the grid, FCVs can also be operated as plug-in fuel-cell vehicles (PFCVs). The main advantages of this architecture include high efficiency, reliability and quiet operation with negligible emissions. While, major concerns are related to fuel cell cost and infrastructure issues for hydrogen conditioning, storage and refilling system.

1.2.6 Final Remarks

Among different types of electrified vehicles, HEV is the only one that currently has the potential to compete with ICEV in terms of performance and driving range. It offers advantages such as extended electric range of operation, good fuel economy, higher efficiency, sufficient onboard power, and better dynamic response. However, the integration of electric and mechanical components increases control complexity and makes HEVs comparatively bulky and costly. Nowadays, HEV technology is growing rapidly and capturing significant market space at a fast growth rate. Plug-in HEVs are currently at the commercialization stage. The efficiency analysis from WTW, the V2G technology and the impact of charging station on the grid are the major issues that need to be better investigated for a successful commercialization.

On the other hand, large-scale adoption of BEVs requires significant improvements in battery technology and charging infrastructures. FCVs are considered an alternative solution for vehicle technology. However, it is necessary to demonstrate that they have the ability to compete with ICEVs on cost, weight, onboard energy density and driving performance while ensuring benefits of BEVs, such as zero emission and high efficiency.

1.3 Electric Propulsion System

The sustainability of EVs is relying on maturity, which depends on technological advancement and development of its components. In detail, the architecture of an EV can be divided in three different section, as illustrated in figure 1.16:

- powertrain subsystem;
- energy source subsystem;
- auxiliary subsystem.

The powertrain subsystem consists of the electric motor and the power converter as well as the mechanical part of the vehicle, such as driving wheels, clutch, gear box, differential. Starting from the control signals of the user (brake and accelerator pedals, steering angle), this section is controlled by means of the electronic controller unit (ECU), named vehicle controller in figure 1.16. In particular, it generates the switching signals for the power converter to manage the power flow between

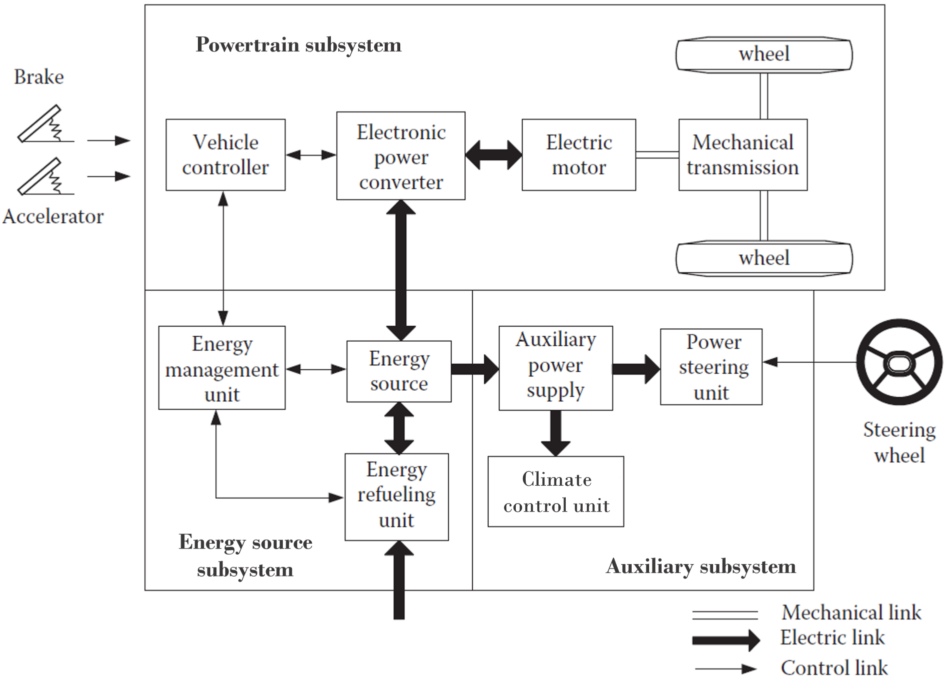

Figure 1.16: Architecture of an EV divided in three main subsystems. [8]

the electric motor and the energy sources and thus propel the vehicle. Moreover, since the energy flow can be bidirectional, the energy flows from the storage to the motor up to the wheels during traction, whereas the energy stored in the inertial masses is conveyed to the energy source through the power converter if regenerative braking is allowable. Otherwise, this stored energy is dissipated in the friction brakes.

The energy source subsystem includes the refueling and the management units. The first one is necessary to allow the recharging of the energy source. The energy management unit cooperates with the ECU in managing the power flows to and from the energy source in order to maximize the driving range and to ensure its safe operating conditions safeguard the energy sources. The auxiliary system consists of the power steering unit, temperature control unit and auxiliary power supply for the additional electric loads, such as heater, air conditioner, radio, indicators and other accessories.

Considering the strong connection between powertrain and energy source subsystems, they are usually grouped, leading to the electric

propulsion system (EPS) of the EV. Therefore, the main components of the EPS include the energy storage system, the electric motor and the electronic power converter. More details about the features of these components are provided in the following sections.
It is important to highlight that EPS plays a key role for the performance of an EV. The required characteristics of electrical drive for EV applications can be summarized as follows:

- high instant power and high power density;
- high torque at low speed;
- fast torque response;
- high efficiency over wide torque-speed range and during regenerative braking;
- high reliability and robustness;
- reasonable costs.

Moreover, EPS has to be sized on the basis of the desired accelerations, maximum speed, climbing capability, braking action, driving range and mission of the vehicle.

1.3.1 Energy Storage Systems

Energy storage system (ESS) represents a crucial aspect for vehicle electrification. Indeed, the efficiency, fuel economy and electric driving range of EVs strongly depend on the onboard ESS of the vehicles. It needs to be properly sized in order to ensure sufficient energy capability (kWh) and provide adequate peak power (kW) for achieving desired driving performance. In particular, the major factors that affect the design of ESSs for vehicular application include energy and power densities, life cycle, size, safety, maintenance and recyclability at projected cost.
The following four technologies of ESS are currently taken into account for EVs and HEVs:

- electrochemical batteries, including lead-acid, nickel-based and lithium-ion technologies;
- ultracapacitors;
- flywheels;
- fuel cells.

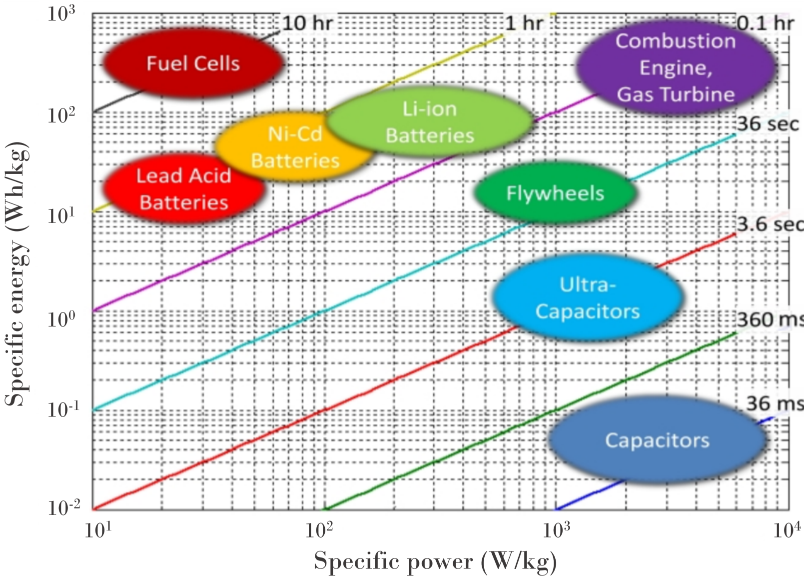

Figure 1.17: Ragone plot of different ESSs for vehicle technology. [9]

In addition, hybrid solutions based on the integration of these ESSs can be adopted as well. Figure 1.17 shows the Ragone plot for the ESSs considered, which highlights their basic characteristics in terms of power and energy densities. As result, ICE still remains the most desiderable solution due to the high specific power and energy of fossil fuels. Ultracapacitors are characterized by high power density, thus they are suitable for providing a high peak power in a very short period (milliseconds). On the other hand, fuel cells have high energy density and require long time period (hours) to be charged or discharged. This limits their applications in vehicle technology since both high power and energy densities are needed. While, among the electrochemicals batteries, Lithium-ion technology provides a reasonable compromise between energy and power densities. Indeed, it is currently considered as an attractive solution for HEVs and BEVs.

1.3.1.1 Battery Technology

Electrochemical batteries consist of positive (cathode) and negative (anode) electrodes immersed in an electrolyte and then inserted in a sealed container. They can convert chemical energy in electric energy bidirectionally. In discharging, electrons migrate from the anode to the cathode thanks to a reduction-oxidation reaction. In charging, the electrochemical reaction is reversed through the ionization of the electrolyte. The overall performance of batteries strongly depends on the electrochemical properties of each battery component. Therefore, numerous materials for electrodes and electrolytes are being selected for achieving the best performance depending on the application requirements [10]. Indeed, high-energy-density batteries are required for BEVs, whereas high-power-density batteries are suitable for HEVs and FCVs. Currently, among all the different battery technologies, the most common solutions for EVs include lead-acid, nickel-based and lithium-ion batteries [11].

Lead-acid batteries

Lead-acid batteries are based on a lead dust as anode (Pb) and a dioxide lead as cathode (PbO2), which are immersed in a solution of sulfuric acid (H2SO4). These represent the most mature and cheapest battery technology available. However, they are characterized by several disadvantages, including low specific energy density (30-40 Wh/kg) and power density (180 W/kg), short lifetime (500-800 cycles), high dependence on temperature, high self-discharge rate and high maintenance requirements.
Lead-acid batteries can be classified in two categories:

- *Shallow cycle batteries*

  Designed to provide high current for a very short period of time and capable of withstanding light overloads without electrolyte loss. These batteries are widely adopted as engine actuators in automotive applications, especially for ICEVs and micro-hybrid vehicles due their strong compatibility with alternators, longevity and reliability.

- *Deep cycle batteries*

  Designed to be frequently discharged up to 80% of their capacity with low discharging currents. These batteries are generally used in Uninterruptible Power Supply (UPS).

Nickel-based batteries

These batteries have a positive nickel electrode and a negative one that can be made with different solutions, including cadmium, zinc,

hydrogen, iron or a metal halide. The two electrodes are separated by a partition, which is selected according to the chemistry of the negative electrode material. After cell construction and packaging, liquid electrolyte is circulated into the porous electrodes. The classical structure of a nickel electrode cell is cylindrical.
The main nickel-based batteries are nickel-cadmium (NiCd) and nickel-metal-hydride (NiMH). However, only NiMH batteries are adopted for automotive applications due to their robustness and reliability. Advantages include very high power density (300-1000 W/kg) and a higher energy density (40-120 Wh/kg) with respect to lead-acid batteries. In addition, since NiMH are characterized by a low internal resistance, they result suitable for performing the charge sustaining mode in HEVs. On the other hand, NiCd batteries are typically used only for stationary applications since they have been prohibited for consumer usage due to the high toxicity of cadmium.

Lithium-ion batteries

Li-ion cell consists of a graphite negative electrode, a metal-oxide positive electrode, an organic electrolyte with dissolved lithium ions and a micro-porous polymer separator. In charging, lithium ions flow from the positive electrode to the negative one, whereas in discharging the reverse flow of ions occurs. The potential of lithium-ion batteries is still not fully explored and maturity level is yet to be achieved. Therefore, this technology is currently considered a very promising solution to enable the electrification of transport. In particular, there are two main aspects that make lithium-ion batteries such interesting for automotive industries:

- high design flexibility, since different cell shapes can be adopted, including cylindrical, prismatic and pouch solutions;
- possibility to achieve high-energy-density or high-power-density cells and high charging/discharging currents depending on the materiales used for electrodes and electrolyte.

Moreover, lithium-ion batteries are characterized by the highest cell voltage among the battery technologies, approximately of 3.7V. This allows for reducing the number of cells to be connected in series for meeting the voltage requirement. However, safety represents the major concern for this battery technology. In particular, most of the metal oxide electrodes are thermally unstable and can decompose at elevated temperatures, releasing oxygen and leading to potential thermal runaway. Therefore, a battery management system is needed for monitoring the operating conditions of the cells and preventing any safety issues. This increases the overall cost of the battery system. Currently, the main task remains to achieve a significant cost reduction with acceptable lifetime and safety.

1.3.1.2 Ultracapacitors

Generally, a capacitor consists of two electrical conductors separated by a non-conducting material, known as dielectric. When a voltage is applied across the conductors, it occurs an electric field in which the energy is statically stored. The capability of the capacitor to store energy is determined by the surface area of the conductors and the distance between them.

Ultracapacitors, also known as supercapacitors, are designed to have a very high capacitance by increasing the surface area of the electrodes. This leads to high specific power and low energy density. Moreover, compared to batteries, ultracapacitors have the advantage of large number of cycles to be charged and discharged with high current without loss in their performance.

Ultracapacitors have been used for ICEVs and submarines starting due to their ability of burst power delivery. In vehicle technology, they can be adopted as energy source for power delivery during starting, acceleration and hill climbing as well as for providing the energy recovery during regenerative braking. Ultracapacitors can also be integrated with batteries for improving the energy performance of EVs. This allows for downsizing and extending the life of a battery, reducing maintenance and replacement costs. The major concern includes the possibility to achieve a desired energy density at reasonable weight and cost.

1.3.1.3 Flywheel

A flywheel is a rotating mechanical device that allows for storing electric energy in form of rotational kinetic energy. In charging, electric energy is used to power a motor/generator that spins a shaft connected to the rotor in order to store energy. In discharging, the kinetic energy stored is extracted and converted back in electric energy thanks to a generator driven by the inertia of the flywheel. The energy is maintained in the flywheel by keeping its rotation at a constant speed. While, a speed increase results in a higher amount of energy stored. Moreover, flywheel rim rotates in an evacuated containment that reduces frictional losses and ensures safety in case of failure. Flywheel could represent a potential candidate as ESS in EVs for performing the energy recovery during regenerative braking. However, its implementation in vehicle technology has been limited due to heavy weight and high cost. Moreover, since high rotational speed is required for increasing the energy stored, the mechanical coupling between EV and flywheel becomes very difficult.

1.3.1.4 Fuel cells

A fuel cell is an electrochemical device that uses hydrogen (H_2) as fuel and oxygen (OH_2) from air to produce electricity with water and heat as by-products. It combines the best features of ICE (they can operate as long as fuel is supplied) and batteries (they can produce electricity directly from fuel, without combustion), thus reducing pollutant emissions and noise while increasing the efficiency. The specific energy of a fuel cell is similar to gasoline, whereas the specific power is very low. Therefore, battery or ultracapacitor needs to be used in conjunction with the fuel cell for improving the performance of FCVs. The main drawbacks of this energy technology include the availability of hydrogen, manufacturing cost, fuel generation and distribution as well as system complexity. In addition, fuel cell only allows for achieving a bidirectional power flow.

1.3.2 Electric Motors

The design of an electric motor (EM) for EVs needs to take into account different requirements with respect to industrial motors, which are usually operated at rated speed under common operating conditions. Indeed, EMs used for EPS should be able to provide:

- high torque for starting and low-speed hill climbing operation;
- high power density for acceleration and high-speed cruising for highway;
- high efficiency over wide torque and speed ranges;
- suitability for regenerative braking;
- overload capability during certain period of time;
- controllability, high reliability and robustness at affordable costs.

Moreover, fault-tolerant capability, minimum torque ripple, temperature management and low acoustic noise represent other important issues for the design.
The commonly used EMs for EPS include dc machine (DCM), induction machine (IM), permanent magnet synchronous machine (PMSM) and switched reluctance machine (SRM). While, EM control strategies can be divided in two categories on the basis of the number of control variables:

- *Scalar control*

  They are based on the steady-state model of the EM and allows for regulating a scalar quantity, such as the rotor speed. This control topology has usually a simple structure and it is used when high performance and high precision are not required. This category includes V/f and sω controls.

- *Vectorial controls*

  These controls are more complex since they are based on the vectorial model of EM, thus two scalar quantities are controlled in the entire machine operating range. This control topologies allows for achieving high accuracy and high dynamics performance. Relevant vectorial controls are the Direct Torque Control (DTC) and the Field Oriented Control (FOC).

DC machine

DCMs have been used prominently for EPS due to its high starting torque and simple speed control. Their torque-speed characteristics exhibits good compliance for automotive applications. However, there are relevant disadvantages that make DCMs unsuitable for EVs, including high costs, high maintenance, low efficiency, problems in dusty areas, low power density and low reliability due to the presence of mechanical commutators and brushes. In addition, technological advancements in power electronic converters and switches have strongly contributed to replace DCMs with commutatorless motors, such as IMs, PMSMs and SRMs. On the other hand, due to simple speed control and technical maturity, DCMs still remains a prominent solution for low-power EPS.

Induction machine

IM-based vehicles are considered as dominating candidate for EPS among various commutatorless motors. Advantages include simplicity, high reliability, robustness, wide speed range, low maintenance, low torque ripple/noise, low cost and ability to operate in hostile environment. However, there are also several concerns that need to be taken into account, such as high losses, poor power factor and low efficiency. Moreover, considering the same power rating, weight and volume of IMs are greater than PMSMs. Efforts are being made to resolve these issues either at design level or by proposing new control schemes and/or converter topologies.

Permanent magnet synchronous machine

In recent times, PMSMs are widely accepted by the leading vehicle manufacturers for designing the existing and upcoming EPS due to their high power density and reduced weight and volume for a specified power rating. This allows for a compact packaging of the machine with advantages in terms of reliability and on-board space saving for the EV. The reduced size of PMSMs enables an efficient cooling as well. Higher efficiency can be also achieved for PMSMs with respect to a IMs. However, PMSMs have several limitations due to the adoption of permanent magnets, which lead to high costs, short constant power region due to limited field weakening capability and fault-tolerant issues.

Switched reluctance machine

SRM is gaining more attention for EPS in automotive applications, especially for HEVs and FCVs. It is characterized by a rotor without magnet and windings, which offers simple and robust construction that is desirable for very-high-speed and high-temperature operation. Other advantages include excellent torque-speed characteristics, fault-tolerant capability, smooth and hazard-free operation, and a larger constant power region with respect to PMSM. The major limitations of SRMs are high acoustic noise, vibrations, high torque ripple, complex control mechanism, and requirement of specified converter topology for the measurement of the air gap field. However, despite the cost of SRMs is relatively high, their mass production is expected to make them as cost-effective as IMs.

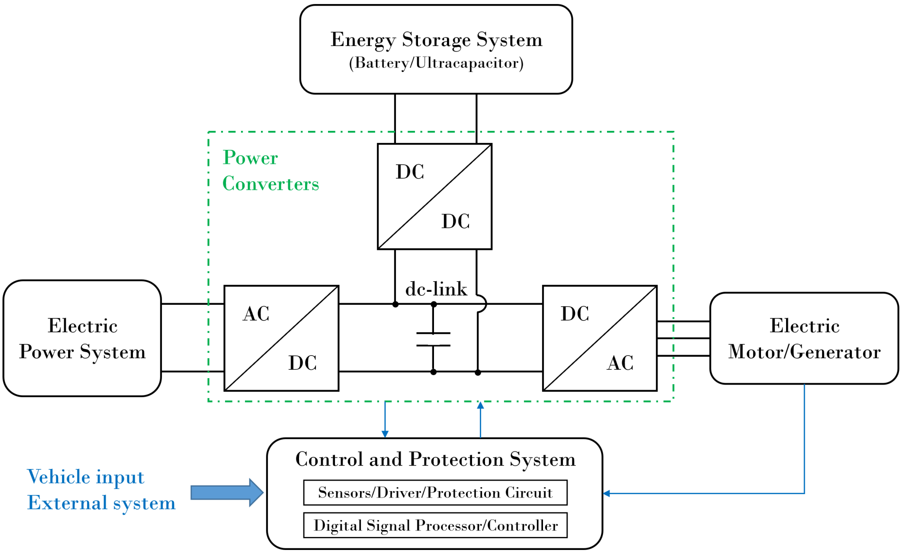

Figure 1.18: Architecture of EPS for EVs.

1.3.3 Power Electronics Converters

Power converters are responsible of controlling, managing and optimizing the power flow among energy sources and vehicle loads, representing a fundamental component in the EPS. In detail, they perform the following critical tasks:

- switching of actuators, valves and equipments;
- power conditioning and voltage/current modulation to create compatibility among the energy sources;
- control of traction motors in order to meet the vehicle requirements in terms of torque and speed;
- manage of auxiliary loads, such as air conditioner, head lamp and power steering.

Figure 1.18 shows the typical architecture of EPS for EVs, including interconnection among electric power system, ESS, powertrain system as well as control and protection system. The main components of the power conversion stage comprise an AC-DC charger, a bidirectional DC-DC converter and a DC-AC traction inverter.
The AC-DC charger with power factor correction (PFC) is needed for recharging the battery pack of BEVs or PHEVs from the electrical

grid. This can be also designed for bidirectional power flows in order to enable V2G technology. A proper charging-discharging profile for transferring energy between ESS and the powertrain system can be achieved by means of a bidirectional DC-DC converter. This also allows for improving ESS performance in terms of SoC and efficiency. The DC-AC traction inverter converts the DC power from the ESS to power the electric traction motor, which provides to propel the vehicle. Furthermore, the traction inverter is usually bidirectional to provide the possibility of recharging the battery pack thanks to the energy recovery during the regenerative breaking. In particular, depending on the electrical characteristics of the EM, four major topologies of traction inverter can be considered:

- H-bridge converter;
- Voltage Source Inverter (VSI);
- multilevel converter;
- resonant converter.

H-bridge converter is used for EPS equipped with DCMs, while VSI results suitable for EVs that adopt three-phase AC machines. Multilevel converters represent a proper solution for EVs as well, especially for high-power and high-voltage motor drives.
On the other hand, the DC-DC converter architectures can be classified as isolated or non-isolated on the basis of the presence of the transformer. Isolated DC-DC converters usually include high-frequency transformer and are used especially in case of hybrid ESS. In detail, it can be necessary when the energy sources cannot be grounded together or when it is necessary a ratio between the sources and the dc-link. The adoption of power transformer causes additional losses and costs. The DC-DC converters adopted for EVs are:

- buck converter;
- buck-boost converter;
- H-bridge converter;
- push-pull converter;
- resonant dc-dc converter.

Moreover, different solutions for the DC-DC conversion stage can be considered when hybrid ESSs need to be integrated. Indeed, the voltage levels and the dynamics are different for each ESS, thus a proper converter architecture is required. In particular, power conversion sys-

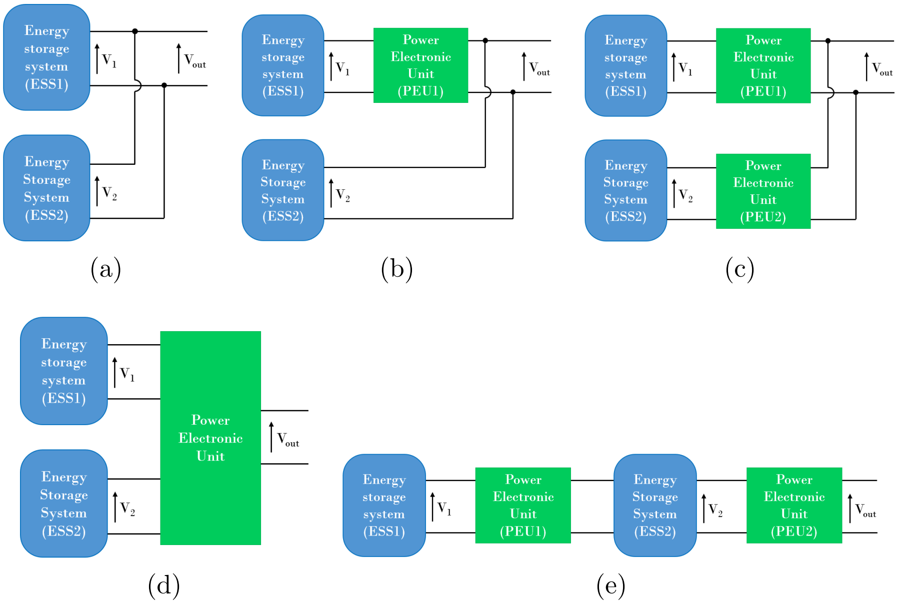

(a) (b) (c) (d) (e)

Figure 1.19: Topologies of hybrid ESSs: (a) direct parallel connection; (b) parallel connection with one converter; (c) parallel connection with two converters; (d) multiple-input converter configuration; (e) cascaded connection.

tems for hybrid ESSs can be grouped in five topologies, as illustrated in figure 1.19. A direct parallel connection topology is shown in figure 1.19a. This solution is used when the voltage levels of the two energy sources are equal to the dc-link voltage of the traction inverter. In this case, the power flow sharing is regulated by means of different impedances of the sources. As example, in case of hybrid battery-ultracapacitor ESS, ultracapacitor has low impedance and provides the power peak, while battery supplies energy.

Other topologies adopt power converters for regulating the power flows coming from the different energy sources with the aim of achieving a more flexible solution. In detail, figure 1.19b shows a topology in which one conversion unit PEU1 regulates the power flow coming from the energy source ESS1. Figure 1.19c reports a solution in which a converter for each ESS is considered and both energy sources are connected in parallel to the same dc-link. Despite this solution is more expensive than the previous ones, it ensures the best performance in terms of efficiency and control of the two ESSs. A multiple-input

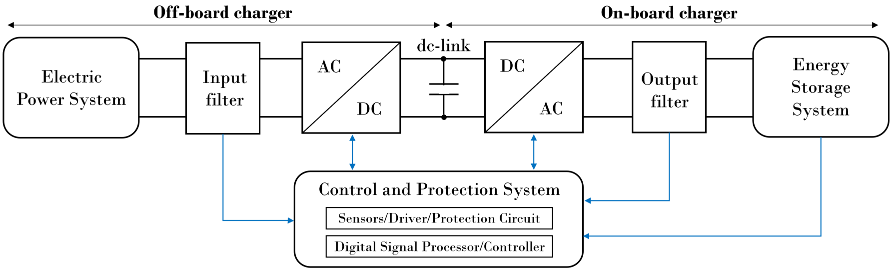

Figure 1.20: Simplified architecture for a battery charger.

converter configuration is shown in figure 1.19d, where both energy sources are controlled by means of an unique and more complex power converter. Moreover, starting from the solution shown in figure 1.19b, a cascaded connection can be performed by adding a DC-DC converter on the dc-link.

1.3.3.1 Battery Charger

Among the power converters for vehicle technology, AC/DC chargers play a critical role in the sustainable development of BEVs and PHEVs. A battery charger should be reliable and efficient with high power delivery capacity at low cost and weight. The availability of charging infrastructures can certainly contribute to reduce the size and capacity of onboard ESS with advantages in terms of cost and driving performance.
Currently, three types of charging stations can be identified on the basis of power-handling capacity, charging time and location of CP. *Type-I* is the slowest method of charging, designed for home or business sites with readily available power outlet and no additional infrastructure is required. While, dedicated infrastructure and charging equipments are needed for *type-II* method. However, BEVs and PHEVs owners are likely to prefer type-II charging technology due to its lower charging time and standardized vehicle-to-charger connection. *Type-III* is a commercialized fast charging method and offers high-power charging capability. It can be installed in highway and city refueling points, similar to conventional fuel stations. Type-I and type-II charging infrastructures are usually equipped on-board, whereas type-III chargers are installed off-board. Figure 1.20 shows a simplified architecture for a battery charger, highlighting the typical on-board and off-board components.

In detail, three different solutions can be considered for a battery charger:

- *On-board and off-board charger*

  The on-board charger is installed in the vehicle and designed for slow charging rate, leading to high charging times. In addition, it needs to be light and compact in design due to limitation in available space in vehicle and payload. The advantage of on-board charger include the possibility to recharge the battery at anyplace where an electric outlet is available. On the other hand, an off-board charger is less constrained by size and weight and provides redundancy in power converters, which adds flexibility in the system. Moreover, both on-board and off-board chargers can be designed for allowing unidirectional or bidirectional power flow. This results fundamental for enabling the V2G technology.

- *Integrated charger*

  This charger can be adopted for overcoming the disadvantages of on-board chargers related to weight, volume cost and space over specific power capacity of the battery. It is based on the possibility to integrate the battery charger with the propulsion inverter-motor drive. In particular, integrated chargers adopt the traction inverter as a bidirectional ac/dc converter and the motor windings as filter inductors. Therefore, this solution results feasible only if the vehicle is at rest. The main advantages of integrated chargers include low cost, high-power-density bidirectional power flow and fast charging with unity power factor. However, extra component requirement, control complexity and specified design for both traction inverter and EM represent the major concerns for its successful implementation.

- *Inductive charger*

  In conductive charging systems, since the battery pack is directly connected to the power outlet through charger connecting cable, vehicles need to be parked and plugged into CP. As alternative, inductive or wireless power charging allows for transferring energy from power outlet to the on-board battery pack magnetically. Figure 1.21 shows a simplified architecture for an inductive charging system.

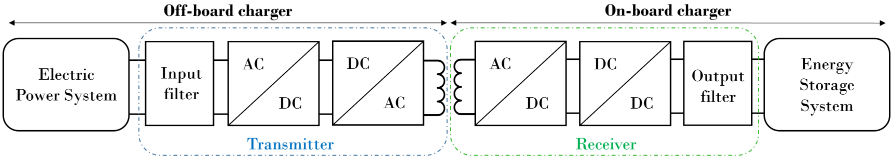

Figure 1.21: Simplified architecture for an inductive charging system.

The working principle is based on the magnetic coupling between two coils of a very-high-frequency transformer. The first coil, known as transmitter, is mounted off-board in the charging station, whereas the second one, named receiver, is installed on-board in the vehicle. Different power conversion stages are needed for converting the low-frequency power from the electric grid in a very high-frequency one. Then, this high-frequency power received from the vehicle coil is converted to DC in order to recharge the battery pack on-board.
The main advantages of inductive charger include the disposal of cable connectors, user convenience and galvanic isolation. Moreover, this solution allows for enabling the charging of the battery pack while driving, leading to a dynamic wireless charging technology. However, relatively low power density and efficiency, high control complexity and manufacturing cost represent several concerns that are limiting a large adoption of inductive chargers.

Chapter 2

Lithium-ion Battery Packs

Currently, lithium-ion battery packs represent a crucial component for the EPS of EVs, since they strongly impact on the performance and the overall cost of vehicles. Therefore, a detailed knowledge of battery features is needed at both cell and pack levels in order to better understanding the limitations of the current technology.

In this chapter, after an introduction related to the main battery terminology, the architecture and the operating principles of lithium-ion cells are illustrated, highlighting the most adopted materials and future trends. Then, major components of the battery pack architecture for automotive applications are discussed. A brief overview regarding the battery modeling approaches, safety and aging conditions is reported as well.

2.1 Terminology

In this section, the key characteristics of batteries are reported, since they will be widely used in the following paragraphs. These are generally referenced to assess the performance of batteries as well.

Open circuit voltage

The open circuit voltage (OCV) is the difference in potential between the battery terminals when there are no current flows for a substantial period of time and thus the battery is fully rested. High-accuracy and specific instruments are requested for measuring the OCV since the majority of voltage meters introduce a low-amplitude current for the measurement, leading to issues in detecting the OCV.

On the other hand, a typical experimental-based approach consists in assuming the OCV equal to the voltage difference between the battery terminals after a suitable rest period to extinguish the electrochemical dynamics. However, depending on the chemistry of the battery and the charging/discharging current profile applied, a different rest period is needed for measuring the OCV, ranging from several minutes to hours. Moreover, the OCV usually depends on temperature and state of charge of the battery.

Terminal voltage

This represents the voltage measurable between the battery terminals when a load or a charger is applied. It varies with the operating conditions of the battery.

Internal resistance

This is the overall resistance measurable between the battery terminals. It strongly depends on current sign (charging or discharging), temperature and state of charge of the battery. As the internal resistance increases, the battery efficiency decreases and thermal stability is reduced since a larger amount of charging/discharging energy is converted into heat. In addition, a higher voltage drop occurs, leading to lower discharging time.

Capacity

The capacity of a battery is the amount of electric charge expressed in Coulomb or Ampere per hour (Ah) that can be stored under specified conditions. Because of the chemical reactions within the battery, the capacity strongly depends on the charging/discharging conditions, such as the magnitude of the current profile, the allowable terminal voltage of the battery and temperature. Indeed, if a battery is charged or discharged at a relatively high rate, the available capacity will be lower than expected. The rated value of the battery capacity is usually defined as the amount of charge that the battery can deliver from fully charged to fully discharged conditions at a very low constant current and an operating temperature of 25°C. Therefore, the capacity is obtained by integrating the current in time, while the battery voltage drops from the maximum to the minimum values prescribed by the manufacturer. Furthermore, the nominal capacity can also be expressed in terms of energy (kJ or kWh) by multiplying for the nominal voltage, which roughly corresponds to the voltage at mid-charge conditions.

C-rate

The C-rate describes the rate of charge or discharge current expressed in a normalized form. Indeed, it is calculated as the ratio between the nominal capacity of the battery and the specific amplitude of the current. The C-rate is typically defined with the expression C/x, where x represents the number of hours to completely discharge the battery at a constant current. The battery manufacturers usually report the impact of C-rates on the battery capacity.

State of Charge

The state of charge (SoC) is a dimensionless value that indicates the amount of usable charge in the battery at a given time. It is usually expressed as a percentage of the rated capacity and it can be measured by integrating the charging/discharging current. However, since this approach (known as Coulomb counting method) results affected by measurement errors, state observers are needed for correctly estimating the SoC. More details related to the estimation methods for the SoC of batteries will be illustrated in section 3.2.4.1. It is important to highlight that batteries are never utilized in their entire SoC range in order to avoid undesired aging and safety conditions. In particular, regarding automotive applications, the usable range of SoC for PHEVs or BEVs is about 75-80%, from 10-15% to 95%. While, a lower usable range (10-20%) is considered for HEVs. For this reason, the battery pack of EVs are usually oversized for meeting the capacity requirement and compensating the reduced usable range of SoC.

Depth of discharge

The depth of discharge (DoD) represents the complement of the SoC and expresses the amount of battery capacity that has been discharged as a percentage of the nominal capacity.

State of energy

The state of energy (SoE) is used in replacement of the SoC to indicate the effective battery capacity in terms of energy content (kJ or kWh). Despite the similarity of these two parameters, the SoE is different from the SoC because it partially takes into account for the effect of the internal resistance and the efficiency of the battery as well. The SoE is generally used in PHEVs and EVs, where a large fraction of the nominal capacity of the battery is used.

Energy density

This represents the amount of energy contained in a specific quantity of battery material. It can be normalized based on the mass (Wh/kg) or the volume (Wh/L) of the battery, leading to the gravimetric or volumetric energy densities, respectively. Energy density strongly influences the design of EVs in terms of weight and handling of the vehicle, including its drivability, stability and overall fuel consumption. Moreover, it is responsible of the electric driving range in BEVs or PHEVs.

Power density

This designates the maximum electrical power available from and to the battery per unit weight. As for the energy density, it can be expressed as gravimetric (W/kg) or volumetric (W/L) power density. It is responsible of the vehicle performance for BEVs or PHEVs. While, it results very important for HEVs since it influences the amount of energy stored during regenerative braking as well as short bursts of drive assist, such as start-and-stop operation and vehicle acceleration.

Self-discharge and Calendar life

This indicates the rate of discharge of batteries when no current flows occur, thus neither charger nor load are connected to the battery. This undesired discharge is governed by chemical reactions that depend on the construction of the battery as well as impurities in the electrodes and electrolyte. Lithium-ion batteries are characterized by the lowest self-discharge rate compared to other battery technologies. The self-discharge rate is also related to the calendar life of batteries, which represents the life expectancy during storage.

Cycle life

The cycle life or Useful Life (UL) represents the life expectancy of a battery when subjected to cycling. It is usually defined as the number of complete charge/discharge cycles that a battery can perform before its nominal capacity falls below 80% of its initial rated capacity. An alternative measure of cycle life is based on the internal resistance of the battery. In detail, it is defined as the number of cycles that the battery can perform before a 50% increase of its internal resistance occurs with respect to the initial value. The measure of the usable life of a battery results fundamental for correctly defining the end-of-life (EoL) condition and thus when a replacement is needed due to performance reduction. However, this is a very difficult parameter to be evaluated since it strongly depends on the operating conditions of the battery during its life in terms of current profiles and temperature. For this reason, the cycle life represents a key issue in the production of EVs, where certain driving range and life expectancy are required.

State of health

The state of health (SoH) is an indication of the condition of a battery compared to its ideal conditions. The battery SoH decreases over time and depending on the operating conditions of the battery. However, unlike the SoC, it does not correspond to particular physical quantity. Therefore, there is not uniformity in the SoH estimation methods adopted for real-world applications. More details related to the SoH estimation methods will be illustrated in section 3.2.4.2. Conventionally, SoH accounts for three indicators: capacity, internal resistance and self-discharge. For what concerns lithium-ion batteries, the SoH generally refers to the capacity since internal resistance and self-discharge remain low under normal usage conditions.

2.2 Cell Architecture

Cells represent the smallest individual electrochemical unit for battery technology. Therefore, the performance characteristics of large battery pack are determined by the basic electrochemistry that occurs at the interfaces of the system components at the cell level. Currently, there are two main advantages that make lithium-ion cells the most promising technology for the EPS of automotive applications. The first one includes the wide design flexibility for the cells, which allows for a better distribution of the battery pack on-board. The second one is related to the possibility of selecting a large variety of materials for the cell components. This leads to specific design of the cells in terms of energy and power densities depending on the application requirements. However, further improvements are required for achieving a successful mass introduction of electrified mobility with market competitive performance. Therefore, advanced lithium-ion cells need to be developed by improving electrochemistry and battery materials.

2.2.1 Construction and Design

The lithium-ion cells are available on the market in four different formats, illustrated in figure 2.1.

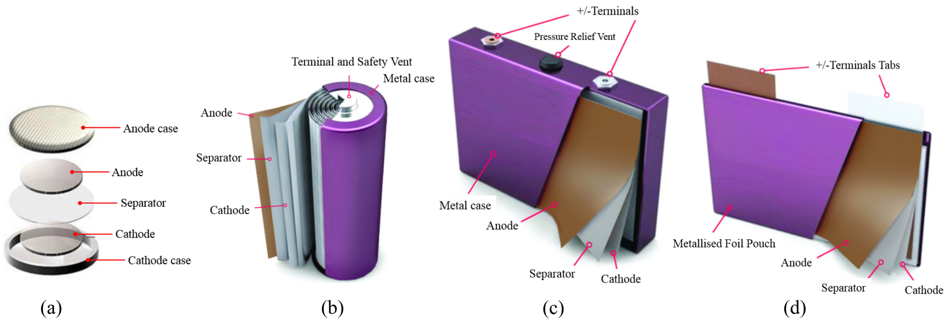

Figure 2.1: Cell formats available on the market: (a) button/coin, (b) cylindrical, (c) prismatic and (d) pouch.

Button/coin

These are very small size cells with a compact design, which are mostly adopted for powering small devices, such as watches, phones, car keys, security wands, medical aids, remote controls, and even small LED flashlights. Indeed, their capacity is very limited, thus they cannot be used for applications that require more power. However, despite they are not expensive, the button design leads to two main drawbacks. Firstly, there is not a safety vent to let out any gases that might be produced in the cell. Secondly, the battery can swell if subjected to high charging C-rates.

Cylindrical

This represents the most widely used packaging style. The cylindrical design has good cycling capabilities, offers a long cell lifespan and it is economical. Other advantages include an easy manufacturing process and mechanical stability since the cylindrical shape can withstand high pressure. However, this cell format tends to be heavy and has a low packaging density due to its space cavities. The majority of the cylindrical cells is characterized by a pressure relief mechanism in which a membrane rupture occurs at high pressures. Since leakages and dry outs may occur once the membrane breaks, these cells have resealable vents with a spring-loaded valve, which opens to relieve the pressure. In addition, many lithium-ion and nickel-based cylindrical cells have a positive thermal coefficient (PTC) switch, which heats up and becomes resistive when high currents passes through it, acting as a short circuit protection. Then, when the PTC cools down, conductivity returns and current can flow. Other lithium-ion cells are

characterized by a charge interruption device that causes physical and irreversible disconnection of the cell when unsafe pressure builds up.
Cylindrical cells are mainly used for power tools, electric bicycles and medical equipment. Manufacturers provide different cell lengths in order to increase their adoption. The 18650 is the most popular cylindrical lithium-ion cell-package available. Other formats include the 20700, 21700, 22700 and 26650 cells, which provide higher capacity with respect to the 18650 format.

Prismatic

This format has been developed in response to the need for thinner cells. Prismatic cells are wrapped in thin cases and make optimal use of space inside the cell by using a layered approach. In detail, they are constructed in a wound or flat plate configuration, leading to different manufacturing process. The first configuration is generally based on wrapping the layers around a bobbin or mandrel, similar to that of a cylindrical cell. While, discrete layers are stacked side by side and pressed together or folded in a flat plate cell. In both configurations, the layers are contained in a rigid case that provides terminal connections and includes a vent plug. Some swelling can occur due to gases building up, which may causes the cell to press against the battery compartment.
Standards are not uniform for this cell format, thus each manufacturer develops prismatic cells on the basis of their specifications and needs. They are mainly adopted in smartphones, tablets and low-level laptops. On the other hand, prismatic cells can also be used in large formats packaged in welded aluminum or steel housings for achieving higher cell capacity compared to the cylindrical format. These large format cells are usually designed for EVs. In particular, despite the lower energy density due to the packaging, they are suitable for heavy-duty vehicles thanks to their high robustness and reliability.

Pouch

These cells use conductive foil tabs that are welded to the electrodes and sealed shut. These tabs or conductors are typically attached in either an axial or radial position, as shown in figure 2.2. Axial placement allows the tabs to be wider, lowering the total series resistance and increasing the ability to conduct heat from the package. Pouch cells offer simple, flexible, and lightweight solutions to battery form factors. Moreover, they can deliver high current loads and represent the most space-efficient cells, achieving about 90% packaging

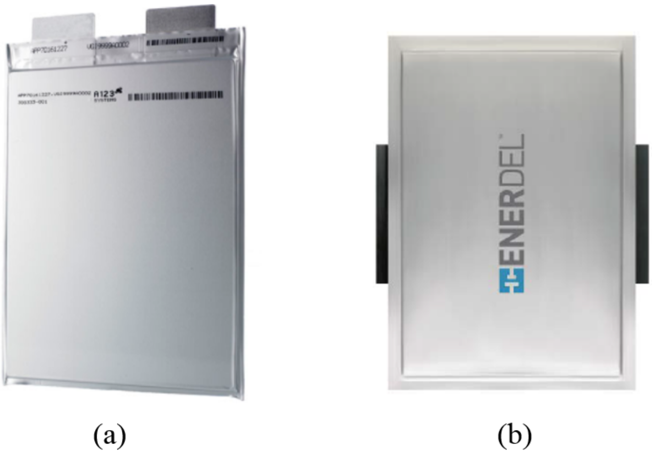

Figure 2.2: Pouch cell with tabs attached in radial (a) or axial (b) position.

efficiency, which is the highest among batteries.
However, improvements to the design need to be performed to solve the excess swelling due to gassing. Indeed, if overcharging or overheating occur, the pouch cell releases gases and may expand, causing the layers to separate. In addition, the pouch material offers little physical protection, thus an external structure is required for the module or battery housing to support, restrain, and protect the pouch cell. As for the prismatic format, no standard size exists for the pouch cells. Typical applications for this cell format include equipment that needs high current loads, resulting very suitable for EVs.

2.2.2 Components

Regardless of form factor, lithium-ion cells consist of four main components:

1. *Cathode* - positive electrode based on an aluminum foil coated with the active cathode material.

2. *Anode* - negative electrode based on a copper foil coated with the active anode material.

3. *Separator* - usually made of some type of polypropylene or polyethylene plastic and divides the two coated foils material, preventing short circuits.

4. *Electrolyte* - is a solution of lithium salts contained in an organic liquid solvent.

Both electrodes are composed by a mixture of three different elements, also known as slurry. The first one is the active material, which is responsible of storing lithium ions during the charge and discharge processes. The second element is the graphite that allows for improving the low conductivity of active materials due to the presence of oxygen. While, the third element is a polymeric binder with good elastic properties. Since several active materials change volume when they accept or emit lithium ions, this polymeric binder results fundamental for avoiding undesired crack propagation during charging and discharging cycles, which would substantially cause a reduction in the amount of material inside the cell or degradation/aging and thus performance reduction in terms of capacity or internal resistance.

The cathode active material is typically metal oxide with layered or tunneled structures on an aluminum current collector. While, the anode active material is typically graphitic carbon with layered structure on a copper current collector. The set of separator and coated electrodes constitutes the basic assembly element of the cells, called jellyroll, which is equal for all lithium-ion cells regardless of shape. Depending on the cell format desired, different assembly procedures need to be performed starting from the jellyroll. Figure 2.3 shows the cell structures for three representative commercial formats.

For a cylindrical cell, a rolled portion of jellyroll will be inserted inside a cylindrical metal container and immersed in the liquid electrolyte. Then, the cylindrical cell is sealed on both sides with plugs, which also allow for connecting electrically the jellyroll current collectors with the external terminals.

For pouch and prismatic cells, an additional intermediate process is needed, which consists in cutting the jellyroll into appropriate sizes and stacked on several layers in order to increase the cell capacity. Then, all the anode and cathode layers are connected and welded together in two different sides of the cells, forming the external current collector tabs. High accuracy are requested for the production of pouch cells since a misalignment among the jellyrolls may cause short circuit conditions or increase the self-discharge rate of the cells. Moreover, for this cell format, the jellyrolls are placed in a package, consisting of plastic inside and metal outside, which is sealed on the sides through the application of pressure and heat. This process must be carried out carefully for avoiding the loss of electrolyte through evaporation during the lifetime of the cell. These production difficul-

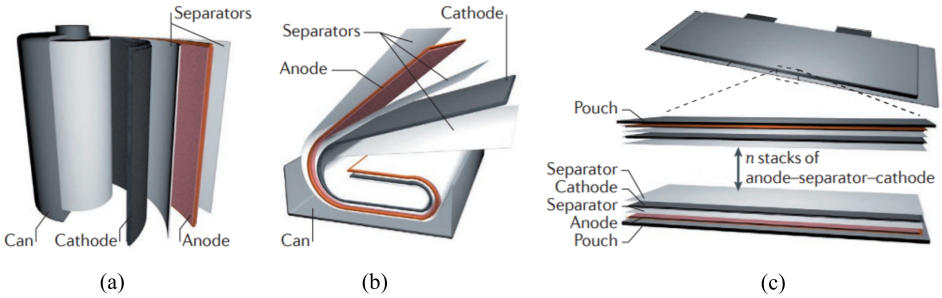

Figure 2.3: Assembly procedures for three representative commercial cell formats: (a) cylindrical, (b) prismatic and (c) pouch. [12]

ties make the pouch cells currently more expensive than the other cell formats.
It is important to highlight that pure lithium oxides instantly when exposed to air. Therefore, during the cell assembly procedure, cathode and anode are completely free of lithium, which is only present in the electrolyte salt. Then, several *formation cycles* are needed in order to force the salt to release the lithium ions and enable the correct functionalities of the cell.

2.2.3 Operating Principles

Basically, the charging and discharging processes occur in a lithium-ion cell thanks to the movement of lithium ions between the electrodes, as illustrated in figure 2.4. In particular, during the discharge, the anode, initially in the form of lithiated graphite, decomposes into graphite and lithium ions, generating an electron for each mole of reactants, which is transferred into the electrolytic solution. Then, considering the effect of the electric field, the lithium ions will move inside the electrolyte, crossing the separator and thus reaching the cathode. Hence, the lithium ions that have passed through the solution recombine with the electron at cathode to form a lithium metal oxide. The process of extracting lithium ions from a solid material is known as deintarcalation or extraction, while the reverse process is known as intercalation or insertion, which consists in inserting lithium ions into the crystalline structure of a material. On the other hand, during charge, the lithium ions migrate from the cathode to the anode. Therefore, the intercalation and extraction processes occur at the anode and the cathode, respectively.

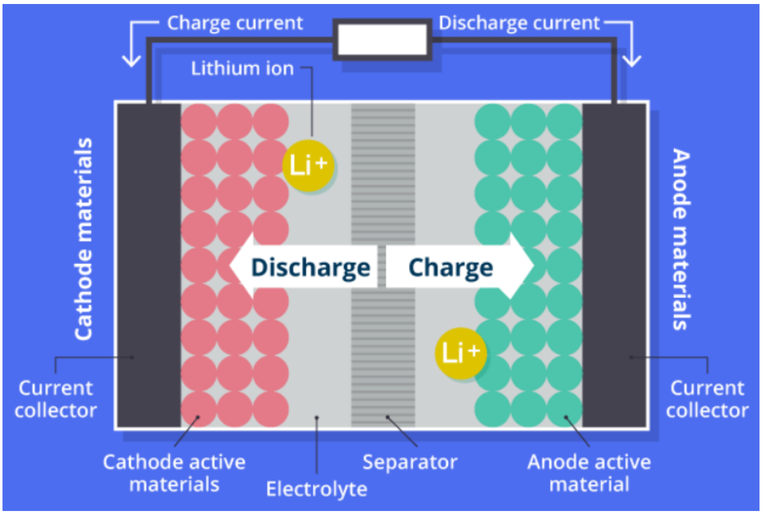

Figure 2.4: Schematic diagram of lithium-ion cell. *Source: TDK*

The nominal OCV associated to the electrochemical reactions and the energy density of a cell strongly depend on the cathode and anode materials. Tables 2.1 and 2.2 report the most adopted materials for the cathode and the anode of lithium-ion cells, where the average potential is defined with respect to the pure lithium potential. Currently, different solution are considered for cathode materials, whereas graphite represents the most common anode material for the majority of the cells commercially available due to its low average potential difference. Indeed, the OCV of a cell results equal to the difference between cathode and anode potentials. Therefore, despite the lower specific capacity, graphite allows for achieving a nominal OCV higher with respect to other anode materials.

Considering that anode and cathode materials often exhibits contrasting properties in terms of specific capacity or energy and average potential difference, it results fundamental to achieve an optimal trade-off for meeting both energy density and voltage requirements.

An important property for the electrolyte solvent is the potential tolerance, since it is subjected to the potential difference between the electrodes. This may cause a highly destabilizing condition for the electrolyte in a specific region of the solution with consequences in terms of electrolytic decomposition and serious aging issues for the cell. In detail, since the products of the decomposition reactions of the electrolyte are highly unstable, they recombine quickly with lithium

Cathode Material	**Average Potential Difference**	**Specific Capacity**	**Specific Energy**
$LiCoO_2$	3.7V	140 mAh/g	0.518 kWh/g
$LiMn_2O_4$	4.0V	100 mAh/g	0.400 kWh/g
$LiNiO_2$	3.5V	180 mAh/g	0.630 kWh/g
$LiFePO_4$	3.3V	150 mAh/g	0.495 kWh/g
$LiCo_{1/3}Ni_{1/3}Mn_{1/3}O_2$	3.6V	160 mAh/g	0.576 kWh/g
$Li(Li_aNi_xMn_yCo_z)O_2$	4.2V	220 mAh/g	0.920 kWh/g

Table 2.1: Most adopted materials for the cathode of lithium-ion cells.

Anode Material	**Average Potential Difference**	**Specific Capacity**	**Specific Energy**
Graphite (LiC_6)	0.1-0.2V	372 mAh/g	0.0372-0.0744 kWh/g
Titanate ($Li_4Ti_5O_{12}$)	1-2V	160 mAh/g	0.16-0.32 kWh/g
$Li_{4.4}Si$	0.5-1V	4212 mAh/g	2.106-4.212 kWh/g
$Li_{4.4}Ge$	0.7-1.2V	1624 mAh/g	1.137-1.949 kWh/g

Table 2.2: Most adopted materials for the anode of lithium-ion cells.

to form stable compounds, leading to a layer of material on the surface of the anode known as Solid-Electrolyte-Interphase (SEI).
The SEI formation has two main drawbacks:

- reduction of the cell capacity due to the decrease of the ionic concentration of lithium ions in the solution, since they are trapped in the SEI;
- increase of the overall internal resistance of the cell due to the lower conductivity of SEI layer with respect to graphite.

2.2.4 Materials

As previously mentioned, the energy density and the nominal OCV strongly depend on the features of the active materials for the electrodes. Figure 2.5 shows the average electrode potential against experimentally accessible (for anodes and intercalation cathodes) or theoretical (for conversion cathodes) capacity. An intercalation electrode is a solid host network into and from which guest ions can be inserted (lithiation) and removed (delithiation) reversibly, whereas the crystalline structure physically changes during lithiation and delithiation in a conversion electrodes. Conversion cathodes and anodes are a highly active area of research for their high theoretical capacity. However, several practical issues related to cyclability and aging are currently delaying their commercial deployment.

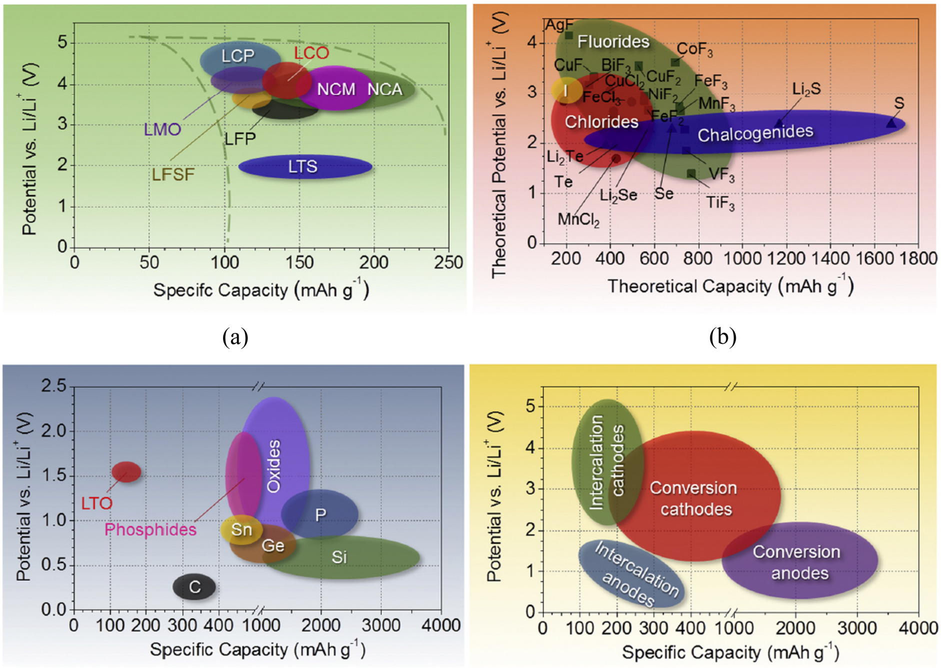

(a)

(b)

(c)

(d)

Figure 2.5: Approximate range of average discharge potentials and specific capacity of some of the most common (a) intercalation-type cathodes (experimental), (b) conversion-type cathodes (theoretical), (c) conversion type anodes (experimental) and (d) all types of electrodes. [13]

The most common cathode materials are based on lithiated transition metal oxides and their main features are illustrated as follows [13, 14].

- *Lithium Cobalt Oxide (LCO)*

  LCO cells have been presented as the first lithium-ion technology able to replace the oldest nickel-cadmium one. Therefore, this cathode material offers the greatest technological maturity. It is characterized by high energy density and moderate cycle life (500-1000 cycles). Therefore, LCO cells have been largely adopted for most consumer electronics with the 18650 cylindrical format. However, they suffer from poor thermal stability and can experience thermal runaway at temperatures as low as 150°C. Other disadvantages include low specific power and issues with cobalt in terms of limited availability and high toxicity, which make these cells very expensive and not suitable for

EVs. Nevertheless, the high-energy dense LCO cells have been adopted for powering the Tesla Roadster and Smart Fortwo electric drive.

- *Lithium Manganese Oxide (LMO)*

  Power capability of LMO-based cells is very high due to the extremely low resistance of this material. Manganese is more abundant and less toxic than cobalt, it has high thermal stability with thermal runaway occurring around 250°C. LMO cathodes have low specific energy and suffer from poor calendar and cycle life due to capacity loss, especially at elevated temperatures. The capacity loss occurs due to the dissolution of the active material into the electrolyte.

- *Lithium Iron Phosphate (LFP)*

  LFP cell offers good electrochemical performance with low resistance, besides high current rating and long cycle life. It is characterized by the highest power density among the lithium-ion cells, but moderate specific capacity. Indeed, its energy storage capability suffers further from a relatively low potential, resulting in a very low energy-dense cell. However, despite the potential is low, LFP cells feature a relatively flat discharge curve, which enables consistent performance across a wide SoC range. While, the reduced energy density of LFP cells leads to larger and heavier battery pack with respect to other cathode materials. The phosphate helps to stabilize the electrode against overcharging and provides a higher tolerance to heat which limits the breakdown of the material. LFP cells have a wide temperature range and can operate between -30°C to 60°C and are much less likely to suffer from a thermal runaway.

- *Lithium Nickel Manganese Cobalt Oxide (NMC)*

  NMC cathode material is a combination of nickel, manganese and cobalt oxides. This allows for designing cells with different features in terms of energy and power densities by properly mixing a certain amount of each material. In particular, nickel-rich and manganese-rich cathodes are used for increasing the energy and power densities, respectively. While, the reduction of cobalt is needed for lowering the costs. The mix of the various materials varies by manufacturer. Combining nickel and manganese enhances each other's strengths, making NMC the most successful lithium-ion cells and suitable for EVs. Indeed, different EV models adopts NMC cells, such as Nissan Leaf, Chevy Volt and BMW i3. Other advantages include respectable cycle and calendar life, better safety than pure cobalt cathodes and good performance at extreme temperatures.

– *Lithium Nickel Cobalt Aluminum Oxide (NCA)*

This cathode material shares similarities with NMC by offering high specific energy and power as well as a long life span. Safety and manufacture cost issues are limiting their adoption for EVs. So far, Tesla is known as the only EV manufacturer who uses NCA chemistry. Indeed, NCA cells are adopted for the Tesla Model 3 and the first Model S by limiting the cobalt content for reducing the cost.

Different active materials can be mixed together to achieve better performance. This leads to composite electrodes that allow manufacturers for improving the balance among energy and power densities, cycle life and cost. As example, composite LMO-NMC cells yield good energy and power densities with improved cycle life and are widely used for PHEVs and BEVs [15].

Figure 2.6 highlights the main features for all the cathodes materials described, including also one of the most adopted solution as anode material. In particular, conventional anodes are based on intercalation reactions, with most important materials being graphite and lithium titanate.

– *Graphite*

This is a layered intercalation compound and represent one of the most widely used lithium anodes due to its relatively high specific capacity and low average potential difference. Other advantages include large availability, low cost and no-toxicity. However, under specific conditions, graphite reacts with atmospheric oxygen, leading to thermal runaway. Moreover, it still remains the issues related to the formation of SEI since the intercalation in graphite occurs at potentials beyond the electrochemical stability window of common electrolytes.

– *Lithium Titanate (LTO)*

Lithium titanate cells have a very high charge/discharge rate but low energy density and high average potential difference, which leads to very low voltage cells. Since the volume change of LTO material during charge and discharge is small compared

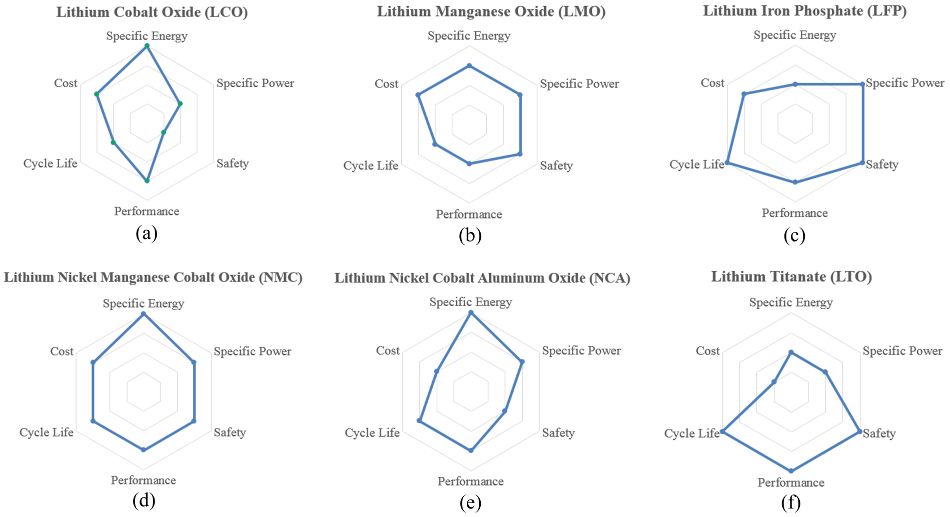
Lithium Cobalt Oxide (LCO)

(a)

Lithium Manganese Oxide (LMO)

(b)

Lithium Iron Phosphate (LFP)

(c)

Lithium Nickel Manganese Cobalt Oxide (NMC)

(d)

Lithium Nickel Cobalt Aluminum Oxide (NCA)

(e)

Lithium Titanate (LTO)

(f)

Figure 2.6: Comparisons of different types of Lithium-ion cells used in EVs (the outer hexagon is most desirable). *Data from [16]*

with graphite, less internal stresses result and the cycle life capability of LTO cells is very high, while the cost is significantly higher than most other cell types. Many LTO cells are capable of more than 10,000 cycles at 80% DoD. This anode material is very attractive due to the possibility to achieve very high charging/discharging and a wide operating temperature range. This also allows for rapid recharging without risk of lithium plating [17] and formation of the SEI, enabling the use of electrolytes with higher conductivities. This results in an extremely high power density for LTO cells.

For what concerns the electrolyte, it is an essential element of the cell, since it provides ionic conductivity enabling lithium ions to shuttle between the two electrodes, while not being electronically conductive. Two major categories of electrolytes can be identified, including liquid (aqueous and organic) and solid (polymer and ceramic) solutions [16].

2.2.5 Future Trends

Currently, the predominant technology in the market consists of high voltage/energy layered metal oxide materials for the cathode, lithiated graphite materials for the anode and lithium salt in organic

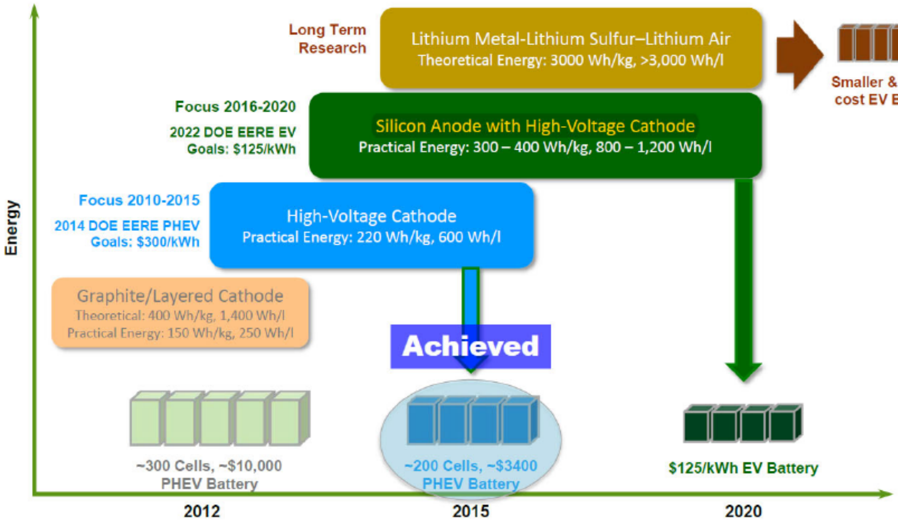

Figure 2.7: Main R&D directions for lithium-ion technology.
Source: US Department of Energy Vehicle Technology Office Annual Merit Review (2016)

liquid solvent for the electrolyte. However, there are still five major concerns that affect the cell materials, limiting the performance.

1. Low energy density and flammability of graphite-based anodes.
2. Contrasting features for conventional cathode materials in terms of energy density and average potential difference. The main task regards the possibility to adopt materials that allows both features to increase.
3. Low potential tolerance of liquid organic electrolyte, which leads to decomposition phenomena and SEI formation.
4. Fast charging tolerance, which requires an increase of power density for the materials.

Some of the main research and development directions for lithium-ion technology are summarized in figure 2.7. Advanced anode materials to overcome the limitation of conventional graphite will include alloy-based (Si, Sn, Al) and metallic lithium (for Li-S and Li-air cells) anodes. Indeed, silicon anodes are considered the primary candidate

Advanced Technology	**Companies**
Silicon-based anodes	3M (Silicon alloy), Enevate (Silicon composite) Amprius (Silicon graphite composite)
Li-S	Sion Power, OXIS Energy
Li-Air	IBM, Bosch
Solid-State Electrolyte	Sakti3, Toyota, Fisher Inc.

Table 2.3: Advanced technologies commercially available.

for the next-gen lithium-ion cells due to high gravimetric energy density, easiness of manufacturing and large availability of this material. Disadvantages include poor cyclability and high-rate capability due to significant volume change (∼300%) of active material, slow reaction kinetics, low value of diffusivity of lithium in silicon and low electronic conductivity [18].

For what concern cathode materials, sulfur is considered a viable candidate to replace the high voltage cathodes of metal oxides thanks to the possibility to increase energy density while reducing the cost. However, there are still several major concerns that need to be properly addressed, including low coulombic efficiency, short cycle life, severe corrosion effects and high self-discharge rate [19].

On the other hand, safety issues and limitations on the operating voltage range associated with the use of liquid electrolytes have led to the introduction of all-solid state cells, where the liquid electrolyte is replaced by a solid-state conductor. Higher operating voltage and less safety concerns represent the main advantages compared to liquid electrolyte. While, disadvantages include instability at low voltages and large grain-boundary resistance [20].

Table 2.3 reports the advanced technologies that have reached currently an interesting stage of development [21].

2.3 Battery Pack Architecture

The design and the architecture of a battery pack strongly depends on the application requirements. HEVs and BEVs have different requirements in terms of power demand and energy content. Moreover, the vehicle concept defines the size and shape as well as the mechanical, electrical and thermal interfaces of the battery pack. Figure 2.8

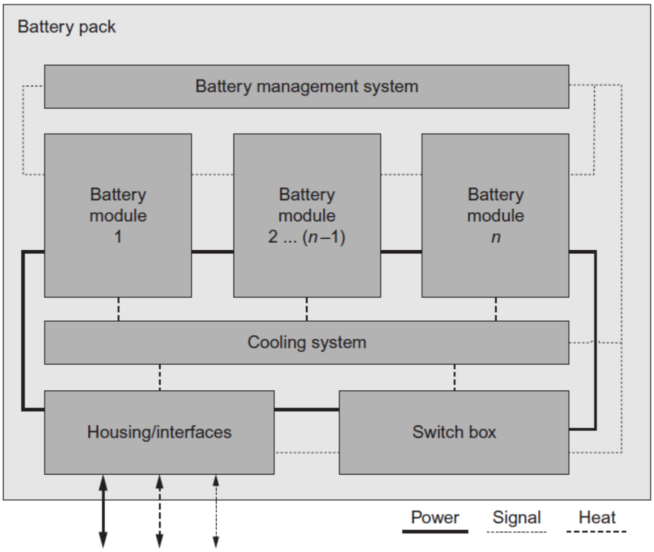

Figure 2.8: Battery pack and its main components. [22]

shows a schematic illustration of a battery pack and its components, which are necessary to fulfill the vehicle requirements.

The battery modules represent the primary components in a battery pack architecture. They are composed of several cells properly connected in series and/or in parallel in order to meet the voltage and capacity requirements. In particular, cells have to be connected in series to achieve the required voltage, whereas they have to be parallelized to increase the available capacity. Typically, two main battery pack architectures can be identified depending on the connection between cells or modules, as illustrated in figure 2.9. Accordingly to the standard IEC60050, the series-parallel (SP) configuration is based on connecting the cells/modules in series first and then in parallel, while the parallel-series (PS) configuration vice versa. It is important to highlight that the selection of the battery pack architecture strongly impacts on the system cost, size and weight. Moreover, different cell-to-cell variations can occur in terms of current and voltage imbalances among the cells [23], leading to different aging and temperature conditions. Currently, for both architectures, high voltage battery packs result to be a suitable solution for EVs due to the possibility to reduce the charging/discharging currents, minimizing the power loss of the system and thus increasing the efficiency. This also allows for reducing cost and weight of the vehicle.

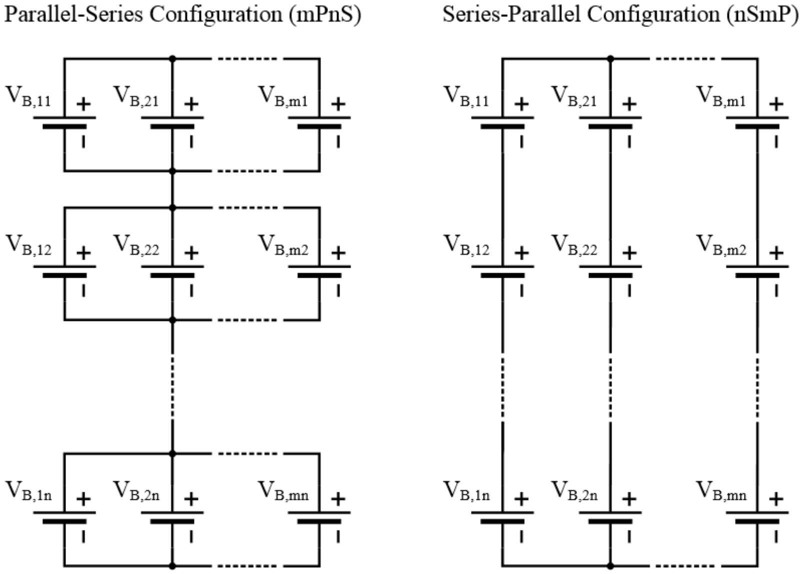

Figure 2.9: Typical battery pack architectures (standard IEC60050).

The individual modules are supervised by a battery management system (BMS), which ensures each cell to operate in safe operating conditions by monitoring cell terminal voltage, battery pack current and temperatures. In addition, it eventually disconnects the battery pack from the vehicle to prevent dangerous failures by means of protection components contained in a switch box, including switches, isolation monitor and current sensor.

The cooling system of the battery pack is responsible for maintaining the cells in a defined temperature range to prevent aging and overtemperature conditions. All these components are enclosed in the battery pack housing and is tightly fixed in order to withstand even the harshest conditions over the whole lifetime of the vehicle. The housing of a battery pack also contains all interfaces to the vehicle, such as the plugs, communication and cooling interfaces. As example, Figure 2.10 shows a battery pack of an EV. It consists of 18 battery modules that are separated by seven cooling plates. The internal components are enclosed in a battery housing made out of carbon-fiber-reinforced plastics (CFRP). The BMS, the switch box and both the electrical and thermal vehicle interfaces are located in the front.

More details about each component of the battery pack are illustrated in the following subsections.

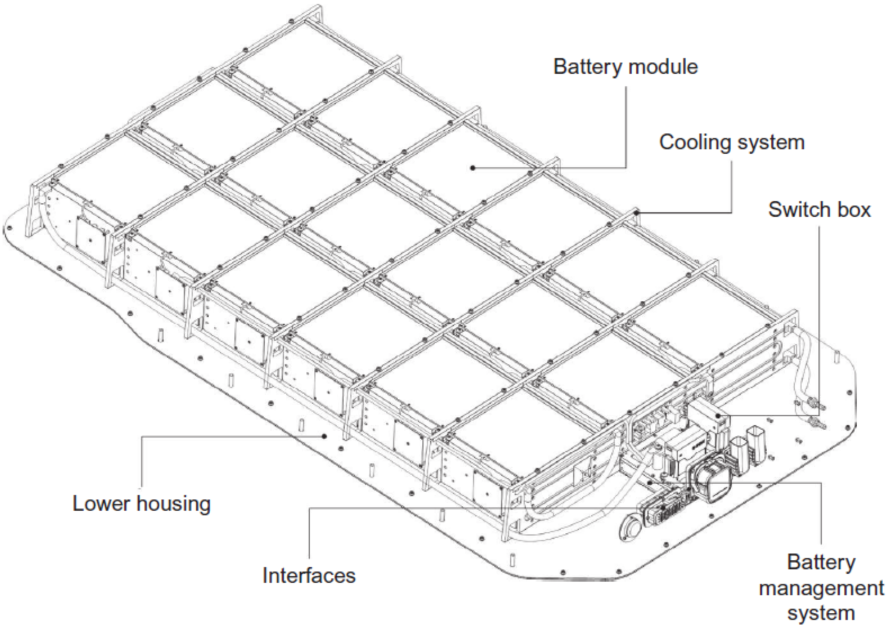

Figure 2.10: Example of a battery pack for EVs based on pouch cells. [22]

2.3.1 Battery Module

The modular approach of a battery pack design results in battery modules containing a fraction of the lithium-ion cells. Typically, it is preferable to maintain the module terminal voltage below 60V (limit for low voltage battery pack) in order to better handle the module during production and transportation without additional and expensive safety precautions.

The cells are grouped in a mechanically stable module and then enclosed in a proper housing. The cell interconnection system is needed for correctly achieved the series and parallel connection among the cells in a module. In particular, the system electrically connects the individual cells and provides the interfaces for the module connectors to the neighboring modules as well. The cells are supervised by means of a module control unit, which monitors the voltages of all series-connected cells and also temperatures at specific locations of the module.

An example of this modular approach for a pouch-based module is reported in figure 2.11. The cells are stacked on top of each other and enclosed in aluminum trays, which allows for fixing the soft pouch cells

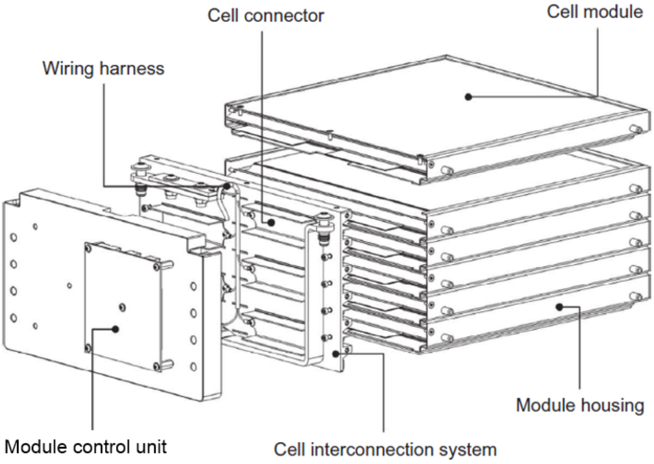

Figure 2.11: Example of a battery module based on pouch cells. [22]

mechanically as well as providing the mounting interfaces to the cooling system and the battery housing. The cell interconnection system located in front of the module connects the individual cells and also provides the electrical interface to the neighboring modules in terms of screw terminals. In detail, it is composed by three major components: cell connectors, the wiring harness, and the housing. The cell connectors are required to electrically connect the cells in series and/or in parallel. While, the wiring harness consists of temperature sensors and voltage sense wires that are connected to the cell connectors as well as a plug or header for interfacing the cell interconnection system to the module control unit.

For what concerns the module housing, it is designed to absorb the forces generated by the cells during operation. Indeed, expansion and contraction of the cells occur during charging and discharging due to temperature, SoC and SoH variations [24]. Moreover, different design of the module housing needs to be developed depending on the cell format selected.

2.3.2 Safety and Control Unit

Lithium-ion cells are very susceptible to abnormal operating conditions that can lead to thermal runaway, including overtemperature, overvoltage/overcharge, undervoltage/overdischarge and extremely high C-rates. Safety and control unit result fundamental for ensuring the battery pack to operate in safe operating conditions and providing

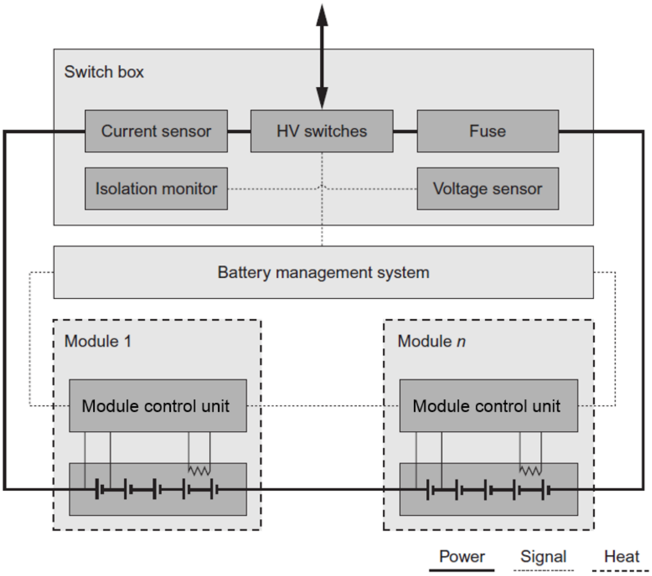

Figure 2.12: Safety and control unit and its individual components. [22]

proper actions for disconnecting it from the vehicle in case of failure. It includes a BMS, the module control units and the switch box. The BMS gathers information from the module control units and controls the high-voltage components of the switch box on the basis on the measured input data. Figure 2.12 shows a schematic illustration of the safety and control unit and its individual components. In this case, the BMS is designed according to a master-slave architecture. Therefore, the central BMS is referred as master and the module control units as slaves. More details regarding different BMS architectures will be illustrated in section 3.1. The module control unit or BMS slave is usually located very near to the battery modules and measures all the cell voltages and the temperature at sufficient measuring points to provide a suitable approximation and estimation of the temperatures of each single cell. Other main functions and characteristics of BMS will be reported in chapter 3, since it represents a crucial component for a battery pack.

The switch box includes two high-voltage relays, which are used to safely disconnect the battery pack from the vehicle, and a mechanical fuse in case of external short circuit. Moreover, a current sensor allows for measuring the battery pack current by evaluating the voltage drop across a high-precision resistor or adopting a current transducer.

Then, since the battery pack needs to be isolated from the ground of the vehicle, an isolation monitor is used for measuring the isolation resistance between ground and the pack terminals.

2.3.3 Cooling and Heating System

There are different sources of heat generation inside a battery pack, mainly due to the internal resistances of the components, including cells, connectors and electronic units. This heat generated has a major impact on the performance and cycle life of a battery pack. Indeed, cells have to operate in a defined temperature range in order to increase lifetime and avoid dangerous issues. High temperatures also accelerate the aging of the cells, influencing the driving range of the EV. Therefore, an efficient thermal management system (TMS) of the battery pack results crucial for the operation of the EV, especially in extreme climate conditions (tropical or arctic regions).

The cooling system allows for dissipating the heat generated during driving and charging operations. On the other hand, the heating system provides the additional heat required in case of cold environment. The cooling and heating of a battery pack are usually operated by air-cooled, liquid-cooled or direct refrigerant-based systems. The main features and design aspects for the TMS of EVs are detailed provided in [25, 26].

2.3.4 Battery Housing

The design of the battery housing depends on several mechanical, safety, service and cost requirements. It is a highly customized component, which is tailormade for the specific application. There are two main aspects that affect the size and the shape of the battery housing. The first one is related to the design space and the mounting points given by the vehicle, whereas the second aspect regards the internal components that have to fit in the housing.

The battery pack is usually positioned at the underbody and the center tunnel of the vehicle for BEVs in order to achieve an optimal balance for the driving dynamics of the vehicle. While, the battery pack of PHEVs is located at different positions depending on the vehicle concept.

Generally, the housing consists of an upper and lower sections, which are separated by a sealing gasket. The seal prevents the ingress of particles and liquids and is designed according to a defined ingress

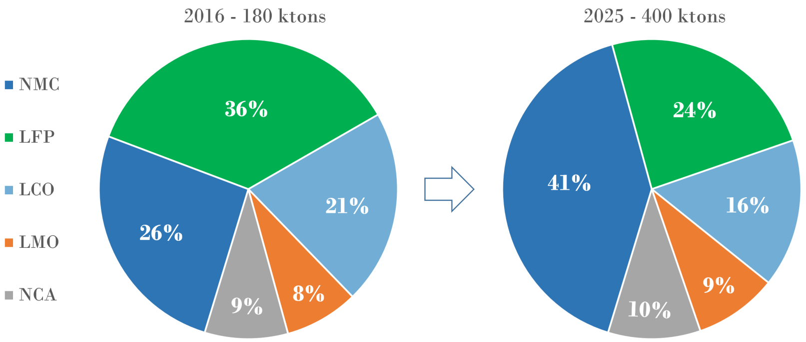

Figure 2.13: Market shares of the leading materials for lithium-ion cells in 2016 and forecasted to 2025. *Data from International Energy Agency*

protection (IP) class. The main class for EVs is the IP 67, which requires the housing to be dust tight and to prevent water ingress. Other components integrated into the battery housing include the pressure equalization element and a device for condensate handling [22].
It needs also to provide power, signal, thermal and mechanical interfaces to the vehicle. Moreover, lightweight design for the battery housing are required for reducing the overall weight of the vehicle and thus reducing its energy consumption and improving vehicle dynamics. Considering the size and the weight of battery packs for EVs, the battery housing can be designed as an integral part of the whole vehicle structure. Therefore, there are challenging requirements concerning stiffness and strength of the casing. Typically, the battery casing is made of CFRP and glass-fiber-reinforced plastics (GFRP).

2.3.5 Battery Pack for Automotive

In this section, an overview of the different battery packs and cell chemistries considered for EVs is reported. Nowadays, LMO, LFP, NCA, and NMC battery technologies have been successfully adopted by many automakers, including Tesla, BMW, BYD, Chevrolet, Mercedes Benz-Daimler, Volkswagen and Nissan. Detailed features for all the main EVs commercially available on the market are reported in [27, 28]. In 2016, NMC, LFP and LCO accounted for 83% of the whole market share, as illustrated in figure 2.13. This value is mainly related to EV applications, except for LCO cells that are largely used for electronic devices (smartphones, tablets, and laptops). By 2025, NMC battery technology is expected to increase its market share from

26% to 41% due to its higher energy density than LFP, whereas NCA and LMO will maintain stable occupancy of the total market.
NCA cells are mainly used by Tesla, while most other automakers adopt LFP, NMC, LMO or blended NMC and LMO chemistries. Considering their relatively mature technologies, these cells will still dominate the EV market in the foreseeable future before advanced battery technologies become mature enough for automotive applications.

2.4 Battery Modeling

Nowadays, the development of an accurate battery model represents a fundamental key for predicting the battery runtime and I-V characteristic in cases of different load profiles as well as improving its performance and cycle life. In addition, numerical results from battery models allows for sizing powertrain components and developing optimized energy management algorithms. This also enables the possibility to achieve reliable information about the SoC and the SoH of the battery, which are not directly measurable. Indeed, battery models are considered as a starting point for developing and testing SoC and SoH estimators.
In recent years, a large variety of battery models with different levels of complexity and accuracy have been proposed in literature [29–32]. They can be classified in four categories: electrochemical, mathematical or analytical, black-box and electrical or equivalent circuit models. Considering the same input current profile for the cell to be modeled, each solution adopts different approaches and parameters for describing the same voltage response, as illustrated in fig. 2.14.
Models can also be combined for achieving optimal accuracy in the results, but this can leads to rather complex models.

2.4.1 Electrochemical Models

Electrochemical models provide a highly accurate description of electrochemical processes inside a cell. Therefore, detailed information on local conditions and performance, such as temperature, voltage, current and electrolyte concentration can be achieved. They rely on first principles, such as Fick's law of diffusion for lithium concentrations and Ohm's law for potentials, to describe the transport, thermodynamic and kinetic phenomena throughout the cell, resulting in a set of coupled, non-linear partial differential equations (PDEs) [33].

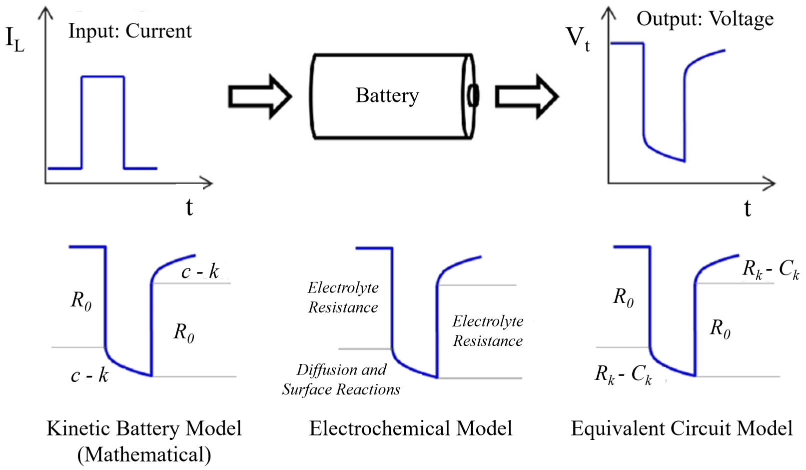

Figure 2.14: Battery model response using different approaches. [32]

The electrochemical models are mainly used to optimize the physical design aspects of the cell and relate its design parameters with macroscopic and microscopic information. However, detailed knowledge of the battery cell chemistry, material structures and other physical characteristics, such as porosity of the active materials or electrolyte volume and density, are essential to achieve high accuracy. Moreover, memory and computing requirements are large, either for model evaluation or parameter identification. Hence, these models are impractical for high-dimensional design and control optimization problems as well as in real-time state estimation applications. They are more suitable for research in the fabrication of the battery components, such as electrodes and electrolyte.

2.4.2 Mathematical Models

These models adopt analytical or stochastic approaches to predict the cell behavior and its characteristics, such as the battery runtime, efficiency or capacity. In particular, all mathematical models are characterized by few equations for describing the cell properties. Kinetic battery model (KiBaM) represents one of the most common analytical model [34], which is developed from an understanding of the chemical process kinetics of the cell.

Stochastic cell models [35] are fast compared to high-fidelity electrochemical models but are still accurate. This type of model works on the principle of the discrete-time Markov chain, which consists of predicting the future of the process based on its present state without knowing its full history. In this way, the changes of the model states only depends on the current state of the system.

Mathematical models can reduce the computational complexity due to the possibility to adopt models that consider a few equations. Nevertheless, they do not provide an overall representation of the electrochemical processes that occur inside cell, resulting abstract. In addition, they are used for specific application and can be inaccurate in predicting the parameters variations of the cell.

2.4.3 Black-Box Models

Black-box models apply artificial intelligence (AI) techniques to capture the relationship between the selected inputs and outputs of cells without the prior knowledge of electrochemical processes inside batteries. AI techniques include neural network (NN) [36], fuzzy logic (FL) [37] and support vector machine (SVM) [38], which adopt training approaches to establish the models based on testing data. To achieve high model accuracy and good generalization ability, testing data should cover sufficient cell operation ranges. Moreover, the parameters in the training approaches need to be effectively tuned.

A large amount of experimental data is required for the training process in order to achieve accurate black-box models. However, under the influence of uncertain operating conditions, such as temperature and driving cycles of EVs, it is difficult to collect a sufficient experimental data in advance to train black box models.

2.4.4 Equivalent Circuit Models

Equivalent circuit models (ECMs) describe cell behaviors using a combination of the lumped circuit parameters, such as resistances, capacitances and voltage or current sources. This modeling technique reflects cell performance macroscopically, resulting highly adaptable. The same model structure can be used to represent different cell technologies with the same accuracy by using appropriate parameter values. Moreover, parameter variation can be included to capture environmental and aging effects [39]. Complexity can easily be added to the model structure to more accurately reproduce cell performance. This increases the computational cost but allows for better fulfilling the model requirements of a specific application.

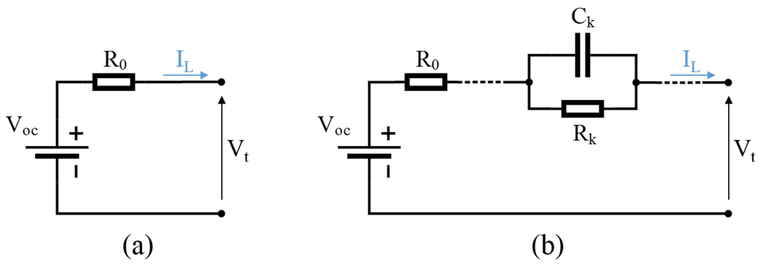

Figure 2.15: (a) Zero order ECM and (b) n-order ECM for $k = 1..n$.

ECMs are particularly attractive due to their simplicity, computational speed and flexibility in capturing voltage dynamics, heat generation and aging characteristics [40]. Different ECMs can be adopted depending on the cell technologies and the level of accuracy desired, as reported in figure 2.15. The voltage source is considered as the OCV of the cell. In particular, OCV and nominal capacity of the cell represent the static part of the model. The zero-order ECM includes only a series resistor for reproducing the cell dynamics, whereas additional parallel branches of resistors and capacitors are commonly included in the n-order ECMs in order to better capture the transport, thermodynamic and kinetic aspects. Despite there is no limit on the number of RC branches, first or second-order ECMs are typically necessary to accurately capture the polarization characteristics, i.e. the nonlinear regions in figure 2.14. Considering a positive current in discharging, the model equations for either zero-order or n-order ECMs are reported as follows:

$$V_t = V_{oc} - R_0 \cdot I_L \tag{2.1}$$

$$\begin{cases} \dfrac{dV_k}{dt} = \dfrac{I_L}{C_k} - \dfrac{V_k}{R_k \cdot C_k} \\ \\ V_t = V_{oc} - R_0 \cdot I_L - \sum\limits_{j=1}^{k} V_j \end{cases} \quad \forall k = 1..n \tag{2.2}$$

where V_t is the terminal voltage, I_L is the load current, R_0 is the series resistance, V_{oc} is the open-circuit voltage, R_k and C_k are the effective resistances and capacitances values of the generalized n-order ECM. R_0 takes into account the ohmic losses related to the physical nature of the electrodes and the electrolyte. It is responsible for power capability, because it causes the biggest share of the total voltage drop at high currents.

ECMs are relatively simple mathematically and numerically such that complicated and intensive computation is minimized or even avoided. Furthermore, cell performance is commonly extrapolated to the pack level for system simulation, design, and control applications. In this case, it is assumed all the cells to be equal and that no temperature gradient occurs in the battery pack, which could induce significant cell-to-cell imbalances in voltage or charge. Therefore, such the battery pack behavior can be scaled from that predicted by the model of an individual cell.

It is important to highlight that despite the accuracy of ECMs generally improves with increasing model order, their performance strongly depends on the parameter identification process.

2.4.4.1 Parameter Identification

ECMs are typically developed starting from test data, since model parameters do not explicitly depend on the physical design or states of the cell. An identification procedure consists of three main parts:

- model structure selection;
- experimental tests design;
- fitness criterion and identification error minimization algorithm selection.

Model parameters are identified from experimental test data during which the selected cell is generally kept in a thermal chamber and connected to a cell cycler (programmable load/supply). Since cell parameters are highly dependent from SoC and temperature values, the thermal chamber maintains a constant temperature and current measurements from the cycler are used for estimating the SoC of the cell by means of the coulomb counting method. In detail, SoC is evaluated considering the amount of charge added to or removed from the cell and the real cell capacity as well.

Typically, testing begins with an individual capacity test, which consists of a complete discharge process starting from a fully charged cell that aims to correctly define the real cell capacity in different operating conditions. Indeed, the capacity strongly depends on the charging/discharging C-rate and temperature. In addition, it can also vary between samples of the same cell technology, leading to the need of performing multiple capacity tests. Low C-rates ($\leq C/3$) are used to

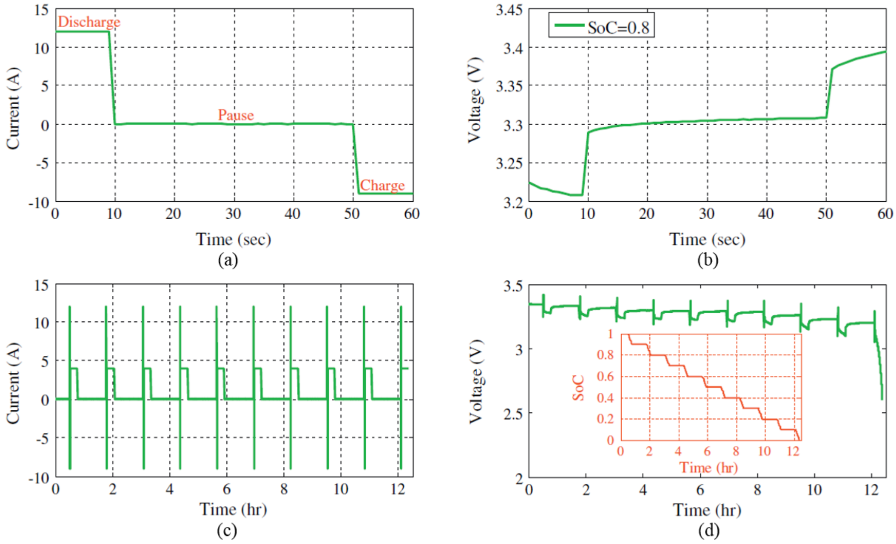

Figure 2.16: (a) Pulse current of HPPC test and (b) cell voltage response at SoC = 0.8; (c) complete HPPC test, (d) cell voltage and SoC response for the complete HPPC test. [44]

measure the fully usable capacity, but the reference nominal capacity adopted in the model can vary depending on the specific application.

Low C-rate, constant-current cycles can also be used to approximate the OCV of the cell. Indeed, it can be assumed the terminal voltage measured during a charging/discharging process at very low C-rates ($\leq C/20$) to be equal to the OCV of the cell. On the other hand, there are several experimental tests that can be carried out for identifying the OCV of a cell when there is not access to the cell electrodes. The Galvanostatic Intermittent Titration Technique (GITT) [41] represents a very accurate experimental test for capturing both thermodynamic and kinetic parameters of the cell. Calibration methods also include dynamic pulse testing, such as the Hybrid Pulse Power Characterization (HPPC) [42] or the RC-Identification test (RCID) [43], in which the OCV is measured at different SoC after one hour rest.

Figure 2.16 shows the standard HPPC. The parameters introduced in section 2.4.4 are calibrated considering the experimental data from a HPPC test or similar dynamic profile. Pulse power tests are segmented by incremental and fixed changes in SoC. High-power, short-duration pulses enable the assumption of constant SoC, and thus constant parameters, while also generating sufficient dynamic behavior for esti-

mating parameter values either in charge or in discharge. A long rest between SoC steps allows the battery for reaching electrochemical and thermal equilibrium, at which the OCV can be measured. More details related to the static and dynamic tests are outlined in [42].
Once the experimental tests are concluded, the model parameters are determined wiht the aim of reducing error between experimental data and model output, avoiding to overfit the data. Given the nominal capacity (C_n) from a capacity test, the SoC is tracked by means of coulomb counting method and updated at each time step:

$$SoC(t+\Delta t) = SoC(t) - \frac{I_L}{C_n} \tag{2.3}$$

Starting from a fully charged cell, once the cell has reached equilibrium after a long rest and while under no load, the terminal voltage is closely representative of the OCV at each SoC step j:

$$V_{oc}(SoC_j) = V_t(t) \tag{2.4}$$

The series resistance R_0 is calculated from the instantaneous voltage drop that occurs before and after the start of a discharge or charge pulse. For a zero-order ECM, this estimation of the terminal voltage results optimistic because the current is applied for a time interval greater than the data-logging frequency. A more conservative model is to consider the terminal voltage at the end of the pulse, underestimating its value in pulses with duration less than that of the test and overestimating otherwise. Considering the pulse being applied at time $t + \Delta t$ and ended at T, the ohmic resistance can be computed generally as follows:

$$R_0(SoC_j) = \frac{V_t(T) - V_t(t)}{I_L(T) - I_L(t)} \tag{2.5}$$

In this way, a higher estimation of R_0 is achieved for the zero-order ECM. This allows for partially compensating the absence of the RC parallel branches for reproducing the dynamic transient. On the other hand, R_0 is calculated considering the voltage and current values at t and $t + \Delta t$ for a n-order ECM.
A minimization algorithm is typically employed to determine the values of the equivalent resistance and capacitance of the RC branches with the aim of maximizing the accuracy or minimizing root mean square error (RMSE). In detail, the time constant of each RC branch

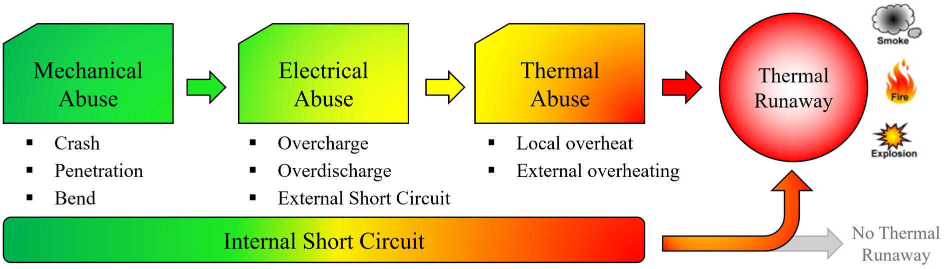

Figure 2.17: Classification of the abuse conditions for lithium-ion cells.

is identified ($\tau_k = R_k \cdot C_k \quad \forall k = 1..n$) and the parameter values are determined through regression [45, 46].
The model calibration generally involves a large amount of experimental tests considering multiple samples, C-rates and temperatures. The end-user should consider the application to determine which rate and temperature are most appropriate or if multiple tests need to be evaluated. At a minimum, parameters are solely functions of SoC. The most complex ECMs consider each parameter to be dependent from SoC, temperature, C-rate and SoH. The parameters are usually stored in lookup tables and interpolated or extrapolated linearly. It is important to point out that these values may be known exactly in a modeling environment, but it is infeasible to have measures of each one in a practical application. Indeed, all of these parameters must be estimated in a real battery system.

2.5 Abuse Conditions

Safety and reliability still remain the major issues to be overcome in order to allow the large-scale application of lithium-ion batteries (LIBs). Indeed, there are several abuse conditions that can induce hazard conditions, such as thermal runaway (TR) of one or more cells in a battery pack, which essentially consists in a series of exothermic reactions inside the cell that generate a large amount of heat, leading to fire and risk of explosion [47]. As illustrated in figure 2.17, the abuse conditions can be mainly classified into three categories: mechanical, electrical and thermal. Most of cases, all these abuse scenarios are followed by an internal short circuit (ISC) of the cell, which is currently considered the main cause of the TR of LIBs.

Mechanical abuse

Destructive deformation and displacement caused by applied force are the two common features of the mechanical abuse. Vehicle collision and consequent crush or penetration of the battery pack are the typical conditions for mechanical abuse. Deformation of the battery pack is quite possible during car collision and may result in two main dangerous consequences:

- the battery separator breaks and the ISC occurs;
- the flammable electrolyte leaks and potentially causes consequent fire.

Penetration is a common phenomenon that may occur during the vehicle collision as well. Comparing with the crush conditions, severe ISC can be instantaneously triggered when penetration starts. Therefore, mechanical destruction and electrical short occur simultaneously, resulting more severe than crush conditions. More details related to the state-of-art techniques for safety-focused mechanical modeling of LIBs from cell to pack level are reported in [48].

Electrical abuse

These abuse conditions include overcharge, overdischarge and external short circuit. The overcharge-induced TR can be harsher than other abuse conditions, since excessive energy is filled into the cell. The heat and gas generation are the two common consequences, which are related to ohmic heat and side reactions [49].

The mechanism of the overdischarge abuse is different from others and the potential hazard may be underestimated. Indeed, the over delithiation of the anode during overdischarge causes the decomposition of SEI, which will produce gases, resulting in the cell swell. This can also lead to capacity degradation and power fade of the cell due to changes of the electrochemical properties of anode [50]. Both overcharge and overdischarge abuse conditions are mainly caused by failure of BMS.

The external short circuit forms when the electrodes with voltage difference are connected by conductors. The external short circuit of the battery pack can be caused by deformation during car collision, water immersion, contamination with conductors or electric shock during maintenance. Generally, unlike the penetration, the heat released on the circuit of external short does not heat the cell. It is more like a fast discharging process, in which the severity of the short current depends on the value of the short resistance and is limited by the highest mass transfer speed of lithium-ion [51].

Thermal abuse

Local overheat represents a typical thermal abuse condition that can occur in a battery pack. Besides the overheat caused by mechanical/electrical abuse, the overheat can be caused by contact loose of the cell connector. In particular, the resistance increases due to this contact loose, which usually originates from manufacturing defect. The connection became loose under vehicle vibration condition. Then, intensive heat generation occurred when high current passed through the particular area, resulting in local overheat and consequent TR. In addition, thermal abuse conditions can also occur due to external overheating.

2.5.1 Internal Short Circuit

Among all the possible causes for TR, the ISC represents the most common one. The probability of inducing the TR strongly depends on the electrical and thermal conduction properties of the materials involved in the ISC. In addition, the severity of the ISC is affected by the cell characteristics and the operating conditions, including chemistry, capacity and size as well as state of charge, initial temperature and aging [52]. Latent manufacturing defects can gradually evolve and develop into a spontaneous ISC during the cell lifetime as well.

The main effects due to the ISC include the increase in self-discharge rate and heat generation. The severity of these effects highly varies depending on the active materials that may come in contact inside the cell, leading to different levels of hazard.

Typically, the ISCs can be classified in four categories, as shows in figure 2.18(a). The Copper-Aluminum short is similar to an external short circuit and involves the largest amount of energy due to the low ISC resistance between the tabs of the cell. While, the Anode-Aluminum short is considered the worst scenario of ISC. Indeed, it has high possibility of inducing thermal runaway due to the low electrical resistivity and the inadequate heat transfer on the anode [52]. On the other hand, because of the poor conductivity of the cathode active material, the other two ISC types (Copper-Cathode and Anode-Cathode) are characterized by a low ISC current.

These ISC scenarios, especially the Anode-Cathode one that is the most common short, need to be properly analyzed because the effect is similar to an increase of the self-discharge of the cell, but it can rapidly evolve in thermal runaway during the cell lifetime. In par-

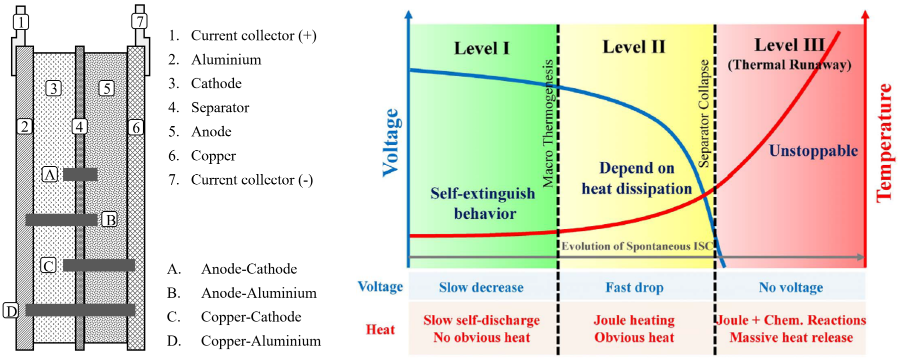

(a) (b)

Figure 2.18: (a) Classification of the ISC depending on the nature of short; (b) the three levels of hazard of ISC.

ticular, there are three levels of hazard, which can be defined on the basis of the self-discharge rate and the severity of the heat generation [47], as illustrated in figure 2.18(b). The first level of hazard is characterized by a slow self-discharge rate and a very low impact on the temperature of the cell, whereas a faster drop of the cell voltage and a quicker rise of temperature can be observed in the second level of hazard. The third one leads to unstoppable thermal runaway with a large amount of heat generation. Therefore, it becomes fundamental to model the ISC in order to potentially detect it before reaching critical safety conditions as well as understanding the interaction between cell-to-cell in a pack configuration.

2.6 Aging Conditions

Currently, increasing the cycle life represents one of the major challenges for lithium-ion cells. Therefore, a detailed understanding of the degradation mechanisms is required. The reduction of the cell performance overtime is related to aging conditions and is evaluated with respect to the Beginning of Life (BoL) characteristics of the cell. This refers to the condition of a pristine cell, which comes directly from the manufacturer. In particular, aging is defined as reduction in performance, cycle life and reliability of a cell. The main effects include capacity decrease and power fading due to internal resistance increase. Moreover, since battery packs can be composed by a large number of cells, aging conditions for a single cell can lead to performance

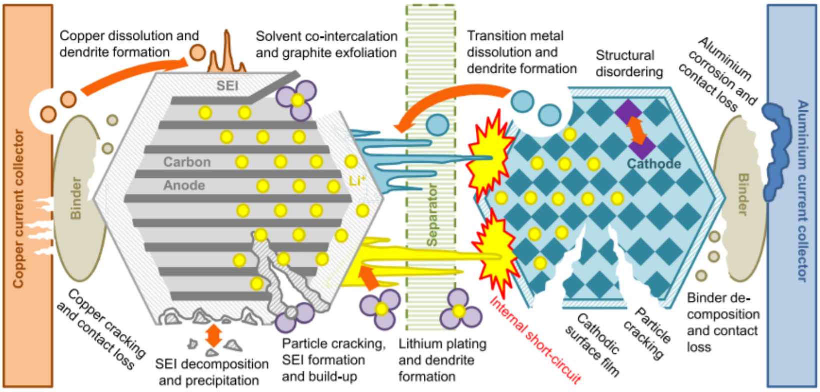

Figure 2.19: Degradation mechanisms in lithium-ion cells. [53]

reduction of the overall system.
An overview of major degradation mechanisms and their interactions has been represented in figure 2.19, highlighting the complexity of aging in lithium-ion cells. In detail, aging mechanisms can be classified in two main categories, which are closely correlated:

- *Chemical degradation*

  These mechanisms can mostly be traced to the electrolyte decomposition and reduction, SEI formation, binder decomposition, solvent co-intercalation, active material dissolution, gas evolution, and loss of lithium. Hence, they are strongly dependent on the side reactions that occur inside the cell during abnormal operating conditions, such as overvoltage or overtemperature.

- *Mechanical degradation*

  They are mainly concerned to the volume changes and subsequent stress generated in the active material particles of anode or cathode within lithium intercalation and extraction. As a consequence of tensile stress, active particles may undergo cracks, loss of contact between each other or from the current collector, leading to isolation issues. Moreover, stress induced over cycling of a cell changes the structure of pores in the separator and leads to lower lithium-ion mobility.

More details related to aging mechanisms as well as different chemical and mechanical modes of degradation are illustrated in [53, 54].

Chapter 3

Battery Management Systems

Nowadays, the increasing interest in lithium-ion battery packs has led to remarkable developments in Battery Management System (BMS) technology, which are progressively pushing their application in EVs with improved driving range. However, as the cell performance increases, advanced BMS are required, leading to targeting cost-effective solutions capable of increasing the pack efficiency, performance and lifetime while enforcing the operation within the safe voltage, current and temperature ranges.

In this chapter, after a description of the main BMS architectures, the requirements and functions are discussed, including details related to sensing and measurement, safety and protection, interface and communication, diagnostics and performance management. An overview of the SoC and SoH estimation methods is reported in the diagnostics section, while the main charging techniques are illustrated in the performance management section. Moreover, a wide description of the equalization circuits is discussed with the aim of evaluating and comparing the balancing performance of each architecture.

3.1 Architectures

On the basis of the application, the BMS design is a complex task since it has to take into account specific needs, the system context as well as the characteristics of the adopted cell technology. The BMS can be realized through the use of general-purpose microcontrollers implemented with the supporting measurement, power and control circuitry. It may be possible to implement the simplest systems using a selection of definite-purpose integrated circuits (ICs), but this architecture is mainly used for consumer electronics applications, which are characterized by smaller systems operating at low voltages. While, the integration of different embedded systems is considered for the BMS of large or high-voltage battery packs. In particular, two different boards can be identified for a BMS architecture, which are the cell/module monitoring unit (CMU) and the battery pack control unit (BCU). Depending on the integration of these boards, the BMS architectures can be classified in two main categories: centralized and distributed configurations. The architecture selection strongly affects cost, reliability, ease of installation and maintenance as well as measurement accuracy of the BMS.

3.1.1 Centralized

Centralized or monolithic BMS architecture represents the simplest solution, in which CMU and BCU are integrated on a single printed circuit board (PCB) to realize all of the functionality. Therefore, centralized systems reduce the need for the design, definition and cost of interfaces between different boards. Figure 3.1(a) shows a centralized BMS architecture for a battery pack composed by n series-connected modules. Monolithic architectures offer the lowest cost and complexity at the expense of flexibility and scalability. Indeed, scalability is limited since the number of cells which can be monitored is bounded by the number of cell-monitoring circuits installed. In several cases it may not be possible to monitor any arbitrary lower number of cells. Moreover, there are no cost savings realized for smaller batteries because the number of BMS components cannot be reduced.

The centralized BMS is typically used in low-capacity and low-voltage applications or small battery systems. Centralized BMSs require a single controller to support the entire pack voltage and all the cell measurement connections. Therefore, proper creepage and clearance distances need to be taken into account for high-voltage battery pack. Connector and component ratings must also be appropriate and the number of possible component choices for a given application may be restricted. Despite a good monolithic design will attempt to reduce the potential difference between adjacent component choices and establish adequate isolation barriers, higher voltages and fault energy may occur in case of fault conditions. Moreover, since the measurement signals of

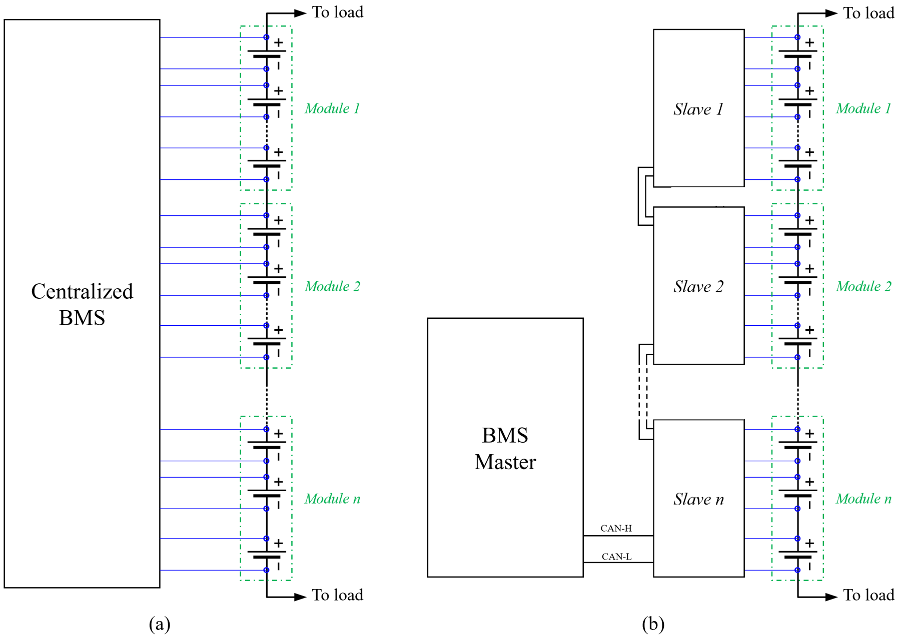

Figure 3.1: (a) Centralized and (b) distributed BMS architectures for a battery pack composed by n series-connected modules.

each cell are transmitted to a single PCB, a large number of complex wires and connectors is required.

3.1.2 Distributed

Distributed BMS, also known as master-slave architecture, allows for achieving a high degree of modularity. The most common design incorporates a single master BCU and, depending on the application, a number of similar or identical slave CMUs that are connected to the battery cells/modules, as illustrated in figure 3.1(b). The master is responsible for fault detection, battery state estimation, switch management, charge and discharge control as well as communication with the slaves and the vehicle controller. While, the slave modules are primarily responsible for measurement of cell voltages and temperatures. In a distributed architecture, there is usually a strict correspondence between the number of battery modules and slave devices. Systems with a high degree of integration may have the sensing slave circuit incorporated directly into the battery module. Different protocols can be adopted for the communication between master and slaves, including proprietary or a commonly available protocol such as CAN, RS-232, or Ethernet.

This architecture is characterized by three main advantages. First, since the function of data collection and calculation functions are separated, the fault is easy to check and the calculation efficiency is high. Second, the structure of the system is simplified, ensuring flexibility and applicability to this BMS solution. Third, modularity and scalability allow for easily extending the battery pack while better distributing master and slaves in application with high space constraints, such as EVs.

On the other hand, distributed BMS are very expensive due to the large number of distributed systems, including communications circuits and support circuits, such as microprocessors, power supplies and isolation. These extra circuits also increase the weight, size and parasitic power consumption of the BMS, compared to a similar implementation of a monolithic architecture. Moreover, the design requirements of the communication network are very challenging because delay can occur, affecting the synchronization of the collected data.

3.2 Requirements and Functions

The complexity of a battery management system (BMS) strongly depends on the individual application. In simple cases, including just a single cell (mobile phones or e-book readers), a fuel gauge IC can be sufficient. These ICs usually are able to measure voltage, temperature and current as well as to perform simple estimation methods for the SoC of the cell. In more complex devices, such as large battery pack for EVs, the BMS has to fulfill more advanced tasks. In detail, regardless of the architecture or application, BMS functional requirements can be classified in five main categories:

- *Sensing and measurement*

  The BMS has to measure cell voltages, module temperatures and battery pack current as well as to detect isolation faults.

- *Safety and protection*

  It includes electronics and logic to protect the operator of the battery-powered system and the battery pack itself against abnormal operating conditions, such as overcharge, overdischarge, overcurrent, cell short circuits and extreme temperatures.

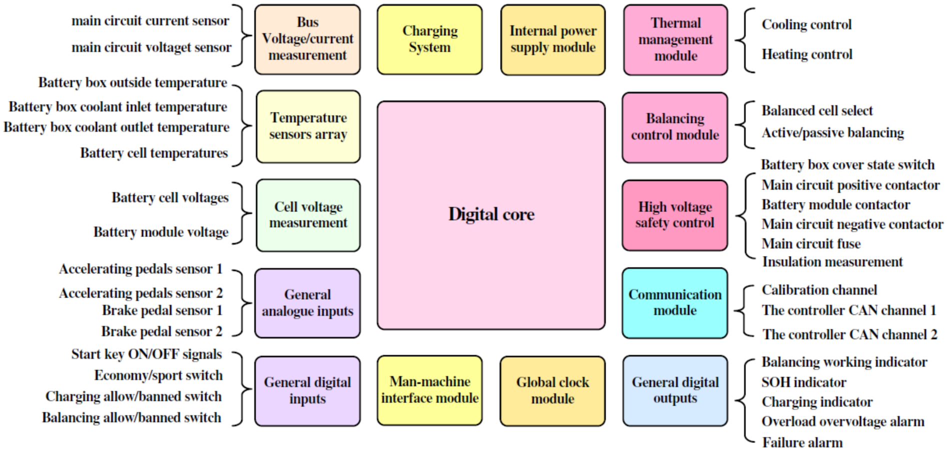

Figure 3.2: Main functional requirements for a BMS in an EV. [55]

- *Interface and communication*

  The BMS has to communicate regularly with the application that the battery pack powers, reporting available energy/power and desired information related to the battery pack status. An additional feature can be represented by recording unusual error or abuse events in permanent memory for technician diagnostics via occasional on-demand download.

- *Diagnostics*

  It is required to estimate relevant cell/pack parameters, such as SoC and SoH, as well as to detect and foresee fault conditions.

- *Performance management*

  The BMS has to compute battery pack available energy and power limits. Moreover, an equalization circuit is needed for maximizing the pack performance by means of balancing strategies for the cells.

In addition, depending on the application, specific functions can be required. As example, the main functional requirements for a BMS in an EV are summarized in figure 3.2.

3.2.1 Sensing and Measurement

This functionality results fundamental for the BMS in order to correctly monitor the operating conditions of the battery pack and its main components. Voltage, current and temperature are the measurements required for ensuring the battery pack to perform in the safe operating area (SOA). Typical requirements to be considered can be costs, bandwidth, precision, measurement range or size.

3.2.1.1 Voltage acquisition

A classical BMS for lithium-ion battery pack needs to have at least one voltage acquisition channel per serially connected cell. Indeed, cell terminal voltages provide a measure of the relative balance of cells in the battery pack and represent a critical input for SoC and SoH estimation algorithms. Out-of-bounds cell voltage can lead to undesired cycle life and safety issue, starting from overcharging/overdischargings up to thermal runaway with possible fire and/or explosion consequences.

Automotive applications require voltage measurements with high accuracy, high common-mode rejection and fast response in difficult environments in terms of electromagnetic interference (EMI), temperature and vibration. Usually, commonly available BMS front-end chips have an absolute accuracy of 1mV and a full range scale of 12 to 16 bits, which leads to a resolution of about 380μV. This can be critical if estimation algorithms are used on cell chemistries characterized by a very flat SoC-OCV curve, such as LFP technology. Figure 3.3 shows the effect of a limited voltage accuracy and its impact on SoC accuracy for LFP and NMC technologies. It results a larger SoC estimation error for LFP due to its flat OCV curve. This highlights that a better voltage accuracy allows for achieving a better SoC estimation, but considering only a voltage acquisition may not be sufficient. Moreover, higher voltage accuracy can be achieved at the expense of higher costs.

A pack voltage acquisition is usually considered as well. This can be defined as the sum of the individual cell voltages or evaluated by a separate measurement unit, consisting of a voltage divider, an impedance converter, a filter and an Analog Digital Converter (ADC). The voltage divider is necessary for scaling down the pack voltage to an adequate measuring voltage, which is in the range of the ADC. It is designed to be highly resistive in order to lower the power losses.

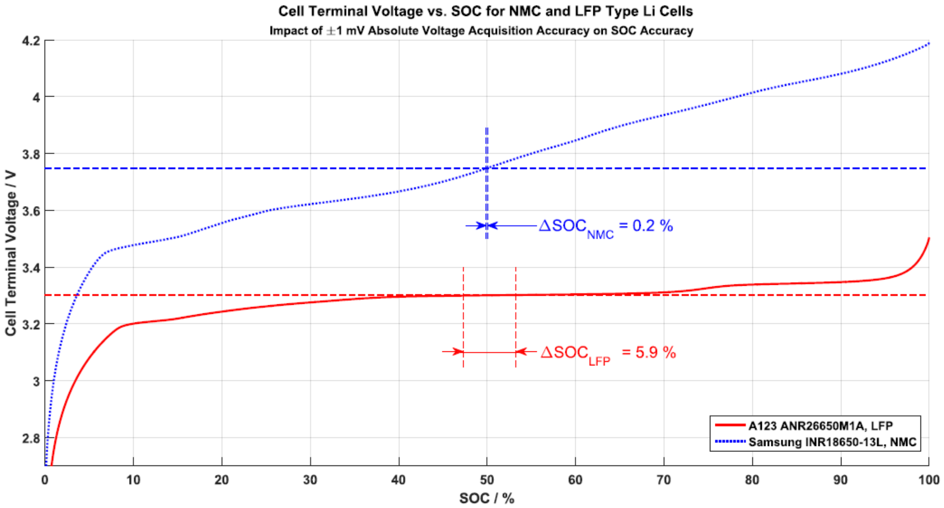

Figure 3.3: Comparison of SoC uncertainty depending on a ±1mV voltage accuracy for LFP and NMC technologies. [56]

3.2.1.2 Temperature acquisition

The definition of the optimal number and location of temperature sensors in a battery pack represents a very challenging task. The knowledge of the temperature distribution among the cells allows for predicting the pack performance as well as managing the TMS in order to maintain the cell temperatures in the SOA. The measurement of the internal temperature of each cell would be the ideal solution. However, since not all the cells commercially available are produced with temperature sensors built in, measurements of cell external temperatures need to be considered.

The main target is to minimize the total number of sensors required and thus reduce the cost. This can be achieved with an accurate pack thermal model, which allows for placing a limited number of temperature sensors external to one or more cells per module and then estimate internal temperatures of all cells. Generally, it can also be important to acquire peripheral temperatures, such as those of the contactors, fuses or even the electric busbars that carry the main current of the battery pack.

Common temperature sensors used for BMS applications are the negative temperature coefficient (NTC) or the positive temperature coefficient (PTC) thermistors, which are based on resistance variations with respect to temperature. In detail, the resistance varies inversely and directly with temperature in NTC and PTC thermistors, respectively. The measurement is realized by capturing the voltage drop while a constant current is flowing through the resistor. Thermistors are relatively cheap, easily applicable and are linear in a certain range, but behave nonlinearly for very low and high temperatures.

A different solution for temperature measurement include the adoption of sensors that are based on digital interface and provide a readily calculated temperature value. These sensors are robust and can be easily connected to a microcontroller environment. However, their performance are strongly affected by EMI induced failures.

Despite other solutions such as PT100, thermocouple or metal-based PTC, could provide higher accuracies and a wider temperature range, they involve higher complexity in terms of electronics.

3.2.1.3 Current acquisition

The current measurement represents a critical input to most SoC and SoH estimation algorithms. It is also needed for detecting any overcurrent conditions and thus providing safety. As reported in figure 3.3, depending on the battery technology, the cell voltage only shows a low dependence on the SoC, leading to estimation errors even in case of high voltage accuracy. While, a precise measurement of the total current allows for determining the SoC by integrating the current.

There are two basic sensor technologies used for measuring the current in a battery pack: galvanically connected and isolated. The first category include the shunt resistor current sensing, which is the widely adopted solution. While, hall-effect sensors are used as isolated current acquisition by evaluating the magnetic field strength due to the current flow.

- *Shunt resistor*

  A current shunt is a low-value and high-precision resistor placed in series with the battery pack. It can be implemented between the positive terminal of the battery pack and the load (high-side measuring) or between the load and ground or the negative terminal of the battery (low-side measuring). The voltage drop across the shunt resistance is measured using a standard ADC converter and the current is computed. The low value of the shunt resistance for maintaining power dissipation low leads to the needed of a voltage amplifier before sensing and calculating the current.

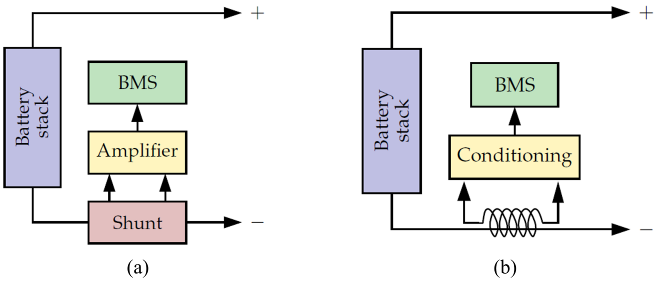

Figure 3.4: (a) Shunt resistor and (b) hall-effect sensor. [57]

The primary advantage of shunt resistors, compared to the Hall-effect sensors, is that they have no offset at zero current, regardless of temperature. However, the amplification and measurement electronics can still introduce an offset, which has to be properly addressed. Moreover, shunt resistors need to be electrically isolated from the low-voltage BMS circuitry, adding complexity to the design. The resistance of the current shunt also changes with temperature, thus additional calibration is needed. Then, the shunt itself introduces some energy losses and the heat generated has to be dissipated via the TMS.

- *Hall-effect sensor*

  Considering a coil wrapped around a primary current-carrying conductor, the electromagnetic field produced by the conductor induces a secondary current in the coil. Hall-effect sensors measure this induced current to infer the primary current. Since there is no direct electrical connection between the sensor and the high-voltage battery pack, they are also named as contactless current sensors.

  Therefore, no additional isolation circuitry is needed. Nevertheless, signal-conditioning circuitry is required for compensating the magnetic hysteresis of the Hall-effect sensor. Generally, several sensors come prepackaged with such circuitry. Moreover, they suffer from measurement offset at zero current, which drifts over time and changes with temperature. Hence, a proper calibration has to be developed and implemented in the BMS.

Figure 3.4 shows a photograph and a block diagram for both shunt resistor and Hall-effect sensors. Besides the sensor technology, the position in the battery pack has to be considered as well. Indeed, in case of nSmP configurations, it can be important to implement a current sensor for each string of series-connected cells and not only for the main battery pack current. In this way, imbalance conditions among the string can be traced during operation.

3.2.1.4 Isolation Sensing

In a standard automobile, the negative terminal of the 12V lead-acid battery can be connected directly to the vehicle frame or chassis because there are not significant safety risks due to the low voltage. This also allows for saving wiring costs since only the positive voltage requires separate wires to distribute power throughout the vehicle.

On the other hand, relevant safety issues may occur in case of isolation lost for high-voltage battery pack. Therefore, all wiring needs to be fully insulated and a proper design of the EPS is required in order to eliminate any direct connection between the high-voltage battery pack and the vehicle chassis. However, despite this greatly enhances safety, mechanical issues (accident, vibration) may break the insulation on the high-voltage wiring, leading the terminals of the battery pack to come in contact with the vehicle chassis through a low-resistance path. This poses a safety hazard, which has to be detected and highlighted for the vehicle operator.

It is important to point out that also an electric insulation or rather an electrically insulating material is generally characterized by its electric resistance. This insulation resistance is distributed over the whole electric circuit. Figure 3.5(a) shows a model of the isolation issues in EVs, where R_p and R_n are the concentrated insulation resistances between the positive and the negative terminals of the high-voltage battery pack and the vehicle chassis. While, C_p and C_n represent the sum of parasitic cable and possibly placed EMC filter capacitances.

A common technique for measuring the insulation resistance is shown in figure 3.5(b). Only two additional switches and two resistors are needed to determine the insulation resistances R_p and R_n while the capacitances C_p and C_n are contributing as disturbances. In detail, when switch S_p is closed, a current I_{sp} flows through R_{sp} and R_n as well. This leads the voltage V_n to increase and consequently V_p to decrease. Therefore, the chassis potential will result shifted with respect to the high-voltage battery pack. In this way, the insulation resistance can be calculated by measuring the different potential at its terminals.

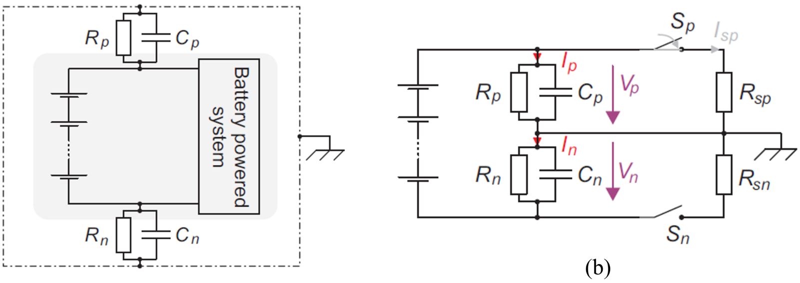

(a)

(b)

Figure 3.5: (a) Insulation model considering concentrated parameters; (b) scheme of a common technique for measuring the insulation resistance. [56]

3.2.2 Safety and Protection

One of the main purposes of BMSs is to minimize the likelihood of occurrence and severity of the hazard conditions associated with the operation of lithium-ion battery packs. Therefore, the BMS needs to properly control electrical/electronic devices in order to prevent fault conditions for the battery pack. In particular, there is a set of electronics hardware that is widely used for both low and high-voltage systems, which includes main and precharge contactors, manual service disconnect (MSD), high-voltage interlock loop (HVIL) and fuses. In addition, bus bars, cell interconnect boards and wiring harness can be adopted for safety concerns as well. Figure 3.6(a) shows an example of a safety and communication battery box, which interconnects the battery pack with the rest of the system. This highlights the BMS and all the main safety components needed. It is designed for both stationary or automotive applications. The target system has a voltage range between 315V and 567V, while being capable to provide a continuous current of up to 320A. The battery pack consists of 14 series-connected modules, each one in a 15S2P configuration of 2.3V 20Ah lithium-ion NMC/LTO prismatic cells. Figure 3.6(b) reports the schematic architecture of this battery box as well. More details related to the safety and communication functions of the BMS are discussed in the following sections.

3.2.2.1 Contactors Control

As discussed in section 3.2.1.4, high-voltage battery packs are designed to be isolated electrically from chassis ground. Moreover, iso-

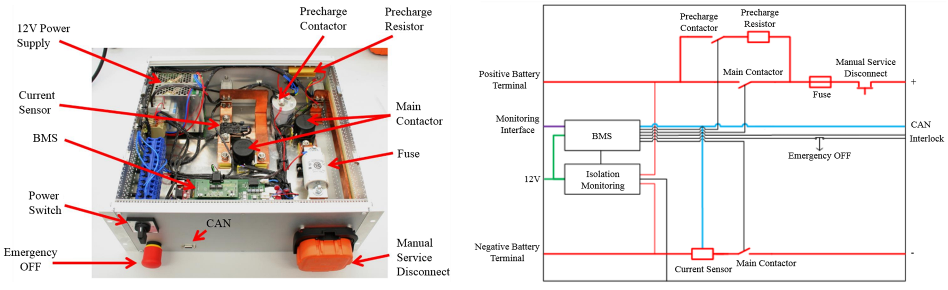

(a) (b)

Figure 3.6: (a) Example of a safety and communication battery box and (b) related scheme. *Source: Fraunhofer*

lation sensing allows for detecting isolation fault or ground fault. For similar safety concerns, the internal high-voltage bus of the battery pack is completely disconnected from the load at both pack external terminals when not in use. This requires two high-current capable relays known as main contactors.

The main contactors used in battery packs are normally-open devices in order to ensure the battery pack to be disconnected from the load in case of BMS fault conditions. Moreover, considering that the motor-driving circuitry in EVs requires large capacitor to filter the transients caused by switching power to the EM, a severe in-rush current can occur by simultaneously closing the contactors, potentially welding the contactors closed or blowing a fuse. Hence, a third precharge contactor is needed.

Figure 3.7 shows the overall startup process for connecting the battery pack to the rest of the EPS. Starting from a complete disconnection of the battery pack, the negative contactor is activated first. Then, the precharge contactor is actived, which limits the current flow by means of a precharge resistor and allows the battery pack for charging up the capacitive load at a controlled and safe rate. Typically, the temperature of the precharge resistor is monitored because the load may have a short circuit fault if it becomes too high. This fault condition can also be detected by evaluating if there is a difference between the pack and the filter capacitor voltages. In both cases, the startup process is aborted and the pack is disconnected from the load. Otherwise, the connection procedure of the battery pack proceeds the BMS can be concluded by closing the positive contactor and then openining the precharge contactor. There is not a standard procedure for disconnecting the battery pack since the danger of contactor fusing/welding

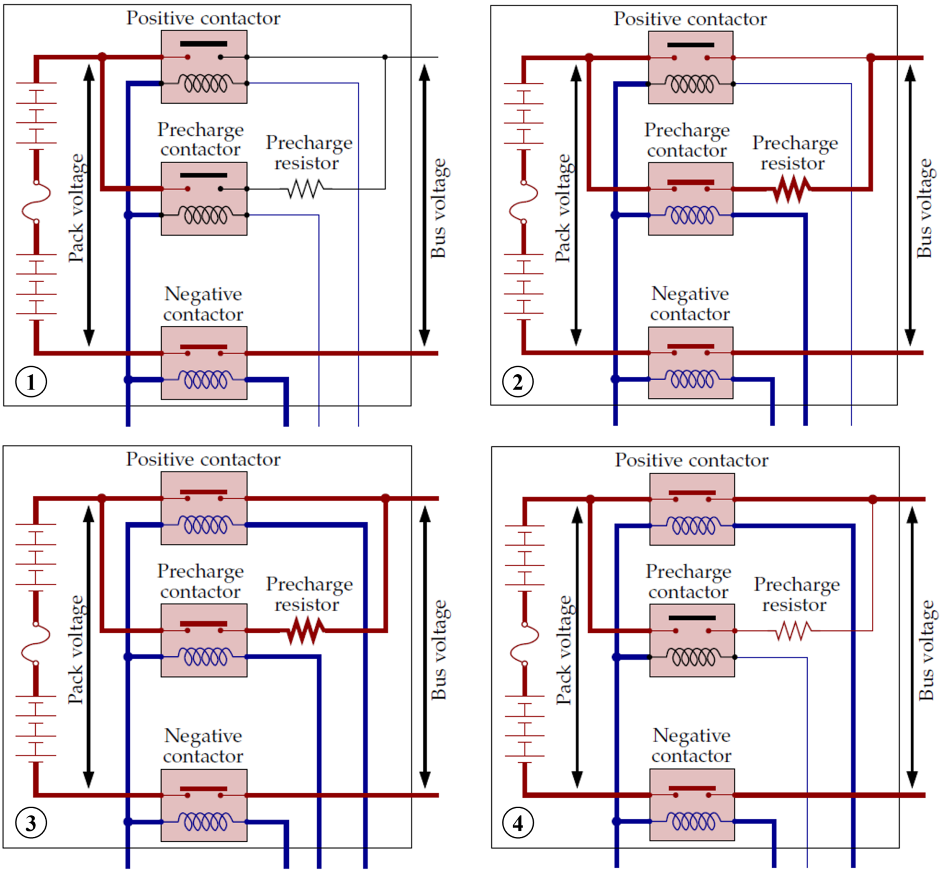

Figure 3.7: Startup procedure for connecting the battery pack to the rest of the EPS. [57]

is not as severe. Generally, if the inductance of the load is small, simply opening the main contactors results sufficient. If not, the startup procedure could be used in reverse to drain the inductive energy prior to complete disconnect the battery pack.

3.2.2.2 High-voltage Interlock Loop

Most of the high-voltage energy storage system (ESS) include HVIL safety features, which essentially creates a closed circuit when the battery pack is sealed. If one part of the pack is opened, the high-voltage bus is compromised and the main contactors remain opened in order to prevent undesired flowing current.

It is important to highlight that the HVIL is not a single component that can be installed in the battery system, but rather a series of components, software and controls that do not allow the opening of the battery pack until the HVIL is disengaged. The aim is to ensure safety conditions during service or maintenance operations.

Two main solutions can be adopted for operating the HVIL. The first one consists in connecting the high-voltage cables to to an interlock circuit that reports the status to the BMS. As soon as one of the interlock circuits is opened, the BMS will send an opening command to the main contactors. The second solution regards the possibility to connect the high-voltage cables through an MSD, which is a manual connector with an integrated fuse. This is also named as mid-pack service disconnect since it is usually placed at or near the middle of the pack. In this way, once the MSD is removed, the voltage or energy of the battery pack will be split in half, resulting in the opening of the HVIL circuit and consequently the opening of the main contactors. These solution are important to protect the high-voltage battery pack from external short circuit as well.

3.2.2.3 Fuses

Generally, depending on the size of the battery pack, fuses are included into the overall design along with the MSD. In particular, only fuses are considered for low-voltage packs, while the MSD results unecessary. Additionally, several manufacturers integrate small fuses directly into the control boards that interconnect the cells. In this way, safety improvements can be achieved in case of failure of any individual cell, limiting the impact on the battery pack. Large ESSs may not include an MSD-type fuse, but usually include a fuse as a safety feature due to the less restrictive constraint in terms of size and volume. Moreover, the fuse may be integrated into a battery disconnect unit (BDU) for very large ESSs. Therefore, fuses need to be properly selected depending on the requirements of the specific application.

3.2.2.4 Battery Disconnect Unit

Most of these safety electronics coponents and subsystem can also be packaged together, leading to the a single physical unit named as BDU. While the BMS is typically mounted separately, the BDU serves as the interface to the EM, vehicle controllers and any communications outside of the vehicle. Several manufacturers have de-

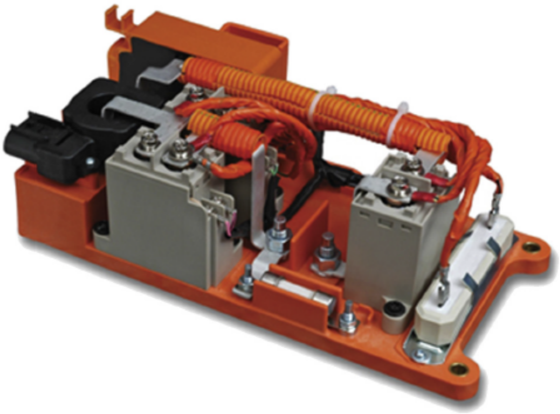

Figure 3.8: Off-the-shelf high-voltage unit provided by Delphi Electronics.

signed these BDUs in standard off-the-shelf units, which consist of main contactors, precharge contactor, fuses, HVIL circuitry and other electronics hardware. Figure 3.8 shows an off-the-shelf high-voltage unit provided by Delphi Electronics.

3.2.2.5 Standard ISO 26262

Defining the risk as the the probability of occurrence of damage and its impact on people, equipments and the environment, the main task of functional safety is to minimize the risk to an acceptable level. The measures that can be employed to reduce risk are classified as fault avoidance, fault detection or fault handling measures. A wide variety of safety standards are available for providing a guidance on required and recommended measures for most of industry sectors, with IEC 61508 focusing on electrical/electronic/programmable electronic safety-related systems. The standard ISO 26262 has been introduced as an adaption of the IEC 61508 to cover the special conditions encountered by electronic systems in series-produced road vehicles with a mass of up to 3500 kg (excluding special-purpose vehicles). Therefore, BMSs developed for EVs need to be compliant with this standard.
The ISO 26262 consists of 10 parts, with parts 1 and 2 introducing the vocabulary and the general principles of the standard, part 3 describing the concept phase of the development process, parts 4-6 and 7 focusing on the product development and the production and operation of the system, respectively. Parts 8-10 provide a guidance on the application of the standard. The ISO 26262 also includes a safety

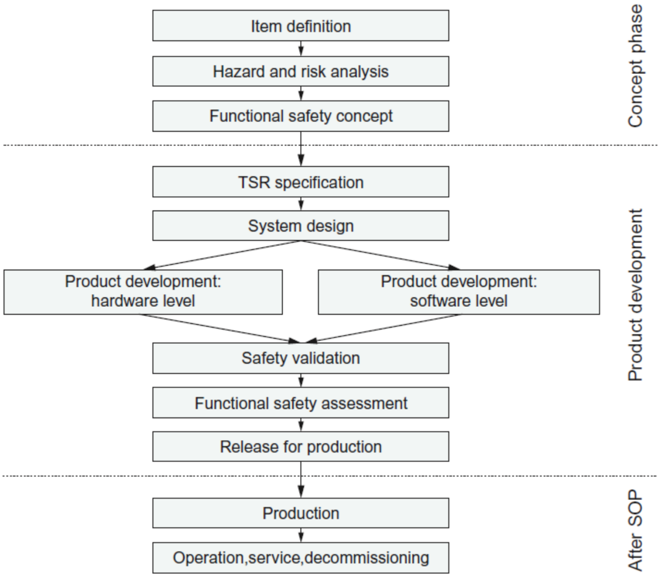

Figure 3.9: Simplified safety cycle life of a system defined by ISO 26262. [58]

cycle life part, which encompasses the entire cycle life of a system from concept to decommissioning. A simplified version of the safety life cycle is illustrated in figure 3.9 a more details about the standard ISO 26262 are illustrated in [58].

3.2.3 Interface and Communication

Suitable protocol standards need to be considered for the communication of the BMS with battery modules and all components of the battery pack. Currently, the control-area network (CAN) bus is one of the most prominent buses used for automotive applications because it is very flexible regarding the number of bus members with a good noise resistance. The simpler Local Interconnect Network (LIN)-bus is also widely adopted since it is less expensive due to reduced hardware efforts at the expense of resulting slower, less flexible and non-differential. Other buses that are mostly used on short distances, such as chip to chip communication, include the SPI interface, I2C interface or the Onewire bus. Due to their non-differential signals, they are not robust against disturbances on a longer, more exposed line, such as inter-module buses. This is the major concern that leads to select CAN bus as reference communication protocol for automotive applications. Despite its very high speed of 1Mbps, the CAN nus may result unsuitable in applications where real-time deterministic capability is required. In this case, the FlexRay bus can be adopted. Otherwise, an Ethernet connection can also be used for connecting the battery system with the application, especially when high communication speed and large data volumes are required.

Automotive applications use the CAN bus almost exclusively for onboard vehicle messaging. It is designed to provide robust communications in the very harsh automotive operating environments with high levels of electrical noise. CAN bus has an electrical specification and a packet protocol. Electrically, it comprises a differential two-wire serial bus designed to network intelligent sensors and actuators. Messaging can operate at two rates: high-priority messages are sent at a higher baud rate, whereas low-priority messages are sent at a lower rate. High-rate messaging is used for critical operations, including engine management, vehicle stability and motion control. On the other hand, low-rate messaging is used for simple switching and control of lighting, windows, mirror adjustments and instrument displays.

The communication protocol defines:

- method of addressing the devices connected to the bus;
- transmission speed and priority settings;
- error detection and handling;
- control signals.

Figure 3.10 shows the data frames that are transmitted sequentially over the bus. They include a 1-bit start-of-frame (SOF) marker, an 11 or 29-bit address for the intended recipient of the message, a 1-bit remote-transmit request (RTR) flag indicating whether this is a data frame or a remote frame, a 6-bit control field, a 16-bit cyclical-redundancy-check (CRC) for transmission error detection, a 2-bit acknowledgment (ACK) field and a 7-bit end-of-frame (EOF) marker. In particular, a CAN buses with 11 or 29-bit identifiers are named as CAN 2.0A and CAN 2.0B, respectively. Generally, most of automotive-grade microcontrollers have built-in CAN communications hardware that properly manage the data frames.

3.2.4 Diagnostics

This represents an important function to be operated by the BMS since it provides an overall performance and state evaluation of the battery pack. In detail, the BMS has to compute diagnostics and re-

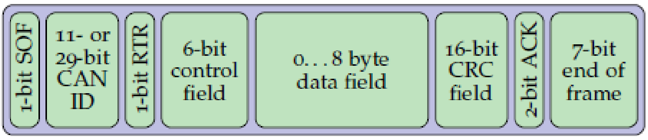

Figure 3.10: CAN2.0 data frames. [58]

port a quantified information on the SoC and the SoH of the battery pack. Accurate estimation of battery states allows for achieving relevant details about the current performance of the battery pack as well as providing assurance of a reliable and safe operation of the EV. This is a very difficult task because currently there are not standards for correctly estimating these parameters. Hence, a combination of mathematical, algorithmic and battery models is performed in order to achieve a suitable estimation depending on the application. A brief overview of the main SoC and SoH estimation approaches is illustrated in the following subsections.

3.2.4.1 SoC Estimation Method

This is one of the main challenges for the successful operation of EVs. Due to non-linear, time-varying characteristics and electrochemical reactions, SoC cannot be observed directly. Moreover, since the performance of the battery pack is highly affected by aging, temperature variation and charge-discharge cycles, the task of estimating an accurate SoC results very challenging. Currently, the existing SoC estimation techniques can be classified into five categories: conventional method, the adaptive filter algorithm, the learning algorithm, the nonlinear observer and the hybrid algorithm.

Conventional Method

This category includes different approaches for estimating the SoC, based on Coulomb counting, OCV, impedance and internal resistance, electrochemical models and ECMs.

– *Coulomb Counting Method*

This is the simplest method to be implemented for SoC estimation due to its low computational complexity. It is based on the integration of the charging/discharging current for calculating the remaining charge of an individual cell or the overall battery pack as follows:

$$SoC(t) = SoC(0) - \frac{1}{C_n} \int_0^t i(t) d\tau \tag{3.1}$$

where $SoC(0)$ is the initial SoC, C_n is the nominal capacity of the cell and $i(t)$ is the charging/discharging current. A more detailed definition of the Coulomb counting method is reported in [59], which also introduces the coulombic efficiency η and the self-discharge rate S_d:

$$SoC(t) = SoC(0) - \frac{T}{C_n} \int_0^t (\eta \cdot i(t) - S_d) d\tau \tag{3.2}$$

where T is the sampling time.

This method allows achieving accurate results if the initial value $SoC(0)$ is correctly defined. However, this is not easy, thus an estimation is needed. It may be defined by using a look-up table based on the SoC-OCV characteristic of the cell or considering conditions where the SoC is known, such as fully charged or discharged cell. Nevertheless, these two conditions are not always reached, especially for automotive applications, where the battery pack is fully charged and discharged rarely.

Moreover, Coulomb counting method is very sensitive to measurement errors. Indeed, a constant error in measuring charging/discharging current is integrated over time producing a drift of the estimated value, which increasingly moves away from the real value of SoC. This error may be reduced by a proper calibration of the measurement. However, the operating conditions strongly affect the current acquisition, resulting in calibration complexity of the Coulomb counting method. In addition, the capacity fade of the cell due to aging needs to be taken into account as well.

- *Open Circuit Voltage*

  This method adopts the SoC-OCV characteristic for estimating the SoC of the cell. Therefore, its performance highly depends on the shape of the OCV and thus on the cell technology considered, as previously illustrated in section 3.2.1.1. As example, since LFP cells have a very flat SoC-OCV characteristic and a significant OCV hysteresis phenomenon, OCV method as SoC estimator results unsuitable.

Moreover, despite the SoC-OCV curve of lithium-ion technology is relatively stable, it varies depending on the environmental temperature and cycle life of the cells. Hence, massive experimental tests in different operating conditions are required for capturing the variations of the OCV curves for a specific cell technology. It is important to highlight that the terminal voltage of the cell is closely representative of the OCV only after a long rest and while under no load. Therefore, depending on the cell technology, a proper rest time is needed for measuring the OCV. This makes the OCV method not suited for estimating SoC in real-time. It may be used for very low power applications, in which low current are required and thus the OCV can be assumed equal to the voltage at cell terminals.

- *Impedance and Internal Resistance*

  This method is similar to the OCV one since it estimates the SoC by measuring the internal resistance or impedance of the cell. In particular, the resistance is calculated by the ratio between the cell voltage and the current variations in DC, while the Electrochemical Impedance Spectroscopy (EIS) is considered for estimating the internal impedance of the cell using inductances and capacitances over a wide range of frequencies [60]. However, the characteristic curve between the SoC and the internal resistance/impedance is not stable as the SoC-OCV one. Indeed, the resistance/impedance value is not sensitive to SoC variations since it could be a nonmonotonic characteristic curve. While, it is very sensitive to temperature variations, aging conditions. Therefore, as for the OCV method, impedance and internal resistance approach results unsuitable in estimating the SoC for EV applications.

- *Electrochemical Model*

  The SoC can also be estimated by evaluating the amount of lithium concentration in the positive or negative electrodes. This involves the adoption of an electrochemical model with partial differential equations. Theoretically, this allows for achieving the most accurate SoC estimation. However, electrochemical models result complex and characterized by a large amount of parameters needed for their implementation. Therefore, they are suitable for off-line design and performance analysis of lithium-ion cells, but not proper for online SoC estimation.

Reduced-order electrochemical models can certainly represent a good trade-off between complexity and accuracy in estimating the SoC [61].

- *Equivalent Circuit Model*

  Currently, ECMs are the most widely used solution for online SoC estimation in automotive applications. An ideal ECM should be able to simulate the real electrical behavior of the cell under any current profiles. Actually, several aspects of a lithium-ion cell cannot be fully represented by circuit elements, including hysteresis or Warburg effects [62].

  The most common ECM parameter for SoC estimation is the OCV. Therefore, it inherits all the disadvantages related to the SoC-OCV characteristic previously illustrated for the OCV method. Compared to electrochemical models, ECMs result more suitable for real-time SoC estimation due to the lower implementation complexity.

  However, there are two major concerns that need to be properly addressed. The first one regards the optimal calibration of the ECM parameters. In detail, time-consuming experimental tests are required considering different operating conditions in terms of current profile, aging and temperature. Secondly, the voltage accuracy from the conventional ECMs in the low SoC range is relatively low [63].

Other SoC Estimation Methods

An overview of the SoC estimation methods for the remaining four categories is reported in figure 3.11. Currently, there is a large amount of techniques that allow for achieving different trade-off between computational cost and accuracy of the SoC estimation [64–66].

Adaptive filter algorithms include Kalman Filter (KF), Particle Filter (PF), Unscented Particle Filter (UPF), $H\infty$ Filter and Recursive Least Square (RLS). Among these methods, Kalman filter represents a promising solution for estimating the SoC. It is a well-designed method, which filters parameters from uncertain, inaccurate observations. It is commonly used in many applications such as EVs, aerospace technologies, radar and navigator tracking. Despite its high computational cost, Kalman filters result attractive also for automotive applications due to their self-correcting nature, which allows for tolerating high variation of current. In detail, they are based on a set

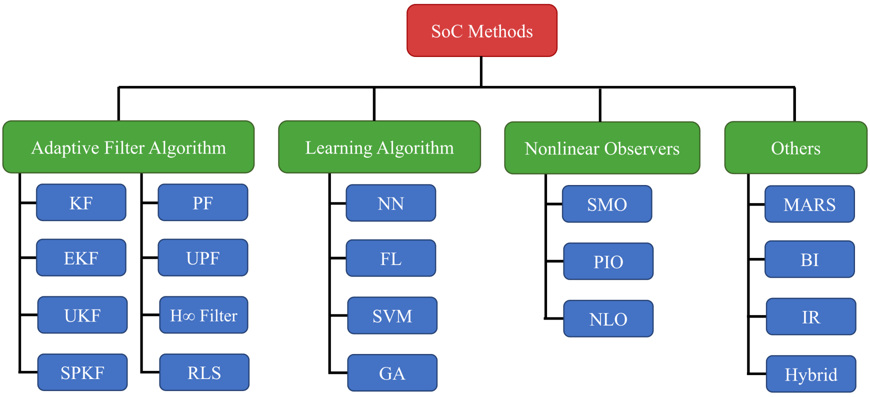

Figure 3.11: Other SoC estimation methods.

of mathematical equations, which predicts and corrects a new state comparing the measured input data and output data from an ECM to calculate the minimum mean squared deviation of the true state. The algorithm provides a recursive solution through a linear optimal filtering for estimating state variables. The equations are operated in state-space form and consider a discrete-time version of the cell dynamics. Starting from the basic Kalman filter that operates with linear systems, different solutions have been proposed in literature for extending its functionality to nonlinear systems, including the Extended Kalman Filter (EKF), the Unscented Kalman Filter (UKF) and the Sigma Point Kalman Filter (SPKF).
Learning algorithms have adaptability and self-learning skills to demonstrate a complex nonlinear model. However, they require a large amount of training data and heavy computation to describe the nonlinear characteristics of lithium-ion cells and thus estimate the SoC. The main methods include Neural Network (NN), Fuzzy Logic (FL), Support Vector Machine (SVM) and Genetic Algorithm (GA).
Nonlinear Observers are designed to handle highly nonlinear systems. Three main categories can be identified: Sliding Mode Observer (SMO), Proportional-integral Observer (PIO) and Nonlinear Observers (NLO).
Other alternative methods include Multivibrate Adaptive Regression Splines (MARS), Bi-linear interpolation (BI), Impulse Response (IR) and Hybrid solutions. MARS, BI and IR adopt extended linear model, two linear interpolations and linear time invariant system, respectively. While, hybrid methods combines different solution for estimating the SoC in order to take the advantages of each method and thus achieve higher performance.

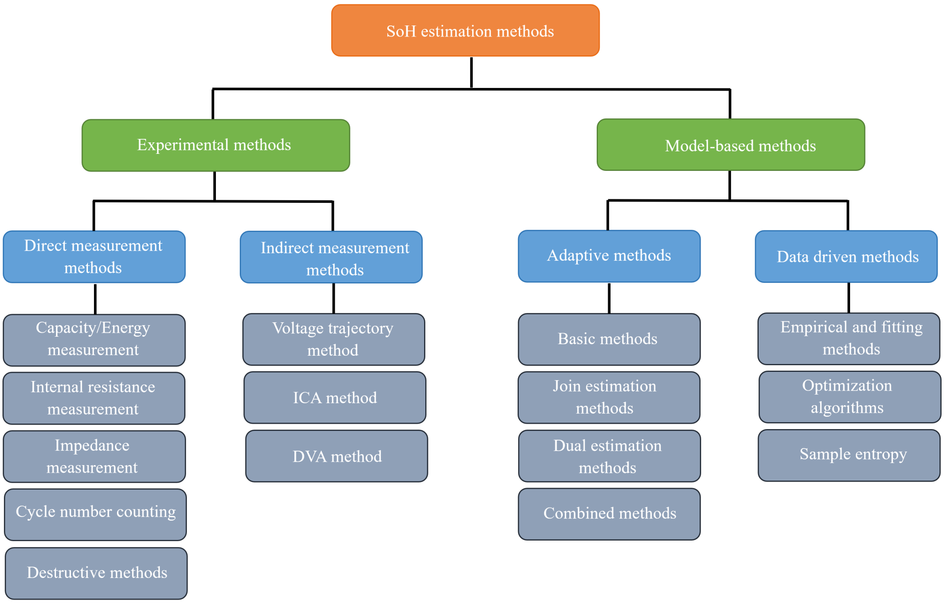

Figure 3.12: Overview of SoH estimation methods.

3.2.4.2 SoH Estimation Method

Generally, SoH estimation refers to a process whereby cell-model internal parameters are estimated and tracked as the cell ages. Since there is no universally agreed-upon definition of SoH, it is common to estimate two measurable indicators of aging: current cell capacity and series resistance. In particular, considering the EVs requirements, a capacity decrease of 20%-30% and/or a resistance increase of 50%-100% highlights the needed for replacing the battery pack. Capacity decrease is also known as capacity fade, whereas resistance increase leads to power fade.

As for the SoC, the SoH can be estimated by means of experimental and model-based methods. The first ones collect relevant data from experimental tests in different operating conditions in order to directly determine the SoH. The model-based methods define the SoH by estimating cell parameters that are sensitive to degradation, thus capacity and internal resistance. Different experimental and model-based approaches can be adopted, as summarized in figure 3.12 and widely illustrated in [67].

For what concern experimental tests, most cell manufacturers usually provide calendar and cycle aging data conducted by applying consecutive charging/discharging cycles at one or multiple temperatures. However, these tests differ significantly from real-world use of cells as part of battery packs. Therefore, experimental methods for characterizing cell degradation need to be performed considering the representative current profiles required from the specific application. These methods have to be optimized in order to achieve easily implementable and repeatable tests with shorter time than real-world for practical reasons. Moreover, most significant factors responsible for cell aging need to be taken into account, including current distribution, SoC, temperature and DoD. Therefore, the main challenge consists in extracting the most important aging characteristics associated with real-world driving and determining a duty cycle that causes the cell aging comparably.

To characterize the degradation processes in lithium-ion cells, an appropriate experimental campaign should be designed, which requires a duration of months or years. In detail, the aging campaign can be split into two main sections [68]:

- *Calendar Aging*

  In this experimental test, the cells are stored at different SoC and temperature conditions. In particular, no load current is applied, SoC is monitored and kept constant using external circuitry and cell temperature is maintained constant by means of thermoelectric cooler or environmental chamber. SoH is assessed periodically via capacity and dynamic tests.

- *Cycle Aging*

  In this case, depending on the specific application, cells are cycled with a pre-designed charging/discharging current cycle, repeated for sufficient number of times to induce degradation. As for the calendar aging test, cell temperature has to be kept fixed and SoH is evaluated by means of periodic assessment with capacity and dynamic tests.

3.2.5 Performance Management

This represents a crucial task for a BMS because it has to maximize the performance of lithium-ion battery packs while ensuring their safe operating conditions. Hence, it has to define proper power limits accordingly with relevant aspects, including SoC and SoH of the battery

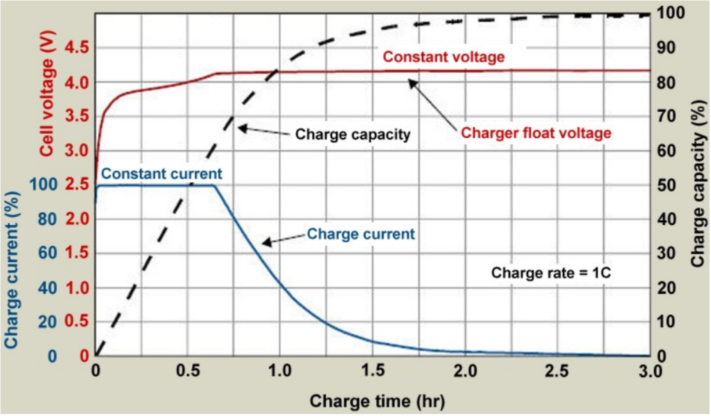

Figure 3.13: Standard charging protocol CCCV.

pack, cell temperatures, maximum charging/discharging C-rates and overvoltage/undervoltage thresholds due to the cell technology [44,57]. Moreover, the performance management involves two main topics that allow for maximizing the usable capacity of a battery pack and extending its cycle life: charging techniques and balancing strategies.

3.2.5.1 Charging Techniques

Nowadays, the adoption of a proper battery charging technique results fundamental for enabling fast charging technology and thus reducing the charging time of EVs. However, overcharging and overtemperature issues need to be carefully taken into account in order to avoid hazard conditions as well as reduction of the cycle life of the battery pack. Therefore, the development of optimal charging strategies represents an essential part of the BMS.
The most common charging technique for lithium-ion cells is the CCCV standard, which it is based on two phases, as illustrated in figure 3.13. In the first phase, the cell is charged with a constant current (CC) until reaching the maximum cell voltage depending on the cell technology. This stage usually provides 60-80% of the nominal capacity. Then, the cell voltage is kept constant and the current starts to decrease, leading to the costant voltage (CV) phase. The complete charge occurs when the charging current drops below a predefined threshold value (usually 3% of the rated capacity) or when a predefined maximum charging time is exceeded.
The charging time is mainly influenced by the constant current value.

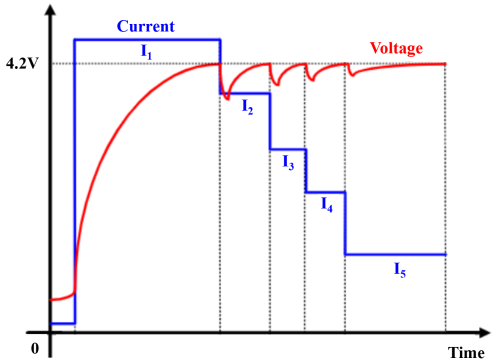

Figure 3.14: MSC charging protocol in case of five stages. [69]

Indeed, higher C-rates allow for achieving lower charging time, which result an important task for enabling large-scale adoption of EVs. However, the maximum C-rate allowable depends on the cell technology and the cooling system considered. Moreover, high C-rate strongly affects aging, leading to lithium plating and possibility of thermal runaway. It also reduces the CC stage because the cell will reach the maximum voltage sooner with consequently increase of the CV stage and thus of the charging time. Therefore, a proper control algorithm is needed for maximizing the energy storable in the battery pack of an EV while minimizing the charging time.

An alternative solution includes the multistage constant current (MSC) charging, in which the CV phase of the CCCV protocol is replaced by a series of CC periods with monotonic decreasing charging currents [69], as shown in figure 3.14. In particular, each time the maximum cell voltage is reached, the C-rate is reduced to a lower value. Then, the charging process is stopped when the maximum cell voltage is reached at the lowest current stage. This charging technique allows for achieving a lower charging time with respect to the CCCV protocol.

Additional charging techniques and more details related to the CCCV and MSC protocols are discussed in [70].

3.3 Equalization Circuits

Depending on the application, a certain number of series and parallel connections of cells are needed to build a battery pack in order to fulfill the voltage and capacity requirements. The inhomogeneity of cell parameters due to manufacturing tolerances, cell degradation,

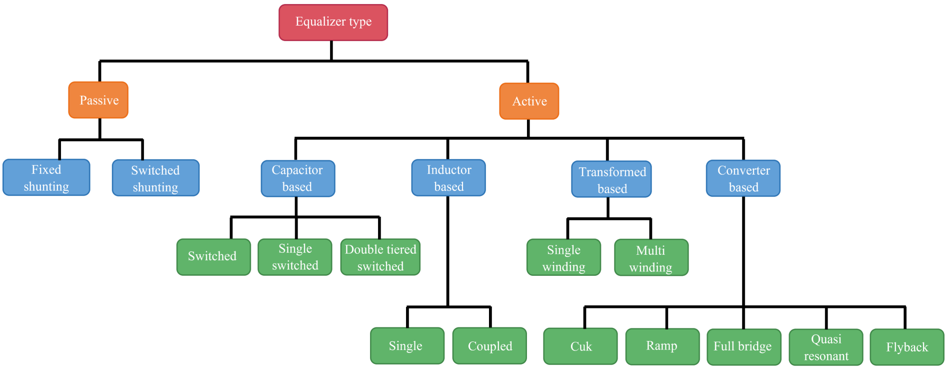

Figure 3.15: Classification of the equalization circuits.

temperature gradients and abuse conditions (electrical, mechanical and thermal), can result in an unbalanced voltage distribution in the series-connected cells. Moreover, if only one cell goes outside of the allowed voltage range, the operability of the battery pack is lost with a reduction of the usable capacity.
To overcome these issues, the BMS includes a cell voltage equalization circuit, with the aim of maximizing the performance of the battery pack by limiting the cell-to-cell voltage variation. In particular, different architectures for cell equalization circuits have been proposed in literature. They are mainly divided in passive and active depending on the strategy used for dissipating or transferring energy among the cells, as illustrated in figure 3.15. The comparison of their performance is usually operated in terms of efficiency, equalization speed, voltage and current stresses on components, hardware and software complexity, size and cost [71–75].

3.3.1 Passive

Passive equalization circuits, also known as energy-consuming, are based on dissipating the excess energy of the most charged cells on a power resistor placed in parallel with every cell. They represent the most common solution adopted in industrial and vehicular applications due to its reliability and low cost [76]. Nevertheless, this architecture has several disadvantages, including low equalization efficiency, unidirectionality of the power flow and thermal issues due to heat generation. Indeed, the Joule's effect on the balancing resistors are relevant when high equalization speed is desired, requiring a spec-

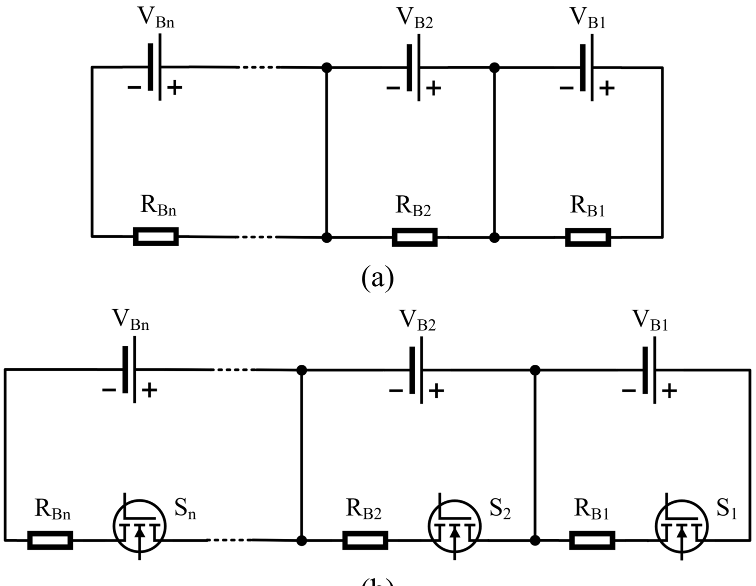

(a)

(b)

Figure 3.16: (a) Fixed shunting resistor and (b) switched shunting resistor architectures for a generalized battery pack composed by n series-connected cells.

ified design of the circuit [77, 78] as well as a proper control strategy for the thermal management [79].

Typically, passive equalization circuits can be classified in two categories: fixed shunting resistor and switched or controlled shunting resistor. Figure 3.16 shows the architectures of both passive solutions for a generalized battery pack composed by n series-connected cells. The main difference is related to the management of the bypass path with the balancing resistor. In detail, the fixed shunting resistor allows for continuous current flows through the balancing resistors for all the cells. Different balancing currents will occur for the cells depending on their terminal voltages. Due to its simplicity and low cost, this architecture is widely used for lead-acid, Ni-Cd and Ni-MH technologies in low power application to avoid overcharging conditions for the cells. The main disadvantages include the continuous energy dissipated as heat for all the cells. This makes the fixed shunting resistor architecture unsuitable for high-performance applications.

On the other hand, power switches are included in the balancing path for a controlled shunting resistor equalization circuit. This allows for operating the balancing process to the most charged cells only, resulting more effective and reliable than the fixed shunting resistor architecture. Therefore, an optimal control of the switches can be performed with respect to the cell operating conditions and depending on the performance required or desired. Moreover, despite the heat dissipation issues still remain, a proper thermal management can be achieved with the controlled shunting resistor architecture by limiting the number of cells in balancing simultaneously.

3.3.2 Active

Active equalization circuits allow for achieving high performance in terms of energy efficiency and equalization speed due to the capability of transferring energy among the cells. Compared to the passive architecture, higher balancing current can be achieved without encountering relevant thermal management issues, resulting in lower equalization time.

Active equalization circuits can be classified with respect to either the storage component adopted or the equalization energy path. For what concerns the storage component, capacitors, inductors and transformers can be adopted. There is also an additional category that can be identified, which includes the converter-based equalizer. In this category, classical power electronics converters are considered as energy transfer method among the cells. Table 3.1 reports all the main architectures presented in literature for each category of active equalization circuit, highlighting the related equalization energy path as well.

In detail, four possible energy transfer techniques can be achieved by means of the active equalization circuits: direct cell-to-cell (DC2C), adjacent cell-to-cell (AC2C), pack-to-cell (P2C) and cell-to-pack (C2P). The DC2C can be performed with both capacitor-based and inductor-based architectures and allows for directly transferring energy between the most and the least charged cells of the battery pack. While, the energy transfers occur only between adjacent cells for the AC2C configuration, which is mainly operated by converter-based architectures. In this case, it results low equalization speed and high implementation cost for large battery packs. Then, transformer-based architectures and flyback converters allow for achieving C2P and P2C energy transfers.

Currently, the active equalization circuits represent a promising solution for increasing the battery pack performance thanks to the possibility of transferring energy among the cells and thus avoiding energy

	Equalizer type	**DC2C**	**AC2C**	**P2C**	**C2P**
Capacitor based	Switched		x		
	Single switched	x			
	Double tiered switched	x			
Inductor based	Single	x		x	x
	Coupled		x		
Transformer based	Single winding			x	x
	Multi-windings			x	x
Converter based	Cuk		x		
	Ramp		x		
	Full bridge		x		
	Quasi resonant		x		
	Flyback			x	x

Table 3.1: Classification of the active equalization circuits with respect to the storage component adopted and the energy transfer technique. $DC2C$: Direct Cell-to-Cell, $AC2C$: Adjacent Cell-to-Cell, $P2C$: Pack-to-Cell, $C2P$: Cell-to-Pack.

dissipation as for the passive equalizers. Moreover, active equalization strategies can also be performed during charging and discharging process, providing a significant contribute in maximizing the energy from and to the battery pack. However, the major concerns that are limiting a large adoption of the active equalization circuits mainly include the number of components needed for the hardware implementation, which leads to size and cost issues. In addition, more complex control algorithms have to be developed for the management of the active architectures with respect to the simplicity of the passive equalization circuits.

3.3.2.1 Capacitor-based

These architectures use capacitors as storage components for transferring energy among the series-connected cells in a battery pack. Three main categories can be identified, including switched capacitor [80,81], single switched capacitor [82,83] and double tiered switched capacitor [84, 85] configurations. There is also another architecture based on the modularization approach [86, 87], which is primarily adopted for large battery packs.

- *Switched Capacitor (SC)*

  In this architecture, a capacitor is connected between each two adjacent cells, as shown in figure 3.17(a). It requires $n-1$ capacitors and $2n$ switches for a generalized battery pack composed by n series-connected cells. The control strategy is very simple since all the switches can be controlled by a common control signal with a fixed duty cycle. The equalization process results to be self-limiting because the amount of energy transferred decreases as the voltage imbalance among the cells lowers. Therefore, ideally no energy transfers occur for a fully balanced battery pack. This also allows for avoiding floating voltage sensing and closed-loop control, resulting in cost-savings for the equalization circuit. The main disadvantages include high number of components and low equalization time, especially for large battery packs. In particular, the worst condition in terms of equalization time occurs when the most charged cell and the least charged one are on the opposite ends of the battery pack. In addition, since all the cells participate to the equalization process, the overall efficiency of this active equalization circuit is affected by high losses as well.

- *Single Switched Capacitor (SSC)*

  The SSC allows for a DC2C equalization among the cells, thus the energy can be transfer directly from the most charged cell to the least charged one in the battery pack. It is characterized by a reduced number of components with respect to the SC architecture, since it only needs 1 capacitor and $n+5$ switches, as illustrated in figure 3.17(b). In this case, a control strategies is required for performing the equalization process. Indeed, the most and the least charged cells need to be identified and the corresponding switches have to be enabled. This also includes the possibility to develop advanced control algorithms that allow for improving the equalization speed. Moreover, short energy transfer paths are achieved due to the DC2C equalization, resulting in a higher efficiency than the SC architecture.

- *Double Tiered Switched Capacitor (DTSC)*

  A derivation of the SC is considered for the DTSC, where two additional capacitor tiers are used for reducing the equalization time to one-fourth with respect to that achievable for the

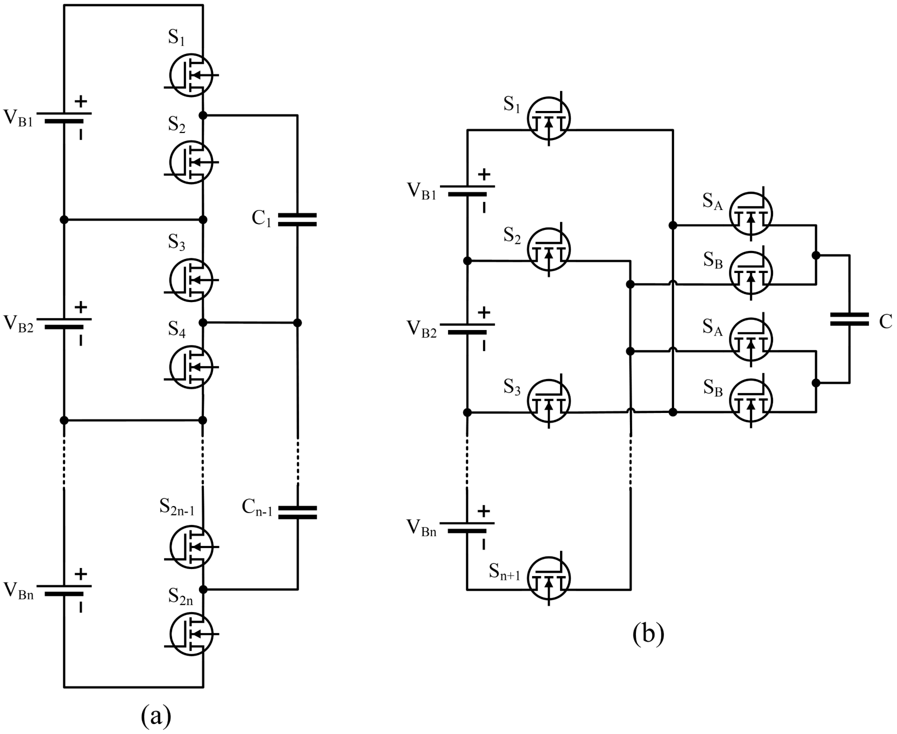

Figure 3.17: (a) Switched capacitor and (b) single switched capacitor architectures for a generalized battery pack composed by n series-connected cells.

SC. Indeed, these capacitor tiers provide additional paths for the energy transfers among the cells. Therefore, cells that are not adjacent can transfer energy through the additional capacitors. Likewise for SSC, a DC2C can be performed with the DTSC, but a large number of components is needed, including n capacitor and $2n$ switches, as shown in figure 3.18(a). Hence, compared to the SC, the DTSC represents a more expensive architecture. However, it allows for increasing both the equalization speed and the overall efficiency of the equalization circuit.

– *Modularized Switched Capacitor*

The modularization approach allows for achieving an easier and more flexible architecture for the equalization circuits. In particular, the modularized system takes into account to control

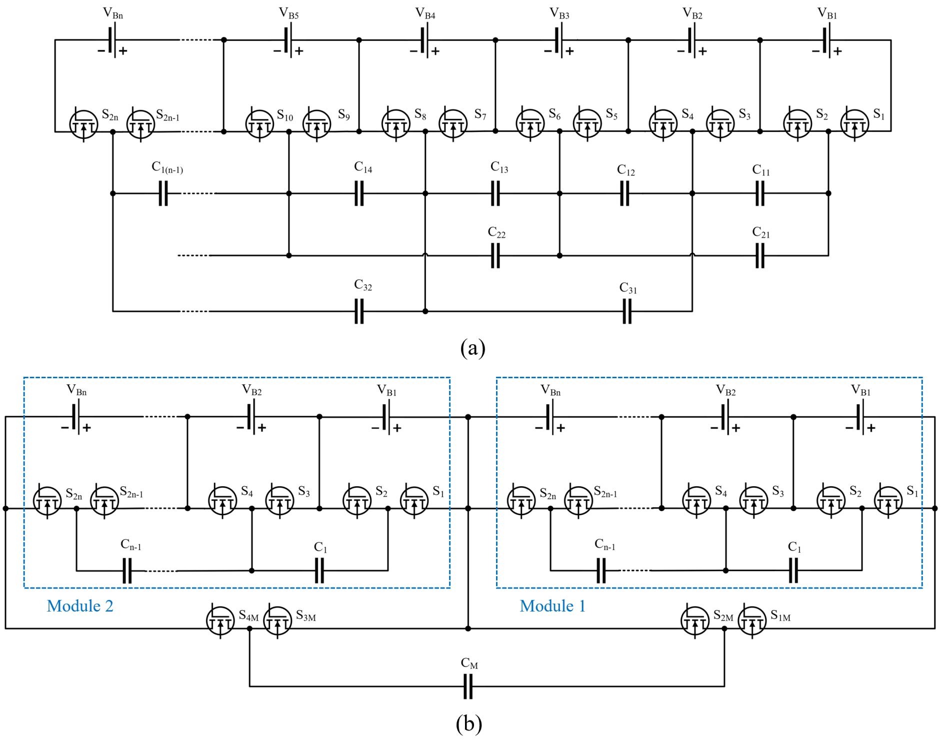

Figure 3.18: (a) Double tiered switched capacitor architecture for a generalized battery pack composed by n series-connected cells; (b) modularized switched capacitor architecture considering two series-connected modules.

the equalization process of the modules in a battery pack.

Figure 3.18(b) shows an example of a modularized SC by considering two series-connected modules. The cells of each module are balanced by means of a SC equalization circuit, whereas a master equalization controller based on a SSC is adopted for balancing the modules. This leads to a faster equalization of the overall battery pack as well as low voltage and current stresses on switches at the expense of complex control algorithms to be developed.

3.3.2.2 Inductor-based

These architectures use inductors as storage components for transferring energy among the series-connected cells in a battery pack. Two

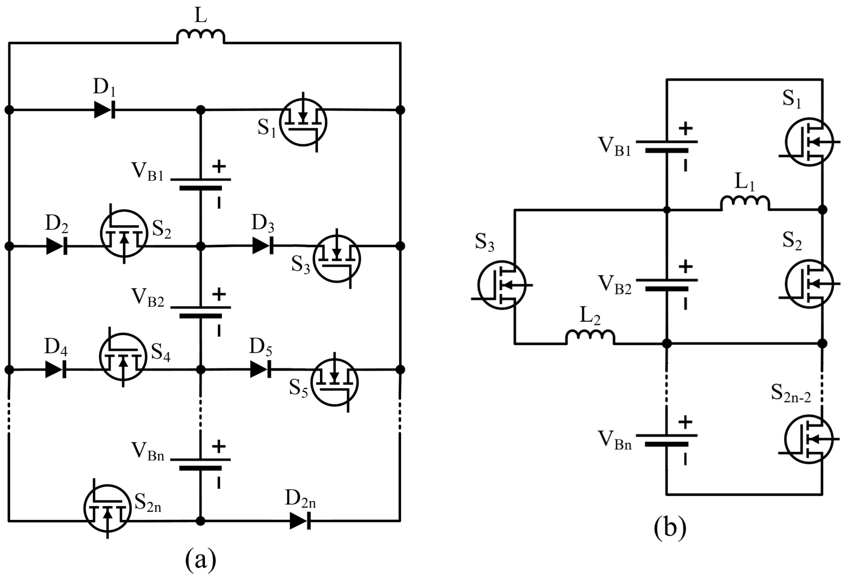

Figure 3.19: (a) Single inductor and (b) coupled inductor architectures for a generalized battery pack composed by n series-connected cells.

main categories can be identified, including single inductor [88] and coupled or multi-inductor [89,90]. Very high balancing current can be achieved with the inductor-based architectures and thus potentially high equalization speed. In this case, diodes are required in order to avoid instantaneous interruptions and undesired paths for the inductive current. Therefore, since these architectures usually operate at high switching frequency, the internal body diodes of MOSFETs can be adopted. The main concern regards the high current stresses on switches due to hard switching operations.

– *Single Inductor*

  Considering a generalized battery pack composed by n series-connected cells, this architecture needs 1 inductor and $2n$ switches for the equalization process, as shown in figure 3.19(a). It allows for achieving different energy transfer paths, such as DC2C, P2C and C2P. Therefore, advanced control strategies are requested for balancing the cells with the lowest equalization time. Despite the similarity to the SSC architecture, $2n$ external freewheeling diodes are needed for single inductor equalization circuits.

- *Coupled Inductor*

  As for the SC architecture, the coupled inductor equalization circuits allow for a AC2C balancing among the cells. It is characterized by a lower number of components with respect to the single inductor architecture, since it needs $2n - 2$ switches and $n - 1$ inductors, as illustrated in figure 3.19(b). In this case, only the internal body diodes of MOSFETs are needed for ensuring the correct and safe functionalities of the coupled inductor architecture. Moreover, unlike the SC architecture, it is not self-limiting, thus a control algorithm is required, which senses the cell voltages and disables the equalization process when the battery pack is balanced. Then, since all the cells participate to the equalization process, the overall efficiency of this active equalization circuit is affected by higher magnetizing losses compared to the single inductor architecture.

3.3.2.3 Transformer-based

These architectures use transformers as storage components for transferring energy among the series-connected cells in a battery pack. Two main categories can be identified, including single winding transformer [91, 92] and multi-windings transformer [93–96]. They allow for performing P2C and C2P energy transfer techniques. In the first one, the energy from the whole battery pack is transferred to the least charged cell. While, the energy from the most charged cell is transferred into the battery pack for a C2P operation. In addition, likewise for the capacitor-based equalization circuits, a modularized approach has been considered for transformer-based architectures as well [87].

- *Single Winding Transformer (SWT)*

  This architecture adopts the switching configuration of the SSC equalizer and replaces the capacitor with a transformer, as illustrated in figure 3.20. For this reason, it is also known as switched transformer. Unlike the SSC architecture, it needs two additional switches, leading to an overall number of switches equal to $n + 7$ for a generalized battery pack composed by n series-connected cells. The main disadvantage is related to the high cost of this solution due to the large number of switches and the needed of a specific design for the transformer.

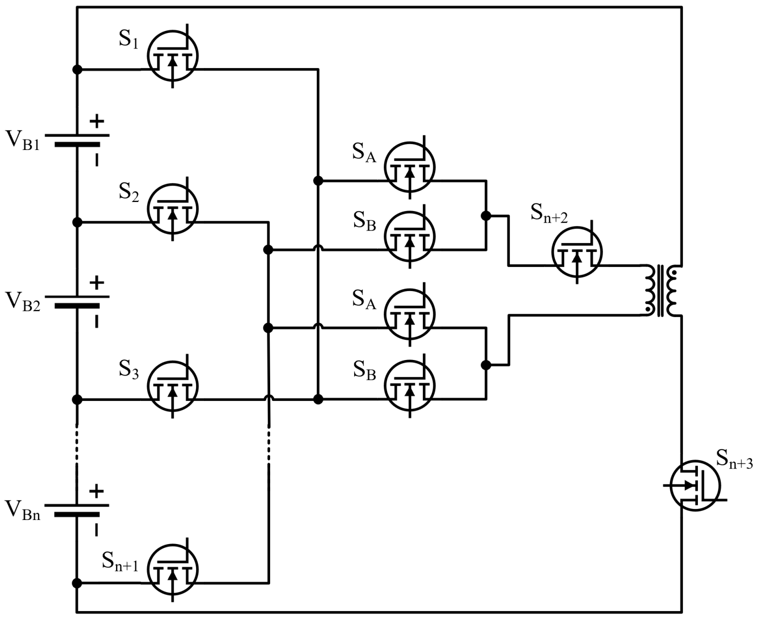

Figure 3.20: Single winding transformer architecture for a generalized battery pack composed by n series-connected cells.

- *Multi-windings Transformer (MWT)*

  The equalization circuits based on MWTs can be further divided in two main categories, which are shown in figure 3.21. In both architectures, $n + 1$ switches are needed. The first one is known as shared transformer, which consists of a single magnetic core with one primary winding connected to the overall battery pack and multi-secondary windings, one for each series-connected cell. While, the second architecture is named as multiple transformer and adopts several multiple core transformers, one core for each cell. The working principles of both MWT equalization circuits are the same. In particular, two operating modes can be performed depending on the desired energy transfer technique. In flyback mode, the switch connected to the primary side is turned on, thus the energy is stored in the transformer. Then, when it is turned off, the energy is transferred to the cells by means of the internal body diodes of the MOSFETs. In forward mode, when a voltage difference among the cells is detected, the switch of the most charged cell is turned on and the energy is transferred to the battery pack

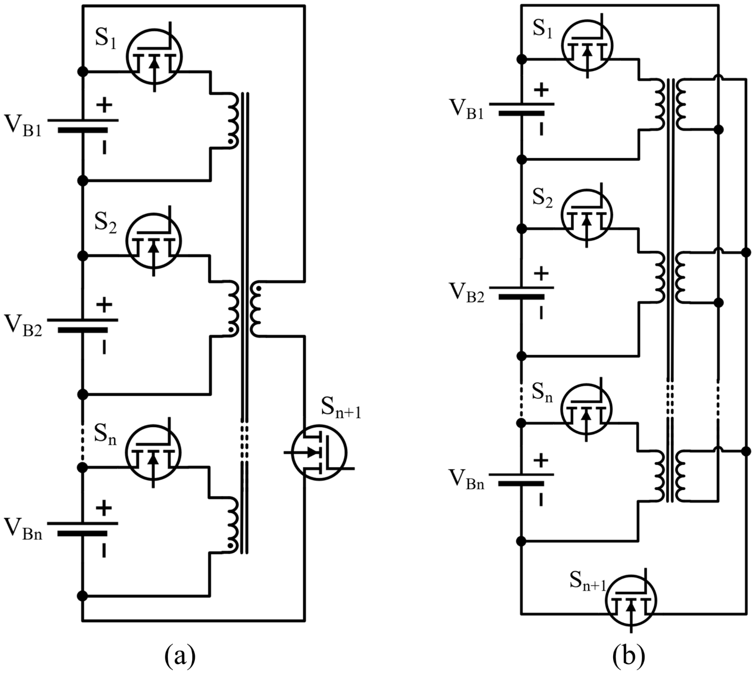

Figure 3.21: (a) Shared transformer and (b) multiple transformer architectures for a generalized battery pack composed by n series-connected cells.

by means of the transformer and the internal body diode of the MOSFET at the primary side. It is important to point out that the reactances of the secondary windings are directly related to the associated cell voltages. In detail, a higher cell voltage will result in a larger reactance and thus a lower balancing current.

The shared transformer architecture suffers from complex magnetic design with increasing number of windings, which limits the flexibility of this equalizer. While, the number of cells is no longer limited and it is simple to connect additional cells for the multiple transformer architecture, resulting a better solution as modular design for equalization circuits. However, size and cost represent the main concerns for both architectures. In addition, a specific design of these transformers is required, especially for large battery packs.

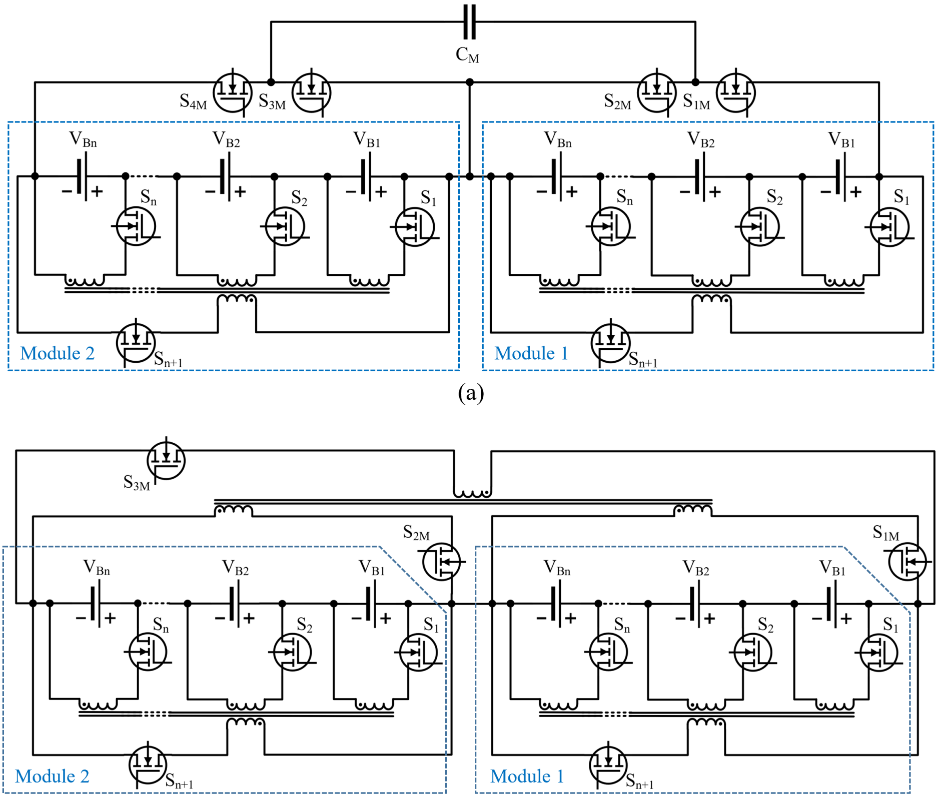

(a)

(b)

Figure 3.22: Example of possible modularized multi-windings transformer architectures considering two series-connected modules. (a) Shared transformer at cell level and SSC at module level; (b) shared transformer at both cell and module levels.

– *Modularized Multi-windings Transformer*

As previously discussed for the capacitor-based, a modularization approach represents an interesting solution for more flexible, efficient and reliable equalization circuits. Two example of possible modularized MWT architectures considering two series-connected modules are reported in figure 3.22. The first one adopts shared transformer solutions for the cells and a SSC architecture for transferring energy among the modules. While, the second one uses shared transformer equalization circuits at either cell or module levels. Both modularized MWT solutions are characterized by higher efficiency than other equalization circuits. Moreover, they result suitable for automotive application thanks to the possibility to achieve high power and high equalization speed. However, they are bulky and costly.

3.3.2.4 Converter-based

These architectures use power converters for transferring energy among the series-connected cells in a battery pack. Five main categories can be identified, including cúk [97, 98], ramp [99], full-bridge [100], resonant [101–103] and flyback converters [104, 105]. The buck-boost is not considered among the converter-based equalization circuits because its architecture is equal to the coupled inductor one. These types of equalization circuits have efficient features with completely control of the balancing. However, the design and implementation are quite costly and complex. In addition, intelligent control algorithms need to be developed for optimally managing each architecture.

– *Cuk Converter*

  This is a bidirectional equalization circuits that allows for achieving AC2C energy transfers. It needs $2n - 2$ switches, $2n - 2$ inductors and $n - 1$ capacitors for a generalized battery pack composed by n series-connected cells, as shown in figure 3.23(a). Major disadvantages include large number of components and low equalization speed due to AC2C balancing.

– *Ramp Converter*

  This converter represents an improved version of the MWT equalization circuit. As illustrated in figure 3.23(b), it only requires one secondary winding for each pair of cells, resulting in a reduced number of secondary windings for the multi-windings transformer. In addition, n switches, n capacitors and n diodes are needed. The ramp converter architecture operates in two phases. During the first half cycle, the odd numbered cells provide energy for charging the capacitors. Then, during the second half cycle, this energy is transferred to the even numbered cells. The opposite operation of the ramp converter can be achieved depending on the direction of the current in primary side of the transformer. Compared to the MTW architecture,

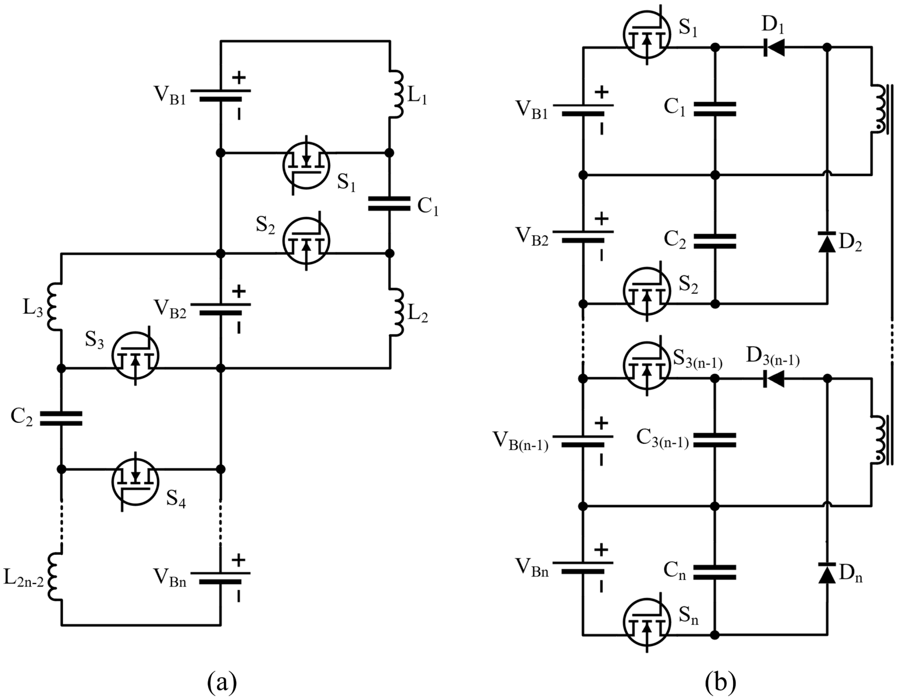

Figure 3.23: (a) Cuk converter and (b) ramp converter architectures for a generalized battery pack composed by n series-connected cells.

this equalization circuit results to be less expensive and bulky due to the winding reduction. However, design and control still remain quite complex.

– *Full-bridge Converter*

This architecture can be considered as a fully controlled energy converter. It consists of a switch bridged network in parallel with each cell or module of the battery pack. In particular, $4n$ switches and n capacitors are needed. The control operations of switches and cell selection are executed by automated intelligent control algorithm. This configuration is more effective in modularized architectures and high-power application, such as PHEVs and EVs. However, major concerns include high costs and large number of components, especially when full-bridges are adopted at a cell level. In addition, high-power applications lead to high voltage and current stresses on switches.

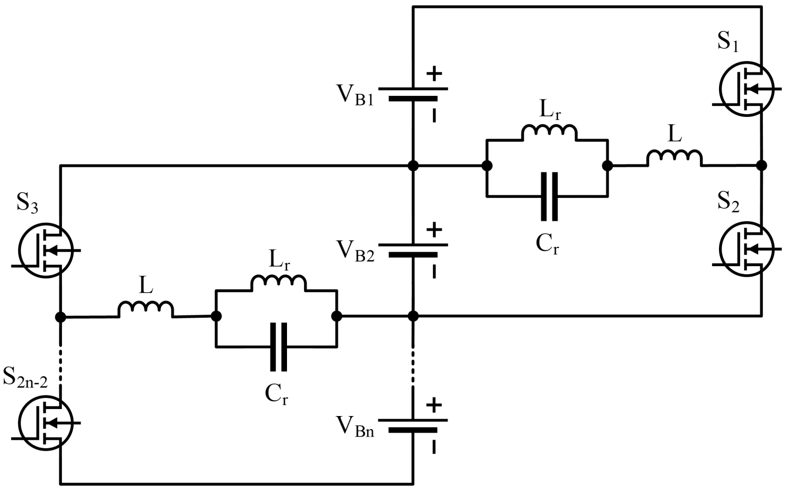

Figure 3.24: Resonant converter architecture for a generalized battery pack composed by n series-connected cells.

- *Resonant Converter*

  This converter uses a resonant circuit for driving the switches and transferring the energy between adjacent cells. It needs $2n - 2$ switches, $4n - 4$ inductors and $n - 1$ capacitors, as shown in figure 3.24. Moreover, two categories can be identified depending on the control strategy, including zero-current quasi-resonant (ZCQR) or zero-voltage quasi-resonant (ZVQR) converters. The resonant tank L_r-C_r is used to achieve zero current switching, while the inductor L is required to store the energy to be transferred between adjacent cells. The resonant converter has a high equalization efficiency due to the negligible switching losses. Nevertheless, the main disadvantages include design cost and implementation complexity.

- *Flyback Converter*

  These converters are adopted in application where isolation is needed. They can be unidirectional or bidirectional for providing P2C and C2P energy transfers. The flyback converter equalization circuits are developed using single winding transformer or multi-windings transformer for centralized, modular, individual or distributed control of the balancing process. The discontinuous conduction mode of switching can be used for efficient balancing with reduced losses and stresses. However, it inherits the disadvantages related to the transformer-based architectures, including complex design of the transformer, cost and size issues.

3.3.2.5 Final Remarks

The equalization circuits plays an important role in maximizing the cell performance as well as improving its efficiency and durability. The development of novel architectures and the improvements of the existing balancing solutions represent the main tasks for high-performance storage systems. The study and research are holding in advanced power electronics areas to produce smart technologies for cell equalization circuits.

Currently, passive equalizers are the most common solution due to low cost and low complexity in design, implementation and control. However, despite high balancing current may be performed, the excessive heat dissipation limits the equalization speed and require a proper thermal management.

Active equalization circuits are characterized by excellent efficiency with negligible power losses. Nevertheless, they suffer in balancing time and control difficulties. Inductor-based architectures are efficient and allows for achieving high balancing current with moderate size at the expense of control complexities. Transformer-based equalization circuits are costly and bulky, thus they are more suitable for high power applications or modularized architectures. Power converters an interesting viable for EVs due to their excellent efficiency and flexibility in different configurations. The resonant converter is very efficient due to the possibility to achieve soft switching operation. The bidirectional flyback converter represents an important solution due to its isolation properties and low magnetizing losses at the expense of high design cost. The full-bridge converter has an excellent efficiency with negligible power losses, very high speed equalization property and medium design difficulty. However, it needs complex control and it has high voltage and current stresses on switches.

Future trends will also include hybrid solutions, which are based on the integration of different equalization circuits. Therefore, optimized balancing architectures will be developed in order to meet the desired performance in terms of size, weight, modularity, efficiency and equalization speed. This integration will take into account for passive-active equalizer as well [106].

3.4 Commercial Available BMS

Nowadays, the distributed BMS architecture is widely adopted in EVs, including Tesla Model S, BMW i3, Roewe eRX5 and BYD Qin. To implement the basic monitoring functionality needed for a safe operation of the cells, several off-the-shelf application-specific integrated circuits (ASICs) are offered by well-known semiconductor manufacturers. An overview of the main BMS ICs currently available on the market is reported in table 3.2, including manufacturers, ICs name, number of voltage and temperature channels, balancing type and current as well as communication interface. The majority of the BMS ICs provide an internal passive balancing (PB) with a maximum balancing current of 300 mA. Higher balancing current can be carried out by adopting external switches. While, Analog Devices and Texas Instruments also introduce commercial solutions for active balancing (AB), mainly based on flyback architectures. Moreover, the ICs by Analog Devices can be combined with the LTC5800 chipset for achieving a wireless BMS, which represents an interesting solution for distributed BMS architectures [107].
In addition, four real-world examples of the application of these ICs in EVs are illustrated as follows.

Mitsubishi i-MiEV

The first example is the battery pack of a Mitsubishi i-MiEV, shown in figure 3.25. It consists of 12 series-connected modules, 10 composed by eight cells and 2 by four cells, which leads to a total amount of 88 prismatic cells. A PCB based on LTC6802G-2 BMS ICs, called as Cell Management Unit (CMU), is mounted on the top of each module. This IC is designed to monitor up to 12 lithium-ion cells. In addition to voltage measurement, each PCB contains three temperature sensors, which are connected to a controller located next to the Linear Technology BMS IC. On the other hand, the battery housing includes contactors needed for either connection to the inverter or to the DC charging, fuses, a service plug, a LEM current transducer and an insulation monitor. Moreover, a thermal management based on air cooling is considered. The service plug splits up the pack into two sections when it is removed. The main fuse also splits the pack in the middle.
The BMS master, called Battery Management Unit (BMU), communicates to the rest of the vehicle. The contactors, the current transducer and the insulation monitor are connected directly to the BMU.

Manufacturer	Name	Voltage Channels	Temperature Channels	Balancing Type	Balancing Current	Comm. Interface
Analog Devices	LTC3300	6	-	Active	10 A (ext.)	SPI
	LT8584	1	-	Active	2.5 A	Serial
	LTC6802	12	2	Passive (int./ext.)	50 mA	SPI
	ADBMS6815	12	7	Passive (int.)	300 mA	Iso-SPI
	LTC6810	6	4	Passive (int.)	300 mA	Iso-SPI
	LTC6811	12	5	Passive (int.)	300 mA	Iso-SPI
	LTC6812	15	9	Passive (int.)	300 mA	Iso-SPI
	LTC6813	18	9	Passive (int.)	300 mA	Iso-SPI
	AD7284	8	4	Passive (ext.)	-	SPI
NXP	MC33772B	6	7	Passive (int.)	300 mA	Iso-SPI
	MC33771B	14	7	Passive (int.)	300 mA	Iso-SPI
Texas Instruments	BQ76PL536A	6	2	Passive (ext.)	-	SPI
	BQ79612	12	8	Passive (int.)	240 mA	UART-SPI
	BQ79616	16	8	Passive (int.)	240 mA	UART-SPI
	BQ79606A	6	6	Passive (int.)	150 mA	UART
	BQ76PL455	16	8	Passive (ext.) or Active	-	UART
	BQ76915	15	1	Passive (ext.)	-	I2C
Maxim	MAX11068	12	2	Passive (int.)	200 mA	I2C
	MAX17853	14	6	Passive (int.)	300 mA	UART-SPI
Renesas	ISL78600	12	4	Passive (ext.)	-	SPI
	BQ78714	14	6	Passive (ext.)	-	SPI

Table 3.2: Overview of the main BMS ICs currently available on the market.

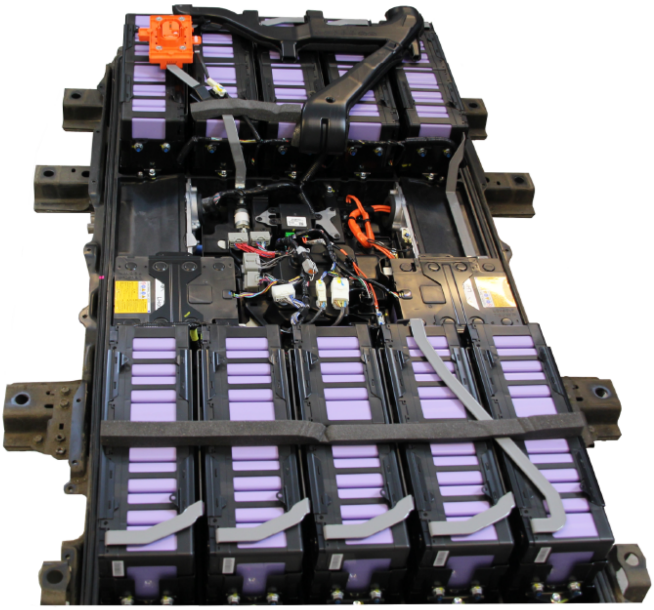

Figure 3.25: Picture of the battery pack of Mitsubishi i-MiEV.

While, the CMUs are connected to each other and to the BMU via an internal CAN bus.

Smart Fortwo Electric Drive

The battery pack of a Smart Fortwo Electric Drive is considered as second example and shown in figure 3.26. It consists of 90 pouch cells connected in series by welded connections. The cells are mounted in plastic frames, organized in three rows and located side by side with cooling plates for providing a liquid cooling system. The basic monitoring tasks are performed by ICs of Texas Instruments with anonymized product code, but very similar to bq76PL536A. Three BMS PCBs have been adopted, each one containing six monitoring ICs and one microcontroller with a galvanically isolated connection to the rest of the system. For what concerns the cell voltage measurement, there are connections of flexible PCB between the cell terminals and the nearest BMS PCB. In addition, several temperature sensors are included. The main contactors and a fuse are placed next to the power connector. The whole BMS is located in the battery housing, it is built very space efficient and uses few cables, resulting in an optimal integrated battery pack design.

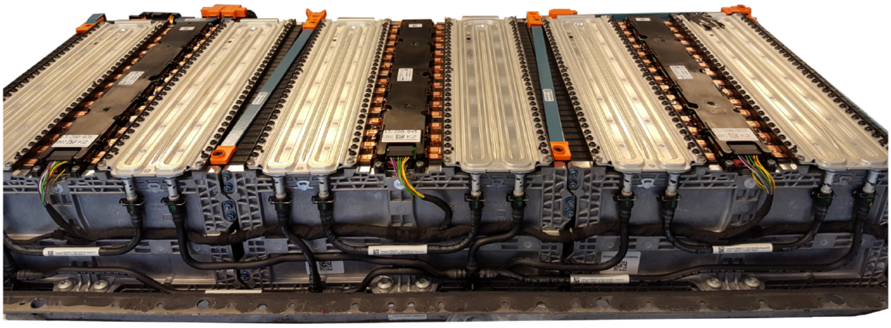

Figure 3.26: Picture of the battery pack of Smart Fortwo Electric Drive.

Volkswagen e-Up

The third example regards the battery pack of a VW e-Up, shown in figure 3.27(a). It is composed by 17 modules, each consisting of six series-connected pairs of two prismatic cells. The e-Up battery pack does not have a cooling system or a service disconnect. The BMS modules are centralized and the white box on the left side of figure 3.27(a) includes the measurement ICs (or BMS slaves) for the whole battery pack. On the right side, contactors, fuse and current measurement can be found as well as an additional white box that contains the BMS master. A large amount of voltage measurement wires connects the individual cells to the slave modules, where MAX11068 IC is used for the measurement and balancing tasks and MAX11081 IC as a secondary protection device. The BMS slave includes nine MAX11068, which are daisy-chained via I2C. This communication protocol is also used for connecting the BMS slaves to the rest of the system. Then, a large amount of balancing resistors takes up most of the space for the BMS slaves.

Tesla Model-S

The last example includes the Tesla Model-S battery pack, shown in figure 3.27(b). It consists of 7104 cylindrical 18650 cells, divided into 16 modules in a 96S74P configuration. This means that each module contains a series connection of 6 x 74 parallel cells. The individual cells are connected via bond-wires, which also act as fuses. The nominal voltage is 355 V and a liquid cooling system is considered. The bq76PL536A-Q1 ICs is used for cell-monitoring functions. The cell voltage measurement is performed using wires welded to the connecting plates of the parallel connections.

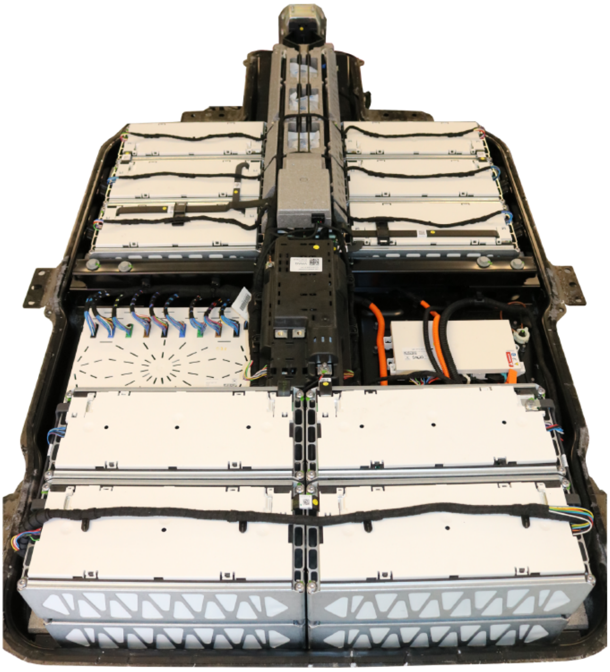

Figure 3.27: Picture of the battery pack of Volkswagen e-Up.

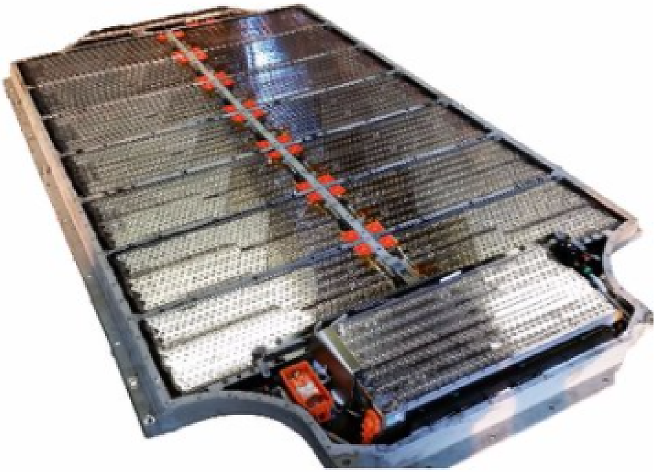

Figure 3.28: Picture of the battery pack of Tesla Model-S.

Chapter 4

Design Methodology for Equalization Circuits

[Original contribute]

The development of design methodologies for the equalization circuits represents a fundamental aspect to be investigated in order to maximize and optimize the performance of lithium-ion battery packs. Moreover, it enables the possibility to correctly select and size the architecture of the equalization circuit depending on the requirements of the specific application.
In this chapter, design strategies for different balancing circuits are illustrated with the aim of achieving the desired performance in terms of equalization time, efficiency and maximum balancing current. In particular, four architectures have been considered, one for each main equalization type, including passive, capacitor-based, inductor-based and transformed-based solutions. A novel architecture for an active equalization circuit has been proposed for the transformer-based equalizer. The impact of parameter variations and the operating conditions of the battery pack on the overall performance of the BMS has been evaluated as well.

4.1 Introduction

As previously discussed in section 3.3, high-performance equalization circuits have to satisfy different requirements, including modularity, scalability, weight and volume, reliability, cost, hardware and software complexity. Currently, the design targets are mainly focused on minimizing the equalization time and the overall size of the circuit. This also implies the definition of a proper thermal management for dissipating the heat generated due to the high balancing currents that may be needed.

However, despite literature and industry standards do not address the problem of the optimal sizing of the equalization circuits, there are relevant aspects that can strongly impact on the design strategies. Firstly, the real operating conditions of both individual cells and the overall battery pack need to be considered in terms of cell technology, temperature, model calibration and voltage imbalances among the cells. Secondly, the real behavior of the components used for the specific equalization circuit and their parameter variations should be taken into account as well.

In the following sections, design methodologies for sizing different equalization circuits are illustrated and the impact of both operating conditions and parameter variations is evaluated.

4.2 Passive Equalizer

The passive balancing (PB) circuits are still the most common solution for the voltage equalization of series-connected cells due to the higher reliability, lower cost and control simplicity compared to the active balancing (AB) ones. However, despite the architecture and the control are very simple, PB circuit hides the need of a proper design to ensure the desired equalization speed and a proper dissipation of the extracted energy [78, 79]. The sizing of the balancing resistor is usually operated with the aim of reducing the equalization time [77, 108] without considering relevant aspects in the design of a PB circuit, such as the cell technology and capacity as well as the cell operating conditions in terms of SoC, SoH and voltage imbalance.

Therefore, a systematic approach for the design of PB circuits for lithium-ion battery packs that takes into account for real cell operating conditions is presented.

4.2.1 Model Equations

As previously illustrated in section 3.3.1, a switched PB circuit is composed by a switch T and a resistor in parallel with each series-connected cell in the battery pack. A schematic representation of the

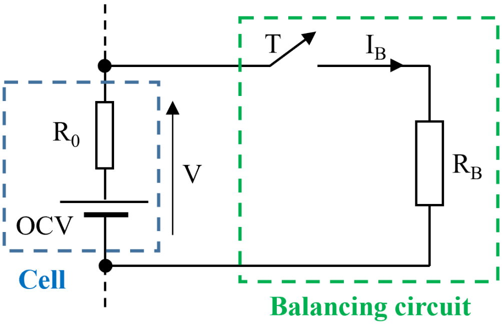

Figure 4.1: Zero order ECM and PB circuit model adopted.

circuit model is reported in fig 4.1. Since the cells do not affect each other during PB, just a single cell can be considered instead of a string of cells. The cell is modeled with a zero-order ECM since a higher order does not add any relevant contribution to the results achieved with the zero-order one due to the slow dynamic of the equalization process [109]. Therefore, the zero-order ECM represents a suitable solution for validating the proposed design methodology with good accuracy. The equations that describe both the cell and the PB circuit models are illustrated as follows:

$$V = OCV - R_0 \cdot I_B \tag{4.1}$$

$$I_B = \begin{cases} 0 & T = 0 \\ \dfrac{V}{R_B} & T = 1 \end{cases} \tag{4.2}$$

$$SoC(t) = SoC(0) - \frac{1}{C_r} \int_0^t I_B d\tau \tag{4.3}$$

where V is the cell terminal voltage, OCV is the open circuit voltage of the cell, R_0 is the internal resistance of the cell, I_B is the balancing current, R_B is the balancing resistor and C_r is the real cell capacity. A positive current is considered in discharging. The SoC of the cell is calculated by using the coulomb counting method.
For what concerns the control algorithm, the PB is usually operated in idle state, when neither charger nor load are connected to the battery pack, but it can be performed during charging as well.

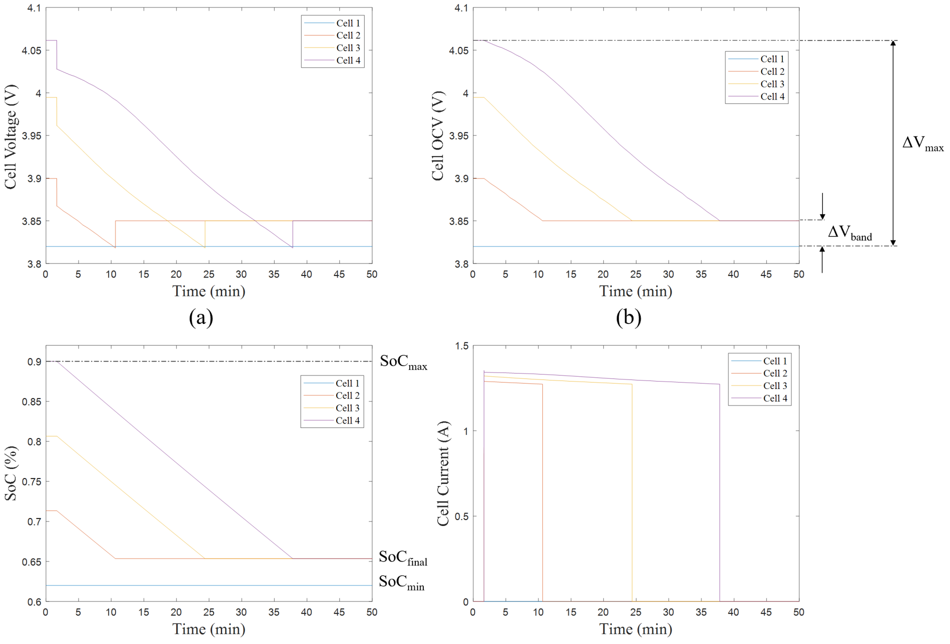

(a) (b)

(c) (d)

Figure 4.2: Control strategy considered for the PB in idle state. (a) Terminal voltage, (b) open circuit voltage, (c) state of charge and (d) current of four series-connected cells.

Figure 4.2 shows the PB in idle state for a battery pack composed by four series-connected cells, highlighting the main parameters of the control strategy considered. Starting from an initial rest period, considering the most charged cell at SoC_{max}, a random distribution of the SoC in the battery pack and a maximum voltage imbalance ΔV_{max}, all the cells with a higher voltage than the minimum one are discharged on their own balancing resistor. The PB is stopped when all the cell voltages are within a desired voltage band ΔV_{band}. It is important to point out that the adoption of ECMs allows for performing the control strategy by evaluating the OCV of the cells and not the terminal voltages, thus more accurate results can be achieved. Indeed, the voltage drop in the terminal voltage measurement due to the internal resistance of the cell strongly impacts on the accuracy of the PB process, especially for equalization circuits designed for high balancing currents. However, it is not always possible to implement an ECM in the BMS, thus the PB is usually operated depending on

the cell terminal voltages in real-world applications.
The performance of the PB in terms of equalization time are mainly defined by the most charged cell, since it takes more time to be balanced. Therefore, according to the parameters reported in figure 4.2, the balancing resistor can be sized depending on the values of SoC_{max} and SoC_{final}. In detail, considering a constant value for R_0, the model equations 4.1, 4.2 and 4.3 can be combined and R_B can be calculated as follows:

$$R_B(T_{cell}) = \frac{\int_0^t OCV(SoC, T_{cell}) d\tau}{C_r(T_{cell}) \cdot [SoC_{max} - SoC_{final}]} - R_0 \tag{4.4}$$

R_B is proportional to the integral of OCV with respect to the time and inversely proportional to the energy to be removed during the equalization process. R_0 has low impact on the R_B, since it is usually an order of magnitude smaller than R_B. All parameters also depend on the cell temperature (T_{cell}), which plays an important role in the R_B selection, especially due to the capacity dependence. Since the OCV is a non-linear function of SoC and temperature, eq. 4.4 cannot be unequivocally solved. Thus, it can be used for the design of a PB circuit if an iterative process or a piecewise approximation is applied.

4.2.2 Design Strategy

According to eq. 4.4, two design strategies have been proposed for sizing the PB circuit. The first one aims to determine the value of R_B for achieving a desired equalization time in specific operating conditions in terms of SoC_{max}, ΔV_{max} and T_{cell}. While, a different approach is considered for the second design strategy. In particular, the target is to evaluate the equalization time achieved in different operating conditions by fixing R_B. The first design strategy is mainly focused on sizing of the equalization circuit, whereas the second one allows for defining optimized control algorithms for maximizing the performance of the balancing process. More details will be provided in the following subsections.

4.2.2.1 Balancing Resistor Sizing

The methodology proposed for sizing the PB circuit is based on an iterative solving process that allows for defining the correct value of R_B for achieving a desired equalization time (t_B^*) in different operating

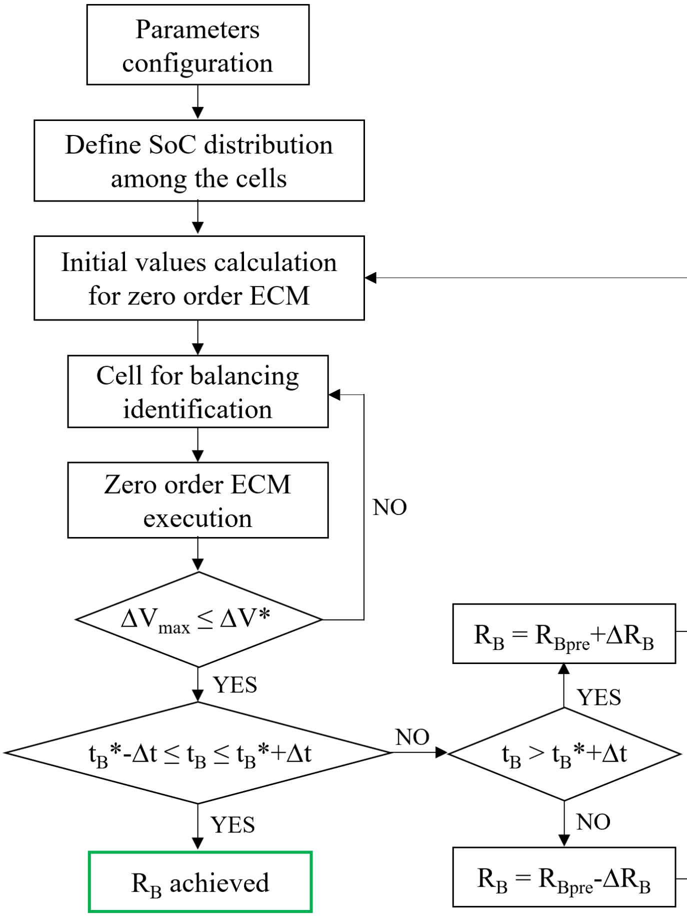

Figure 4.3: Block diagram of the proposed iterative process.

conditions. The block diagram of the proposed iterative process is reported in figure 4.3. Firstly, the parameters of the simulation are set, which include the number of cell in series connection (N_S), SoC_{max}, ΔV_{max} and T_{cell}. Then, the parameters for the iterative algorithm are defined. These parameters include the minimum cell voltage (V^*) in the battery pack, ΔV_{band}, t_B^*, the maximum time error allowable (Δt) with respect to t_B^*, the balancing resistor step (ΔR_B) used for the iteration process and the time step (t_s) with which the PB process is performed.

The value of R_B for the first iteration is considered equal to the ratio of the absolute maximum voltage of the cell technology adopted and the desired maximum balancing current (I_{max}). At the first iteration, the cells to be balanced are identified and discharged until reaching $V^* + \Delta V_{band}$. Hence, the eqs. 4.1, 4.2 and 4.3 are used for calculating the voltages and the SoC of the cells at each t_s during the iteration. At the end of the first iteration, when all cell voltages are within a voltage band equal to ΔV_{band}, the equalization time obtained t_B is evaluated. If the difference between t_B and t_B^* is lower than Δt, the PB process is stopped and R_B is achieved. Otherwise, the value of R_B is increased or decreased of ΔR_B depending on the value of t_B and a new iteration is processed. An adaptive method is implemented for ΔR_B definition. In particular, ΔR_B is adjusted on the basis of the difference between t_B and t_B^* in order to speed up the research of R_B.

The proposed design methodology has been implemented in MATLAB© with the aim of demonstrating the validity of the PB sizing as well as describing the impact of system parameters on the R_B selection. In particular, different aspects and operating conditions have been considered, including the cell technology, the ECM calibration method, SoC_{max}, ΔV_{max} and T_{cell}.

In order to better understand the dependency of R_B with the cell parameters, two different cell technologies have been considered for the analysis, the 3-Ah EFEST IMR18650 and the 3-Ah SONY VTC6. Table 4.1 reports the main features of both cell technologies.

Numerous experimental tests have been performed for characterizing the electro-thermal behaviour of these two cells as well as experimentally calibrating the zero order ECMs, in which all the cell parameters depend on SoC, T_{cell} and charging/discharging C-rate. Since I_{max} has been set equal to 1 A for the sizing iterative process, the ECM parameters have been calibrated at a C-rate equal to C/3. These cell models also include temperature effects on either the ECM parameters or the capacity of the cells, as shown in table 4.1.

Impact of ECM calibration

According to eq. 4.4, the OCV represents an important parameter for the sizing of the PB circuit. However, as illustrated in section 2.4.4.1, there are several experimental tests that can be carried out for identifying the cell OCV when there is not access to the cell electrodes. In this case, two methods for the estimation of the OCV are used to show the impact on the R_B evaluation. In detail, the RCID and the depurated capacity tests at C/3 and 23°C have been carried out for the 3-Ah SONY VTC6 cell. The depurated capacity test can be used to estimate the OCV by depurating the cell terminal voltage of the

	EFEST	**SONY**
Chemistry	LMO	NMC
Nominal Capacity	3 Ah	3 Ah
Max. Charging Current	4 A (1.33C)	6 A (2C)
Max. Discharging Current	35 A (11.67C)	30 A (10C)
Temp. Range Charge	0 - 45°C	0 - 60°C
Temp. Range Discharge	-20 - 75°C	-20 - 60°C
Real Capacity	2.5257 Ah (0°C) 2.8356 Ah (23°C) 2.9016 Ah (45°C)	2.8243 (0°C) 3.0029 (23°C) 3.0114 (45°C)
Internal Resistance	209÷320 mΩ (0°C) 56÷92 mΩ (23°C) 35÷68 mΩ (45°C)	63÷130 mΩ (0°C) 35÷67 mΩ (23°C) 27÷57 mΩ (45°C)

Table 4.1: Main features of EFEST and SONY cells, including capacity and internal resistance variability with respect to T_{cell}.

related voltage drop due to the internal resistance. Compared to the OCV acquired after long rest time, as for the RCID calibration, the capacity test is less accurate, but it provides a continuous OCV curve, as shown in figure 4.4(a).

The results of the iterative process are shown in figure 4.4(b), where $\Delta V_{max} = 100$ mV, $T_{cell} = 23$°C, $\Delta V_{band} = 10$ mV, $t_s = 1$s and $t^*_B = 1$h are adopted. Since R_B strongly varies depending on the SoC, the iterative process is performed considering different SoC_{max} conditions, ranging from 20% to 100% with a fixed SoC step. In detail, SoC steps equal to 10% and 1% are used when the OCV curves achieved with the RCID test and the depurated capacity one are considered, respectively. The possibility to adopt different SoC steps is related to the shape of OCV curves. Indeed, as previously discussed, the RCID test provides a very accurate estimation of the OCV, but the resolution of the OCV curve is usually limited by the number of points, while the depurated capacity test allows providing a continuous OCV curve. This also results in achieving additional details about the shape of the R_B size, as shown in figure 4.4(b).

The error in estimating R_B ranges from ±5% to ±20%. While, a larger error equal to ±60% is observed for $SoC_{max} = 100\%$ due to the

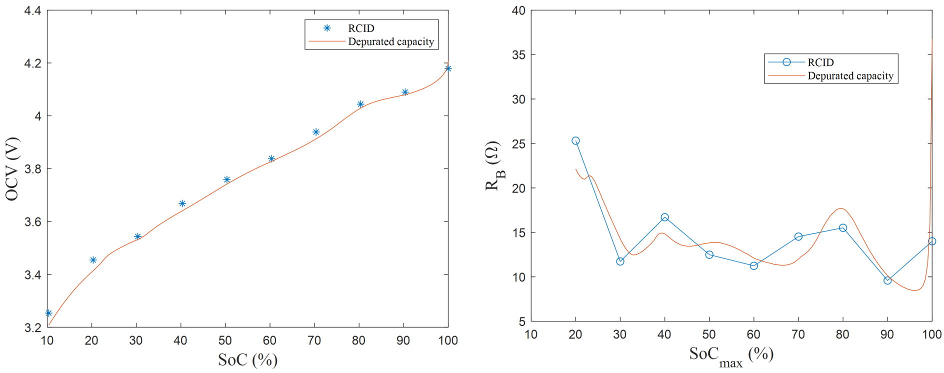

(a)

(b)

Figure 4.4: (a) Comparison between the OCV curves of the SONY cell achieved with RCID and depurated capacity tests (T_{cell} = 23°C); (b) numerical results from the iterative process by considering the cell parameters calibrated with RCID and depurated capacity tests (ΔV_{max} = 100mV, T_{cell} = 23°C and t_B^* = 1h)

different resolution of the OCV curves from the RCID and the depurated capacity tests. Nevertheless, since the proposed design strategy is mainly focused on evaluating the impact of different parameters on the sizing of a PB circuit rather than the investigation of the optimal method for calibrating the OCV curve, the ECM parameters from the RCID test will be adopted in the following design analyses.

Impact of ΔV_{max} and T_{cell}

The variability of R_B with respect to SoC_{max}, ΔV_{max} and T_{cell} has been evaluated for the 3-Ah SONY VTC6. The iterative process has been performed for ΔV_{max} ranging from 50 mV to 200 mV as well as for three different T_{cell} (0°C, 23°C, 45°C). SoC_{max} starting from 20% to 100% with SoC steps of 10% has been considered and t_B^* = 1h has been set for all operating conditions.

Moreover, it is important to point out that V^* is calculated on the basis of SoC_{max} and ΔV_{max}, thus there may be operating conditions for which V^* becomes lower than the minimum OCV point available. This issue mainly includes the operating conditions in which low SoC_{max} and high ΔV_{max} are set. In these cases, the iterative process cannot be operated and no results are reported.

Figure 4.5(a) shows the variability of R_B with respect to SoC_{max} and ΔV_{max} at 23°C, whereas figure 4.5(b) reports the R_B dependency from

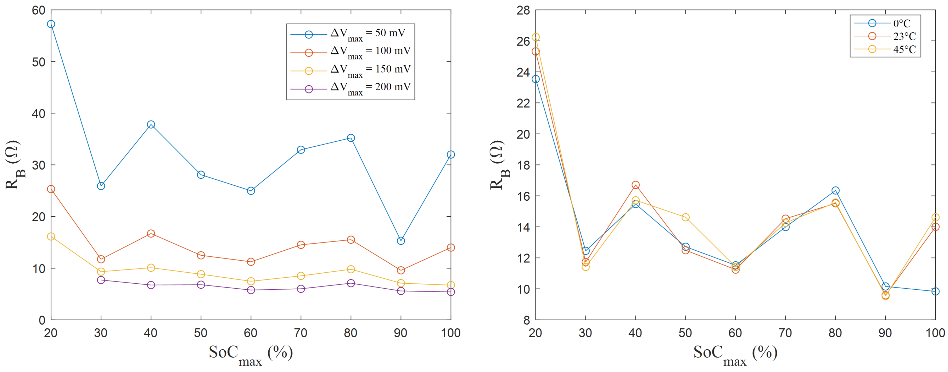

(a)

(b)

Figure 4.5: (a) Variability of R_B with respect to SoC_{max} and ΔV_{max} considering the SONY cell (T_{cell} = 23°C and $t_B^* = 1$h); (b) variability of R_B with respect to SoC_{max} and T_{cell} considering the SONY cell ($\Delta V_{max} = 100$ mV and $t_B^* = 1$h).

SoC_{max} and T_{cell} when $\Delta V_{max} = 100$ mV. These results highlight a strong dependency of the R_B from ΔV_{max}. Indeed, considering a fixed desired t_B^*, a higher value of R_B (thus a lower balancing current) is needed for lower ΔV_{max} due to the reduced amount of energy to be dissipated during PB process. On the other hand, a low impact of the T_{cell} for the SONY cell technology is observed in figure 4.5(b). Therefore, since both the OCV curve and the cell capacity depend on the T_{cell}, this result demonstrates that their contributions to the sizing of the PB circuit are equivalent.

Impact of cell technology

The impact of the cell technology on the sizing of the PB circuit has been taken into account as well. Figure 4.6 reports the comparison results considering the EFEST and SONY cells. As previously illustrated, T_{cell} has low impact on the R_B variability, thus just one temperature condition (23°C) has been evaluated and compared for both cell technologies. While, different ΔV_{max} conditions have been performed, starting from 50 mV to 200 mV. A strong impact of the battery cell technology on the R_B variability is observed. This highlights the needed of a specific design of the PB circuit depending on the technology adopted for maximizing the performance of the equalization process.

In addition, considering all the results achieved, different design strate-

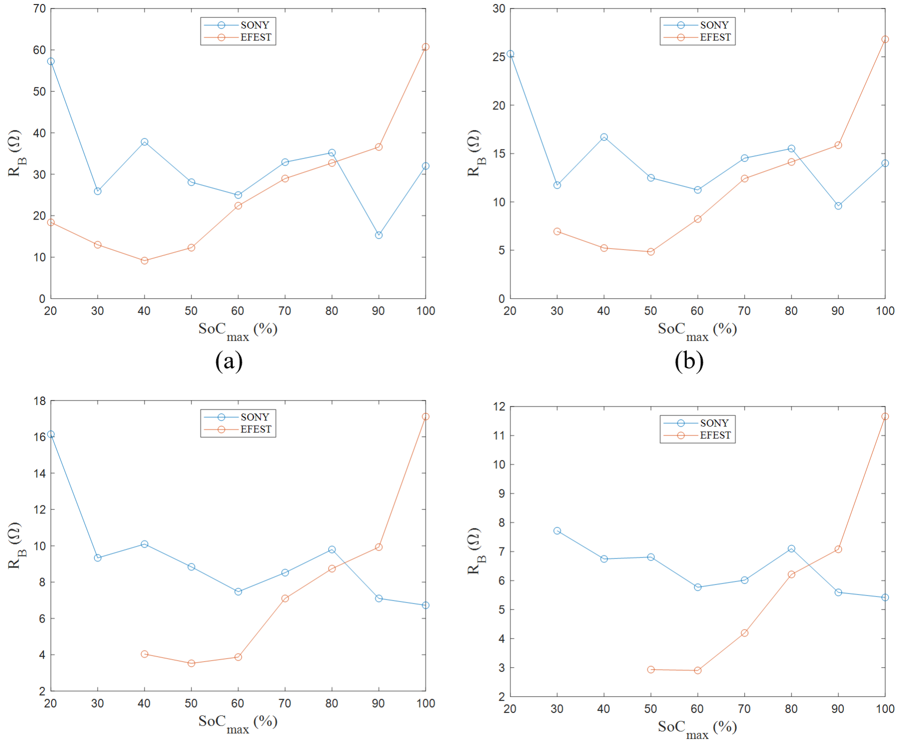

(a) (b) (c) (d)

Figure 4.6: (a) Variability of R_B with respect to the cell technology (SONY and EFEST) and SoC_{max} considering ΔV_{max} equal to (a) 50 mV, (b) 100 mV, (c) 150 mV and (d) 200 mV (T_{cell} = 23°C and t_B^* = 1h).

gies can be adopted for sizing the PB circuit. The first one aims to select the lower value of R_B at the maximum ΔV_{max} allowable, leading to higher balancing currents. In this way, a lower equalization time than t_B^* can be achieved in all the operating conditions. However, this design solution involves severe heat dissipation on the balancing resistors, thus a proper thermal management needs to be considered with cost and size concerns. On the other hand, a more conservative approach consists in selecting the higher value of R_B, which corresponds to the lowest ΔV_{max} condition considered for the sizing process. In this case, a higher equalization time than t_B^* is achieved in all the operating conditions, but the thermal issues result limited. These two design methodologies represent the limit cases for sizing the PB circuit. However, as an alternative solution, a suitable trade-off between the maximum and the minimum values of R_B can be considered depending on the requirements of the specific application.

4.2.2.2 Equalization Time Evaluation

This design strategy aims to evaluate the equalization times achieved considering a fixed R_B and different operating conditions. Therefore, it can be adopted as an evaluation tool for the design methodology previously described. Indeed, starting from the R_B selection, quantitative results of the equalization times in each operating condition can be obtained *a priori*. Alternatively, this design strategy can be used for maximizing the performance of the balancing process by evaluating the operating conditions in which lower equalization times can be performed.

In this case, unlike the iterative solution used for sizing R_B, an analytical approach has been adopted. This increases the computational cost, but it allows for directly solving the eq. 4.4 and extracting the equalization time. In detail, considering the mean value theorem for integrals, it can be yield:

$$t_{eq} = \frac{C_r \cdot [SoC_{max} - SoC_{final}]}{\overline{OCV}}(R_B + R_0) \tag{4.5}$$

where t_{eq} is the equalization time and $\overline{OCV}$ is the mean value of the OCV calculated at SoC_{max} and SoC_{final}. It is important to highlight that the accuracy of the t_{eq} results strongly depends on the definition of $\overline{OCV}$. Indeed, considering the nonlinear SoC-OCV curve of lithium-ion cells, high accuracy errors may occur, especially when large ΔV_{max} are adopted. As shown in the example in figure 4.7, the best solution is to consider a piecewise approximation and calculate the overall t_{eq} as the sum of the equalization times achieved for smaller SoC intervals between the SoC_{max}-SoC_{final} range. Analytically, dividing the ΔV_{max} interval in m sub-ranges, it results as follows:

$$\begin{aligned} t_{eq}(\Delta V_{max}, SoC_{max}) &= \sum_{j=1}^{m-1} t_{eq}\left(\frac{\Delta V_{max}}{m}, SoC_j\right) = \\ &= \sum_{j=1}^{m-1} \frac{C_r \cdot [SoC_j - SoC_{j+1}]}{\frac{OCV_j + OCV_{j+1}}{2}}(R_B + R_0) \end{aligned} \tag{4.6}$$

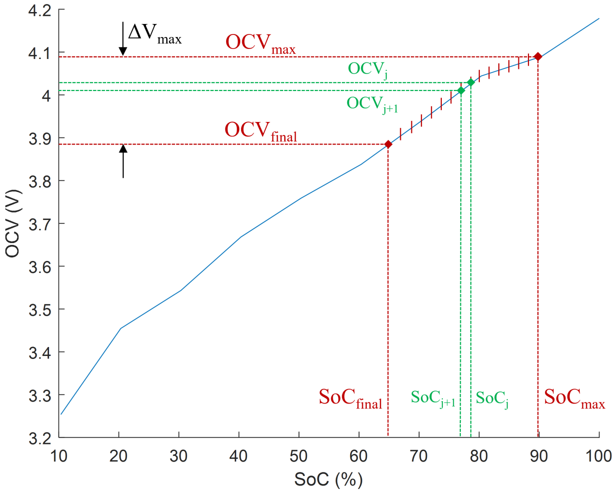

Figure 4.7: Example of the piecewise approximation considered for calculating the overall t_{eq} while minimizing the accuracy errors.

Therefore, the overall t_{eq} for a specific ΔV_{max} and SoC_{max} is calculated by the sum of the equalization times achieved at voltage imbalance steps equal to $\Delta V_{max}/m$ and for a decreasing SoC_{max} equal to SoC_j. The number of sub-ranges m needs to be properly set depending on the accuracy desired for the results and the shape of the SoC-OCV curve of the cell technology considered.

Cell Type	**Chemistry**	**Capacity**	**Power Density**	**Energy Density**
A123 26650	LFP	2.5 Ah	2600 W/kg	108 Wh/kg
SONY VTC6	NMC	3 Ah	1582 W/kg	237 Wh/kg
SAMSUNG 30T	NMC	3 Ah	1826 W/kg	157 Wh/kg
EFEST18650	LMO	3 Ah	1574 W/kg	257 Wh/kg
EFEST26650	LMO	4.2 Ah	1439 W/kg	200 Wh/kg
KOKAM	NMC	12 Ah	522 W/kg	260 Wh/kg

Table 4.2: Main features of the cell technologies considered for testing the design methodology based on the evaluation of t_{eq}.

Unlike the iterative process for sizing the PB circuit, an extended number of cell technologies has been considered for testing this design methodology based on the evaluation of t_{eq}. Table 4.2 reports

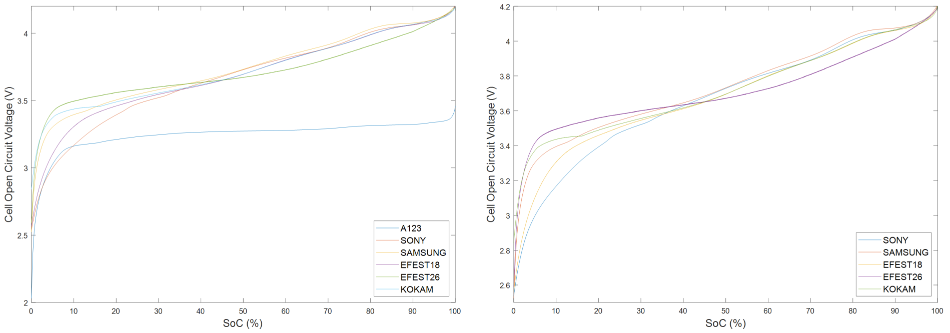

(a) (b)

Figure 4.8: The SoC-OCV characteristics of the cells considered (a) with and (b) without A123.

their main features, including type, chemistry, nominal capacity and energy/power characteristics. Likewise for the analyses previously illustrated in section 4.2.2.1, numerous experimental tests have been performed for characterizing the electro-thermal behavior of these cells as well as experimentally calibrating the zero-order ECMs, in which all the cell parameters depend on SoC, T_{cell} and charging/discharging C-rate. This calibration also includes the temperature dependency of the capacity of the cells. Moreover, it is important to point out that the ECM parameters of each cell technology, such as capacity and internal resistance, have been calculated with the aim of achieving an equivalent 3-Ah cell. In this way, a proper comparison of the t_{eq} results can be operated. The SoC-OCV curves of the cells, shown in figure 4.8, have been carried out by means of depurated capacity tests in order to capture additional details on the variability of t_{eq}.

Figure 4.9 shows the t_{eq} achieved for all the cell technologies adopted. Different operating conditions have been considered in terms of ΔV_{max} and SoC_{max} steps, whereas fixed values for T_{cell} and R_B have been set equal to 23°C and 10 Ω, respectively. In particular, ΔV_{max} ranges from 50 mV to 200 mV and steps of 1% for SoC_{max} are used.

The results allow for highlighting two main aspects. The first one is that the same PB circuit performs differently depending on the cell technology. Indeed, considering the same operating conditions for all the cells, the balancing process requires different t_{eq}. In addition, while the range of variability for KOKAM, SAMSUNG, EFEST18650 and SONY is similar, A123 and EFEST26650 are characterized by higher t_{eq}, mainly due to the flat SoC-OCV curves of these two cell technologies.

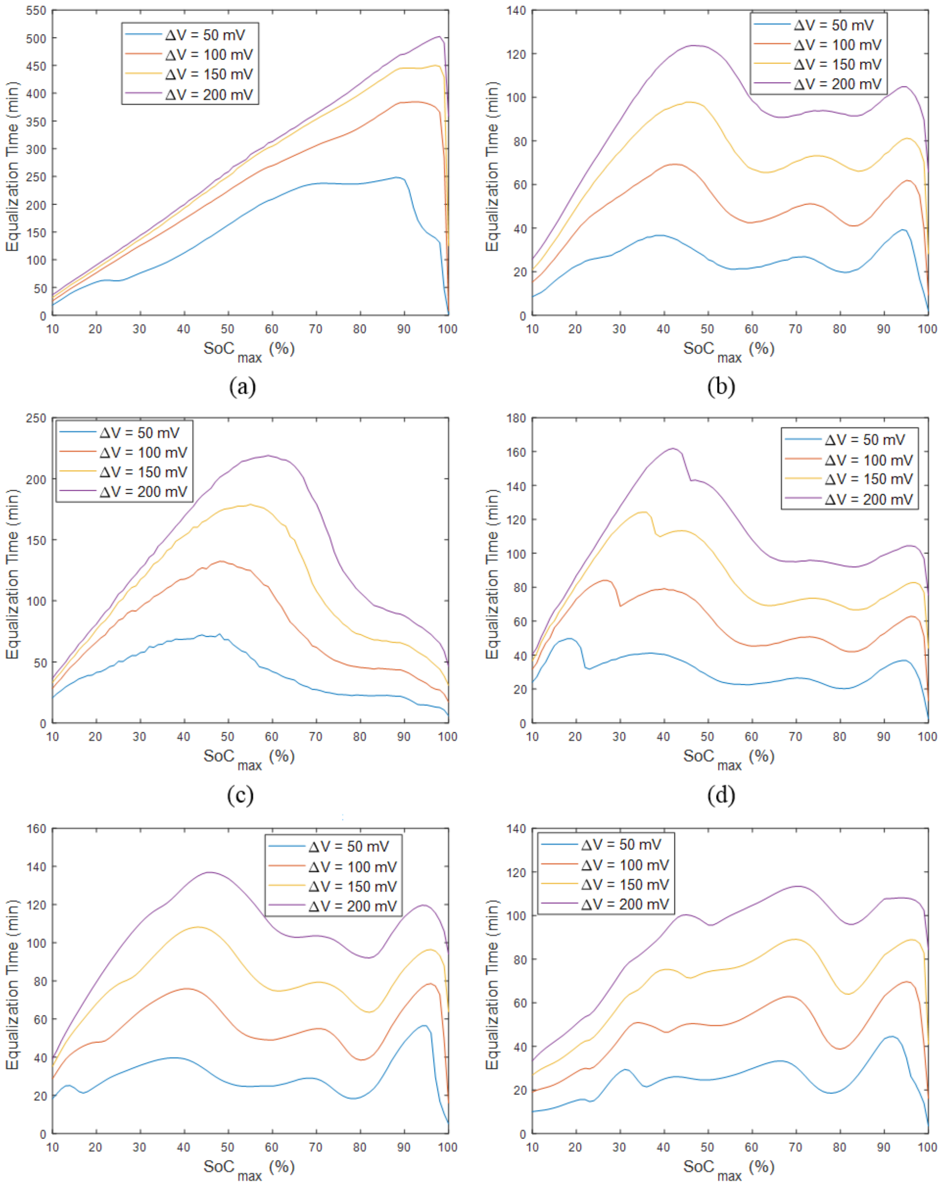

(a) (b) (c) (d) (e) (f)

Figure 4.9: Variability of t_{eq} with respect to cell technology considering different operating conditions in terms of ΔV_{max} and SoC_{max} ($T_{cell} = 23°\text{C}$ and $R_B = 10\ \Omega$).

The second aspect to be highlighted is that an optimal SoC range can be identified to minimize t_{eq} depending on the cell technology.
Indeed, as possible to notice in figure 4.9, there are several local minimum points in the SoC_{max}-t_{eq} curves in which performing the PB process results more convenient. This enables the possibility to design the PB circuit for high balancing current and to perform the equalization process only in specific operating conditions, leading to a good trade-off between the equalization speed and the thermal management issues. Furthermore, these results represent a relevant aspect to be taken into account for the development of optimized charging strategies.
The variability of the energy dissipated (E_{diss}) on R_B in different operating conditions has been evaluated as well. Considering the model equations 4.1, 4.2 and 4.3 of the PB circuit, it can be calculated as follows:

$$\begin{aligned} E_{diss} &= P_{diss} \cdot t_{eq} = \\ &= \overline{OCV} \cdot \frac{R_B}{R_B + R_0} \cdot C_r \cdot [SoC_{max} - SoC_{final}] \end{aligned} \tag{4.7}$$

where the power dissipated (P_{diss}) on R_B is expressed as:

$$P_{diss} = \overline{OCV}^2 \cdot \frac{R_B}{(R_B + R_0)^2} \tag{4.8}$$

It is important to point out that P_{diss} does not take into account for the power dissipated on the internal resistance of the cells for the proposed analysis. Indeed, from the perspective of the design of a PB circuit, only the variability of the power dissipated on R_B is relevant. Moreover, the contribution of R_0 to the power dissipation is very low compared to that of R_B due to the different order of magnitude. Hence, considering also that the balancing current has to be limited due to thermal management issues, it can be neglected.
Figure 4.10 shows the energy dissipated on the R_B for all the cell technologies adopted. As for the t_{eq} results, different operating conditions have been considered in terms of ΔV_{max} and SoC_{max} steps, whereas fixed values for T_{cell} and R_B have been set equal to 23°C and 10 Ω, respectively.
As result, the shape of the SoC_{max}-E_{diss} curves are similar to that related to the SoC_{max}-t_{eq} ones. Therefore, most of cases, a lower E_{diss} corresponds to a lower t_{eq}. However, according to figures 4.9 and 4.10, it is also possible to identify operating points in which low t_{eq} requires large amount of E_{diss} or vice versa.

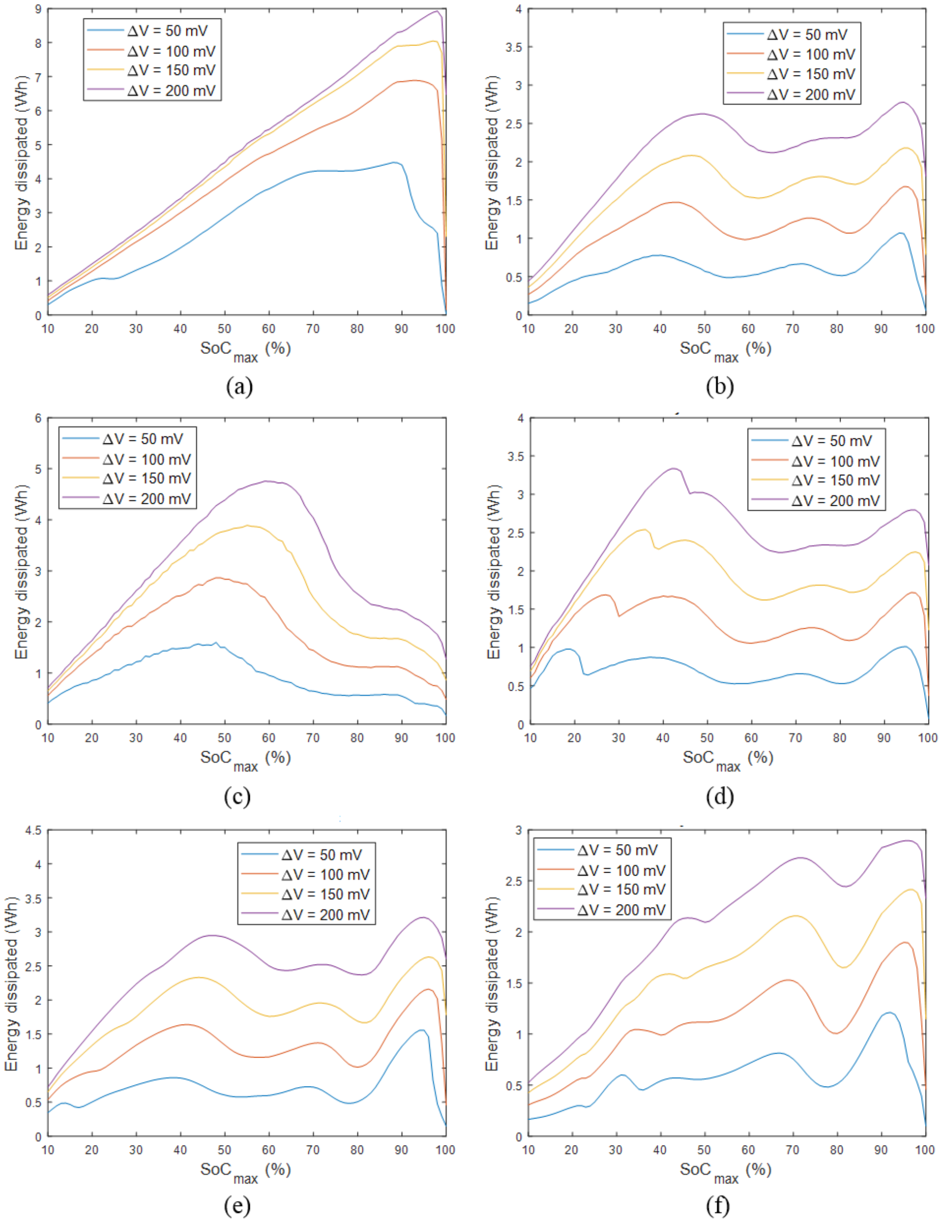

Figure 4.10: Variability of E_{diss} with respect to cell technology considering different operating conditions in terms of ΔV_{max} and SoC_{max} ($T_{cell} = 23$°C and $R_B = 10\ \Omega$).

As example, considering the EFEST18650 cell, a large t_{eq} and a low E_{diss} occur for SoC_{max} ranging from 40% to 50%.
Hence, on the basis of these results, the control strategy for the PB circuit can be optimized by performing the balancing process in operating conditions that allow for minimizing either t_{eq} or E_{diss}. Nevertheless, since there are several operating points characterized by low t_{eq} and large E_{diss} for each cell technology, this can lead to a reduction of the possible SoC_{max} ranges in which the equalization process can be operated. Therefore, depending on the application requirements, an alternative solution consists in performing the balancing process with the aim of minimizing only one parameter between t_{eq} and E_{diss}. As example, it may be more convenient to minimize E_{diss} in applications that require low cost and size for the thermal management system.
Regarding the variability of t_{eq} with respect to T_{cell}, figure 4.11 shows the results achieved with the SONY cell in different operating conditions in terms of ΔV_{max} and SoC_{max}. It is possible to notice that different local maximum and minimum points can be achieved depending on T_{cell}. Therefore, T_{cell} also needs to be taken into account for optimizing the control strategy of the PB circuit.

4.3 Capacitor-based Equalizer

Among the capacitor-based equalization circuits, a design methodology has been proposed for the switched capacitor architecture. This active solution has been previously illustrated in 3.3.2.1 for a generalized battery pack composed by n series-connected cells. However, all the operating conditions involve just two cells and one capacitor, thus a simplified architecture can be adopted for defining design strategies as well as evaluating the performance of the SC equalization circuit. This also allows for extending the proposed design methodology to the other capacitor-based architectures since the energy transfers occur between two cells and one capacitor for both AC2C and DC2C techniques.
Analytical models have been developed for the SC architecture considering either ideal or real conditions. These also include an efficiency model that takes into account for conduction and switching losses of the switches. Then, a proposed design methodology has been presented, which allows for sizing the capacitor in order to achieve the desired performance. On the basis of this design strategy, the impact of both parameter variations of the circuit components and the operating conditions of the cells has been evaluated as well.

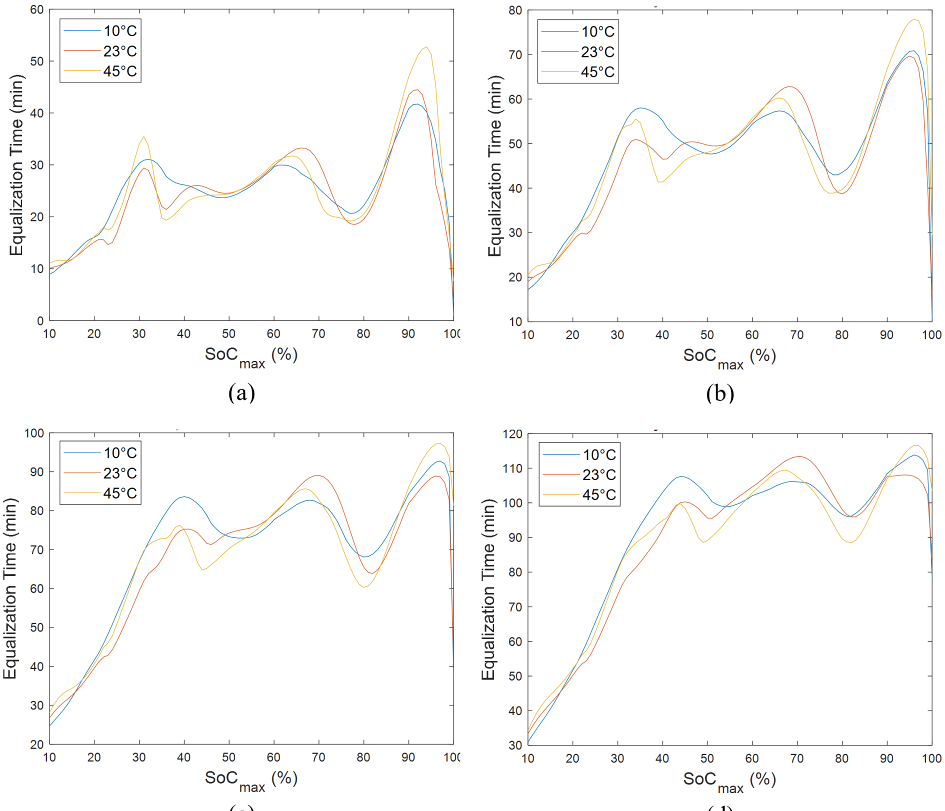

(a) (b) (c) (d)

Figure 4.11: Variability of t_{eq} with respect to SoC_{max} and T_{cell} considering the SONY cell and a fixed R_B equal to 10 Ω. (a) ΔV_{max} = 50 mV, (b) ΔV_{max} = 100 mV, (c) ΔV_{max} = 150 mV and (d) ΔV_{max} = 200 mV.

The models developed have been implemented in MATLAB© in order to validate the correct functionality of the proposed design strategy.

4.3.1 Model Equations

Figure 4.12 shows the simplified architecture of the SC equalization circuit for two cells and the related control algorithm in both ideal and real conditions. Only the series resistance of the capacitor (R_C) has been considered in ideal condition, whereas the real condition also includes the internal resistance (R_0) of the zero-order ECM adopted for the cells as well as the static and dynamic parameters of the switches. It is important to point out that a fully ideal condition should not

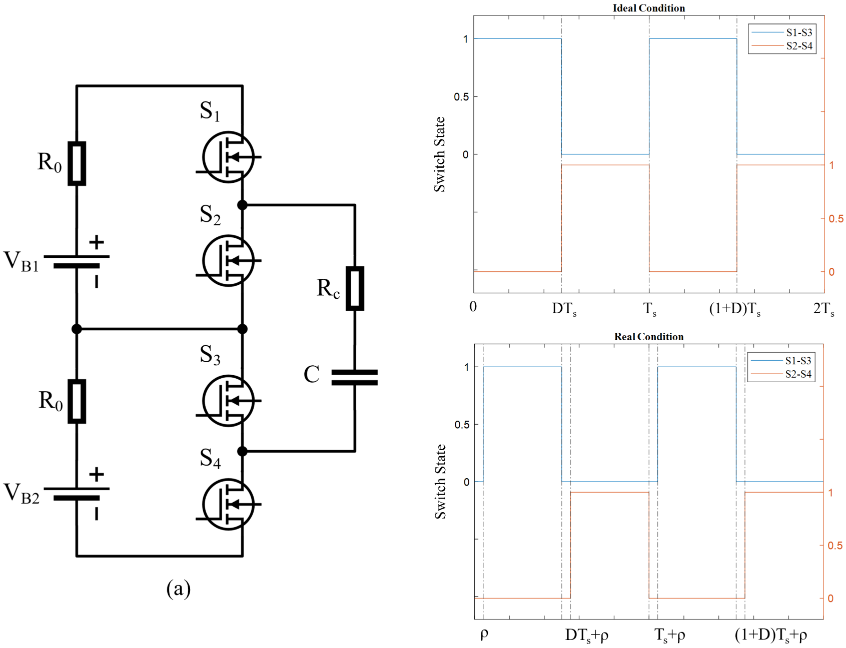

(a)

(b)

Figure 4.12: (a) Simplified architecture of the SC equalization circuit for two cells and (b) the control algorithm in both ideal and real conditions.

include R_C either. However, this would lead to a pulse charging and discharging of the capacitor, making the SC architecture infeasible.

For what concern the static parameters, considering MOSFETs as switches, they are represented by the drain-source on-state resistance (R_{ds}) and the forward voltage of the internal body diode (V_d). On the other hand, the dynamic parameters are mainly related to the switching characteristics, such as rise and fall times. In order to take into account for these dynamic parameters, a dead time (ρ) has been considered for the control strategy of the SC equalization circuit.

According to the SC architecture and the control algorithm illustrated in figure 4.12, the same pulse-width modulation (PWM) signal is adopted for the switches, considering a specific switching period (T_s) and duty cycle (D). In detail, assuming the voltage of the top cell (V_{B1}) greater than that of the bottom one (V_{B2}), the switches S_1-S_3 are turned on and S_2-S_4 are turned off during the t_{on} period. Therefore, the energy is transferred from the most charged cell to the capacitor. Then, during the t_{off} period, the opposite configuration of

the switches is operated, leading to the charging of the least charged cell by means of the energy previously stored in the capacitor.
The model equations that describe the voltage across the capacitor v_c in ideal conditions can be yield as follows:

$$v_c(t) = \begin{cases} V_{B1} + (V_1 - V_{B1})e^{-\frac{t}{\tau_c}} & 0 \leq t \leq DT_s \\ V_{B2} - (V_{B2} - V_2)e^{-\frac{t-DT_s}{\tau_c}} & DT_s \leq t \leq T_s \end{cases} \tag{4.9}$$

where τ_c is the time constant of the voltage transient due to R_c, V_1 and V_2 represent the initial values of the capacitor voltage at the beginning of the t_{on} and t_{off} periods, respectively.
However, considering the real conditions for the SC architecture and the related control algorithm, the model equations that describe V_c become:

$$V_c(t) = \begin{cases} V_1 & 0 \leq t \leq \rho \\ V_{B1} + (V_1 - V_{B1})e^{-\frac{t-\rho}{\tau_{tot}}} & \rho \leq t \leq DT_s \\ V_2 & DT_s \leq t \leq DT_s + \rho \\ V_{B2} - (V_{B2} - V_2)e^{-\frac{t-DT_s-\rho}{\tau_{tot}}} & DT_s + \rho \leq t \leq T_s \end{cases} \tag{4.10}$$

where $\tau_{tot} \neq \tau_c$ is the time constant of the voltage transient due to the overall circuit resistance R_{tot}, which includes R_0, R_{ds} and R_c. In particular, since two switches are involved in the balancing current path during both t_{on} and t_{off} periods, it results:

$$R_{tot} = R_0 + 2R_{ds} + R_c \tag{4.11}$$

As shown in figure 4.12(b), a dead time is included in real conditions for taking into account for the dynamic characteristics of the switches. It mainly consists in introducing a delay time between the opening of S_1-S_3 and the closing S_2-S_4 or vice versa. The dead time is always adopted in real-world applications since it allows for avoiding undesired short circuit conditions for the cells. However, this leads to additional time intervals with respect to the ideal condition in which the balancing current stops to flow and the V_c remains constant, resulting in a reduction of the effective duty cycle.
Figure 4.13 shows the capacitor voltage and current waveforms during steady-state in both ideal and real conditions. Fixing the size of the

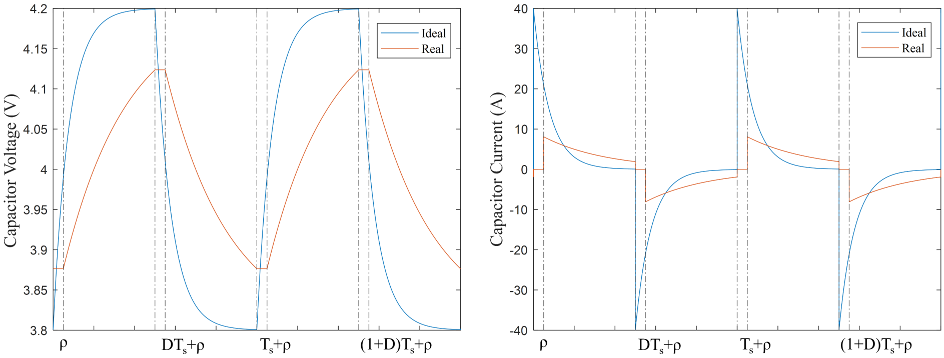

(a) (b)

Figure 4.13: (a) Voltage and (b) current waveforms for the capacitor during steady-state in both ideal and real conditions ($V_{B1} = 4.2$V and $V_{B2} = 3.8$V).

capacitor, it results $\tau_c < \tau_{tot}$, thus faster voltage and current transients occur for the ideal condition with respect to the real one.
In addition, a lower voltage ripple is achieved in real conditions due to the higher time constant and the larger overall circuit resistance. On the other hand, a higher in-rush current is observed in ideal conditions, which allows for achieving a higher charge/discharge current for the capacitor at the expense of oversizing the switches. In real conditions, the reduction of this charge/discharge current depends on either the dead time or the R_{tot}. Indeed, the first one limits the time interval for which the balancing current can flow, whereas the amplitude of R_{tot} affects the in-rush current as well as the voltage and current transients.

4.3.1.1 Mean Balancing Current

In both ideal and real conditions, it results that the mean value of the charge current during the t_{on} is equal to the mean value of the discharge current during the t_{off}. In particular, the mean current of the capacitor ($\bar{I}_c$) can be expressed as the amount of charge transferred (ΔQ) in a specific time interval (Δt):

$$\bar{I}_c = \frac{\Delta Q}{\Delta t} = \frac{C \cdot \Delta V_c}{\Delta t} \tag{4.12}$$

where C is the capacitor size and ΔV_c is the voltage ripple. Hence, the maximum value of $\bar{I}_c$ can be achieved by identifying the maximum ΔV_c condition for the SC architecture. It is possible to analytically demonstrate that the highest ΔV_c occurs when $D = 0.5$ is adopted for the PWM signal. Indeed, according to the model equations 4.10, the ΔV_c can be yield as follows:

$$\Delta V_c = \frac{V_{B1} - V_{B2}}{1 - e^{-\frac{T_s - 2\rho}{\tau_{tot}}}} \left[1 - e^{-\frac{DT_s - \rho}{\tau_{tot}}} - e^{-\frac{T_s - DT_s - \rho}{\tau_{tot}}} - e^{-\frac{T_s - 2\rho}{\tau_{tot}}} \right] \tag{4.13}$$

Therefore, the demonstration of $D = 0.5$ is carried out by imposing the derivative of ΔV_c with respect to D equal to zero. This result allows for achieving a more compact equation for ΔV_c:

$$\Delta V_c = (V_{B1} - V_{B2}) \cdot tanh\left(\frac{0.5T_s - \rho}{2\tau_{tot}}\right) \tag{4.14}$$

Consequently, according to eq. 4.12 and considering $\Delta t = T_s/2$:

$$\bar{I}_c = \frac{2C}{T_s}(V_{B1} - V_{B2}) \cdot tanh\left(\frac{0.5T_s - \rho}{2\tau_{tot}}\right) \tag{4.15}$$

This represents a fundamental equation because it correlates $\bar{I}_c$ to all the main static and dynamic parameters that affect the performance of the SC architecture. It also includes the contribution of the operating conditions of the system in terms of voltage imbalance among the cells and switching frequency. Moreover, eq. 4.15 can be adopted for defining the mean balancing current of the cells ($\bar{I}$). In this case, it is necessary to evaluate the mean value over the entire switching period, resulting as follows:

$$\bar{I} = \frac{\bar{I}_c}{2} = \frac{C}{T_s}(V_{B1} - V_{B2}) \cdot tanh\left(\frac{0.5T_s - \rho}{2\tau_{tot}}\right) \tag{4.16}$$

4.3.1.2 Efficiency

A detailed efficiency model has been also developed for the SC architecture, including conduction and switching losses for the switches. In particular, it has been defined on the basis of the mean values of the input and output powers:

$$\eta = \frac{\overline{P_{out}}}{\overline{P_{in}}} = 1 - \frac{2R_{tot} \cdot \bar{I}}{V_{B1}} - \frac{P_{sw}}{V_{B1} \cdot \bar{I}} \tag{4.17}$$

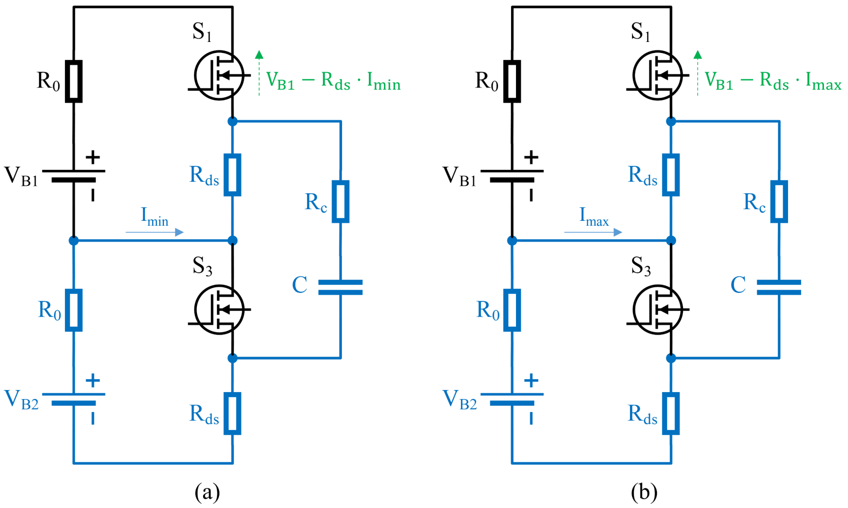

(a) (b)

Figure 4.14: Example of the circuits adopted for calculating the P_{sw} of the switch S_1 that occur during (a) the turning on and (b) the turning off.

where P_{sw} represents the switching losses, whereas the conduction losses for the switches are included in R_{tot}. In this way, P_{in} corresponds to the power provided by the most charged cell and P_{out} is defined as the power received by the least charged cell depurated of all the power losses of the equalization circuit. Hence, it takes into account of the power losses that occur during both t_{on} and t_{off}.
For what concerns P_{sw}, the contribution of each switch for turning on and off operations has been considered. Figure 4.14 shows an example of the circuits adopted for calculating the P_{sw} of the switch S_1. In this case, the model equations can be yield as follows:

$$P_{S1,on} = \frac{1}{2}[V_{B1} - R_{ds} \cdot I_{min}] \cdot I_{max} \cdot T_{rise} \cdot f_s \tag{4.18}$$

$$P_{S1,off} = \frac{1}{2}[V_{B1} - R_{ds} \cdot I_{max}] \cdot I_{min} \cdot T_{fall} \cdot f_s \tag{4.19}$$

where $P_{S1,on}$ and $P_{S1,off}$ are the switching losses of S_1 that occur during the turning on and the turning off, respectively; f_s is the switching frequency, T_{rise} and T_{fall} are the rise and fall times of the switches; I_{max} and I_{min} are the current values at the beginning and the ending of t_{on}, respectively. These current values can also be evaluated during

the t_{off} due to the symmetry of the capacitor current for $D = 0.5$. Moreover, I_{max} corresponds to the in-rush current that occurs at each half period ($T_s/2$). It is important to highlight that I_{min} may be different from zero depending on the ratio between the time constant of the circuit and the switching period. In this case, the switches operate in hard switching mode.
According to model equations 4.10, I_{max} and I_{min} can be analytically calculated considering the constitutive correlation between current and voltage for a capacitor:

$$I_{min} = \frac{C}{\tau_{tot}}(V_{B1} - V_{B2}) \cdot \left[\frac{1}{1 + e^{\frac{DT_s - \rho}{\tau_{tot}}}}\right] \tag{4.20}$$

$$I_{max} = \frac{C}{\tau_{tot}}(V_{B1} - V_{B2}) \cdot \left[\frac{e^{\frac{DT_s - \rho}{\tau_{tot}}}}{1 + e^{\frac{DT_s - \rho}{\tau_{tot}}}}\right] \tag{4.21}$$

Then, P_{sw} has been achieved by the sum of the contributions to the power losses of all the switches:

$$\begin{aligned} P_{sw} &= \sum_{j=1}^{4} P_{Sj,on} + P_{Sj,off} = \\ &= [V_{B1} - (R_0 + 2R_{ds}) \cdot I_{min} + V_{B2}] \cdot I_{max} \cdot T_{rise} \cdot f_s + \\ &+ [V_{B1} - (R_0 + 2R_{ds}) \cdot I_{max} + V_{B2}] \cdot I_{min} \cdot T_{fall} \cdot f_s \end{aligned} \tag{4.22}$$

4.3.2 Design Strategy

A design strategy has been defined for the SC architecture, which can be adopted for all the capacitor-based equalization circuits. The capacitor has been sized in real conditions in order to directly compensate the performance reduction due to the presence of the static and dynamic parameters. Table 4.3 summarizes the values selected for the design of the capacitor. On the basis of the data available from components manufacturer, the lowest values have been considered for R_0, R_{ds} and R_s. In addition, a minimal value for ρ has been adopted with respect to the T_{rise} and T_{fall}. The control algorithm has been operated with $D = 0.5$ in order to exploit the compact equations previously described.

Internal resistance of the cells	$R_0 = 20m\Omega$
Drain-source on resistance for the switches	$R_{ds} = 5m\Omega$
Forward voltage of the internal body diodes	$V_d = 0.7V$
Series resistance of the capacitor	$R_c = 10m\Omega$
Rise time	$T_{rise} = 50ns$
Fall time	$T_{fall} = 75ns$
Dead time	$\rho = 250ns$

Table 4.3: Summary of the values selected for the design of the capacitor.

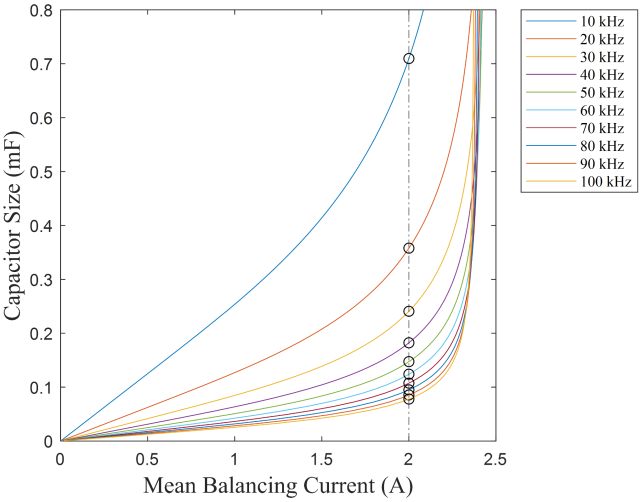

Figure 4.15: Results of the design strategy for the capacitor.

Then, according to eq. 4.16, the design strategy has been performed with the aim of achieving a desired mean balancing current equal to 2A for a maximum imbalance among the cells ($\Delta V = V_{B1} - V_{B2}$) of 400mV. Figure 4.15 shows the results of the sizing procedure for the capacitor. As possible to notice, different combination of C and f_s can be selected for carrying out the desired performance. Therefore, the selection has been operated by considering the combination characterized by the highest efficiency. Moreover, for each combination, different aspects have been investigated for a switching frequency range between 10kHz and 100kHz, as illustrated in table 4.4. According to eq. 4.17, the worst conditions for the efficiency have been considered, including the lowest value for the most charged cell ($V_{B1} = 3$V) and the maximum voltage imbalance allowable ($\Delta V = 400$mV).

C (μ**F**)	$\mathbf{f_s}$ **(kHz)**	η **(%)**	$\mathbf{P_{cond}}$ **(mW)**	$\mathbf{P_{sw}}$ **(mW)**	**In-rush energy (mAs)**
709.7	10	94.2	199.6	29.6	2.50
357.9	20	93.7		59.3	1.20
240.7	30	93.2		89.0	0.83
182.2	40	92.7		118.9	0.62
147.2	50	92.2		148.7	0.50
123.9	60	91.7		178.7	0.42
107.3	70	91.2		208.8	0.36
94.9	80	90.7		238.9	0.32
85.3	90	90.2		269.2	0.28
77.7	100	89.7		299.5	0.26

Table 4.4: Main results of the design strategy for the different combinations of capacitor and switching frequency.

As result, higher C and lower f_s allows for achieving higher efficiency for the SC architecture. This is mainly due to the impact of the switching losses, which strongly increase as the f_s rises. On the other hand, the conduction losses (P_{cond}) are equal for all the operating conditions evaluated since each combination C-f_s provides the same mean balancing current as for design requirements.

It is important to point out the high in-rush currents that occur in capacitor-based equalization circuits. The in-rush current is proportional to the imbalance between the voltage of the most charged cell (V_{B1}) and the residual voltage across the capacitor, whereas it is inversely proportional to the overall circuit resistance. There are two main in-rush currents to be considered. The first one occurs during the initialization of the circuit, when the capacitor is fully discharged and V_{B1} is directly applied to its terminals. In this case, an in-rush current equal to 105A is achieved by considering the circuit parameters defined in table 4.3 and $V_{B1} = 4.2V$. The second one occurs during the normal operating conditions of the circuit, when the capacitor is being charged by the most charged cell or discharged to the least charged one. In this case, the higher voltage imbalance across the capacitor results to be equal to ΔV and a maximum in-rush current of 10A is achieved.

Therefore, considering the high amplitude of the in-rush currents, they need to be properly taken into account for the design of capacitor-based architectures. Typical solutions can be the oversizing of the switches and the protection devices or the adoption of precharge resistors for limiting the most severe in-rush current at the initial stage of operation. However, this increases both size and cost of the SC architecture as well as adds complexity to the control algorithm. An additional aspect to be evaluated includes the in-rush energy, which represents the energy associated with the capacitor current profile during the first t_{on} of the circuit, thus when the most sever in-rush current occurs. This is an important parameters because the majority of switches allow for tolerating high in-rush currents for a certain amount of time. Hence, the switches can be properly selected by evaluating the in-rush energy due to the specific design of the SC architecture.

4.3.3 Sensitivity Analysis

As previously discussed, the design strategy for the SC architecture has been operated in real conditions. In detail, the lowest values available on the market have been selected for each component of the equalization circuit. This allows for sizing the capacitor in the best condition in terms of real components and then evaluating the performance reduction of the balancing circuit due to potential increasing parameter variations.

In this section, a sensitivity analysis is illustrated for quantitatively defining the impact of the operating conditions and parameter variations on the performance of the SC architecture, including efficiency, mean balancing current and amount of charge transferred among the cells. According to the sizing results achieved from the design strategy, a switching frequency of 10kHz and a capacitor of 709.7μF have been adopted.

Figure 4.16 shows the impact of the operating conditions and the parameters variations on the overall efficiency of the SC architecture. It is important to highlight that each η point is characterized by a different mean input/output power since both operating conditions and parameter variations affect the amplitude of the mean balancing current. Therefore, an effective evaluation cannot be achieved and the results shown in figure 4.16 only provide a qualitative indication of the variability of η. In particular, figure 4.16(a) reports its variability with respect to the maximum voltage imbalance among the cells ΔV, the voltage of the most charged cell V_{B1} and the mean output power $\overline{P_{out}}$, which corresponds to the mean input power depurated of all the circuit losses. The design parameters have been considered, including a dead time ρ of 250ns and an overall resistance R_{tot} of 40mΩ.

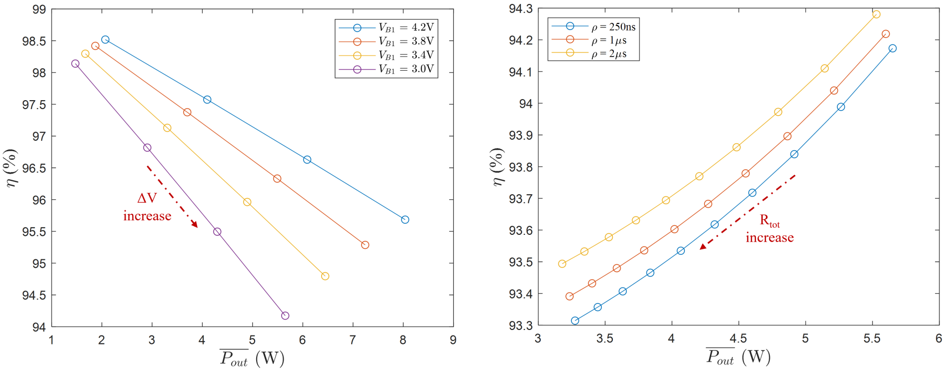

(a) (b)

Figure 4.16: Variability of the efficiency of the SC architecture with respect to mean output power considering the impact of (a) the operating conditions (ΔV, V_{B1}) and (b) the parameter variations (ρ, R_{tot}).

It results that the balancing circuit operates at higher η for larger V_{B1} and lower ΔV. This also confirms the worst conditions for η, which have been adopted for carrying out the results in table 4.4. On the other hand, figure 4.16(b) shows the variability of η with respect to $\overline{P_{out}}$ and the parameter variations (ρ and R_{tot}). The worst conditions for η have been set ($V_{B1} = 3$V and $\Delta V = 400$mV), while ρ ranges from 250ns to 2μs and a maximum 100% increase of R_{tot} has been considered. A reduction of both η and $\overline{P_{out}}$ is observed as R_{tot} increases. This highlights a lower reduction of the mean input power with respect to $\overline{P_{out}}$. In addition, considering the same R_{tot}, an increase of ρ leads to a reduction of the mean balancing current and consequently to a small increase of η.

For what concerns the reduction of the mean balancing current, a performance parameter has been defined as follows:

$$\Delta \bar{I} = \frac{\bar{I} - \bar{I}_{des}}{\bar{I}_{des}} \tag{4.23}$$

where $\bar{I}_{des}$ is the desired mean balancing current (equal to 2A from the design strategy) and $\bar{I}$ is the actual one, which varies based on the operating conditions and the parameter variations. Hence, negative $\Delta \bar{I}$ represents a reduction of the mean balancing current with respect to the desired one. Figure 4.17 shows the performance reduction of the SC architecture in terms of mean balancing current with respect to different operating conditions and parameter variations.

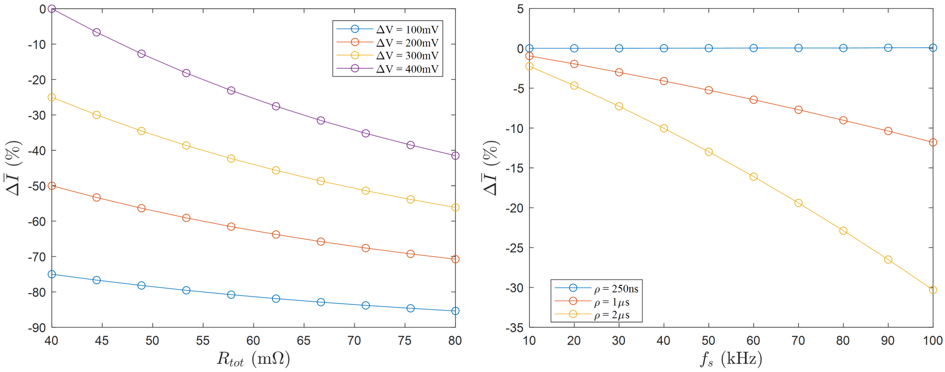

(a) (b)

Figure 4.17: Performance reduction in terms of mean balancing current with respect to different operating conditions and parameter variations.

A strong impact of ΔV and R_{tot} on the variability of $\Delta\bar{I}$ expressed in percentage is highlighted in figure 4.17. It results a higher performance reduction as R_{tot} increases and ΔV decrease.
According to the design strategy, $\bar{I}$=$\bar{I}_{des}$ only for ΔV = 400mV and R_{tot} = 40mΩ. In this condition, the severity of the performance reduction has been also evaluated with respect to ρ and the switching frequency. In detail, on the basis of the design results reported in table 4.4, the correct size of the capacitor has been set for each f_s value. In this way, a proper comparison can be performed since all the different combinations C-f_s allow for achieving $\bar{I}_{des}$ for ρ = 250ns. As possible to notice in figure 4.17(b), a larger impact of ρ on $\Delta\bar{I}$ is achieved for higher f_s. Indeed, higher ρ leads to severe reduction of the effective duty cycle of the PWM signal and thus lower mean balancing current, especially for smaller switching period.
An additional aspect to be evaluated is represented by the amount of charge transferred among the cells. According to eq. 4.16, it can be analytically defined as follows:

$$Ah_{Ts} = \frac{C \cdot \Delta V}{3600} \cdot tanh\left(\frac{0.5T_s - \rho}{2\tau_{tot}}\right) \tag{4.24}$$

where Ah_{Ts} represents the amount of charge transferred among the cells in Ah over the switching period. Hence, it strongly depends on the f_s considered for the PWM control signal. However, this does not allow for properly comparing different architectures of equalization circuits since different f_s may be adopted for each one.

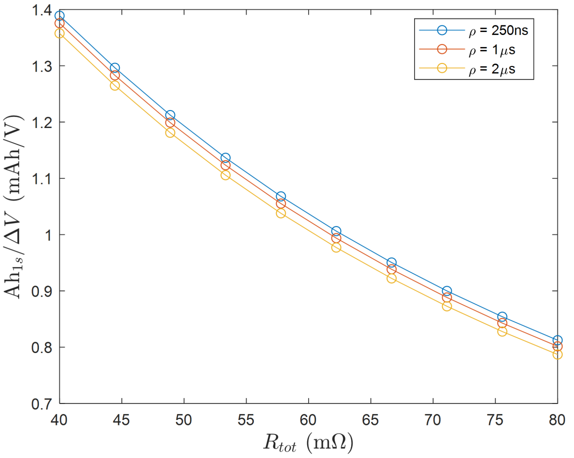

Figure 4.18: Sensitivity analysis for Ah_{1s} over ΔV with respect to parameter variations (R_{tot} and ρ).

Therefore, a more suitable definition of the amount of charge transferred among the cells can be performed by multiplying eq. 4.24 for the f_s considered. In this way, the indication of the Ah transferred over one second Ah_{1s} can be achieved, enabling the possibility to correctly evaluate the differences in the charge transfers among the equalization circuits. Moreover, both Ah_{Ts} and Ah_{1s} can be also defined over ΔV in order to obtain a more generalized result.
Figure 4.18 shows a sensitivity analysis for Ah_{1s} over ΔV with respect to the parameter variations. Both increases of R_{tot} and ρ result in a reduction of charge transferred among the cells, since both affect the amplitude of the mean balancing current. However, a larger impact of R_{tot} is observed compared to ρ. In addition, Ah_{1s} is proportional to ΔV, thus larger charge transfers among the cells occur for higher voltage imbalances.

4.3.4 Equalization Time Evaluation

The model equations have been implemented in MATLAB© with the aim of demonstrating the validity of the design strategy as well as evaluating the performance of the SC architecture. The design parameters reported in table 4.3 have been considered, including $C = 709.7\mu$F and $f_s = 10$kHz. The functionality of the equalization circuit have been tested for two series-connected cells in the worst efficiency condition, thus $V_{B1} = 3$V and $\Delta V = 400$mV. The experimentally cali-

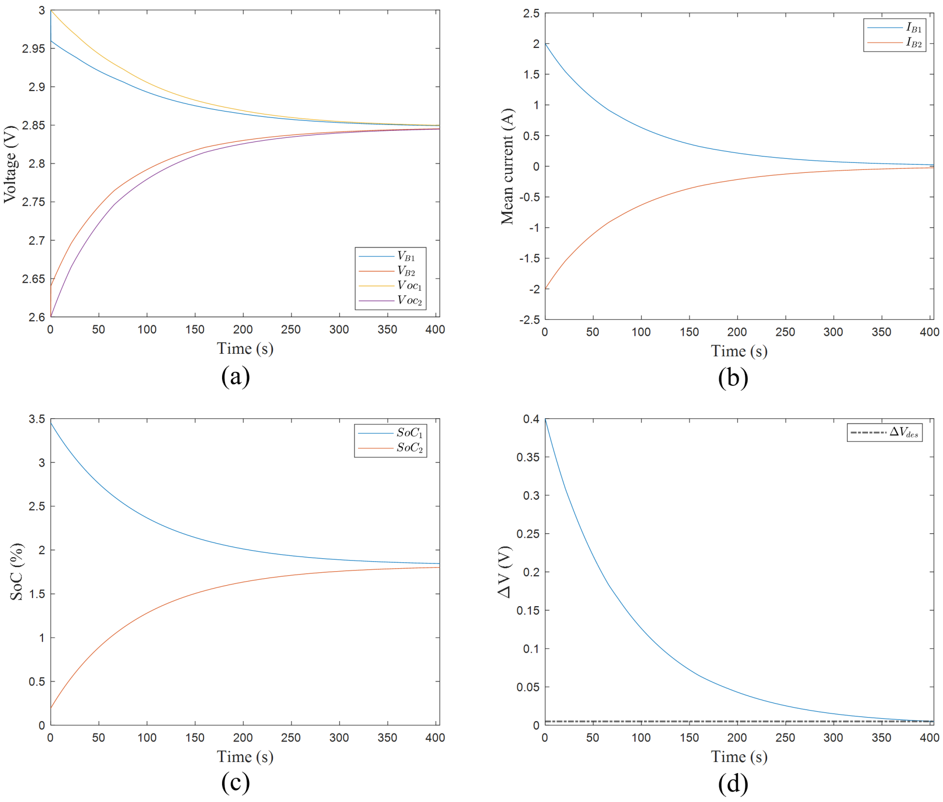

Figure 4.19: Functionality of the SC architecture in terms of (a) terminal voltage and OCV of the cells, (b) mean current, (c) SoC and (d) ΔV.

brated zero-order ECM of EFEST18650 technology has been adopted for the cells. The control algorithm has been developed in order to stop the equalization process when ΔV is equal or lower than a desired voltage imbalance ΔV_{des} of 5mV.

Figure 4.19 shows the functionality of the SC architecture in terms of terminal voltage and OCV of the cells, mean balancing current, SoC and ΔV. Starting from an initial ΔV of 400mV, the equalization process allows for transferring the energy between the most and the least charged cells until reaching ΔV_{des}. As previously discussed, considering $D = 0.5$, the mean current values during the t_{on} and t_{off} periods are equal. Therefore, the discharging of the most charged cell and the charging of the least charged one occur with the same C-rate. In addition, according to eq. 4.16, the amplitude of the mean balancing current decreases as ΔV lowers. As possible to notice, the worst

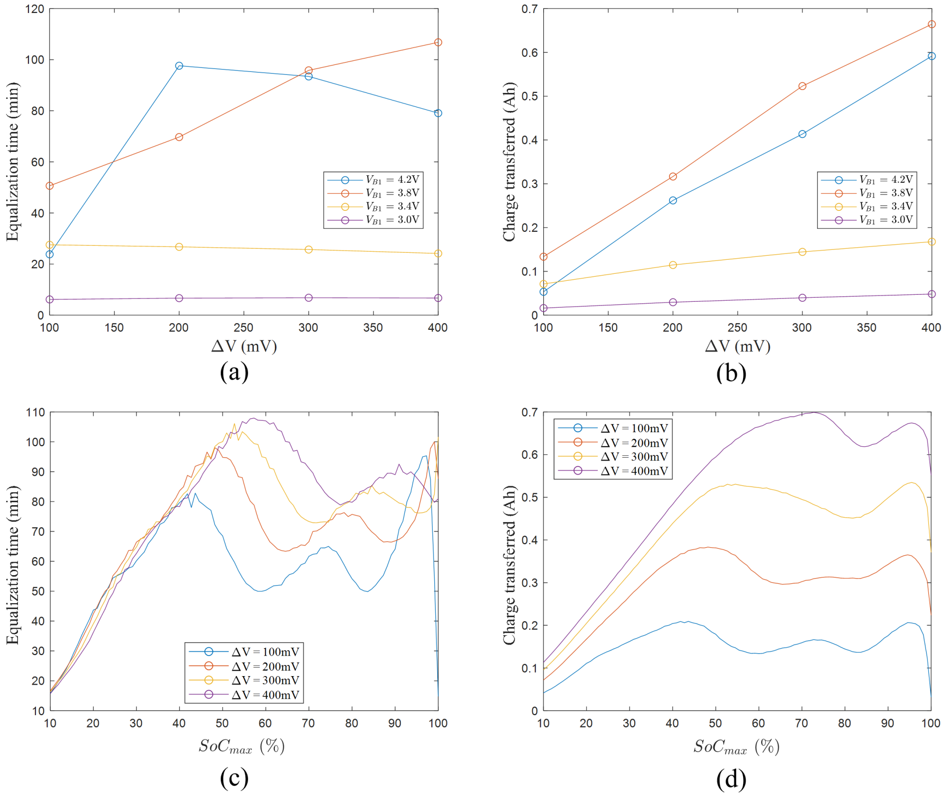

Figure 4.20: Variability of the equalization time and the amount of charge transferred among the cells with respect to ΔV and V_{B1} (a,b) and for different SoC_{max} (c,d).

efficiency condition corresponds to a very low SoC for the cells.

As for the passive equalizer, the impact of the operating conditions on the equalization time and the amount of charge transferred among the cells has been evaluated. In particular, figures 4.20(a) and (b) shows the variability with respect to ΔV and V_{B1}, while figures 4.20(c) and (d) reports the variability for different SoC_{max}, which represents the SoC of the most charged cell. A lower impact of ΔV on the equalization time is observed for $V_{B1} < 3.4V$, mainly related to the shape of the OCV curve in this voltage range. Indeed, since it corresponds to the exponential region of the OCV curve, a fast increase or decrease of the cell voltages occurs for a charging or discharging, leading to low equalization time and low impact of ΔV. This can also be observed in figure 4.20(c), where the equalization times are not highly affected by ΔV for $SoC_{max} < 40\%$. On the other hand, a strong variability of the equalization times is achieved depending on the operating conditions for $V_{B1} > 3.4V$ and $SoC_{max} > 40\%$. Likewise for the passive equalizer, these results highlight the possibility to develop a proper balancing strategy for minimizing the equalization time and thus increasing the performance of the SC architecture.

Similar considerations can be made for what concerns the charge transferred. In detail, two main results can be highlighted. The first one regards the higher amount of charge transferred for a lower cell voltage ($V_{B1} = 3.8V$) than the maximum one ($V_{B1} = 4.2V$). Then, because of the strong variability of the charge transferred shown in figure 4.20(d), the second main result includes the possibility to enable the balancing process in specific operating conditions that allow for minimizing both the equalization time and the charge transferred.

4.4 Inductor-based Equalizer

Among the inductor-based equalization circuits, a design methodology has been proposed for the coupled or multi-inductor architecture, which also corresponds to a buck-boost converter configuration. This active solution has been previously illustrated in 3.3.2.2 for a generalized battery pack composed by n series-connected cells. However, all the operating conditions involve just two cells and one inductor, thus a simplified architecture can be adopted for defining design strategies as well as evaluating the performance of the multi-inductor equalization circuit. This also allows for extending the proposed design methodology to the other inductor-based architectures since the energy transfers occur between two cells and one inductor for all the techniques, including AC2C, DC2C, P2C and C2P.

Analytical models have been developed for the multi-inductor architecture considering either ideal or real conditions. These also include an efficiency model that takes into account for conduction and switching losses of the switches. Then, a proposed design methodology has been presented, which allows for sizing the inductor in order to achieve the desired performance. On the basis of this design strategy, the impact of both parameter variations of the circuit components and the operating conditions of the cells has been evaluated as well.

The models developed have been implemented in MATLAB© in order to validate the correct functionality of the proposed design strategy.

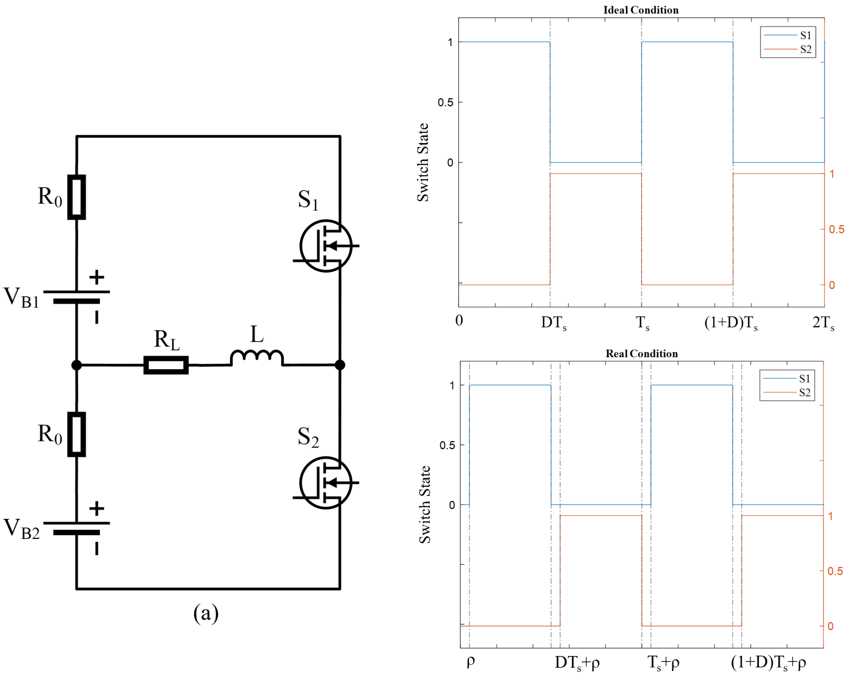

(a)

(b)

Figure 4.21: (a) Simplified architecture of the multi-inductor equalization circuit for two cells and (b) the control algorithm in both ideal and real conditions.

4.4.1 Model Equations

Figure 4.21 shows the simplified architecture of the multi-inductor equalization circuit for two cells and the related control algorithm in both ideal and real conditions. In this case, unlike the capacitor-based architectures, a fully ideal condition can be achieved since no pulse charging or discharge can occur due to the characteristic relationship between voltage and current of the inductor. Therefore, only the inductor (L) has been considered in ideal condition, whereas the real condition includes the internal resistance (R_0) of the zero-order ECM adopted for the cells, the series resistance of the inductor (R_L) as well as the static and dynamic parameters of the switches.

For what concern the static parameters, considering MOSFETs as switches, they are represented by the drain-source on-state resistance (R_{ds}) and the forward voltage of the internal body diode (V_d). On the other hand, the dynamic parameters are mainly related to the switching characteristics, such as rise and fall times. In order to take into account for these dynamic parameters, a dead time (ρ) has been considered for the control strategy of the multi-inductor equalization circuit.

According to the multi-inductor architecture and the control algorithm illustrated in figure 4.21, the same pulse-width modulation (PWM) signal is adopted for the switches, considering a specific switching period (T_s) and duty cycle (D). In detail, assuming the voltage of the top cell (V_{B1}) greater than that of the bottom one (V_{B2}), the switch S_1 is turned on and S_2 is turned off during the t_{on} period. Therefore, the energy is transferred from the most charged cell to the inductor. Then, during the t_{off} period, the opposite configuration of the switches is operated, leading to the charging of the least charged cell by means of the energy previously stored in the inductor.

The model equations that describe the inductor current i_L in ideal conditions can be yield as follows:

$$i_L(t) = \begin{cases} \dfrac{V_{B1}}{L} t & 0 \le t \le DT_s \\ I_{max,id} - \dfrac{V_{B2}}{L}(t - DT_s) & DT_s \le t \le T_s \end{cases} \tag{4.25}$$

where $I_{max,id}$ represents the peak value of the inductor current calculated at $t = DT_s$ in ideal condition. However, considering the real conditions for the multi-inductor architecture and the related control algorithm, the model equations that describe i_L become:

$$i_L(t) = \begin{cases} 0 & 0 \le t \le \rho \\ \dfrac{V_{B1}}{R_{tot}} \left[1 - e^{-\frac{t-\rho}{\tau_{tot}}} \right] & \rho \le t \le DT_s \\ I_{max,r} \cdot e^{-\frac{t-DT_s}{\tau_r}} + \dfrac{V_{B2} + V_d}{R_r} \left[e^{-\frac{t-DT_s}{\tau_r}} - 1 \right] & DT_s \le t \le DT_s + \rho \\ I_{min,1} \cdot e^{-\frac{t-DT_s-\rho}{\tau_{tot}}} + \dfrac{V_{B2}}{R_{tot}} \left[e^{-\frac{t-DT_s-\rho}{\tau_{tot}}} - 1 \right] & DT_s + \rho \le t \le T_s \end{cases} \tag{4.26}$$

where R_{tot} is the overall circuit resistance; R_r is a portion of R_{tot}, equal to the sum of R_0 and R_{ds}; τ_{tot} and τ_r are the time constant of the current transient due to R_{tot} and R_r, respectively; $I_{max,r}$ is the peak inductor current calculated at $t = DT_s$ in real condition, while $I_{min,1}$ represents the current value at $t = DT_s + \rho$. In particular, since only one switch is involved in the balancing current path during both t_{on} and t_{off} periods for the multi-inductor architecture, it results:

$$R_{tot} = R_0 + R_{ds} + R_L \tag{4.27}$$

$$R_r = R_0 + R_L \tag{4.28}$$

It is important to highlight that, unlike the capacitor-based equalizer, the duty cycle of the PWM signal needs to be modified in both ideal and real conditions depending on the voltage difference between the two cells (ΔV) for ensuring the correct functionality of the multi-inductor equalization circuit. In particular, it is preferable to operate at the limit of the continuous conduction mode (LCCM) for the specific application of the cell balancing. Figure 4.22 shows the issues related to the adoption of duty cycle greater or lower than D_{LCCM}, which represents the value that allows the circuit for operating at LCCM. In ideal conditions, the inductor current rises and decreases without reaching the steady-state condition for $D{>}D_{LCCM}$ and $D{<}D_{LCCM}$, respectively. Therefore, the equalization circuit can operate only at LCCM. In real conditions, a dead time is also included for taking into account for the dynamic characteristics of the switches. It mainly consists in introducing a delay time between the opening of S_1 and the closing S_2 or vice versa. The dead time is always adopted in real-world applications since it allows for avoiding undesired short circuit conditions for the cells. However, this introduces additional time intervals with respect to the ideal condition, in which the equalization circuit performs differently depending on the duty cycle, as illustrated in figures 4.22(c) and (d).

When $D{>}D_{LCCM}$, the inductor current rises during the transient until reaching a specific positive mean value in steady-state. This condition allows for achieving a higher mean balancing current with respect to the LCCM operation. Moreover, the two additional dead time intervals contribute to further recharge the least charged cell. Indeed, because of the current sign, the internal body diode of the switch S_2 results positively polarized in both intervals after t_{on} and t_{off}, acting as a viable path for the freewheeling current. This allows for transferring the energy stored in the inductor also during the dead time intervals.

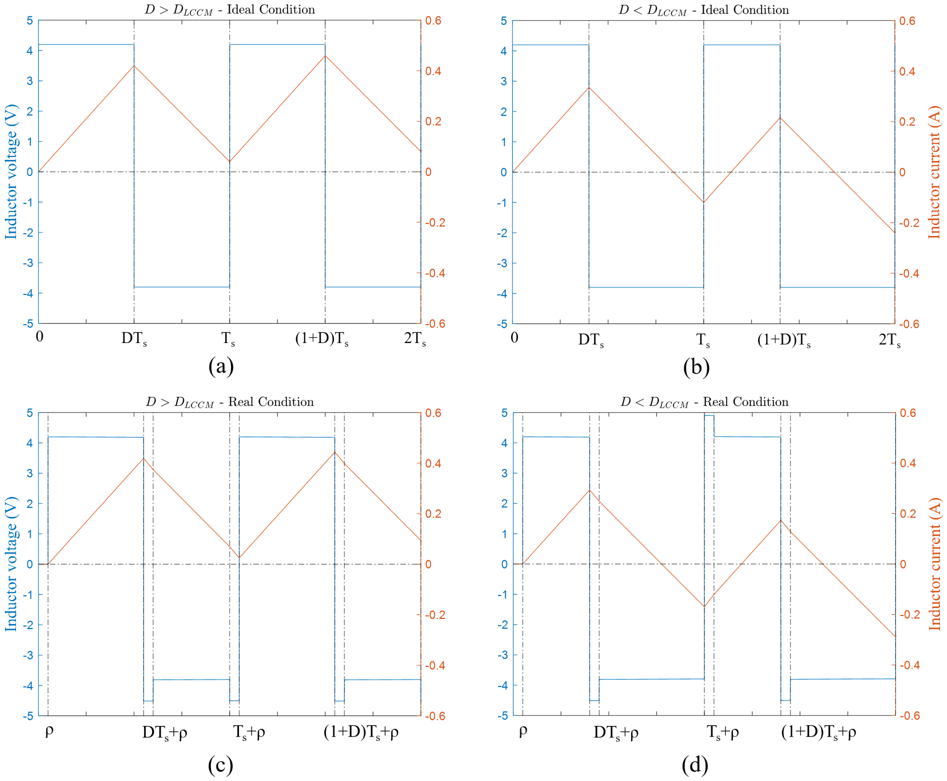

(a) (b)

(c) (d)

Figure 4.22: Voltage and current of the inductor for duty cycle greater or lower than D_{LCCM} in both ideal (a) and real conditions (b).

Nevertheless, despite the benefits of this operating condition, it is still preferable to perform the balancing process at LCCM due to the possibility to better control the energy flows among the cells. In this way, the equalization process can be interrupted easily after each T_s and the issues related to the freewheeling currents can be avoided.

On the other hand, when $D<D_{LCCM}$, the inductor current decreases during the transient until reaching a specific negative mean value in steady-state. This condition has to be avoided because it causes the incorrect functionality of the multi-inductor equalization circuit. Indeed, due to the negative sign of the inductor current, it results the most charged cell to be recharged by the least charged one.

Figure 4.23 shows the steady-state voltage and current waveforms for the multi-inductor architecture operating at LCCM in both ideal and real conditions. The D_{LCCM} can be analytically defined by imposing

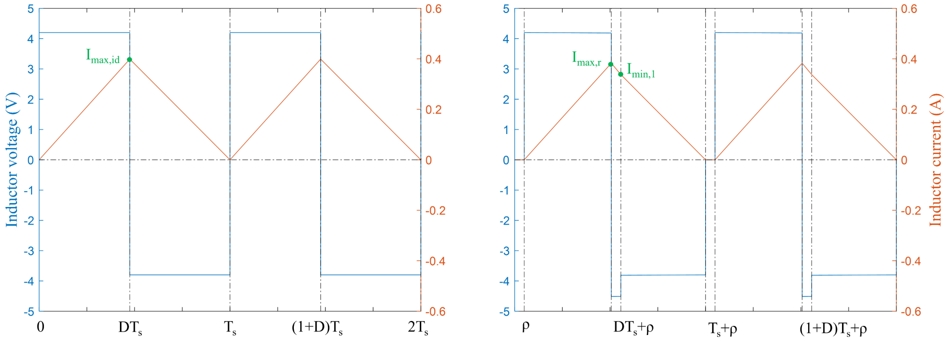

(a) (b)

Figure 4.23: Voltage and current waveforms for the multi-inductor equalization circuit operating at LCCM in both (a) ideal and (b) real conditions ($V_{B1} = 4.2$V and $V_{B2} = 3.8$V).

$i_L(t = T_s) = 0$. According to eq. 4.25, it results in ideal condition:

$$D_{LCCM} = \frac{V_{B2}}{V_{B1} + V_{B2}} \tag{4.29}$$

Therefore, the duty cycle can be directly calculated on the basis of the voltage imbalance among the cells. On the other hand, a direct relationship between the D_{LCCM} and the circuit parameters cannot be achieved in real conditions due to the complexity of the model. Indeed, by imposing $i_L(t = T_s) = 0$ in eq. 4.26, it is not possible to extrapolate the duty cycle without using a Taylor approximation. Alternatively, an iterative process can be adopted for defining D_{LCCM} in real conditions.

4.4.1.1 Mean Balancing Current

Unlike the capacitor-based architectures, the mean value of the charge current during the t_{on} is not equal to the mean value of the discharge current during the t_{off} in both ideal and real conditions for an inductor-based equalization circuit. Considering the analytical definition, the mean value of the cell currents in ideal condition can be yield as follows:

$$\bar{I}_{1,id} = \frac{V_{B1}}{2L} D^2 T_s \tag{4.30}$$

$$\bar{I}_{2,id} = (1-D)\cdot T_s \cdot \left[\frac{V_{B1}+V_{B2}}{L}D - \frac{V_{B2}}{2L}(1+D)\right] \tag{4.31}$$

where $\bar{I}_{1,id}$ and $\bar{I}_{2,id}$ are the mean currents of the most and least charged cells, respectively. In order to simplify the notation, the duty cycle at LCCM is reported as D. Likewise, the mean currents can be defined in real conditions, leading to more complex expressions:

$$\bar{I}_{1,r} = \frac{V_{B1}}{R_{tot}}\left[\frac{DT_s-\rho}{T_s} + \frac{\tau_{tot}}{T_s}\left(e^{-\frac{t-\rho}{\tau_{tot}}}-1\right)\right] \tag{4.32}$$

$$\begin{aligned}\bar{I}_{2,r} = &I_{max,r}\cdot\frac{\tau_r}{T_s}\left(1-e^{-\frac{\rho}{\tau_r}}\right) + \frac{V_{B2}+V_d}{R_r}\left[\frac{\tau_r}{T_s}\left(1-e^{-\frac{\rho}{\tau_r}}\right) - \frac{\rho}{T_s}\right]+\\ &+ I_{min,1}\cdot\frac{\tau_{tot}}{T_s}\left(1-e^{-\frac{T_s-DT_s-\rho}{\tau_{tot}}}\right)+\\ &+\frac{V_{B2}}{R_{tot}}\left[\frac{\tau_{tot}}{T_s}\left(1-e^{-\frac{T_s-DT_s-\rho}{\tau_{tot}}}\right) - \frac{T_s-DT_s-\rho}{T_s}\right]\end{aligned} \tag{4.33}$$

These equations are certainly more complete with respect to the ideal ones, since they include all the main static and dynamic parameters of the equalization circuit. However, as previously discussed for the duty cycle in real conditions, eqs. 4.32 and 4.33 do not allow for directly defining the size of the inductor. Hence, they cannot be used for a design purpose, but only for providing accurate details of the performance of the multi-inductor architecture in terms of balancing current. In addition, the size of the inductor and the duty cycle are closely related to each other, thus the D_{LCCM} needs to be calculated based on L and vice versa.

As matter of the fact, eqs. 4.30 and 4.31 are adopted for defining the design strategy of the inductor-based equalizer. In particular, the sizing of the inductor can be performed by considering a desired $\bar{I}_{1,id}$ or $\bar{I}_{2,id}$. However, since the multi-inductor architecture inherits the properties of a buck-boost converter, it results:

$$\frac{V_{B1}}{V_{B2}} = \frac{\bar{I}_{2,id}}{\bar{I}_{1,id}} \tag{4.34}$$

A higher mean balancing current occurs for the least charged cell due to the lower voltage. Hence, a proper design strategy considers $\bar{I}_{2,id}$ for sizing the inductor-based equalization circuit.

4.4.1.2 Efficiency

A detailed efficiency model has been also developed for the multi-inductor architecture, including conduction and switching losses for the switches. In particular, considering the real conditions, it has been defined on the basis of the mean values of the input and output powers:

$$\eta = \frac{\overline{P_{out}}}{\overline{P_{in}}} = \frac{V_{B1} \cdot \bar{I}_{1,r} - R_{tot} \cdot (\bar{I}_{1,r} + \bar{I}_{2,r}) - P_{sw}}{V_{B1} \cdot \bar{I}_{1,r}} \tag{4.35}$$

where P_{sw} represents the switching losses, whereas the conduction losses for the switches are included in R_{tot}. In this way, $\overline{P_{in}}$ corresponds to the power provided by the most charged cell and $\overline{P_{out}}$ is defined as the power received by the least charged cell depurated of all the power losses of the equalization circuit. Hence, it takes into account of the power losses that occur during both t_{on} and t_{off}.
For what concerns P_{sw}, the contribution of each switch for turning on and off operations has been considered. In this case, unlike the capacitor-based equalizer, the turning on of the switch S_1 and the turning off of the switch S_2 occur at zero current since the LCCM operations are performed. Therefore, only two contributions can be taken into account for P_{sw}. Figure 4.24 shows the circuits adopted for calculating these two contributions, while the model equations can be yield as follows:

$$P_{S1,off} = \frac{1}{2}[V_{B1} + V_{B2} + R_0 \cdot I_{max,r} + V_d] \cdot I_{max,r} \cdot T_{fall} \cdot f_s \tag{4.36}$$

$$P_{S2,on} = \frac{1}{2}[V_{B1} + V_{B2} - (R_0 + R_{ds}) \cdot I_{max,r}] \cdot I_{max,r} \cdot T_{rise} \cdot f_s \tag{4.37}$$

where $P_{S1,off}$ and $P_{S2,on}$ are the switching losses related to the turning off of the switch S_1 and the turning on of the switch S_2, respectively; f_s is the switching frequency, T_{rise} and T_{fall} are the rise and fall times

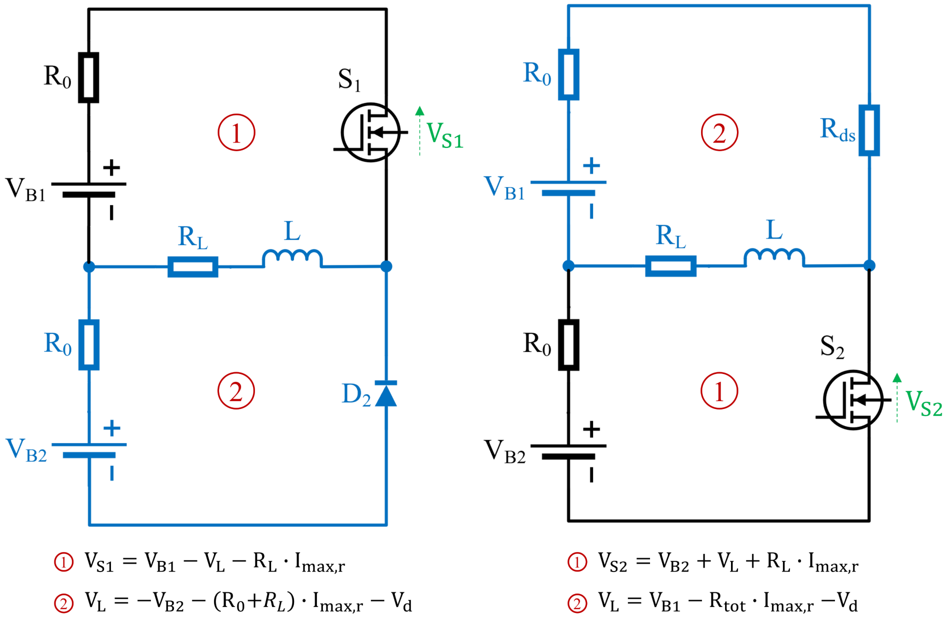

(a) (b)

Figure 4.24: Circuits adopted for calculating the contributions to P_{sw} related to (a) the turning off of the switch S_1 and (b) the turning on of the switch S_2.

of the switches. In this case, both switching operations occur at the peak current $I_{max,r}$, leading to hard switching conditions especially when high mean balancing currents are required.
Then, the overall P_{sw} has been achieved by the sum of these two contributions:

$$P_{sw} = P_{S1,off} + P_{S2,on} \tag{4.38}$$

4.4.2 Design Strategy

A design strategy has been defined for the multi-inductor architecture, which can be adopted for all the inductor-based equalization circuits. The inductor has been sized in ideal conditions since the model equations developed in real conditions cannot be adopted for a design purpose, as discussed in the previous section. The control algorithm has been operated with a variable duty cycle in order to ensure the LCCM in all the operating conditions. In particular, according to

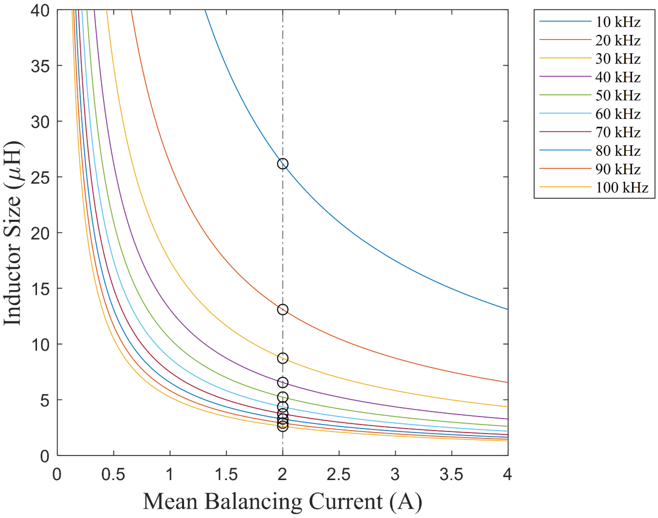

Figure 4.25: Results of the design strategy for the inductor.

eqs. 4.29 and 4.31, the inductor size can be expressed as a function of V_{B1} and the voltage imbalance among the cells ΔV as follows:

$$L = \frac{V_{B1} \cdot (V_{B1} - \Delta V)}{2V_{B1} - \Delta V} \frac{T_s}{\bar{I}_{2,r}} \left[1 - \frac{3V_{B1} - 2\Delta V}{4V_{B1} - 2\Delta V} \right] \tag{4.39}$$

The design strategy has been performed with the aim of achieving a desired mean balancing current $\bar{I}_{2,r}$ equal to 2A for specific operating conditions, including $V_{B1} = 4.2$V and a maximum ΔV of 400mV. Figure 4.25 shows the results of the sizing procedure for the inductor. As possible to notice, different combination of L and f_s can be selected for carrying out the desired performance. Therefore, the selection has been operated by considering the combination characterized by the highest efficiency. It is important to point out that while all the combinations have been achieved in ideal conditions, the efficiency for each one has been evaluated in real conditions. In detail, table 4.5 summarizes the parameters selected. On the basis of the data available from components manufacturer, the lowest values have been considered for R_0, R_{ds} and R_s. In addition, a minimal value for ρ has been adopted with respect to the T_{rise} and T_{fall}.

Moreover, for each combination L-f_s, different aspects have been investigated for a switching frequency range between 10kHz and 100kHz, as illustrated in table 4.6.

Internal resistance of the cells	$R_0 = 20m\Omega$
Drain-source on resistance for the switches	$R_{ds} = 5m\Omega$
Forward voltage of the internal body diodes	$V_d = 0.7V$
Series resistance of the capacitor	$R_L = 10m\Omega$
Rise time	$T_{rise} = 50ns$
Fall time	$T_{fall} = 75ns$
Dead time	$\rho = 250ns$

Table 4.5: Summary of the parameters selected for calculating the efficiency in real conditions for each combination L-f_s.

L (μ**H**)	$\mathbf{f_s}$ **(kHz)**	$\boldsymbol{\eta}$ **(%)**	$\mathbf{P_{cond}}$ **(mW)**	$\mathbf{P_{sw}}$ **(mW)**	$\mathbf{D_{LCCM}}$ **(%)**
26.2	10	96.2	123.2	25.6	48.25
13.1	20	95.2	122.0	51.1	48.41
8.7	30	94.9	120.8	76.5	48.56
6.5	40	94.2	119.6	101.8	48.72
5.2	50	93.6	118.4	127.0	48.87
4.4	60	92.9	117.2	151.1	49.03
3.7	70	92.3	116.0	177.1	49.19
3.3	80	91.6	114.8	201.2	49.34
2.9	90	90.9	113.7	226.8	49.50
2.6	100	90.3	112.5	251.5	49.65

Table 4.6: Main results of the design strategy for the different combinations of inductor and switching frequency.

According to eq. 4.35, the worst conditions for the efficiency have been considered, including the lowest value for the most charged cell ($V_{B1} = 3$V) and $\Delta V = 400$mV.

As result, likewise for the SC architecture, higher L and lower f_s allows for achieving higher efficiency for the multi-inductor equalization circuit. This is mainly due to the impact of the switching losses, which strongly increase as the f_s rises. In this case, the conduction losses (P_{cond}) are not equal for all the operating conditions evaluated since different mean balancing current occur for both the most and the least charged cells in real operating conditions. Indeed, the desired performance in terms of mean balancing current can only be achieved in ideal conditions. In particular, as f_s increases, a reduction of the P_{cond} is observed, which is primarily due to the reduction of

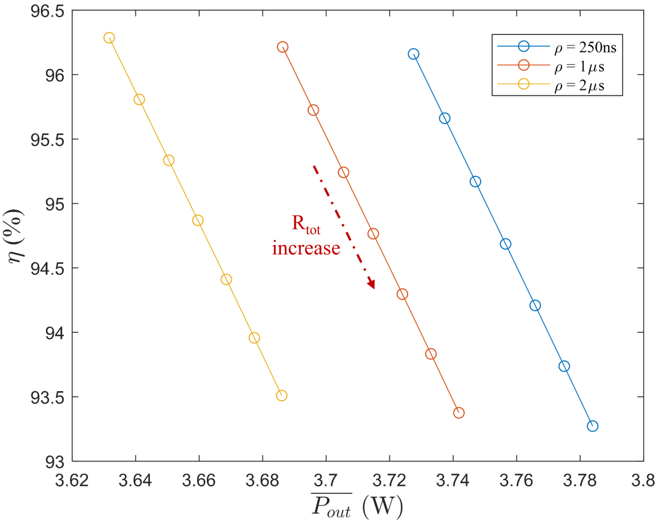

Figure 4.26: Variability of the efficiency of the multi-inductor architecture with respect to the mean output power considering the impact of the parameter variations (ρ, R_{tot}).

the mean values of either the input or output powers. This is related to the fact that the multi-inductor architecture operates as a buck-boost converter. Therefore, since the circuit needs to operate at the LCCM, an increase of f_s leads to a reduction of the current ripple and consequently of $I_{max,r}$, $\bar{I}_{1,r}$ and $\bar{I}_{2,r}$.
Table 4.6 also reports the variability of the duty cycle required for ensuring the LCCM operations for all the design combinations L-f_s.

4.4.3 Sensitivity Analysis

As for the capacitor-based equalizer, a sensitivity analysis is illustrated in this section for quantitatively defining the impact of the operating conditions and parameter variations on the performance of the multi-inductor architecture, including efficiency, mean balancing current and amount of charge transferred among the cells. According to the sizing results achieved from the design strategy, a switching frequency of 10kHz and an inductor of 26.2μH have been adopted.
Figure 4.26 shows the impact of the parameter variations on the overall efficiency of the multi-inductor architecture. Unlike the capacitor-based equalizer, the operating conditions (ΔV, V_{B1}) do not provide any relevant contribution to the variability of η in the inductor-based

equalization circuit, thus these results have not been reported in the sensitivity analysis.
It is important to highlight that each η point is characterized by a different mean input/output power since the parameter variations affect the amplitude of the mean balancing current. Therefore, an effective evaluation cannot be achieved and the results shown in figure 4.26 only provide a qualitative indication of the variability of η. In particular, it reports its variability with respect to $\overline{P_{out}}$ and the parameter variations (ρ and R_{tot}). The worst conditions for η have been set (V_{B1} = 3V and ΔV = 400mV), while ρ ranges from 250ns to 2μs and a maximum 100% increase of R_{tot} has been considered. In addition, according to the specific parameter variation, a proper duty cycle for the PWM signal has been adopted in order to allow the equalization circuit for operating at LCCM. A reduction of η and an increase of $\overline{P_{out}}$ are observed for higher R_{tot}. This highlights a larger increase of the mean input power with respect to $\overline{P_{out}}$. In addition, considering the same R_{tot}, an increase of ρ leads to a reduction of $\overline{P_{out}}$, which results in a lower mean balancing current and consequently to a small increase of η.
For what concerns the reduction of the mean balancing current, $\bar{I}_{2,r}$ has been considered and a performance parameter has been defined as follows:

$$\Delta\bar{I} = \frac{\bar{I}_{2,r} - \bar{I}_{des}}{\bar{I}_{des}} \tag{4.40}$$

where $\bar{I}_{des}$ is the desired mean balancing current (equal to 2A from the design strategy) and $\bar{I}_{2,r}$ is the actual one, which varies based on the operating conditions and the parameter variations. Hence, $\Delta\bar{I}$ represents the reduction of the mean balancing current corresponding to the least charged cell with respect to the desired one. Figure 4.27 shows the performance reduction of the multi-inductor architecture in terms of mean balancing current with respect to different operating conditions and parameter variations.
In this case, since the design strategy has been performed in ideal conditions, $\bar{I}_{2,r}$ will result always lower than $\bar{I}_{des}$. Considering a fixed ρ = 250ns, the impact of ΔV and R_{tot} on the variability of $\Delta\bar{I}$ expressed in percentage is highlighted in figure 4.17. A reduction of the performance is observed for higher R_{tot} and ΔV.
However, compared to the SC architecture, a lower impact is observed. Hence, higher balancing currents can be achieved by means of an inductor-based equalizer. An additional difference includes the relationship between $\Delta\bar{I}$ and ΔV. Indeed, the multi-inductor architecture

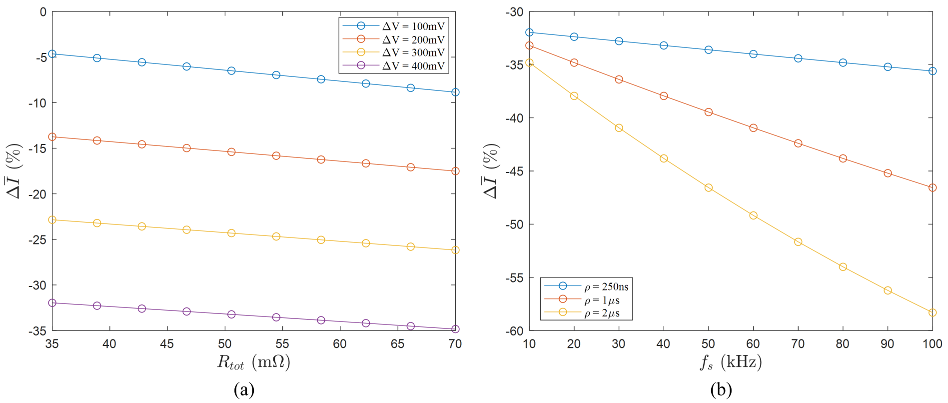

Figure 4.27: Performance reduction in terms of mean balancing current with respect to different operating conditions and parameter variations.

performs higher balancing currents as ΔV decrease, while the opposite operation occurs for the capacitor-based equalizer.
On the other hand, considering $\Delta V = 400$mV and $R_{tot} = 35$mΩ, the severity of the performance reduction has been also evaluated with respect to ρ and the switching frequency. In detail, on the basis of the design results reported in table 4.6, the correct size of both the inductor and D_{LCCM} have been set for each f_s value. In this way, a proper comparison can be performed since all the different combinations L-f_s allow for achieving $\bar{I}_{des}$ in ideal conditions. As possible to notice in figure 4.27(b), a larger impact of ρ on $\Delta\bar{I}$ is achieved for higher f_s. Indeed, higher ρ leads to severe reduction of the effective duty cycle of the PWM signal and thus lower mean balancing current, especially for smaller switching period. Moreover, a higher impact is observed in the multi-inductor architecture with respect to the SC one.
An additional aspect to be evaluated is represented by the amount of charge transferred among the cells. As previously discussed for the capacitor-based equalizer, it is more convenient to define this performance parameter by considering the Ah transferred over the switching period. This allows for properly comparing different architectures of equalization circuits that operate at different f_s. Moreover, according to eqs. 4.32 and 4.33, two different contributes can be evaluated, including the Ah transferred by the most charged cell ($Ah_{tr,1s}$) and the Ah provided to the least charged cell ($Ah_{pr,1s}$).
Figure 4.28 shows a sensitivity analysis for both Ah_{tr} and Ah_{pr} with respect to the parameter variations. The worst efficiency conditions have been considered ($V_{B1} = 3$V and $\Delta V = 400$ mV). Both increases

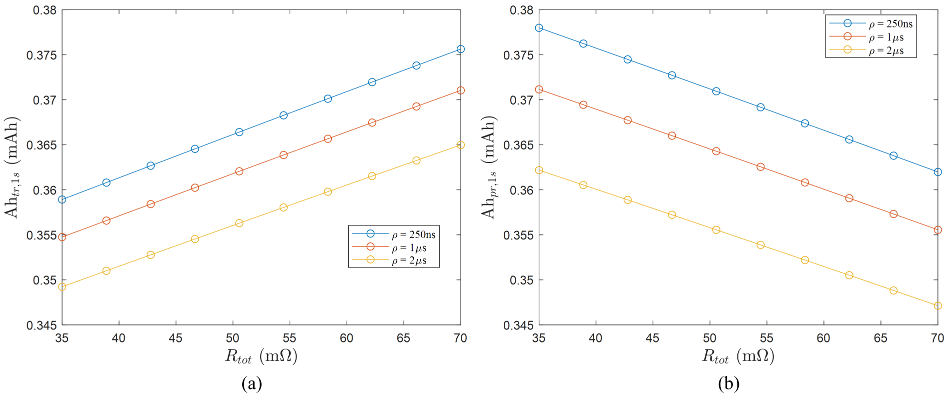

(a) (b)

Figure 4.28: Sensitivity analysis for (a) $Ah_{tr,1s}$ and (b) $Ah_{pr,1s}$ with respect to parameter variations (R_{tot} and ρ).

of R_{tot} and ρ lead to a reduction of $Ah_{pr,1s}$, whereas a different result is observed for $Ah_{tr,1s}$. In particular, an increase of $Ah_{tr,1s}$ occurs for higher R_{tot} and lower ρ.

4.4.4 Equalization Time Evaluation

The model equations have been implemented in MATLAB© with the aim of demonstrating the validity of the design strategy as well as evaluating the performance of the multi-inductor architecture. The design parameters reported in table 4.5 have been considered, including $L = 26.2\mu$H and $f_s = 10$kHz. The functionality of the equalization circuit have been tested for two series-connected cells in the worst efficiency condition, thus $V_{B1} = 3$V and $\Delta V = 400$mV. The experimentally calibrated zero-order ECM of EFEST18650 technology has been adopted for the cells. The control algorithm has been developed in order to stop the equalization process when ΔV is equal or lower than a desired voltage imbalance ΔV_{des} of 5mV.
Figure 4.29 shows the functionality of the multi-inductor architecture in terms of terminal voltage and OCV of the cells, mean balancing currents, SoC and ΔV. Starting from an initial ΔV of 400mV, the equalization process allows for transferring the energy between the most and the least charged cells until reaching ΔV_{des}. As the operating conditions vary, the duty cycle is calculated over time for ensuring the circuit to operate at LCCM. Compared to the SC architecture, higher mean balancing currents can be observed, leading to low equalization

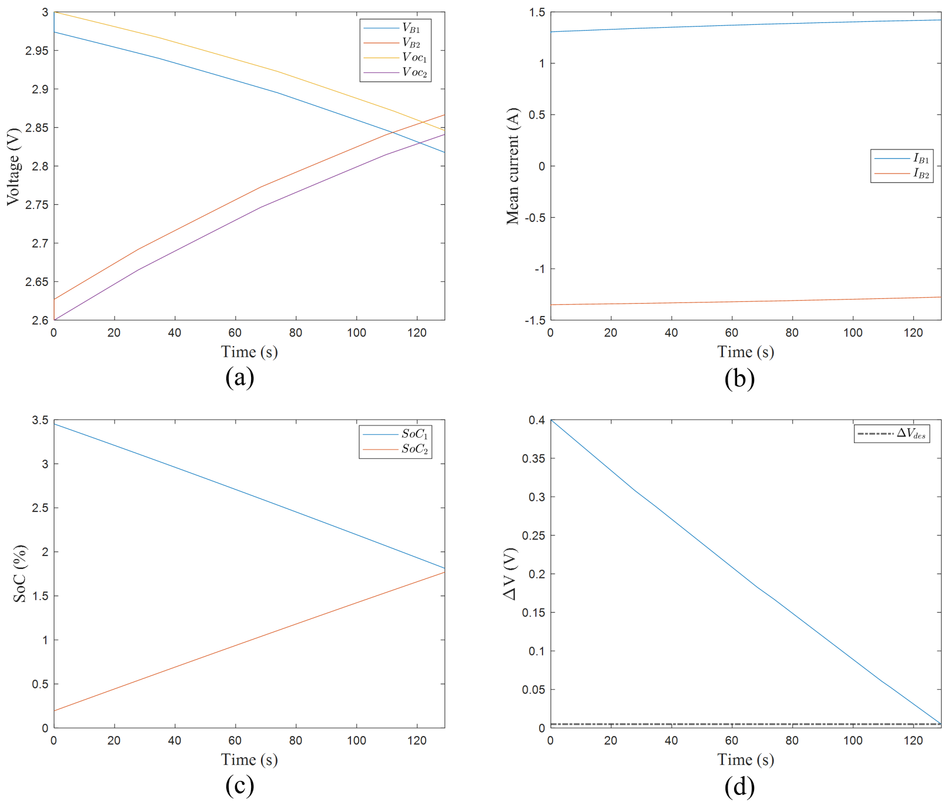

Figure 4.29: Functionality of the multi-inductor architecture in terms of (a) terminal voltage and OCV of the cells, (b) mean balancing currents, (c) SoC and (d) ΔV.

time. This also affect the terminal voltages of the cells since a higher voltage drop occurs. In particular, as shown in figure 4.29(a), the terminal voltage of the least charged cell results higher than the most charged one after a certain amount of time. However, it is important to highlight that this condition occurs only because an ECM is adopted and the balancing algorithm is performed based on the OCV of the cells. In real-world applications, this condition is not encountered since the equalization process is usually operated by evaluating the terminal voltages of the cells. Moreover, a slight increase of the mean balancing currents is observed in figure 4.29(b), which is in line with the results previously shown in the sensitivity analysis.

As possible to notice in figure 4.29(c), the worst efficiency condition corresponds to a very low SoC for the cells.

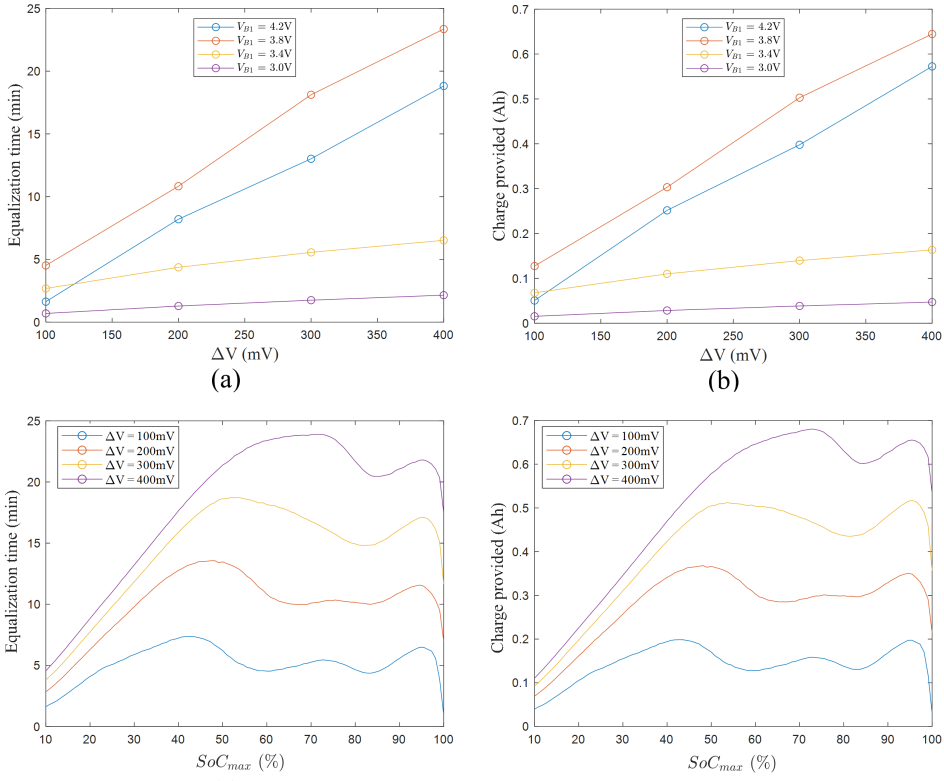

(a) (b)

(c) (d)

Figure 4.30: Variability of the equalization time and the amount of charge transferred among the cells with respect to ΔV and V_{B1} (a,b) and for different SoC_{max} (c,d).

As for the passive and the capacitor-based equalizers, the impact of the operating conditions on the equalization time and the amount of charge transferred among the cells has been evaluated as well. In detail, the charge provided to the least charged cell Ah_{pr} has been considered. Figures 4.30(a) and (b) shows the variability with respect to ΔV and V_{B1}, while figures 4.30(c) and (d) reports the variability for different SoC_{max}, which represents the SoC of the most charged cell. It results a lower equalization time than that achieved with the SC architecture for all the operating conditions due to the higher mean balancing current. Moreover, the equalization time and the charge provided are equally affected by ΔV, V_{B1} and SoC_{max} variations.
In particular, a lower impact of ΔV is observed for $V_{B1} < 3.4V$, mainly related to the shape of the OCV curve in this voltage range. Indeed,

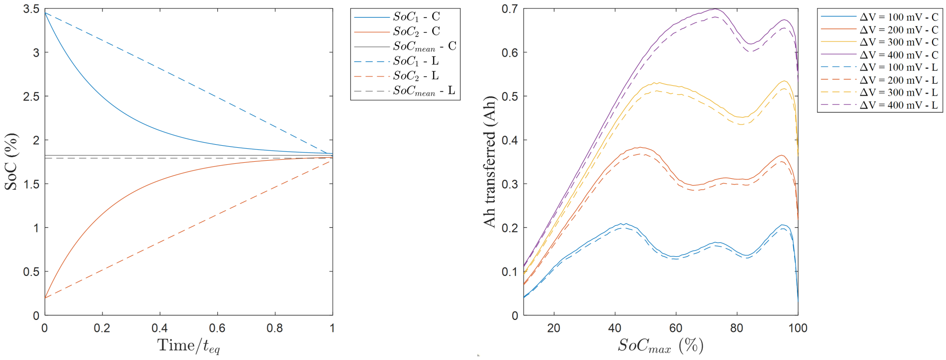

(a) (b)

Figure 4.31: Comparison between the results achieved with both SC and multi-inductor architectures considering the same operating conditions. (a) Different mean SoC values at the end of the equalization process and (b) different amount of energy transferred among the cells.

since it corresponds to the exponential region of the OCV curve, a fast increase or decrease of the cell voltages occurs for a charging or discharging, leading to low equalization time and Ah_{pr}, thus low impact of ΔV.

Likewise for the passive and the capacitor-based equalizers, these results highlight the possibility to develop a proper balancing strategy for minimizing the equalization time and thus increasing the performance of the multi-inductor architecture.

For what concerns the amount of energy transferred among the cells, according to figures 4.20(b,d) and 4.30(b,d), very similar results can be noticed for both SC and multi-inductor architectures. This is reasonable because the same amount of energy needs to be transferred among the cells starting from the same initial conditions.

However, while the mean balancing currents for the cells are equal for the capacitor-based architecture, different amplitudes occur for the most and the least charged cells in the multi-inductor equalizer, leading to a slight variation of the results, as illustrated in figure 4.31. In particular, according to the functionality of both architectures, 4.31(a) shows the SoC of the cells during the equalization process, starting from the same operating conditions. Since the equalization time achieved with the capacitor-based equalizer is larger than that obtained with the inductor-based equalizer, the time axis has been normalized on the basis of the specific equalization time (t_{eq}). In this case, a slight reduction of the mean SoC value at the end of the equal-

ization process is observed for the multi-inductor equalizer.
On the other hand, 4.31(b) reports the differences in the amount of energy transferred among the cells for both architectures with respect to SoC_{max}. The Ah_{pr} has been considered for the multi-inductor equalizer. In this case, a small reduction of the Ah transferred can be noticed for the inductior-based architecture as well.

4.5 Transformer-based Equalizer

When comparing these equalization circuits, the transformer-based architectures result more convenient since they can achieve high equalization speed and good control of the equalization dynamic, at the expenses of increasing complexity and cost of hardware and software. The multi-winding transformer (MWT) for active balancing has the capability of enabling the simultaneous equalization of the cells in a pack. However, the equalization efficiency and speed can be limited by the losses of the power converters as well as not proper design of the transformer. Therefore, more architectures need to be investigated as well as proper design strategies those can reduce cost while increasing performance.
In this section, a novel architecture and control of an active equalization circuit based on MWT is proposed. A self-balancing of the cells can be performed with the proposed topology thanks to the possibility to simultaneously transfer energy among the cells. Therefore, it allows for achieving a cells-to-cells energy transfer technique, which currently has not been discussed in literature. Moreover, a control strategy is proposed for reducing the complexity of the implementation as well as for improving the performance of the equalization process. A model of the MWT is defined with the specific aim of analyzing the performance of the equalization circuit and defining design strategies.

4.5.1 Architecture and Control

The architecture of the proposed active equalization circuit is based on a Multiple Active Bridge (MAB), in which every cell is equipped with a H-bridge converter and then connected to a medium-frequency MWT, as reported in fig. 4.32. This circuit topology has been previously proposed for medium-voltage grid-connected system [110], while it is here exploited for cell equalization purpose since it allows for a modular and flexible cells-to-cells operation, with the potential of in-

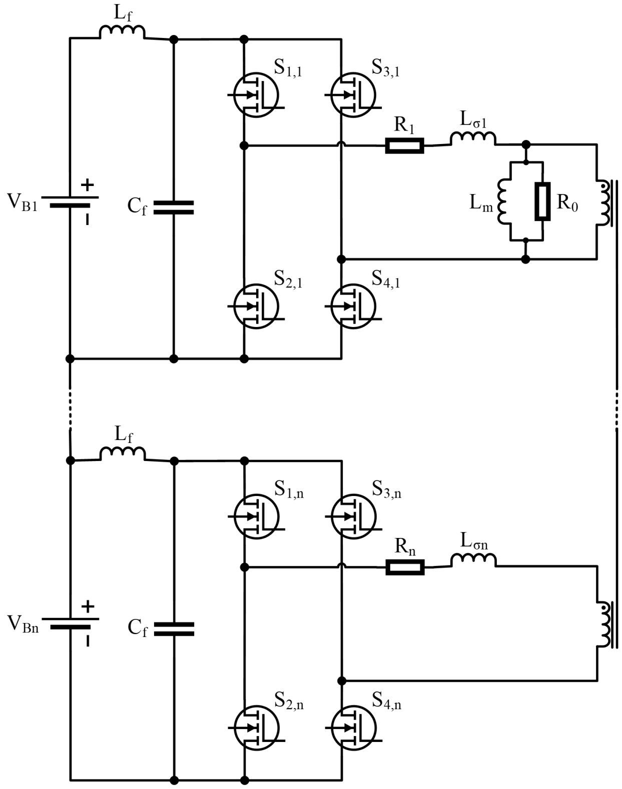

Figure 4.32: Architecture of the proposed transformer-based equalizer.

creasing the equalization speed and efficiency if a proper design strategy is considered.

Assuming a battery pack composed of n series-connected cells, the proposed balancing circuit requires n inductor filters (L_f), n H-bridges with snubber capacitors (C_f) and a transformer with n windings having the same number of turns. Moreover, the model parameters of the MWT are reported in figure 4.32, including the winding resistances (R_k) and leakage inductances $(L_{\sigma k})$ as well as the magnetization inductance (L_m) and the resistance that takes into account for the iron losses (R_0).

Despite the hardware complexity due to the presence of a MWT and the H-bridges, the proposed structure has several advantages, including short and bi-directional energy transfer path between cells, modularity, scalability, and the capability of limiting the balancing currents by means of the transformer leakage inductance. High equalization speed can be achieved by simultaneously transferring energy among a desired number of cells of the battery pack (cells-to-cells balancing). The issue of managing a large number of switches is solved thanks to a proper control algorithm based on a phase-shift modulation technique using a common PWM signal (S). A fixed phase shift (equal to π) is implemented between two legs of each H-bridge, allowing for the generation of a single PWM signal for controlling the n power conversion units. The PWM signal is characterized by a duty cycle equal to 50% and a constant frequency.

The control algorithm requires the measurement of the cell voltages $\{V_{Bk}\ \forall k = 1..n\}$ to verify if the cells are within the desired voltage band ΔV_{band} (e.g. voltage difference between the highest and lowest cell voltages) or to apply the balancing action. In detail, if the cells are unbalanced, the PWM signal S is provided to all the drivers of the n H-bridges. Therefore, depending on the cell voltage levels, a current flow will be established from the cells with higher voltages to the ones with lower voltages.

In principle, the control of the rectification stage could be disabled taking advantages of the freewheeling diodes. However, to reduce the losses due to the diode forward voltages and to minimize the voltage drop, the rectification stage has been controlled as a synchronous rectifier through the same PWM signal S. The balancing action is stopped when the cell voltages are all contained in the desired ΔV_{band}.

It is important to mention that this balancing architecture can operate even when the battery pack is in charge or discharge mode. This also allows for minimizing the equalization time required in idle state, when neither load nor charger is connected to the battery pack. Moreover, it does not require a very accurate estimation of the SoC, since the equalization of the cells is automatically and dynamically guaranteed by the voltage-controlled energy transfer across the transformer and by the unique control signal S. However, the selection and design of both the electronic components and the transformer have a great impact on the accuracy of the voltage balancing as well as on the equalization efficiency.

4.5.2 Model of the Multi-winding Transformer

The design of the MWT results fundamental for increasing the performance of the equalization process of the proposed BMS architecture. Indeed, high balancing current, thus high equalization speed, can be achieved by properly sizing the transformer parameters, such as L_m and $L_{\sigma k}$. The generalized model of a n-winding transformer can be represented by the following system of equations:

$$\begin{aligned} v_k(t) = e(t) + R_k{\cdot}i_k(t) + L_{\sigma k}\frac{di_k(t)}{dt} \\ + \sum_{\substack{j=1 \\ j\neq k}}^{n} M_{k,j}\frac{di_j(t)}{dt} \quad \forall k = 1..n \end{aligned} \tag{4.41}$$

where $v_k(t)$ are the winding voltages, $i_k(t)$ are the winding currents, $e(t)$ is the electromotive force (EMF) and $M_{k,j}$ are the mutual leakage inductances. In addition, the following equations need to be considered for achieving the overall MTW model:

$$e(t) = L_m\frac{di_m(t)}{dt} \tag{4.42}$$

$$i_m(t) + i_0(t) = \sum_{k=1}^{n}\frac{N_k}{N_1}i_k(t) \tag{4.43}$$

$$i_0(t) = \frac{e(t)}{R_0} \tag{4.44}$$

where i_m is the magnetization current, i_0 is the current related to the iron losses and N_k are the winding turns.

The system of equations include $[n(n+1)+2]/2$ unknown variables and $n+3$ equations, resulting an under-determined system. Several assumptions can be made with the aim of achieving a reduced-order system that allows for defining physic-based relations between the transformer design parameters (L_m, $L_{\sigma k}$):

1. The iron losses are neglected:

$$R_0 \rightarrow \infty$$

2. The winding resistances are neglected:

$$R_k \rightarrow 0 \quad \forall k = 1..n$$

3. There are no losses in the inductive coupling among the windings due to mutual leakage inductances:

$$M_{k,j} \to 0 \quad \forall k = 1..n, \forall j \neq k$$

4. All the self-leakage inductances are typically equal due to the symmetrical structure of the MWT:

$$L_{\sigma k} = L_{\sigma} \quad \forall k = 1..n$$

5. In the specific application the turn ratio is unitary:

$$\frac{N_k}{N_1} = 1 \quad \forall k = 1..n$$

6. All the winding voltages are in phase because of the control strategy adopted for the proposed BMS architecture, illustrated in section 4.5.1.

7. The model equations are evaluated in steady-state condition using a phasors representation $\bar{X}^{(h)}$, where X is a generic variable and h is the harmonic order. This allows for taking into account the harmonic contribution introduced by the voltages of the H-bridge converters.

Note that in the specific application of the cell equalization circuit, these assumptions result reasonable because of the low values of voltage and current for each winding. In this way, the reduced-order system of equations can be achieved:

$$\begin{cases} \bar{V}_k^{(h)} = \bar{E}^{(h)} + jh\omega L_{\sigma} \bar{I}_k^{(h)} \quad \forall k = 1..n \\ \bar{E}^{(h)} = jh\omega L_m \bar{I}_m^{(h)} \\ \bar{I}_m^{(h)} = \sum_{k=1}^{n} \bar{I}_k^{(h)} \end{cases} \tag{4.45}$$

Therefore, a compact expression can be yield for the EMF:

$$\bar{E}^{(h)} = \frac{1}{n} \sum_{k=1}^{n} \bar{V}_k^{(h)} \left(\frac{1}{1 + \frac{L_{\sigma}}{nL_m}} \right) = \gamma \bar{V}_{mean}^{(h)} \tag{4.46}$$

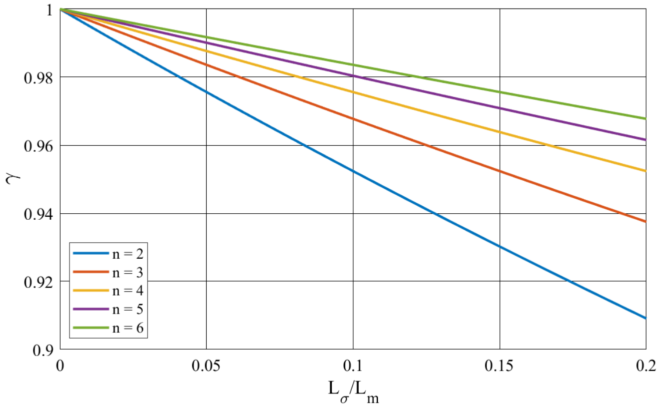

Figure 4.33: The factor γ with respect to the ratio L_σ/L_m and the number of windings n.

In detail, the EMF results proportional to the mean value of the winding voltage ($\bar{V}_{mean}^{(h)}$) and a factor γ which depends on L_σ/L_m. γ is equal to 1 in case of ideal transformer, while it represents a quality factor for a real transformer. Fig. 4.33 shows the impact of the ratio L_σ/L_m and the number of windings n on the γ factor. In most of the traditional grid-connected applications, a high γ value is preferred, since L_σ is directly correlated to the transformer efficiency. As matter of fact, for the specific application of the battery equalizer, $\gamma = 1$ would correspond to the impossibility of transferring energy among the cells. Hence, L_σ needs to be properly sized considering the allowed voltage imbalance among the cells while minimizing the transformer losses.

4.5.3 Design of the Multiple Active Bridge

In this section, relevant aspects related to the design of the MAB are illustrated. This primarily includes the sizing of the main parameters of the MWT (L_σ,L_m) with reference to specific performance metrics, such as equalization speed. It is clear that the equalization time can be reduced by increasing the balancing current for the specified voltage imbalance among the cells. However, the condition that generates the maximum current among the cells will correspond to the fastest equalization, while representing the worst case scenario for the equalization circuit components, including switches and transformer. Therefore, the proposed sizing approach of the MWT aims at defining the L_σ and L_m those enable the maximum current condition. Eq. 4.45 and the assumptions reported in section 4.5.2 allow for calculating the module of each winding current:

$$|\bar{I}_k^{(h)}| = \frac{|V_k^{(h)} - E^{(h)}|}{h\omega L_\sigma} = \frac{\delta V_k^{(h)}}{h\omega L_\sigma} \quad \forall k = 1..n \tag{4.47}$$

where $\delta V_k^{(h)}$ represents the voltage difference between the k^{th} winding and the EMF. The worst case scenario can be related to the operating conditions in which the windings of the transformer are subject to the maximum $\delta V_k^{(h)}$. Therefore, two limit case scenarios can be identified and investigated with the aim of formally defining the worst case scenario:

$$Case\ (a): \begin{cases} V_1^{(h)} = V_M^{(h)} \\ V_k^{(h)} = V_m^{(h)} & \forall k = 2..n \\ \delta V_a^{(h)} = V_M^{(h)} - E^{(h)} \end{cases} \tag{4.48}$$

$$Case\ (b): \begin{cases} V_1^{(h)} = V_m^{(h)} \\ V_k^{(h)} = V_M^{(h)} & \forall k = 2..n \\ \delta V_b^{(h)} = E^{(h)} - V_m^{(h)} \end{cases} \tag{4.49}$$

where the subscript M and m represent the winding connected to the cells with the maximum and minimum voltages, respectively. By combining eq.s 4.46 and 4.47, $\delta V_a^{(h)}$ and $\delta V_b^{(h)}$ can be yield as follows:

$$\delta V_a^{(h)} = V_M^{(h)} - \left[\frac{V_M^{(h)} + (n-1)V_m^{(h)}}{n}\right] \cdot \gamma \tag{4.50}$$

$$\delta V_b^{(h)} = \left[\frac{V_m^{(h)} + (n-1)V_M^{(h)}}{n}\right] \cdot \gamma - V_m^{(h)} \tag{4.51}$$

In this way, the worst condition can be defined by evaluating the difference between $\delta V_a^{(h)}$ and $\delta V_b^{(h)}$:

$$\delta V_a^{(h)} - \delta V_b^{(h)} = \left[V_M^{(h)} + V_m^{(h)}\right] \cdot (1 - \gamma) > 1 \tag{4.52}$$

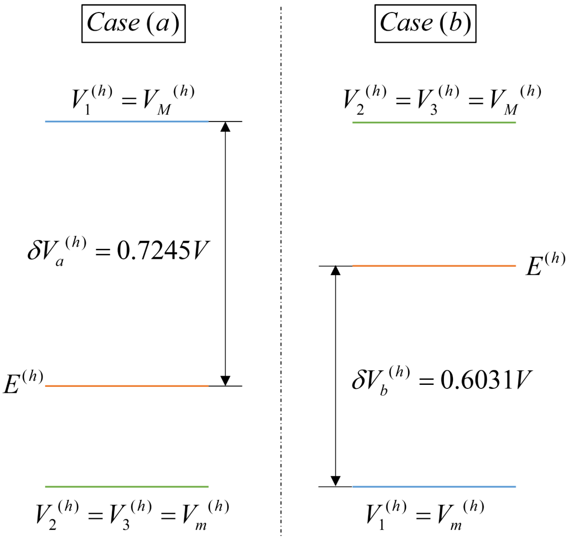

Figure 4.34: Example of the two limit case scenarios corresponding to the maximum current operation for the MWT. In both cases, $V_M^{(h)} = 4V$, $V_m^{(h)} = 3V$, $n = 3$, $L_\sigma = 180nH$ and $L_m = 3.4\mu H$ are considered.

Since $0 < \gamma < 1$, $\delta V_a^{(h)}$ is always greater than $\delta V_b^{(h)}$, resulting case (a) as the worst condition. Figure 4.34 shows a numerical example of case (a) and case (b) scenarios considering $V_M^{(h)} = 4V$ and $V_m^{(h)} = 3V$, which validates the proposed analysis. Therefore, this operating condition is adopted for the design of the MWT.

In particular, in the worst case scenario, the system of equations 4.45 results:

$$\begin{cases} \bar{V}_1^{(h)} = \bar{V}_M^{(h)} = \bar{E}^{(h)} + j\omega h L_\sigma \bar{I}_M^{(h)} \\ \bar{V}_k^{(h)} = \bar{V}_m^{(h)} = \bar{E}^{(h)} + j\omega h L_\sigma \bar{I}_m^{(h)} \qquad \forall k = 2..n \\ \bar{E}^{(h)} = j\omega h L_m \left[\bar{I}_M^{(h)} + (n-1)\bar{I}_m^{(h)} \right] \end{cases} \tag{4.53}$$

where $\bar{I}_M^{(h)}$ and $\bar{I}_m^{(h)}$ represent the winding currents related to the windings with the highest and the lowest voltages, respectively. This system of equations includes three equations and four unknown variables (L_σ, L_m, $\bar{E}^{(h)}$, $\bar{I}_m^{(h)}$), resulting under-determined.

Hence, two different design solutions can be adopted:

1. The first one is based on fixing the magnetization inductance L_m and calculating L_σ as a result.
2. The second solution is based on fixing $\bar{I}_m^{(h)}$.

In the following analysis, the second design solution has been considered. Hence, the sizing of L_σ and L_m can be performed by evaluating the overall RMS value of both winding voltage and current in order to take into account for the harmonic contribution. In detail, since each cell is connected to the MWT by means of an H-bridge converter, the RMS value of each winding voltage can be obtained as follows:

$$\begin{cases} V_k^{(h)} = \dfrac{1}{h} V_k^{(1)} = \dfrac{1}{h} \dfrac{4V_{Bk}}{\pi\sqrt{2}} \\ \\ V_{RMS,k} = \sqrt{\sum_{h=1}^{\infty} \left[V_k^{(h)}\right]^2} = V_{Bk} \end{cases} \quad \forall k = 1..n \tag{4.54}$$

As results, the overall RMS value of each winding voltage $V_{RMS,k}$ is equal to the voltage of the cell V_{Bk} connected to that specific winding. Likewise, the RMS value of the winding current can be achieved as follows:

$$\begin{cases} I_k^{(h)} = \dfrac{1}{h^2} I_k^{(1)} \\ \\ I_{RMS,k} = \sqrt{\sum_{h=1}^{\infty} \left[I_k^{(h)}\right]^2} = \beta_h I_k^{(1)} \quad \forall k = 1..n \\ \\ \beta_h = \sqrt{\sum_{h=1}^{\infty} \dfrac{1}{h^4}} \end{cases} \tag{4.55}$$

Therefore, considering the RMS values, the size of both L_m and L_σ can be yield from the system of equations 4.53:

$$L_\sigma = \frac{4}{\pi\sqrt{2}} \frac{\beta_h (V_{B,max} - V_{B,min})}{\omega (I_{RMS,max} + I_{RMS,min})} \tag{4.56}$$

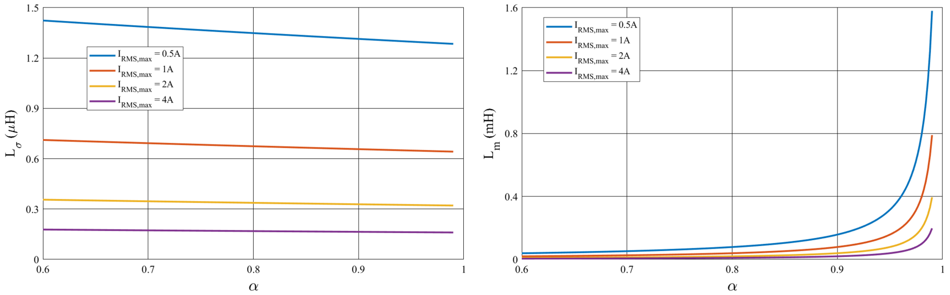

(a) (b)

Figure 4.35: Sensitivity analysis for L_m (a) and L_σ (b) with respect to α and $I_{RMS,max}$ by fixing $V_{B,max} = 4.2V$, $V_{B,min} = 3.8V$, $frequency = 80kHz$, $h = 1, .., 11$ and $n = 4$.

$$L_m = \frac{4\beta_h}{\pi\sqrt{2}\omega}\left[\frac{V_{B,max}}{I_{RMS,max}(1-\alpha)} - \frac{(n-1)(V_{B,max}-V_{B,min})}{I_{RMS,max}(1-\alpha)[(n-1)+\alpha]}\right] \tag{4.57}$$

with

$$\alpha = \frac{(n-1)I_{RMS,min}}{I_{RMS,max}} \tag{4.58}$$

where α represents a performance parameter of the MWT, while $V_{B,max}$ and $V_{B,min}$ are the maximum and the minimum cell voltages, respectively. Figure 4.35 shows a sensitivity analysis for L_m and L_σ with respect to α and $I_{RMS,max}$ by fixing $V_{B,max}$, $V_{B,min}$, ω, h and n. In particular, the maximum cell voltage ($V_{B,max}$ = 4.2V) and the maximum allowable voltage imbalance among the cells ($\Delta V = V_{B,max} - V_{B,min}$ = 400 mV) have been set.
As result, specified values of L_σ and L_m need to be considered for achieving the desired performance in terms of α and $I_{RMS,max}$. In detail, lower values allow for increasing the balancing current and thus reducing the equalization time. Moreover, for a specified $I_{RMS,max}$, a further reduction of L_σ as well as a strong increase of the L_m need to be considered for improving the performance of the equalization circuit ($\alpha \rightarrow 1$).

Chapter 5

Prototyping of Equalization Circuits

[Original contribute]

Besides the development of design strategies for passive and active equalization circuits, real prototypes have been sized and implemented as well. In particular, a modular architecture for passive equalizer and the novel active equalizer have been prototyped with the aim of validating their performance in real-world environments. These prototypes also allow for managing high-voltage battery packs or hybrid systems, which are composed by different technologies of batteries (second life applications). Automotive applications have been considered as reference for the development of the BMSs due to the high performance required in terms of charging/discharging currents, size, cost, reliability and modularity of the architecture. Moreover, a detailed comparison between the prototypes developed has been carried out in order to highlight their main features in different operating conditions, including charging, discharging and idle state.

5.1 Prototype of Passive Equalizer

This section deals with the implementation of a passive equalizer for high-power battery packs, designed for meeting the restricted specifications of automotive applications. In detail, the battery pack of a high-performance 50HP electric kart has been considered. A modular architecture has been developed for the passive equalizer, including

one BMS master and several BMS slave units depending on the number of cells or modules that compose the battery pack. A proper control algorithm has been also proposed, which allows for managing the passive balancing in all the operating conditions while providing safety and low equalization time.
Moreover, a thermal model of the BMS slave unit has been calibrated for taking into account the heat dissipation issues due to high balancing currents. Then, on the basis of the temperatures reached by the BMS slave units, a further improvement of the balancing algorithm has been proposed, which allows for defining the optimal number of cells to be balanced for minimizing the equalization time of the whole battery pack. Numerical and experimental analyses have been carried out for validating the performance of the proposed modular architecture for passive equalizer.

5.1.1 Design of the Battery Pack

The battery pack of a 50HP electric kart, FIA regulations compliant, has been designed and assembled. It is composed of a series connection of 40-Ah high-power NMC cells, model SLPB100216216H. These cells by KOKAM are suitable for automotive applications due to their high charge/discharge C-rates, long cycle and calendar life, high gravimetric and volumetric power density as well as low impedance and heat generation for improved safety. Indeed, the pouch shape of these NMC cells allows for a more efficient thermal transfer than prismatic or cylindrical types due to their very large surface area. This also enables the ability to operate in extreme temperatures without safety issues. In addition, these cells are characterized by high efficiency and good energy density. Table 5.1 summarizes the main specifications of the 40-Ah NMC cells adopted.
In detail, the overall battery pack is composed by 24 series-connected cells, which are distributed in four modules. It is important to highlight that the weights have to be properly distributed on the chassis of the electric kart in order to ensure stability and optimal driving performance. Therefore, the battery pack has been divided in two equal sections, each one composed by two modules and inserted in an aluminum case opportunely sized for providing compactness and safety during operations.
Figure 5.1 shows the design of one section of the overall battery pack drawn by means of a 3D designer software. Each module consists of six series-connected cells directly packaged in a single unit and coated

Parameter		Specification
Nominal Capacity		40 Ah
Energy Density		159 Wh/kg
Power Density		1260 W/kg
Weight		940 g
Voltage	Nominal	3.7 V
	Lower Limit	2.7 V
	Upper Limit	4.2 V
Current	Continuous Charging	120 A (@3C)
	Continuous Discharging	320 A (@8C)
	Peak Discharging (≤10s)	480 A (@12C)
Cycle Life at 90% DoD	@1C - 25°C	≤6000
Temperature	Charging	0°C - 45°C
	Discharging	-20°C - 55°C

Table 5.1: Main specifications of the 40-Ah NMC cells adopted.

with a green material casing that ensures flexibility and robustness. All the positive or the negative current collectors of the cells are welding together, leading to unique positive (red) and negative (black) terminals for each module. Moreover, two connectors for cell voltage and temperature measurements are available. Each section of the battery pack also includes a high-current fuse, the positive/negative main contactor and the master-slave BMS configuration. In detail, since the BMS slave units have been designed for meeting the requirements of a single module, two units need to be implemented in each battery pack section. On the other hand, only one BMS master is required for managing and communicating with all the four BMS slave units of the battery pack. Therefore, depending on the design strategies, it can be included in one of the battery pack section or located outside in a specific part of the electric kart chassis. Furthermore, two connectors are needed for separating the communication wiring and the power cables, for which a MSD is considered. In this way, the external short circuit of the modules can be avoided when the battery pack is disconnected. Both the aluminum case and the connectors have been designed or selected in order to achieve a battery pack compliant with the safety standard IP67.

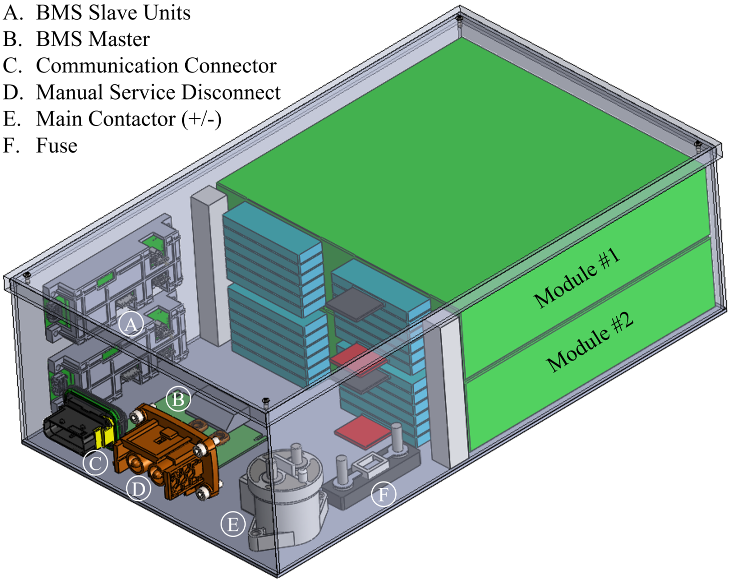

Figure 5.1: 3D design of one section of the overall battery pack.

5.1.2 Modular Architecture

According to the design of the battery pack previously illustrated, the passive equalization circuit has been designed for a single module of six series-connected 40-Ah cells. Figure 5.2 shows the prototype developed as BMS slave. It consists of two boards optimally integrated with the aim of minimizing the size of the BMS and distributing the heat dissipation over a scalar structure.
The bottom one is defined as power board, where all the dissipative components are located, including resistors and switches. Indeed, despite different commercially-available BMS ICs provides internal passive balancing (section 3.4), external power resistors and switches have been adopted for the proposed passive equalizer with the aim of achieving high equalization speed. In particular, balancing resistors of 3.3Ω have been selected, which ensure a maximum balancing current higher than 1A. Considering the high capacity of the cells used, this balancing current amplitude represents a good trade-off between the equalization speed and the heat dissipation.
Moreover, an insulated metal substrate (IMS) has been adopted for the bottom layer of the power board in order to further reduce the thermal issues due to the passive balancing of the cells. The IMS consists of an aluminum baseplate covered by a thin layer of dielectric and a layer

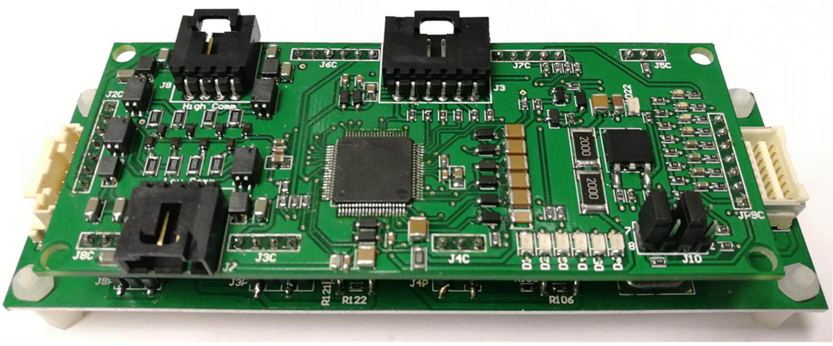

Figure 5.2: Prototype of the proposed passive equalizer (BMS slave) for six series-connected cells.

of copper. Compared to a classical PCB, this solution provides an effective cooling of the surface-mount components located on the top layer of the power board. In addition, a properly sized heatsink can be attached to the aluminum baseplate for improving the heat transfer. Two temperature sensors have been also distributed on the top layer of the power board in order to evaluate the temperature distribution.

The control board on the top is based on the BQ76PL455A-Q1 BMS IC by Texas Instruments©, which is an integrated battery monitoring and protection device, designed for high-reliability automotive applications. It allows for acquiring all the cell voltages and temperatures coming from each module as well as performing the balancing action by providing control signals for the switches. In particular, despite the proposed passive equalizer has been designed only for six cells, this BMS IC is able to manage up to 16 series-connected cells. Moreover, the management of high-voltage battery packs can be achieved by means of just one microcontroller thanks to the possibility to control a maximum of 16 BQ76PL455-Q1 BMS ICs in daisy-chain, leading to an overall nominal voltage about 1kV. An integrated high-speed, differential, capacitor-isolated Universal Asynchronous Receiver/Transmitter (UART) interface allows the microcontroller for communicating with all the BMS slave units.

In addition, the BQ76PL455A-Q1 BMS IC monitors and detects several different fault conditions, including overvoltage, undervoltage, overtemperature and communication faults. It also provides six GPIO ports and eight analog ADC inputs, which are adopted for temperature measurements. Among the different BMS ICs commercially available on the market, the BQ76PL455A-Q1 one has been selected due to the

possibility to potentially perform active balancing and thus enable future developments.
According to the battery pack of the 50HP electric kart, four BMS slave units have been connected in daisy-chain in order to meet the voltage requirement of 88.8V. Figure 5.3 shows the block diagram of the proposed modular BMS architecture for the overall battery pack. The microcontroller unit, known as BMS master, receives the data from all the BMS slave units and enables the balancing process on the basis of the voltage imbalance intra-module and outer-module. The data includes the cell voltages ($V_k \ \forall k = 0..6$) and temperatures ($T_k \ \forall k = 1..6$) as well as two temperature measurements for each BMS slaves (T_{pb1}, T_{pb2}). This is necessary to control the maximum temperature reached by the power boards and thus properly enable/disable the passive balancing. Moreover, a safety signal is available for disabling the equalization process or the charging/discharging of the battery pack in case of any type of faults, which provides a further improvement of the reliability of the overall BMS architecture.

5.1.3 Control Algorithm

Since the BQ76PL455-Q1 BMS IC provides only the elementary balancing functions, the control algorithm needs to be developed and implemented in an external microcontroller (BMS master). In this section, an optimized algorithm is proposed, which allows for correctly managing either charging/discharging processes or faults that can occur during normal operation. In particular, system faults, device faults and communication faults are monitored with the aim to achieve a complete supervision of the overall BMS architecture.
Moreover, considering the reduction of the equalization time during the charging process as an important target, the proposed control algorithm provides a proper management of the balancing process of the cells in all the operating conditions, including charging, discharging and idle state, when neither charger nor load is connected to the battery pack. In this way, the cell voltage imbalance can be reduced before the charging process starts with advantage in terms of equalization time.
The flowchart of the proposed control algorithm is reported in figure 5.4. Firstly, the battery pack parameters, such as overvoltage and undervoltage thresholds, are set and both charger and load connections with the battery pack are enabled in order to ensure the desired charging or discharging.

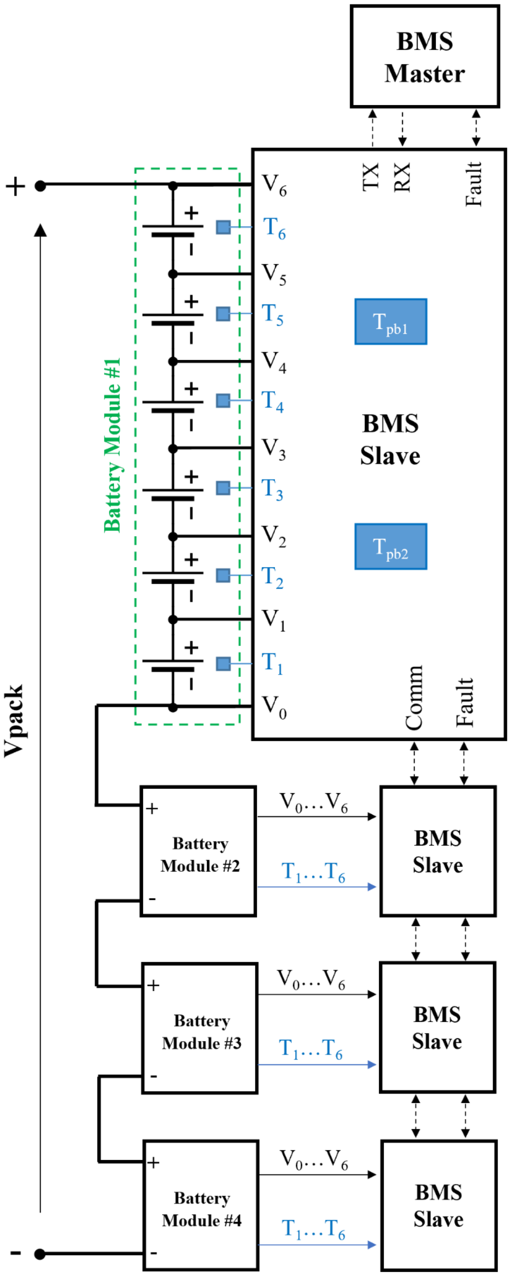

Figure 5.3: Block diagram of the proposed modular BMS architecture for the battery pack of the 50HP electric kart.

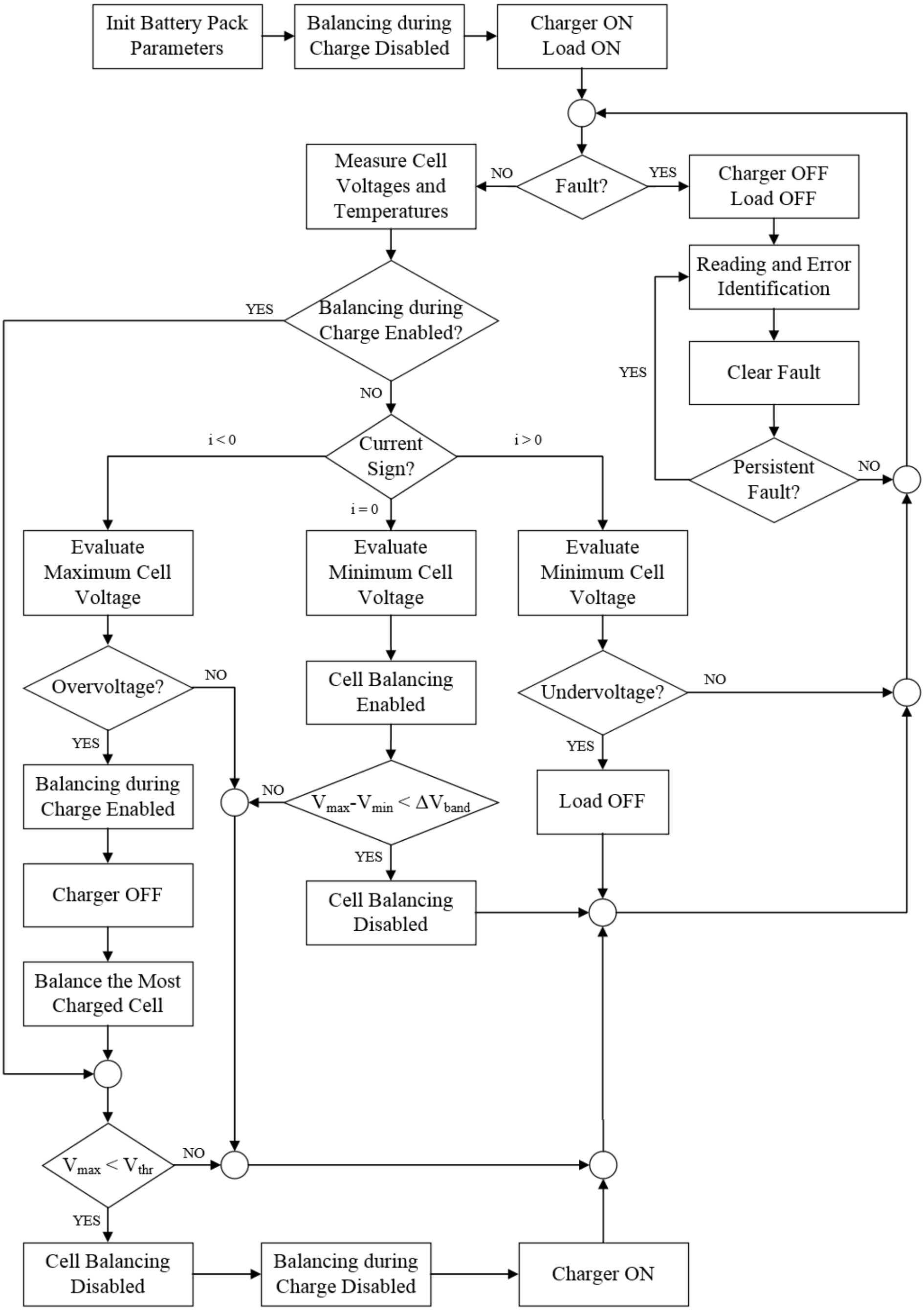

Figure 5.4: Flowchart of the proposed control algorithm for the BMS.

Then, the presence of fault conditions is verified. In case of fault, both charger and load are disconnected from the battery pack and the fault type is identified. A clear command is used for verifying if the fault condition still occurs. Therefore, this fault loop remains active until no fault condition is detected. On the other hand, in case of no fault, the cell voltages and temperatures as well as the battery pack current are acquired.

The proposed balancing algorithm can be divided in three different cases depending on the sign of the current.

In *discharging*, when the load is connected to the battery pack and a negative current flows ($i < 0$), the minimum cell voltage is evaluated. If a lower value than the desired undervoltage threshold occurs, the load is disconnected from the battery pack and thus the discharging process is disabled. After this condition, since the battery pack results fully discharged, a charging process needs to be operated before starting with an other discharging process. In particular, two main reference parameters can be considered for defining when the discharging process can be enabled again, including a specific charging time or a certain amount of Ah stored in the battery pack. It is important to highlight that no balancing algorithm is operated in discharging due to the dissipative nature of the passive equalizer.

In *idle state*, when no current flows occur ($i = 0$), the cell balancing is performed with the aim of reducing the voltage imbalance among the cells up to a desired voltage band (V_{band}). In particular, considering the maximum (V_{max}) and the minimum (V_{min}) cell voltages in the battery pack, the balancing process is enabled for all the cells with voltages greater than $V_{min} + V_{band}$. The cell balancing results terminated and thus disabled when all the cell voltages are within the desired V_{band}.

In *charging*, when the charger is connected to the battery pack and a positive current flows ($i > 0$), the maximum cell voltage is evaluated. If a higher value than the desired overvoltage threshold occurs, the charger is disconnected from the battery pack and thus the charging process is disabled. Therefore, the passive balancing process is operated only for the most charged cell until V_{max} reaches a specific voltage threshold (V_{thr}). In this case, V_{thr} needs to properly define depending on the balancing current and the related voltage drop due to the internal resistance. Indeed, if the difference between V_{max} and V_{thr} is lower than the voltage drop, undesired repetitive enabling and disabling of the charging process occur. When the most charged cell is discharged up to V_{thr}, the passive balancing for the most charged cell is disabled and the charging process of the overall battery pack starts again. It is important to highlight that only one cell is discharged, whereas the remaining cells maintain their charge during the time interval in which the balancing process is performed. In this way, it is possible to achieve a cell balancing even during the charging processes.

5.1.4 Thermal Model of BMS Slave

According to the prototype of the passive equalizer shown in figure 5.2, a thermal model of the BMS slave unit has been calibrated for improving the balancing algorithm taking into account the maximum temperature allowable for the power boards.

In detail, only the IMS of the power board has been considered as heatsink of the BMS slave unit. Indeed, considering the reduced space available in the battery pack of the electric kart (figure 5.1), any additional heatsink cannot be added in the design due to volume and weight constraints. Moreover, despite the aluminum cases can be certainly used as heatsink, it is preferable to calibrate the thermal model of the BMS slave unit in the worst condition, thus when no additional heatsinks are adopted.

Considering only convection as heat transmission, the thermal behavior of the BMS slave unit can be modeled by means of the following differential equation:

$$C\frac{df(\theta(t))}{dt} = P_{loss} - A\theta \tag{5.1}$$

where $\theta(t)$ is the overtemperature of the IMS with respect of the ambient one, C is the thermal capacity of IMS, P_{loss} represents the power losses of the equalization process and A is a constant coefficient, which can be expressed as a function of the convection factor and the surface of IMS.

An experimental characterization has been performed in order to determine the parameters of the thermal model. In detail, figure 5.5 shows the $\theta(t)$ of IMS during the warming and the cooling transients. The power losses has been set equal to 5.3W, which corresponds to the discharging of one fully charged cell ($V = 4.2V$) on the balancing resistor of 3.3Ω. Table 5.2 reports the thermal model parameters achieved from the experimental results.

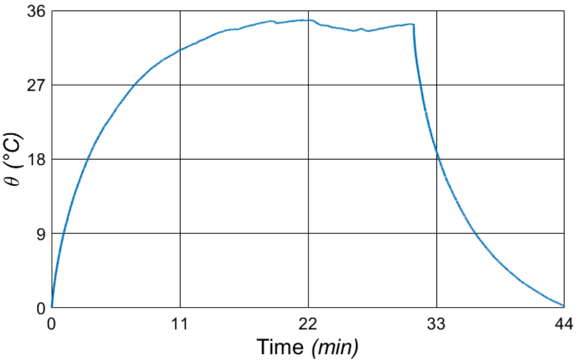

Figure 5.5: Warming and cooling transients for the IMS of the power board considering a balancing power of one fully charged cell.

Parameter	**Value**
C	22.9 J/°C
A	0.14 W/°C

Table 5.2: Thermal model parameters for the BMS slave unit.

5.1.5 Thermal Management Optimization

Besides the passive equalization of the cells, the control algorithm has been further improved taking into account the thermal management of each BMS slave unit. Hence, an optimized control algorithm has been proposed, which allows for correctly enabling and disabling the passive balancing of each battery module depending on the maximum temperature reached by the power board of the BMS slave unit connected to that battery module.

In detail, considering the overtemperature with respect to the environmental temperature, two threshold values are defined, including the maximum allowable (θ_{max}) and the minimum (θ_{min}) overtemperatures for the power board of the BMS slave units. The balancing process is operated in order to maintain the overtemperature for the power board of all the BMS slave units lower than θ_{max}. If the overtemperature of the power board becomes higher than θ_{max}, the equalization process is stopped for the related BMS slave unit until the cooling transient reaches θ_{min}. Therefore, the overtemperature ranges between θ_{max} and θ_{min}, as illustrated in figure 5.6. In particular, figure 5.6(b) shows the comparison among the thermal transients achieved with differ-

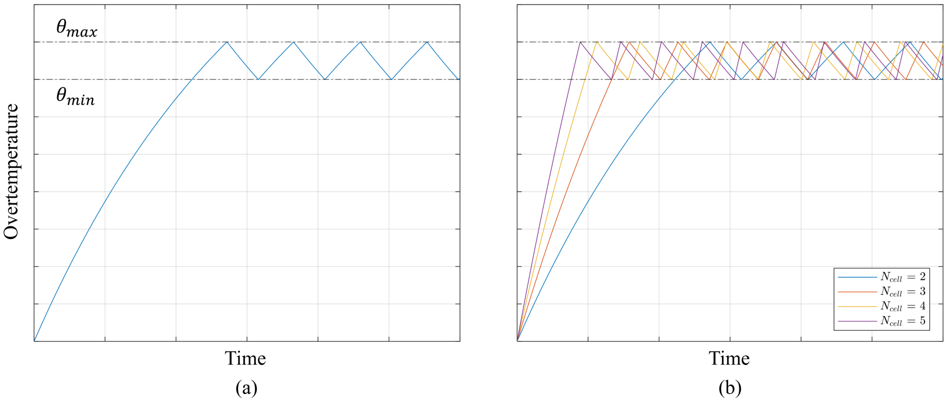

Figure 5.6: (a) Overtemperature thresholds for $N_{cell} = 2$; (b) comparison among the thermal transients achieved with different N_{cell} and the same overtemperature thresholds.

ent values for the maximum number of cells in balance at the same time (N_{cell}) by considering the same overtemperature thresholds. This comparison does not include the case with $N_{cell} = 1$ since θ_{max} is not reached for this condition due to the lower energy dissipated. It is important to point out that a larger N_{cell} causes higher heat dissipations and thus faster warming transients. This leads to higher number of interruptions for the balancing process depending on the θ_{max} and θ_{min} considered. Hence, it results fundamental to identify the optimal value of the N_{cell}, defined as Ns_{cell}, that allows for minimizing the equalization time for specific θ_{max} and θ_{min} values.

The proposed control algorithm for optimizing both the thermal management and the balancing process of the passive equalizer can operate in two different configurations. The first one, named as single state configuration, is based on fixing an unique and equal N_{cell} for all the BMS slave units during the entire balancing process. In this configuration, the Ns_{cell} can be determined by means of numerical analysis thanks to the adoption of the calibrated thermal model of the BMS slave unit.

The second configuration is based on a proposed adaptive control, which dynamically changes N_{cell} for further minimizing the equalization time achieved with Ns_{cell} under the same thermal constraints. The idea is to find a combination of N_{cell} for each battery module that allows for maximizing the energy dissipated with respect to that obtained in the optimal single state configuration (Ns_{cell}).

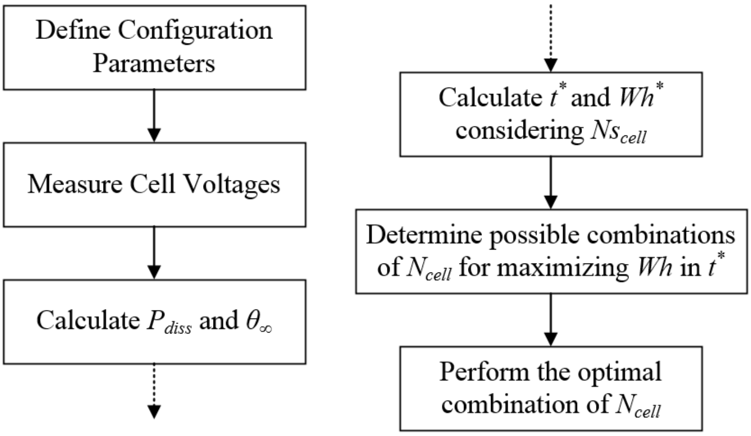

Figure 5.7: Block diagram of the proposed adaptive algorithm.

The block diagram of the proposed adaptive algorithm is illustrated in Figure 5.7. Firstly, the configuration parameters are set, including the overvoltage and undervoltage thresholds, θ_{max} and θ_{min} values. Then, after measuring all the cell voltages, a maximum to minimum sorting of these values is performed for each battery module in order to correctly select the cells to be balanced for meeting the requirement of the desired maximum N_{cell}. Considering a fixed value of the balancing resistor (3Ω) for each cell, the power dissipation P_{diss} and thus the maximum overtemperature reached by the power boards without any control of the temperature (θ_∞) can be calculated by means of the thermal model of the BMS slave unit. Therefore, both P_{diss} and θ_∞ are related to N_{cell}.

Considering the Ns_{cell} for a single state configuration and fixing the θ_{max} and θ_{min} values, it is possible to analytically predict the time t^* needed for reaching θ_{max} as follows:

$$\theta_{max} = (\theta_{min} - \theta_\infty)e^{(-\frac{t^*}{\tau})} + \theta_\infty \tag{5.2}$$

where τ is the time constant representative of the thermal behavior of the BMS slave unit. In this way, the energy dissipated Wh^* during the warming transient considering the Ns_{cell} can be calculated by means of time integration. Then, the research of an optimal combination of N_{cell} starts, which allows for dissipating an amount of energy Wh greater than Wh^* during t^*. In detail, a combination of two possible configuration of N_{cell} is considered during t^*. Therefore, starting with the initial configuration of N_{cell}, the following system of equations

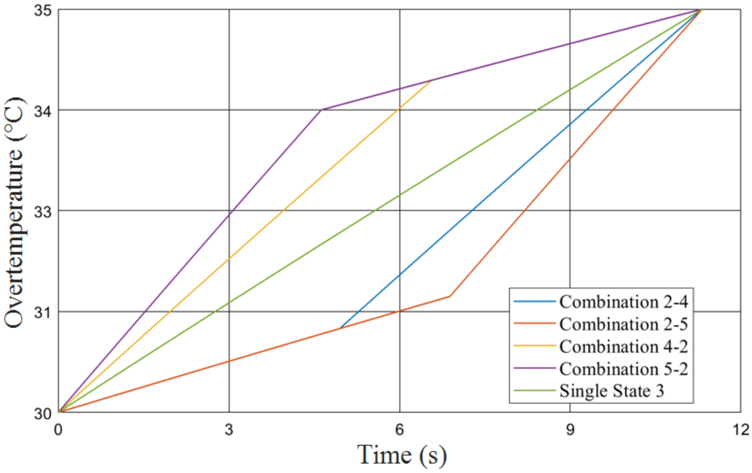

Figure 5.8: Example of the possible combinations considering $\theta_{max} = 35°C$ and $\theta_{min} = 30°C$ compared to the single state configuration ($Ns_{cell} = 3$).

needs to be solved for defining the time step t_{off} for which the second configuration has to be applied according to the selected combination:

$$\begin{cases} \theta_1 = (\theta_{min} - \theta_{\infty 1})e^{(-\frac{t_{off}}{\tau})} + \theta_{\infty 1} \\ \theta_{max} = (\theta_1 - \theta_{\infty_2})e^{(-\frac{t^* - t_{off}}{\tau})} + \theta_{\infty_2} \end{cases} \tag{5.3}$$

where θ_{∞_1} and θ_{∞_2} represent the maximum overtemperature reached by the power boards without any control of the temperature when the first and the second configuration of N_{cell} are applied, respectively; θ_1 is the overtemperature reached by the power boards at the end of the time interval for which the first configuration is applied.

Figure 5.8 shows the possible combinations of N_{cell} considering $\theta_{max} = 35°C$ and $\theta_{min} = 30°C$. In this case, the optimization is performed considering the $Ns_{cell} = 3$ for the single state configuration. As possible to notice, the t_{off} is correctly defined in all the possible combinations. Furthermore, only the combinations of N_{cell} that allows for meeting the requirements in terms of θ_{max} and t^* can be taken into account. It is important to highlight that the proposed adaptive algorithm performs the optimization strategy during each cooling transient of the power boards due to the needed of measuring the cell voltages when the passive balancing is disabled. In this way, an effective and more accurate equalization of the cells can be achieved. In addition, a single state configuration with the Ns_{cell} is performed by the proposed

ΔV (mV)	N_{cell} #1	#2	#3	#4	#5
200	26.4 h	**24.4** h	24.5 h	24.7 h	24.7 h
300	40.7 h	**36.2** h	36.4 h	37.1 h	37.1 h
400	51.1 h	**44.4** h	45.1 h	45.6 h	45.6 h
500	99.8 h	**81.8** h	82.2 h	83.8 h	84.0 h

Table 5.3: Average equalization time for different operating conditions in terms of ΔV and N_{cell}; 20 random distributions for the SoC of the cells are considered for each operating condition.

adaptive algorithm when there are not possibilities of maximizing the energy dissipated in t^*.

5.1.6 Numerical Results

The overall architecture of the BMS for the battery pack of the 50HP electric kart and the related control algorithm have been implemented in Simulink-MATLAB© with the aim of validating the proposed thermal management optimization. Firstly, the numerical analysis has been mainly focused on the identification of the Ns_{cell} that allows minimizing the equalization time of the single module. Then, this analysis has been extended to the overall battery pack and the optimized control algorithm.

Starting from the initial approach, different operating conditions have been considered in terms of maximum voltage imbalance between the most and the least charged cells (ΔV). Moreover, for each ΔV selected, different distributions for the SoC of the cells have been considered. In detail, 20 different random distributions of the SoC have been selected and table 5.3 reports the average equalization time achieved for ΔV ranging from 200 mV to 500 mV when θ_{max} = 35°C and θ_{min} = 30°C are adopted. As result, $Ns_{cell} = 2$ allows for carrying out the minimum equalization at the module-level in all the operating conditions. Generally, high equalization times (hours) can be observed in each condition due to the low balancing current of the passive equalizer compared to the high capacity of the cells used for the battery pack of the 50HP electric kart. However, higher balancing currents are not advisable since they cause severe thermal management issues related to the heat dissipations.

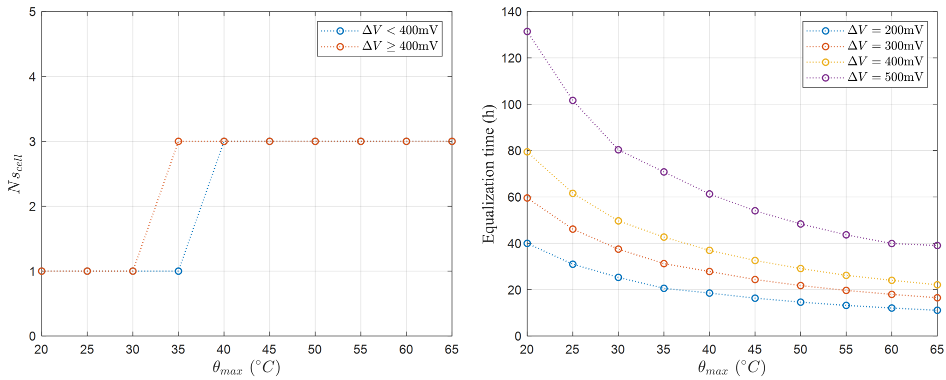

(a) (b)

Figure 5.9: (a) Variability of the Ns_{cell} achieved with the single state configuration and (b) average equalization time achieved with $Ns_{cell} = 3$ by considering different values of ΔV and θ_{max}.

Numerical analyses have been also performed with the aim of evaluating the Ns_{cell} at a pack-level as well as validating the proposed control algorithm for the thermal management optimization. In this case, the Ns_{cell} corresponds to the optimal value of the maximum number of cells in balance at the same time for all the BMS slave units that allows for minimizing the equalization time of the overall battery pack. Likewise for the previous results, different operating conditions have been considered in terms of ΔV and θ_{max}, while random distributions have been selected for the SoC of the cells. In detail, the same ΔV range has been adopted, from 200mV to 500mV, whereas θ_{max} varies from 20°C up to 65°C.

Figure 5.9(a) shows the variability of the Ns_{cell} achieved with the single state configuration when different values of ΔV and θ_{max} are adopted. As possible to notice, the results for $\Delta V \geq 400mV$ are very similar to those for $\Delta V < 400mV$. The only difference is referred to $\theta_{max} = 35$°C, where Ns_{cell} is equal to 1 or 3 depending on the ΔV value. This is mainly due to the thermal behavior of the BMS slave unit. Indeed, the maximum overtemperature of 32°C is reached by the power boards when $N_{cell} = 1$, thus there are not cooling transients for $\theta_{max} = 35$°C. This results convenient for $\Delta V < 400mV$, while a lower equalization time is achieved for larger ΔV.

However, considering θ_{max} higher than 35°C, $Ns_{cell} = 3$ represents the best solution for minimizing the equalization time in all the operating conditions. Hence, according to the results reported in table 5.3,

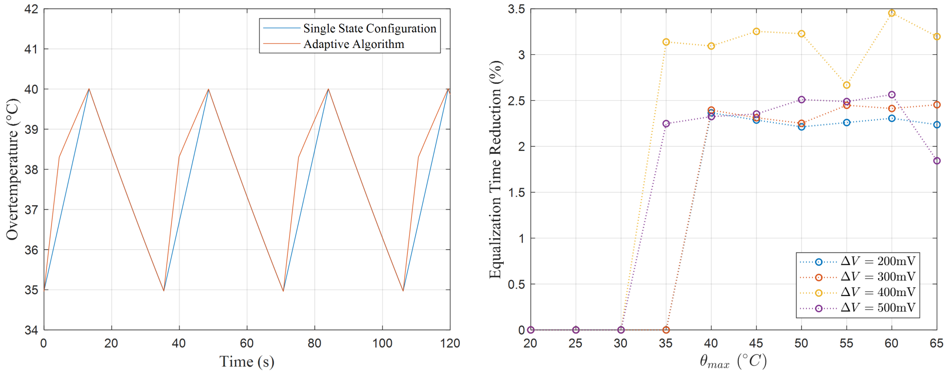

(a) (b)

Figure 5.10: (a) Comparison between the warming and the cooling transients of both the single state configuration with $Ns_{cell} = 3$ and the adaptive algorithm; (b) percentage reduction of the average equalization time thanks to the adaptive algorithm.

different Ns_{cell} are required for minimizing the equalization time at a module-level or a pack-level. Detailed results of the average equalization time achieved with $Ns_{cell} = 3$ by considering different ranges of θ_{max} and ΔV are shown in figure 5.9(b). In this case, ten random distributions have been selected for the SoC of all the 24 cells. It results that higher θ_{max} allows for reducing the equalization time, but the contribute to the reduction lowers as θ_{max} increases. Indeed, as example, the reduction of the equalization time that occurs between 20°C and 25°C is higher than that between 60°C and 65°C.

The performance of the single state configuration has been compared with the one of the proposed adaptive algorithm as well. Figure 5.10(a) shows a comparison between the warming and the cooling transients of both the single state configuration with $Ns_{cell} = 3$ and the adaptive algorithm. In detail, $\theta_{max} = 40$°C and $\theta_{min} = 35$°C have been adopted, whereas a 5-2 combination of N_{cell} has been selected by the proposed adaptive algorithm, as it is possible to notice from the different slopes of the red line.

Numerical analysis has been carried out with the aim of evaluating the improvement in terms of equalization time achievable thanks to the proposed adaptive algorithm. In detail, all the operating conditions considered for the research of the Ns_{cell} have been implemented in order to compare the results. The proposed adaptive algorithm allows for achieving a percentage reduction from 2% up to 3.5%, as illustrated in figure 5.10(b). It is important to highlight that the optimization cannot be performed when the $Ns_{cell} = 1$ since there are not possible configurations to solve the system of equations 5.3. Hence, the positive effects regarding the reduction of the equalization time can be achieved only for θ_{max} higher than 35°C.

5.1.7 Experimental Results

The modular architecture proposed for the passive BMS has been designed and experimentally implemented in order to its performance as well as validate the numerical results. Firstly, experimental tests have been carried out with the aim of verifying if the $Ns_{cell} = 2$ represents the best configuration for minimizing the equalization time at a module-level. The test conditions include $\Delta V = 400$mV, $\theta_{max} = 40$°C and $\theta_{min} = 35$°C. In particular, the SoC of the cells has been distributed in order to achieve the following initial condition for the voltages:

$$\begin{cases} V_1 = 4.020V \\ V_2 = 3.949V \\ V_3 = 3.913V \\ V_4 = 3.739V \\ V_5 = 3.685V \\ V_6 = 3.620V \end{cases} \tag{5.4}$$

Figure 5.11(a) shows the equalization time achieved considering different N_{cell}. As possible to notice, $N_{cell} = 2$ is the configuration that allows for minimizing the equalization time, confirming the numerical results. Then, the overall BMS architecture proposed has been set up and properly connected with the battery pack of the 50HP electric kart, as illustrated in figure 5.11(b). Therefore, only one BMS master and four passive equalizer prototypes (BMS slave units), one for each module of the battery pack, have been adopted. The BMS master is based on a dsPIC30F4011 Microchip© microcontroller, which allows for communicating with all the BMS slave units as well as performing the proposed balancing algorithm. On the other hand, the four KOKAM modules are interfaced to the BMS slave units, which are connected by daisy-chain to the BMS master.

The results achieved from both numerical and experimental analyses have been used for testing the performance of the passive balancing

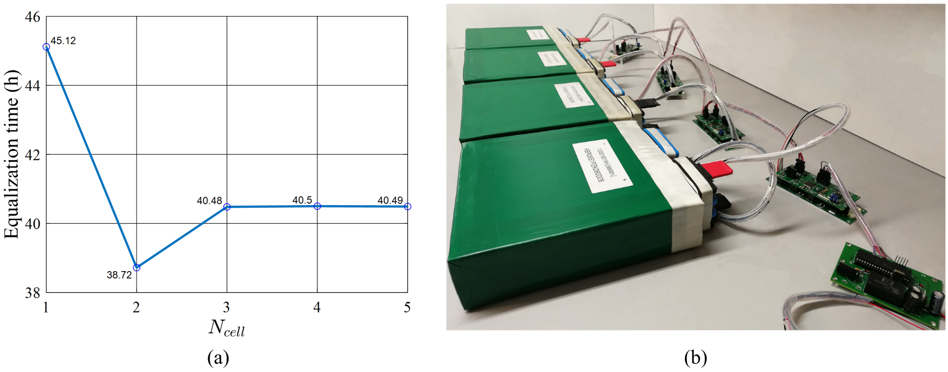

(a)

(b)

Figure 5.11: (a) Equalization time achieved for ΔV equal to 400 mV considering different N_{cell}; (b) experimental set-up of the overall BMS architecture for the battery pack of the 50HP electric kart.

and the correct functionality of the overall BMS architecture. Figure 5.12 shows the equalization process for each module by performing the balancing algorithm with $N_{cell} = 2$. All the cells with a voltage higher than the minimum one (located in the module 3) need to be discharged. However, since $N_{cell} = 2$ is set, only two cell can be balanced at the same time for each module. Hence, when more cells reach the same voltage level, the passive balancing is performed alternatively among these cells in order to meet the N_{cell} constraint. The results highlight the correct functionality of the passive balancing, validating the proposed control algorithm.

The overall BMS architecture has been integrated in the battery pack of the 50HP electric kart as well. Indeed, according to the design discussed in section 5.1.1 and shown in figure 5.1, the battery pack has been assembled and the passive equalizers have been integrated inside the aluminum cases. Figure 5.13(a) reports one half of the overall battery pack, while the 50HP electric kart is depicted in figure 5.13(b). As possible to notice, a specific design of the passive equalizer has been required due to the high space constraints.

5.2 Prototype of Novel Active Equalizer

The novel active equalizer illustrated in section 4.5.1 has been designed and implemented in order to validate its functionality. It is based on a Multiple Active Bridge (MAB), in which every cell is con-

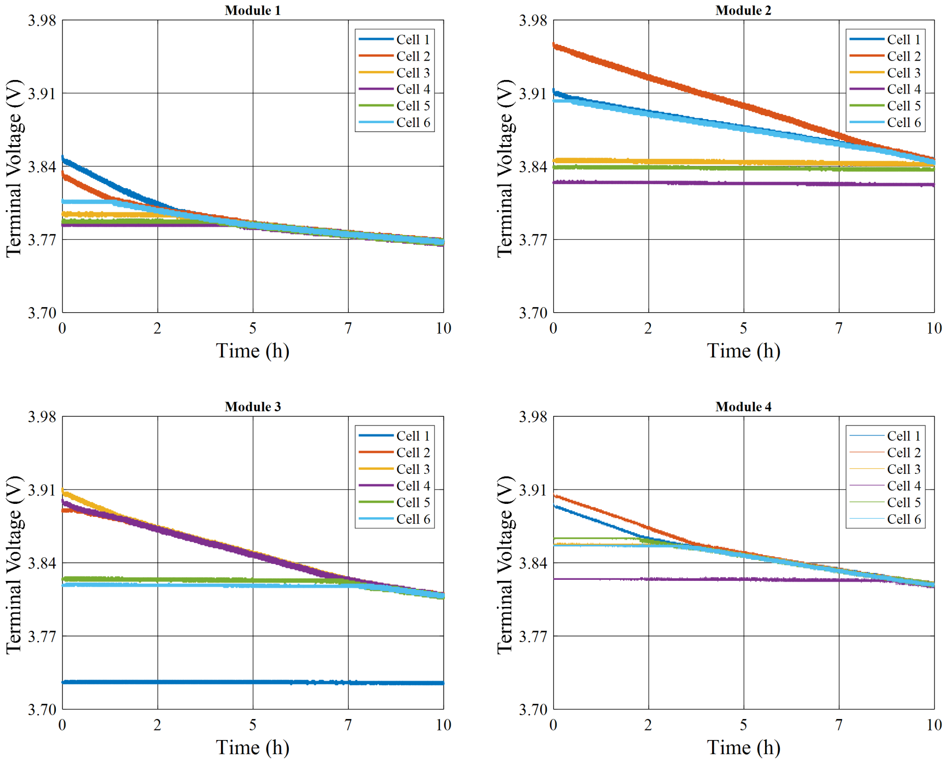

Figure 5.12: Terminal voltages of all the cells that compose the battery pack, divided in the four modules.

nected to a medium-frequency multi-winding transformer (MWT) by means of a H-bridge converter. While traditional equalization circuits based on MWT perform cell-to-pack or pack-to-cell energy transfer techniques, the proposed active equalizer has the innovative characteristic of allowing cells-to-cells equalization. The energy transfer is automatically achieved depending on the voltage imbalance among the cells. Two prototypes have been developed. In particular, the first one has been designed for four series-connected cells with the aim of demonstrating the effectiveness and the potentiality of the proposed solution. On the other hand, the second prototype has been designed for six series-connected cells. Different improvements have been included in order to reduce both size and hardware complexity. In this way, it has been properly compared with the prototype of the passive equalizer developed.

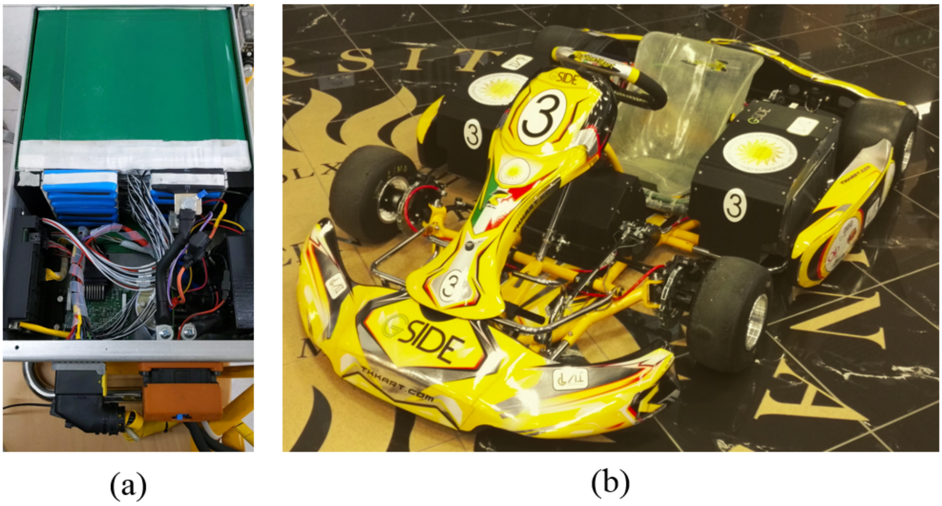
(a) (b)

Figure 5.13: (a) One half of the overall battery pack in which the BMS master and two BMS slave units are integrated; (b) 50HP electric kart.

5.2.1 First Prototype

The first prototype, shown in figure 5.14 has been designed for four series-connected cells. The H-bridge converters are based on Infineon MOSFET IRLB8721PBF1 with bootstrap driver IR2104STRPBF. For each PWM signal, the isolation between the control unit and each H-bridge converter has been achieved by an optocoupler (HCPL-3120). The Wurth Elektronik 749196547 MWT has been selected and operated at 80 kHz. More details related to the parameters of components adopted are reported in table 5.4.
The battery pack used is composed by a string of four LG 18650HG2 cylindrical cells. Through hole MOSFETs have been considered, distributed on the board in order to enable the possibility to adopt heatsinks is needed. Indeed, all the components selected for the proposed first prototype have the ability to achieve high balancing currents, even greater than 1A, as for the prototype of the passive equalizer. Therefore, the overall power losses of the equalization circuit may not be negligible. Furthermore, it is important to highlight that on the market there is a lack of suitable MWTs for the proposed equalization circuit. This leads to the adoption of MWTs that are not optimized for achieving high performance, as reported by the following numerical analysis. Indeed, according to the performance parameters defined in section 4.5 for the design strategy of transformer-based

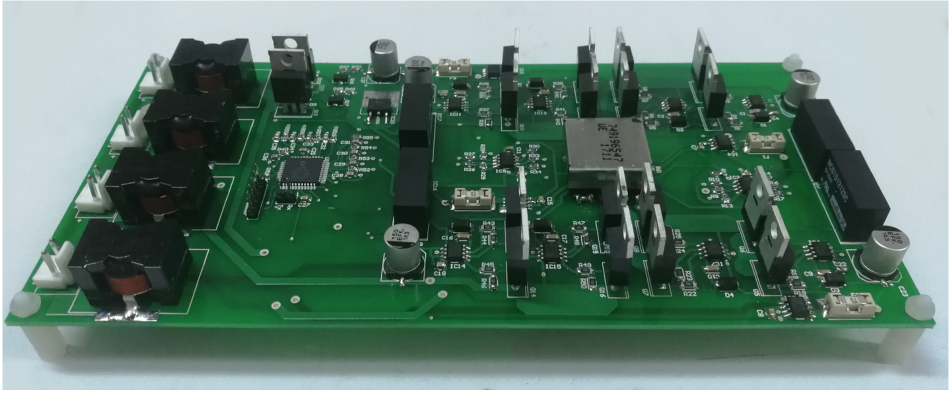

Figure 5.14: First prototype for the proposed active equalizer.

equalization circuit, it results $\alpha = 0.445$ and $\gamma = 0.987$ by considering $V_{B,max} = 4.2V$, $V_{B,min} = 3.8V$, $frequency = 80kHz$, $h = 1,..,11$, $n = 4$ and the parameters reported in table 5.4.
These results confirm the low performance of the commercially available MWTs. Therefore, a proper design procedure is required for maximizing the performance of the proposed equalization circuit. However, the commercially available MWT is here used to provide a validation of the proposed equalization circuit and control technique.
Numerical and experimental tests have been carried for confirming the effectiveness and the potentiality of the proposed solution as well as demonstrating the ability of performing cells-to-cells energy transfer technique.

5.2.1.1 Numerical Results

The proposed equalization circuit and related control strategy have been implemented in MATLAB$^{©}$ using Simulink-Simscape. Accurate models of the cells, MWT and H-bridge converters have been calibrated and implemented in the simulation environment, including detailed models of the power losses of the components. A first-order ECM of the cell has been calibrated by means of experimental data at different charging and discharging C-rates, while datasheet parameters have been considered for the MWT as well as the conduction and switching losses of the power switches.
The performance of the proposed active equalizer has been evaluated in idle state by considering an initial ΔV among the cells equal to 100 mV. Figure 5.15 shows the results of the numerical analysis.

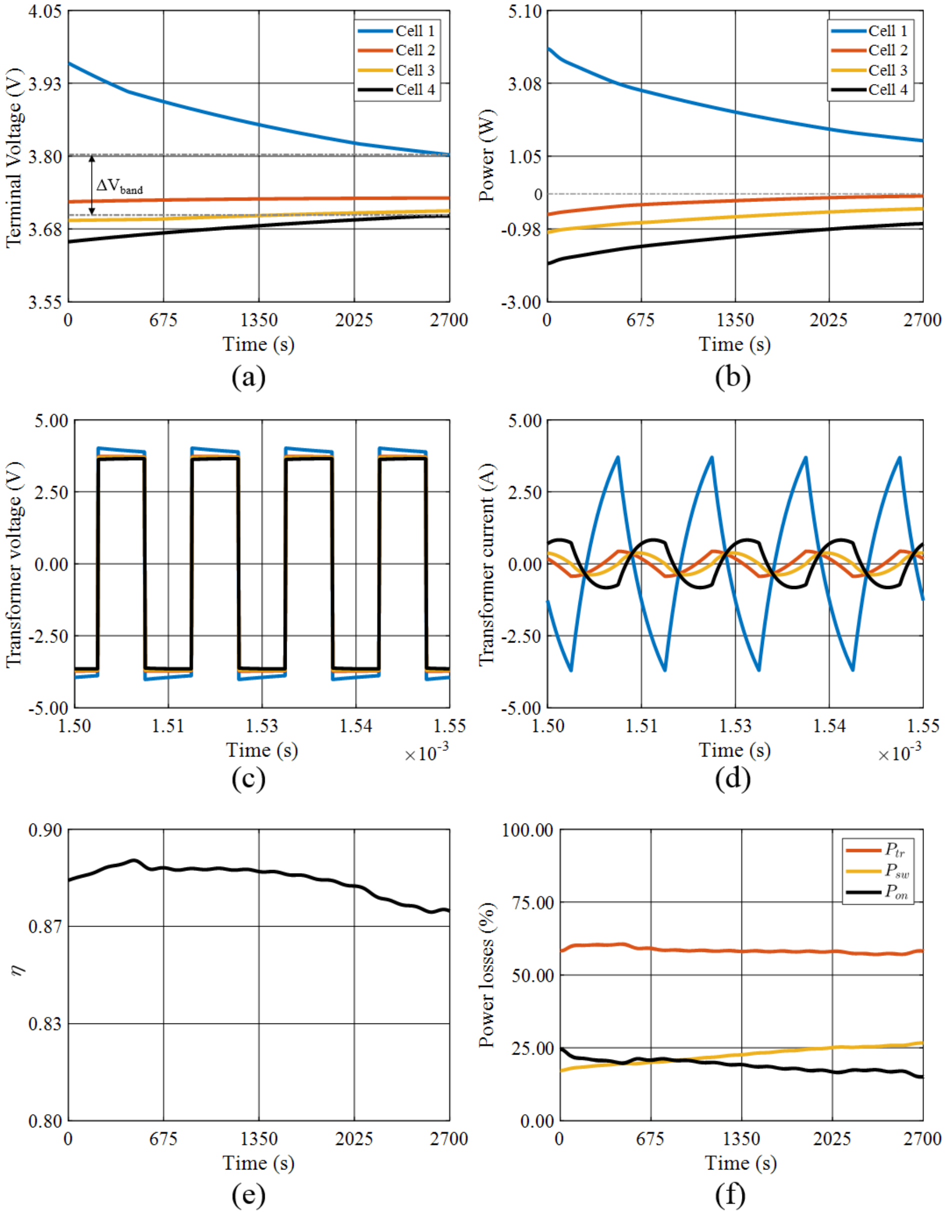

Figure 5.15: Numerical results for the proposed active equalizer.
(a) Terminal voltages and (b) powers of the cells during the equalization process; (c) winding voltages and (d) currents for the MWT; (e) overall efficiency and (f) power losses expressed in percentage of P_T during the equalization process.

Parameter	**Value**
Battery cell LG 18650HG2	
Nominal Capacity	3 Ah
Energy Density	235 Wh/kg
Nominal Voltage	3.6 V
Cut-Off Voltage	2 V
Nominal Charging Current	1.5 A (@0.5C)
Maximum Charging Current	4 A (@1.3C)
Maximum Discharging Current	20 A (@6.6C)
Infineon MOSFET IRLB8721PBF1	
Drain-to-source on resistance	8.7 mΩ
Switching frequency	80 kHz
Rise time	93 ns
Fall time	17 ns
Multi-winding transformer	
Inductance base	3.4 μH
Rated current base	2.3 A
Saturation current base	3.93 A
DC resistance base	36 mΩ
Leakage inductance base	0.18 μH
Filter Inductance (L_f)	33 μH
Filter Capacitance (C_f)	340 μF

Table 5.4: Parameters of the main components adopted for the proposed transformer-based active equalizer.

In particular, figures 5.15(a) and (b) report the cell terminal voltages and powers during the equalization process of the battery pack, respectively. The initial SoC distribution for the cells has been set as follows:

$$\begin{cases} SoC_1 = 87.6\% \\ SoC_2 = 46.0\% \\ SoC_3 = 44.0\% \\ SoC_4 = 30.0\% \end{cases} \tag{5.5}$$

In this case, the most charged cell provides energy to the other cells. Moreover, different balancing contributes can be observed depending on the voltage imbalance among the cells. As result, all the cell

voltages are within a desired voltage band (V_{band}) at the end of the equalization process.
Figures 5.15(c) and (d) show the the voltage and current waveforms of the MWT during the modulation period (equal to $12.5\mu s$), respectively. The winding voltages are in phase, while the phases of the winding current are related to the sign of the balancing current. Indeed, current and voltage are in phase only for the winding corresponding to the highest cell voltage since it is providing energy to the other cells.
The overall efficiency of the proposed equalization circuit has been also evaluated, as illustrated in figure 5.15(e). In particular, the MWT power losses (P_{tr}), the switching (P_{sw}) and conduction (P_{on}) losses of H-bridge converters have been taken into account. The equalization efficiency depends on the power processed by balancing circuit and it is higher than 87.2% with a peak equal to 88.9%. In addition, figure 5.15(f) reports the percentage impact of each contribute to the power losses with respect to the total power losses P_T. As result, the major contribute to P_T is related to the MWT power losses, while P_{on} decrease as the voltage imbalance among the cells lowers.

5.2.1.2 Experimental Results

To evaluate the performance of the proposed equalization circuit and the related control strategy, two case scenarios have been considered and experimentally implemented in idle state. The first case scenario is similar to the SoC distribution adopted for the numerical analysis. Cell 1 has the higher SoC, whereas cells 2, 3, and 4 have a lower SoC. Therefore, likewise of the numerical results, only the most charged cell transfers energy to the other ones. Figures 5.16(a) and (b) show the voltage and current of all the cells during the equalization process, validating the numerical results.
In this conditions, the overall efficiency has been calculated as well by considering the values of cell voltages $\{V_{B,1} = 4.015V$, $V_{B,2} = 3.719V$, $V_{B,3} = 3.689V$, $V_{B,4} = 3.629V\}$ and currents $\{I_{B,1} = 1.058A$, $I_{B,2} = -0.2414A$, $I_{B,3} = -0.3065A$, $I_{B,4} = -0.4482A\}$. The calculated efficiency for this operating point, equal to 86%, is in line with the results achieved from the numerical analysis.
In the second case scenario, the SoC distribution of the cells has been operated with the aim of achieving two cells with higher SoC and two with lower SoC, as illustrated in figure 5.16(c) and (d). In this case, cell 1 and 2 transfer energy to the other cells and the amplitudes

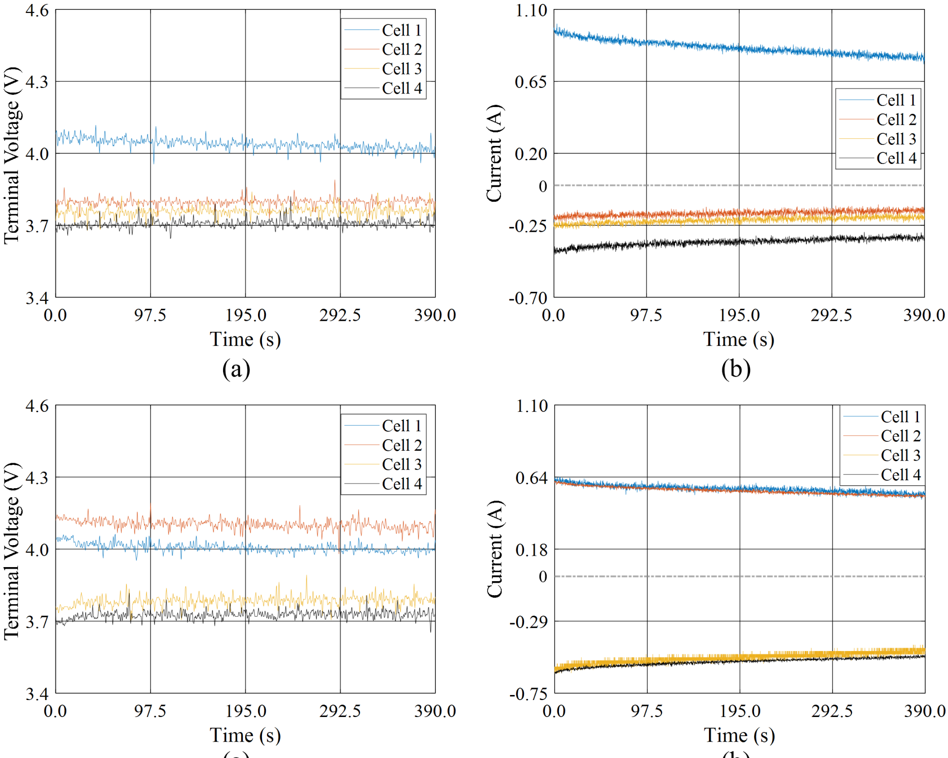

(a) (b)

(a) (b)

Figure 5.16: Experimental results for the proposed active equalizer. Terminal voltages and currents of the cells during the equalization process considering (a,b) the first and (c,d) the second case scenarios.

of the balancing currents depend on the voltage imbalance among the cells. Hence, the experimental results confirm the validity of the proposed active equalization circuit, which allows for simultaneously transferring energy among the cells.

5.2.2 Second Prototype

The first prototype has been improved in order to be properly compared the proposed equalization circuit with the prototype of the passive equalizer developed. Therefore, a second prototype has been designed for six series-connected cells, shown in figure 5.17, with the aim of reducing both size and hardware complexity.

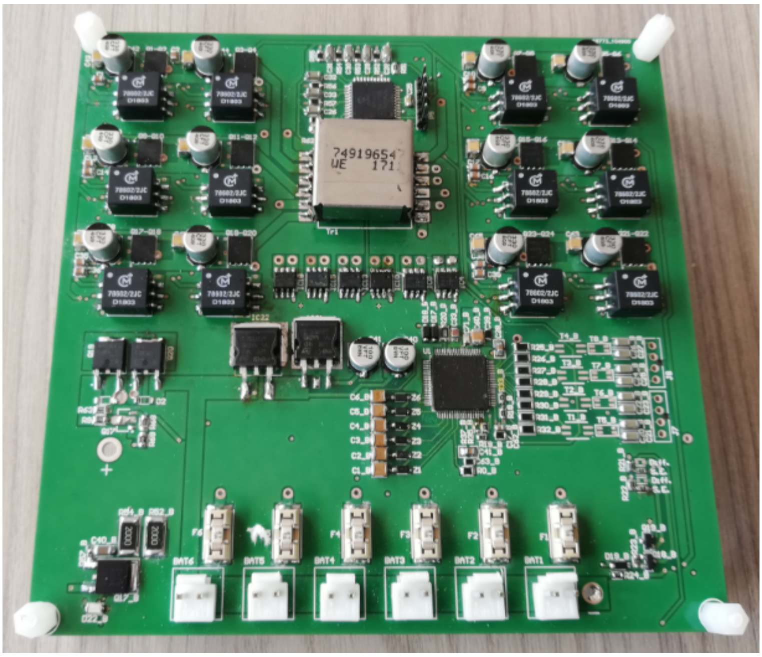

Figure 5.17: Second prototype for the proposed active equalizer.

All components have been selected for potentially achieving high balancing currents, even greater than 1A, which corresponds to the maximum value considered for the design of the passive equalizer.

Dual N-Channel OptiMOS^{TM} MOSFETs by Infineon© (BSC0911ND model) have been adopted for the H-Bridge converters due to their small packages. Their advantages also include low drain-source on-state resistances and low rise/fall times, which allow for achieving low conduction and switching losses, respectively. The control strategy is simple, it is based on a phase-shift modulation technique in which just one common PWM signal at a constant frequency of 80 kHz and duty cycle equal to 50% is adopted. In particular, a fixed phase shift equal to π is implemented between two legs of each H-bridge converter. This PWM signal is provided by a microcontroller to power drivers by Microchip© (TC4427ACOA model) and pulse transformers by Murata Power Solutions© (78602/2JC-R model), which ensure an optimal isolation between the control unit and each H-bridge converter. The MWT represents the crucial component in the design of this active equalizer. Indeed, as discussed in section 4.5, the transformer parameters, such as leakage and magnetization inductances as well as the winding resistances, strongly affect the performance of the equalization circuit in terms of balancing currents and power losses. Likewise for the first prototype, the MWT by Wurth Elektronik© (749196547 model) has been selected.

The cell voltages are accurately acquired by means of the bq76PL455A-Q1 BMS ICs by Texas Instruments©, whereas bidirectional current sensors by Allegro Microsystems©(ACS722LLCTR-05AB-T model) are used for measuring the balancing currents that flows from the most charged cells to the least charged ones. In addition, a temperature sensor close to the MWT is included for evaluating any overheating.

It is important to highlight that, unlike the passive equalizer, a microcontroller and a charge/discharge enabling circuit are integrated in the improved prototype of the proposed active equalizer. This circuit is needed for disconnecting the battery pack from the charger or load in case of faults, such as overvoltage, undervoltage, overcurrent or overtemperature.

5.3 Performance Analysis

Currently, as discussed in section 3.3, different architectures for the equalization circuits have been illustrated in literature. However, since the requirements depend on the field of application, it becomes very difficult to identify the optimal solution for an equalizer circuit as well as to define performance parameters for correctly comparing the different architectures. So far, the comparison has been operated by describing advantages and disadvantages of the equalization circuits without providing qualitative or quantitative analyses that can fully highlight the effectiveness of the different solutions.

In this section, a quantitative analysis for comparing the prototypes developed for the passive and the novel active equalizers is presented. Both architectures have been designed for a battery pack composed by six series-connected cells.

The comparison has been performed in terms of equalization speed, power losses, complexity of both hardware and software implementation, size and cost. The different functionalities of the equalization process in both passive BMS (P-BMS) and active BMS (A-BMS) have been verified in charging, discharging and idle state. Numerical and experimental analyses have been carried out to validate the performance of each equalization circuit.

5.3.1 Comparison

The hardware complexity of both architectures has been evaluated in terms of size (area), cost and number of components, as reported in table 5.5. These parameters are defined for the A-BMS in percentage with respect to those obtained for the P-BMS. Furthermore, since the microcontroller and the charge/discharge enabling circuits are only integrated in the A-BMS, their features have been evaluated separately and included in the overall results for the P-BMS. In this way, a proper comparison between the prototypes adopted can be achieved.

Parameter	**Value**
Cost	+87%
Size	+60%
# Components	+50%

Table 5.5: Comparison parameters for A-BMS with respect to P-BMS.

The A-BMS results to be more expensive and larger than the P-BMS. Moreover, a higher number of components needs to be considered as well. It is important to highlight that this comparative analysis does not take into account the possibility to adopt a heatsink for compensating the high heat dissipation due to the high balancing currents in the P-BMS.

For what concerns the control complexity, the A-BMS allows for managing all the H-Bridge converters by means of just a single common PWM signal, leading to an easier control algorithm despite the hardware complexity. On the contrary, six control signals are required in the P-BMS, one for each cell that composes the battery pack.

From a fault tolerance point of view, fault conditions on switches result in different issues for the P-BMS or the A-BMS. In particular, since switches and power resistors are connected in parallel with every cell in the P-BMS, a fail closed switch leads to an overdischarge of the corresponding cell. This overdischarge may be accelerated because of the high balancing current for which the P-BMS has been designed. On the other hand, a short circuit can potentially occur in the A-BMS in case of the simultaneous closing of both switches in a H-Bridge converter leg. Nevertheless, a short circuit can be interrupted by adopting a fuse, whereas it is more complicated to reduce the risk related to the switch failure in the P-BMS. An additional switch can be considered for the P-BMS to increase fault tolerance.

5.3.2 Numerical Results

All components of both P-BMS and A-BMS have been modeled and implemented in Matlab© using Simulink-Simscape. Accurate models for the cells, the MWT and the H-Bridge converters have been adopted. The battery pack is composed by six 3-Ah cylindrical cells (model SONY VTC6) in series connection. A zero-order model has been calibrated by means of experimental tests considering different C-rate, current direction, SoC and temperature. The models of MWT and power switches have been implemented taking into account the datasheet parameters, including either the conduction or the switching power losses for the H-Bridge converters. The balancing strategy in different operating modes for each BMS architecture has been developed and implemented, as reported in figure 5.18. Firstly, the control parameters are set, which include the maximum/minimum cell voltage thresholds ($V_{th,up}$,$V_{th,down}$), the initial SoC of the cells as well as all the design parameters of both P-BMS and A-BMS for executing the numerical tests. Then, the operating mode is defined, including charging, discharging and idle state.

In *idle state*, after measuring all cell voltages, the voltage imbalance between the most charged cell (V_{max}) and the least charged one (V_{min}) is evaluated. If this difference is higher than a desired voltage band (ΔV_{band}), the equalization process is performed. In detail, different balancing strategies are operated in idle state for the P-BMS and the A-BMS, as illustrated in figures 5.18(a) and 5.18(b). In the former, all the cells with a voltage value V_k greater than $V_{min} + \Delta V_{band}$ are discharged on their parallel resistor until they reach the desired ΔV_{band}. Hence, one control signal is needed for each cell. On the other hand, the equalization process of the A-BMS is activated for all the cells if only one cell is outside the desired ΔV_{band}.

In *discharging*, no equalization action is activated for the P-BMS, since the discharge process will be limited by the least charged cell. The activation of the A-BMS in this operating condition allows for transferring energy from cells-to-cells with the aim of extending the discharge process until reaching $V_{th,down}$.

In *charging*, either the passive or the active balancing can be enabled in order to maximize the stored energy in the battery pack. Then, as soon as one cell voltage reaches $V_{th,up}$, the charging is disabled and the balancing process is stopped.

The numerical results shown in figure 5.19 demonstrate the effectiveness of the A-BMS and P-BMS in different operating modes. Different voltage imbalance (ΔV) among the cells have been taken into account

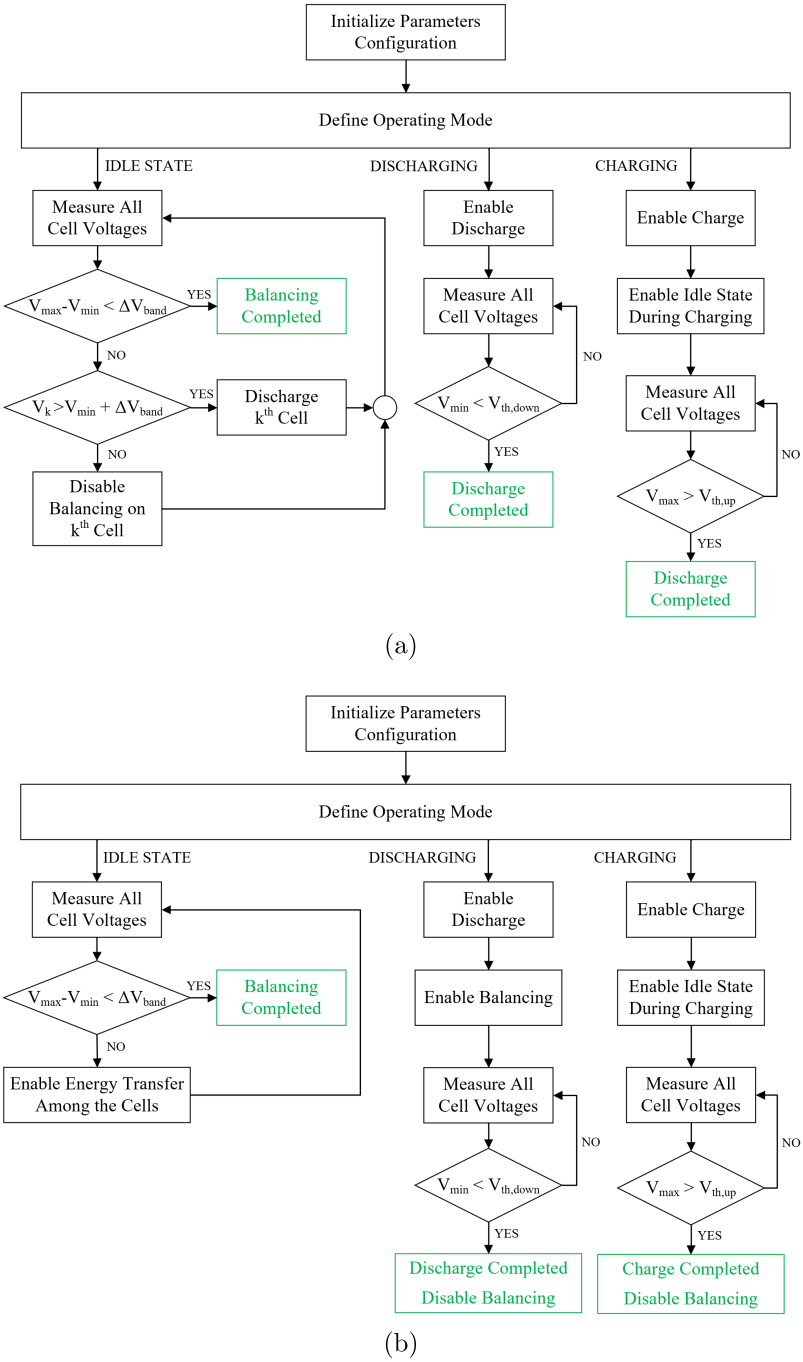

Figure 5.18: Balancing strategy in different operating modes for the P-BMS (a) and A-BMS (b).

as initial condition. In detail, the initial SoC of the most charged cell (SoC_{init}) has been set equal to 100% for the idle state/discharging and 40% for charging. Therefore, a linear distribution of the initial SoC of the cells has been adopted on the basis of SoC_{init} and ΔV.

For what concerns the comparison between the P-BMS and the A-BMS in idle state, t_{eq} (figure 5.19(a)) represents the time interval needed for equalizing the voltages of the cells within a desired ΔV_{band} equal to 30mV, whereas E_{bal} (figure 5.19(b)) represents the amount of energy involved in both BMS architectures during the equalization process. In particular, E_{bal} is equal to the energy dissipated on the balancing resistors for the P-BMS and the energy transferred between the most charged cells and the least charged ones depurated of the energy dissipated for the A-BMS.

In discharging, t_{disch} (figure 5.19(c)) and E_{prov} (figure 5.19(d)) are the time interval for which the battery pack is able to provide energy and the amount of energy provided in t_{disch}, respectively. It is important to highlight that the balancing action is performed in discharging only for the A-BMS, thus the results for the P-BMS represent the discharge of the battery pack without any balancing.

Similar comparison parameters have been considered for the charging, including the time interval t_{ch} (figure 5.19(e)) in which the charging is enabled and the energy $E_{charger}$ (figure 5.19(f)) provided by the charger in t_{ch}. The difference between the performance of the A-BMS with respect to the P-BMS is reported in figure 5.19 as percentage.

From the numerical analysis, it results that the P-BMS allows achieving high equalization speed, especially for ΔV lower than 150mV. This is related to the possibility to perform the equalization process in the P-BMS with greater balancing currents. Indeed, high balancing currents can be obtained in the A-BMS only for larger ΔV, whereas very low variations in the balancing current occur for the P-BMS. Nevertheless, a considerable reduction of the E_{bal} can be achieved by adopting the A-BMS. This means that a lower amount of energy needs to be transferred among the cells with respect to the energy that needs to be dissipated in the P-BMS for bringing all cell voltages within the same desired ΔV_{band}. In addition, better performance can be obtained from the A-BMS either in charging or in discharging. In detail, more energy can be provided in discharging by the battery pack. Furthermore, the improvement in E_{prov} increases for higher ΔV. In charging, unless the results for ΔV equal to 50mV for which the A-BMS cannot exhibit its best performance, lower t_{ch} is achieved and a smaller amount of energy is required.

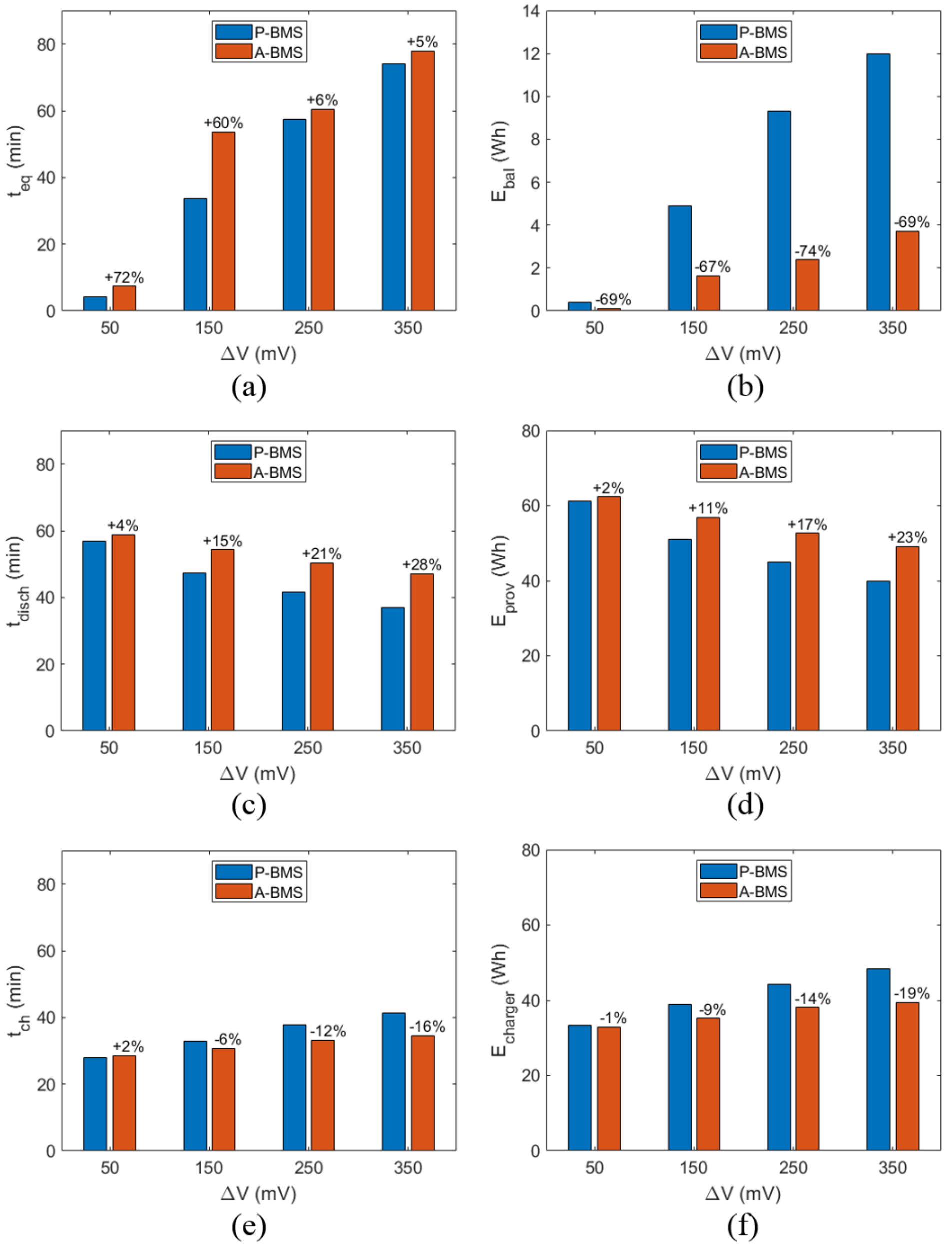

Figure 5.19: Numerical results for the comparison between P-BMS and A-BMS in the different operating modes. (a) t_{eq} and (b) E_{bal} in idle state; (c) t_{disch} and (d) E_{prov} in discharging; (e) t_{ch} and (f) $E_{charger}$ in charging.

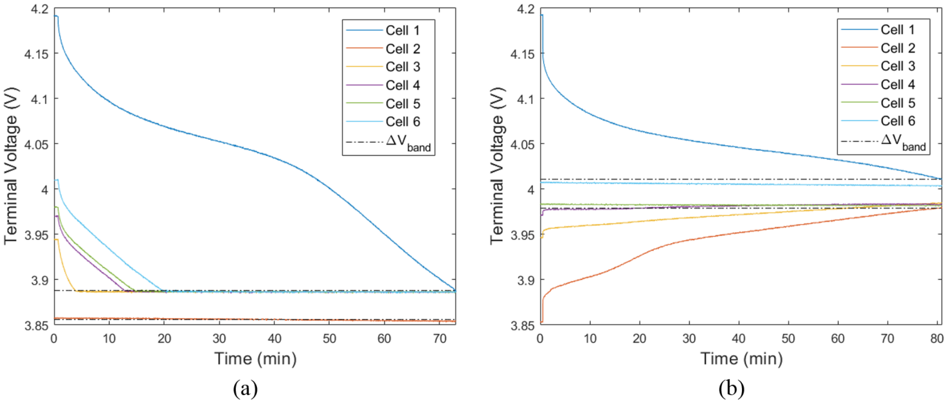

(a) (b)

Figure 5.20: Experimental results in idle state for the P-BMS (a) and the A-BMS (b).

5.3.3 Experimental Results

The experimental setup for both the P-BMS and the A-BMS have been carried out with the aim of validating the numerical results and the functionality of these two architectures in idle state. ΔV equal to 350mV and SoC_{init} equal to 100% have been considered for the experimental tests. The results are reported in figure 5.20. Likewise of the numerical analysis, the equalization process has been stopped when all cell voltages were in a ΔV_{band} equal to 30mV.

The experimental results highlight the correct functionality of either the P-BMS or A-BMS. The equalization times achieved with the P-BMS and the A-BMS are equal to 73 min and 81 min, respectively. Moreover, these results are in line with the ones obtained in the numerical analysis. Indeed, the differences in t_{eq} between the results achieved for the P-BMS and the A-BMS with respect to the numerical results are equal to +1% and +4%, respectively. In addition, the differences between the t_{eq} achieved with the P-BMS and the A-BMS in the same operating conditions are equal to 5% and 11% in the numerical and experimental results, respectively. This fully confirms the validity of the numerical analysis and the goodness of the comparison between the prototypes developed.

Conclusions

In this dissertation, design methodologies for passive and active equalization circuits that take into account for relevant aspects of both battery pack and power electronics components have been presented. This also includes the development of the model equations that describe the behavior of each equalization circuit selected, including detailed efficiency models as well. In particular, design strategies have been proposed for four BMS architectures, one for each main equalization type, including passive, capacitor-based, inductor-based and transformed-based solutions. Moreover, a novel architecture for an active equalization circuit has been developed for the transformer-based equalizer, which allows for achieving a cells-to-cells energy transfer. Real operating conditions of both individual cells and the overall battery pack have been considered in terms of cell technology, temperature, model calibration and voltage imbalances among the cells. Likewise, real behavior of the components used for the specific equalization circuit and their parameter variations have be taken into account.

A sensitivity analysis for each BMS architecture considered has been carried out for evaluating the impact of both the operating conditions and the parameter variations on the performance in terms of mean balancing current and equalization time.

Then, real prototypes have been sized and implemented. In detail, a modular architecture for the passive equalizer of a 50HP electric kart and the novel active equalizer have been prototyped with the aim of validating their performance in real-world environments. Moreover, a detailed comparison between the prototypes developed has been carried out in order to highlight their main features in different operating conditions, including charging, discharging and idle state. Both numerical and experimental results confirm the validity of the models adopted and the goodness of the prototypes developed.

In conclusion, depending on the specific application, the research activity presented in this dissertation has provided an overall knowledge that allows for correctly defining the main aspects related to the implementation of a lithium-ion battery pack, including the selection of the appropriate cell technology and pack architecture, the evaluation of hazard conditions for the battery pack as well as the design and prototyping of the BMS.

Future improvements and developments of the research activity presented in this dissertation will regard both academic and industrial aspects. In particular, according to the design methodologies illustrated, optimized equalization circuits can be prototyped and adopted in real-world applications. This will also enable the possibility to properly compare the different BMS architectures and thus select the one that allows for ensuring the desired performance in terms of cost, size, number of components, efficiency and balancing current.

On the other hand, from an academic point of view, additional BMS architectures can be investigated for extending the analysis proposed in this dissertation as well as designing novel equalization circuits with a systematic approach. Moreover, the sensitivity analysis presented can be considered for developing proper control strategies with the aim of maximizing the performance of the specific equalization circuit in different operating conditions.

List of Figures

List of Tables

Bibliography

[1] "European roadmap electrification of road transport," in *European Road Transport Research Advisory Council (ERTRAC)*, 2017.

[2] "Electric vehicles from life cycle and circular economy perspectives term 2018: Transport and environment reporting mechanism (term) report," in *European Environment Agency*, 2018.

[3] "The role of battery electric vehicles, plug-in hybrids and fuel cell electric vehicles," in *A portfolio of power-trains for Europe: a fact-based analysis*, 2010.

[4] Bloomberg, "Electric vehicle outlook 2020," 2020.

[5] McKinsey, "Electric vehicle index: Europe cushions a global plunge in ev sales," 2017.

[6] C. Bae and J. Kim, "Alternative fuels for internal combustion engines," *Proceedings of the Combustion Institute*, vol. 36, no. 3, pp. 3389 – 3413, 2017.

[7] R. M. Dell, P. T. Moseley, and D. A. Rand, "Chapter 5 - progressive electrification of road vehicles," in *Towards Sustainable Road Transport*, R. M. Dell, P. T. Moseley, and D. A. Rand, Eds. Boston: Academic Press, 2014, pp. 157 – 192.

[8] C. Chan, "The state of the art of electric, hybrid, and fuel cell vehicles," *Proceedings of the IEEE*, vol. 95, pp. 704 – 718, 05 2007.

[9] M. Farag, "Lithium-ion batteries: Modelling and state of charge estimation," Ph.D. dissertation, 06 2013.

[10] A. Eftekhari, Ed., *Future Lithium-ion Batteries.* The Royal Society of Chemistry, 2019.

[11] P. Kurzweil and J. Garche, “2 - overview of batteries for future automobiles,” in *Lead-Acid Batteries for Future Automobiles*, J. Garche, E. Karden, P. T. Moseley, and D. A. Rand, Eds. Amsterdam: Elsevier, 2017, pp. 27 – 96.

[12] J. Choi and D. Aurbach, “Promise and reality of post-lithium-ion batteries with high energy densities,” *Nature Reviews Materials*, vol. 1, p. 16013, 03 2016.

[13] N. Nitta, F. Wu, J. Lee, and G. Yushin, “Li ion battery materials: Present and future,” *Materials Today*, vol. 18, 11 2014.

[14] G. Zubi, R. Dufo-Lopez, M. Carvalho, and G. Pasaoglu, “The lithium-ion battery: State of the art and future perspectives,” *Renewable and Sustainable Energy Reviews*, vol. 89, pp. 292 – 308, 2018.

[15] M. A. Cusenza, S. Bobba, F. Ardente, M. Cellura, and F. Di Persio, “Energy and environmental assessment of a traction lithium-ion battery pack for plug-in hybrid electric vehicles,” *Journal of Cleaner Production*, vol. 215, pp. 634 – 649, 2019.

[16] Y. Miao, P. Hynan, A. von Jouanne, and A. Yokochi, “Current li-ion battery technologies in electric vehicles and opportunities for advancements,” *Energies*, vol. 12, pp. 1074–1094, 03 2019.

[17] Q. Liu, C. Du, B. Shen, P. Zuo, X. Cheng, Y. Ma, G. Yin, and Y. Gao, “Understanding undesirable anode lithium plating issues in lithium-ion batteries,” *RSC Adv.*, vol. 6, pp. 88 683–88 700, 09 2016.

[18] M. T. McDowell, S. W. Lee, W. Nix, and Y. Cui, “25th anniversary article: Understanding the lithiation of silicon and other alloying anodes for lithium-ion batteries.” *Advanced materials*, vol. 25 36, pp. 4966–85, 2013.

[19] A. Eftekhari and D.-W. Kim, “Cathode materials for lithium-sulfur batteries: a practical perspective,” *J. Mater. Chem. A*, vol. 5, pp. 17 734–17 776, 2017.

[20] X. Yao, B. Huang, J. Yin, G. Peng, Z. Huang, C. Gao, D. Liu, and X. Xu, “All-solid-state lithium batteries with inorganic solid electrolytes: Review of fundamental science,” *Chinese Physics B*, vol. 25, p. 018802, 01 2016.

[21] T. Placke, R. Schmuch, S. DÃ¼hnen, and M. Winter, “Lithium-ion, lithium metal and alternative rechargeable battery technologies: The odyssey for high energy density,” *Journal of Solid State Electrochemistry*, vol. DOI: 10.1007/s10008-017-3610-7, 07 2017.

[22] C. Linse and R. Kuhn, “10 - design of high-voltage battery packs for electric vehicles,” in *Advances in Battery Technologies for Electric Vehicles*, ser. Woodhead Publishing Series in Energy, B. Scrosati, J. Garche, and W. Tillmetz, Eds. Woodhead Publishing, 2015, pp. 245 – 263.

[23] Y. Cai, M. Cancian, M. D’Arpino, and G. Rizzoni, “A generalized equivalent circuit model for large-scale battery packs with cell-to-cell variation,” in *2019 IEEE National Aerospace and Electronics Conference (NAECON)*, 2019, pp. 24–30.

[24] J. Siegel, A. Stefanopoulou, P. Hagans, Y. Ding, and D. Gorsich, “Expansion of lithium ion pouch cell batteries: Observations from neutron imaging,” *Journal of the Electrochemical Society*, vol. 160, pp. A1031–A1038, 04 2013.

[25] D. Chen, J. Jiang, G.-H. Kim, C. Yang, and A. Pesaran, “Comparison of different cooling methods for lithium ion battery cells,” *Applied Thermal Engineering*, vol. 94, pp. 846 – 854, 2016.

[26] G. Xia, L. Cao, and G. Bi, “A review on battery thermal management in electric vehicle application,” *Journal of Power Sources*, vol. 367, pp. 90 – 105, 2017.

[27] Y.-L. Ding, Z. Cano, A. Yu, J. Lu, and Z. Chen, “Automotive li-ion batteries: Current status and future perspectives,” *Electrochemical Energy Reviews*, vol. 2, pp. 1–28, 03 2019.

[28] G. Zubi, R. Dufo-Lopez, M. Carvalho, and G. Pasaoglu, “The lithium-ion battery: State of the art and future perspectives,” *Renewable and Sustainable Energy Reviews*, vol. 89, pp. 292 – 308, 2018.

[29] S. Mousavi G. and M. Nikdel, “Various battery models for various simulation studies and applications,” *Renewable and Sustainable Energy Reviews*, vol. 32, pp. 477 – 485, 2014.

[30] H. Hinz, “Comparison of lithium-ion battery models for simulating storage systems in distributed power generation,” *Inventions*, vol. 4, p. 41, 08 2019.

[31] C. Zhang, K. Li, S. Mcloone, and Z. Yang, “Battery modelling methods for electric vehicles - a review,” 06 2014, pp. 2673–2678.

[32] A. Fotouhi, D. J. Auger, K. Propp, S. Longo, and M. Wild, “A review on electric vehicle battery modelling: From Lithium-ion toward Lithium-Sulphur,” *Renewable and Sustainable Energy Reviews*, vol. 56, no. C, pp. 1008–1021, 2016.

[33] G. Fan, K. Pan, M. Canova, J. Marcicki, and X. Yang, “Modeling of li-ion cells for fast simulation of high c-rate and low temperature operations,” *Journal of The Electrochemical Society*, vol. 163, pp. A666–A676, 02 2016.

[34] Q. Zhang, Y. Li, Y. Shang, B. Duan, N. Cui, and C. Zhang, “A fractional-order kinetic battery model of lithium-ion batteries considering a nonlinear capacity,” *Electronics*, vol. 8, p. 394, 04 2019.

[35] L. Tao, J. Ma, Y. Cheng, A. Noktehdan, J. Chong, and C. Lu, “A review of stochastic battery models and health management,” *Renewable and Sustainable Energy Reviews*, vol. 80, pp. 716 – 732, 2017.

[36] D. Yang, Y. Wang, R. Pan, R. Chen, and Z. Chen, “A neural network based state-of-health estimation of lithium-ion battery in electric vehicles,” *Energy Procedia*, vol. 105, pp. 2059 – 2064, 2017, 8th International Conference on Applied Energy, ICAE2016, 8-11 October 2016, Beijing, China.

[37] D. Jiani, L. Zhitao, W. Youyi, and W. Changyun, “A fuzzy logic-based model for li-ion battery with soc and temperature effect,” in *11th IEEE International Conference on Control Automation (ICCA)*, 2014, pp. 1333–1338.

[38] W. Junping, C. Quanshi, and C. Binggang, “Support vector machine based battery model for electric vehicles,” *Energy Conversion and Management - ENERG CONV MANAGE*, vol. 47, pp. 858–864, 05 2006.

[39] H. Zhang and M.-Y. Chow, “Comprehensive dynamic battery modeling for phev applications,” 08 2010, pp. 1 – 6.

[40] X. Zhang, W. Zhang, and G. Lei, “A review of li-ion battery equivalent circuit models,” *Transactions on Electrical and Electronic Materials*, vol. 17, pp. 311–316, 12 2016.

[41] Z. Mao, M. Farkhondeh, M. Pritzker, M. Fowler, and Z. Chen, “Dynamics of a blended lithium-ion battery electrode during galvanostatic intermittent titration technique,” *Electrochimica Acta*, vol. 222, pp. 1741 – 1750, 2016.

[42] D. USABC, “National laboratories: Electric vehicle battery test procedures manual rev 3. 2015.”

[43] Y. Hu, S. Yurkovich, Y. Guezennec, and B. Yurkovich, “A technique for dynamic battery model identification in automotive applications using linear parameter varying structures,” *Control Engineering Practice*, vol. 17, no. 10, pp. 1190 – 1201, 2009.

[44] H. He, R. Xiong, H. Guo, and S. Li, “Comparison study on the battery models used for the energy management of batteries in electric vehicles,” *Energy Conversion and Management*, vol. 64, pp. 113 – 121, 2012, iREC 2011, The International Renewable Energy Congress.

[45] F. Sun, R. Xiong, H. He, W. Li, and J. E. E. Aussems, “Model-based dynamic multi-parameter method for peak power estimation of lithium-ion batteries,” *Applied Energy*, vol. 96, pp. 378 – 386, 2012, smart Grids.

[46] h. Hongwen, R. Xiong, and F. Jinxin, “Evaluation of lithium-ion battery equivalent circuit models for state of charge estimation by an experimental approach,” *Energies*, vol. 4, 12 2011.

[47] X. Feng, M. Ouyang, X. Liu, L. Lu, Y. Xia, and X. He, “Thermal runaway mechanism of lithium ion battery for electric vehicles: A review,” *Energy Storage Materials*, vol. 10, pp. 246 – 267, 2018.

[48] J. Zhu, T. Wierzbicki, and W. Li, “A review of safety-focused mechanical modeling of commercial lithium-ion batteries,” *Journal of Power Sources*, vol. 378, pp. 153–168, 02 2018.

[49] Q. Yuan, F. Zhao, W. Wang, Y. Zhao, Z. Liang, and D. Yan, “Overcharge failure investigation of lithium-ion batteries,” *Electrochimica Acta*, vol. 178, pp. 682 – 688, 2015.

[50] X. Lai, Y. Zheng, L. Zhou, and W. Gao, “Electrical behavior of overdischarge-induced internal short circuit in lithium-ion cells,” *Electrochimica Acta*, vol. 278, pp. 245 – 254, 2018.

[51] R. Spotnitz and J. Franklin, “Abuse behavior of high-power, lithium-ion cells,” *Journal of Power Sources*, vol. 113, no. 1, pp. 81 – 100, 2003.

[52] S. Santhanagopalan, P. Ramadass, and J. Z. Zhang, “Analysis of internal short-circuit in a lithium ion cell,” *Journal of Power Sources*, vol. 194, no. 1, pp. 550 – 557, 2009.

[53] C. Birkl, M. Roberts, E. McTurk, P. Bruce, and D. Howey, “Degradation diagnostics for lithium ion cells,” *Journal of Power Sources*, vol. 341, pp. 373–386, 02 2017.

[54] M. Kabir and D. Demirocak, “Degradation mechanisms in li-ion batteries: A state-of-the-art review,” *International Journal of Energy Research*, vol. 41, 11 2017.

[55] L. Lu, X. Han, J. Li, J. Hua, and M. Ouyang, “A review on the key issues for lithium-ion battery management in electric vehicles,” *Journal of Power Sources*, vol. 226, pp. 272 – 288, 2013.

[56] M. Lelie, T. Braun, M. Knips, H. Nordmann, F. Ringbeck, H. Zappen, and D. Sauer, “Battery management system hardware concepts: An overview,” *Applied Sciences*, vol. 8, p. 534, 03 2018.

[57] G. Plett, *Battery Management Systems, Volume II: Equivalent-Circuit Methods.* Artech House, 2015.

[58] A. Hauser and R. Kuhn, “12 - cell balancing, battery state estimation, and safety aspects of battery management systems for electric vehicles,” in *Advances in Battery Technologies for Electric Vehicles*, ser. Woodhead Publishing Series in Energy, B. Scrosati, J. Garche, and W. Tillmetz, Eds. Woodhead Publishing, 2015, pp. 283 – 326.

[59] C. Zhang, K. Li, L. Pei, and C. Zhu, "An integrated approach for real-time model-based state-of-charge estimation of lithium-ion batteries," *Journal of Power Sources*, vol. 283, pp. 24 – 36, 2015.

[60] M. Li, "Li-ion dynamics and state of charge estimation," *Renewable Energy*, vol. 100, pp. 44 – 52, 2017, special Issue: Control and Optimization of Renewable Energy Systems.

[61] G. Fan, X. Li, and M. Canova, "A reduced-order electrochemical model of li-ion batteries for control and estimation applications," *IEEE Transactions on Vehicular Technology*, vol. PP, pp. 1–1, 08 2017.

[62] J. Gomez, R. Nelson, E. E. Kalu, M. H. Weatherspoon, and J. P. Zheng, "Equivalent circuit model parameters of a high-power li-ion battery: Thermal and state of charge effects," *Journal of Power Sources*, vol. 196, no. 10, pp. 4826 – 4831, 2011.

[63] M. Ouyang, G. Liu, L. Lu, J. Li, and X. Han, "Enhancing the estimation accuracy in low state-of-charge area: A novel onboard battery model through surface state of charge determination," *Journal of Power Sources*, vol. 270, pp. 221 – 237, 2014.

[64] R. Zhang, B. Xia, B. Li, L. Cao, Y. Lai, W. Zheng, H. Wang, and W. Wang, "State of the art of lithium-ion battery soc estimation for electrical vehicles," *Energies*, vol. 11, p. 1820, 07 2018.

[65] M. Hannan, M. Lipu, A. Hussain, and A. Mohamed, "A review of lithium-ion battery state of charge estimation and management system in electric vehicle applications: Challenges and recommendations," *Renewable and Sustainable Energy Reviews*, vol. 78, pp. 834 – 854, 2017.

[66] Y. Zheng, M. Ouyang, X. Han, L. Lu, and L. Jianqiu, "Investigating the error sources of the online state of charge estimation methods for lithium-ion batteries in electric vehicles," *Journal of Power Sources*, vol. 377, 12 2017.

[67] *Battery State of Health Estimation.* John Wiley and Sons, 2019, ch. 4, pp. 95–130.

[68] I. Baghdadi, O. Briat, J.-Y. DelÃ©tage, P. Gyan, and J.-M. Vinassa, “Lithium battery aging model based on dakin’s degradation approach,” *Journal of Power Sources*, vol. 325, pp. 273 – 285, 2016.

[69] L. Jiang, Y. Li, Y. Huang, J. Yu, X. Qiao, Y. Wang, C. Huang, and Y. Cao, “Optimization of multi-stage constant current charging pattern based on taguchi method for li-ion battery,” *Applied Energy*, vol. 259, p. 114148, 2020.

[70] P. Keil and A. Jossen, “Charging protocols for lithium-ion batteries and their impact on cycle life-an experimental study with different 18650 high-power cells,” *Journal of Energy Storage*, vol. 6, pp. 125 – 141, 2016.

[71] M. M. Hoque, M. A. Hannan, A. Mohamed, and A. Ayob, “Battery charge equalization controller in electric vehicle applications: A review,” *Renewable and Sustainable Energy Reviews*, vol. 75, pp. 1363–1385, 03 2017.

[72] M. Daowd, N. Omar, P. Van Den Bossche, and J. Van Mierlo, “Passive and active battery balancing comparison based on matlab simulation,” in *2011 IEEE Vehicle Power and Propulsion Conference*, 2011, pp. 1–7.

[73] J. Gallardo-Lozano, E. Romero-Cadaval, M. Milanes-Montero, and M. Guerrero-Martinez, “Battery equalization active methods,” *Journal of Power Sources*, vol. 246, pp. 934–949, 01 2014.

[74] F. Baronti, R. Roncella, and R. Saletti, “Performance comparison of active balancing techniques for lithium-ion batteries,” *Journal of Power Sources*, vol. 267, 11 2014.

[75] M. Caspar, T. Eiler, and S. Hohmann, “Systematic comparison of active balancing: A model-based quantitative analysis,” *IEEE Transactions on Vehicular Technology*, vol. 67, no. 2, pp. 920–934, 2018.

[76] L. H. Saw, Y. Ye, and A. A. Tay, “Integration issues of lithium-ion battery into electric vehicles battery pack,” *Journal of Cleaner Production*, vol. 113, pp. 1032 – 1045, 2016.

[77] U. Abronzini, C. Attaianese, M. D. Monaco, F. Porpora, G. Tomasso, M. Granato, and G. Frattini, “Optimal modular

bms for high performances nmc battery pack," in *2018 IEEE International Conference on Electrical Systems for Aircraft, Railway, Ship Propulsion and Road Vehicles International Transportation Electrification Conference (ESARS-ITEC)*, Nov 2018, pp. 1–6.

[78] U. Abronzini, C. Attaianese, M. D. Monaco, F. Porpora, and G. Tomasso, "Real time balancing for modular passive battery management system," in *PCIM Europe 2019; International Exhibition and Conference for Power Electronics, Intelligent Motion, Renewable Energy and Energy Management*, May 2019, pp. 1–6.

[79] U. Abronzini, C. Attaianese, M. D'Arpino, M. D. Monaco, F. Porpora, and G. Tomasso, "Thermal management optimization of a passive bms for automotive applications," in *AEIT Automotive 2019; International Conference of Electrical and Electronic Technologies for Automotive*, 2019, pp. 1–6.

[80] Y. Ye and K. Cheng, "An automatic switched-capacitor cell balancing circuit for series-connected battery strings," *Energies*, vol. 9, p. 138, 02 2016.

[81] Y. Shang, C. Zhang, N. Cui, and C. C. Mi, "A delta-structured switched-capacitor equalizer for series-connected battery strings," *IEEE Transactions on Power Electronics*, vol. 34, no. 1, pp. 452–461, 2019.

[82] M. Daowd, M. Antoine, N. Omar, P. Van den Bossche, and J. Van Mierlo, "Single switched capacitor battery balancing system enhancements," *Energies*, vol. 6, pp. 2149–2174, 04 2013.

[83] Y. Shang, B. Xia, F. Lu, C. Zhang, N. Cui, and C. C. Mi, "A switched-coupling-capacitor equalizer for series-connected battery strings," *IEEE Transactions on Power Electronics*, vol. 32, no. 10, pp. 7694–7706, 2017.

[84] A. C. Baughman and M. Ferdowsi, "Double-tiered switched-capacitor battery charge equalization technique," *IEEE Transactions on Industrial Electronics*, vol. 55, no. 6, pp. 2277–2285, 2008.

[85] R. Fukui and H. Koizumi, “Double-tiered switched capacitor battery charge equalizer with chain structure,” 11 2013, pp. 6715–6720.

[86] M. Kim, C. Kim, J. Kim, and G. Moon, “A chain structure of switched capacitor for improved cell balancing speed of lithium-ion batteries,” *IEEE Transactions on Industrial Electronics*, vol. 61, no. 8, pp. 3989–3999, 2014.

[87] H. Park, C. Kim, K. Park, G. Moon, and J. Lee, “Design of a charge equalizer based on battery modularization,” *IEEE Transactions on Vehicular Technology*, vol. 58, no. 7, pp. 3216–3223, 2009.

[88] S. Yarlagadda, T. T. Hartley, and I. Husain, “A battery management system using an active charge equalization technique based on a dc/dc converter topology,” *IEEE Transactions on Industry Applications*, vol. 49, no. 6, pp. 2720–2729, 2013.

[89] T. H. Phung, J. Crebier, A. Chureau, A. Collet, and V. Nguyen, “Optimized structure for next-to-next balancing of series-connected lithium-ion cells,” in *2011 Twenty-Sixth Annual IEEE Applied Power Electronics Conference and Exposition (APEC)*, 2011, pp. 1374–1381.

[90] A. Farzan Moghaddam and A. Van den Bossche, “An efficient equalizing method for lithium-ion batteries based on coupled inductor balancing,” *Electronics*, vol. 8, p. 136, 01 2019.

[91] M. Kim, J. Kim, and G. Moon, “Center-cell concentration structure of a cell-to-cell balancing circuit with a reduced number of switches,” *IEEE Transactions on Power Electronics*, vol. 29, no. 10, pp. 5285–5297, 2014.

[92] S. Park, K. Park, H. Kim, G. Moon, and M. Youn, “Single-magnetic cell-to-cell charge equalization converter with reduced number of transformer windings,” *IEEE Transactions on Power Electronics*, vol. 27, no. 6, pp. 2900–2911, 2012.

[93] S. Li, C. C. Mi, and M. Zhang, “A high-efficiency active battery-balancing circuit using multiwinding transformer,” *IEEE Transactions on Industry Applications*, vol. 49, no. 1, pp. 198–207, 2013.

[94] Y. Shang, B. Xia, C. Zhang, N. Cui, J. Yang, and C. C. Mi, "An automatic equalizer based on forward-flyback converter for series-connected battery strings," *IEEE Transactions on Industrial Electronics*, vol. 64, no. 7, pp. 5380–5391, 2017.

[95] Y. Chen, X. Liu, Y. Cui, J. Zou, and S. Yang, "A multiwinding transformer cell-to-cell active equalization method for lithium-ion batteries with reduced number of driving circuits," *IEEE Transactions on Power Electronics*, vol. 31, no. 7, pp. 4916–4929, 2016.

[96] C. Lim, K. Lee, N. Ku, D. Hyun, and R. Kim, "A modularized equalization method based on magnetizing energy for a series-connected lithium-ion battery string," *IEEE Transactions on Power Electronics*, vol. 29, no. 4, pp. 1791–1799, 2014.

[97] R. Ling, Q. Dan, L. Wang, and D. Li, "Energy bus-based equalization scheme with bi-directional isolated cuk equalizer for series connected battery strings," in *2015 IEEE Applied Power Electronics Conference and Exposition (APEC)*, 2015, pp. 3335–3340.

[98] X. Lu, W. Qian, and F. Z. Peng, "Modularized buck-boost + cuk converter for high voltage series connected battery cells," in *2012 Twenty-Seventh Annual IEEE Applied Power Electronics Conference and Exposition (APEC)*, 2012, pp. 2272–2278.

[99] A. Farzan Moghaddam and A. Van den Bossche, "A single transformer for active cell equalization method of lithium-ion batteries with two times fewer secondaries than cells," *Electronics*, vol. 8, p. 951, 08 2019.

[100] L. Maharjan, S. Inoue, H. Akagi, and J. Asakura, "State-of-charge (soc)-balancing control of a battery energy storage system based on a cascade pwm converter," *IEEE Transactions on Power Electronics*, vol. 24, no. 6, pp. 1628–1636, 2009.

[101] M. Uno and A. Kukita, "Bidirectional pwm converter integrating cell voltage equalizer using series-resonant voltage multiplier for series-connected energy storage cells," *IEEE Transactions on Power Electronics*, vol. 30, no. 6, pp. 3077–3090, 2015.

[102] K. Lee, Y. Chung, C. Sung, and B. Kang, "Active cell balancing of li-ion batteries using lc series resonant circuit," *IEEE Transactions on Industrial Electronics*, vol. 62, no. 9, pp. 5491–5501, 2015.

[103] M. Uno and A. Kukita, "Single-switch single-transformer cell voltage equalizer based on forward-flyback resonant inverter and voltage multiplier for series-connected energy storage cells," *IEEE Transactions on Vehicular Technology*, vol. 63, no. 9, pp. 4232–4247, 2014.

[104] C. Kim, M. Kim, and G. Moon, "A modularized charge equalizer using a battery monitoring ic for series-connected li-ion battery strings in electric vehicles," *IEEE Transactions on Power Electronics*, vol. 28, no. 8, pp. 3779–3787, 2013.

[105] Y. Shi and R. Song, "A novel high-efficiency double-input bidirectional dc/dc converter for battery cell-voltage equalizer with flyback transformer," *Electronics*, vol. 8, p. 1426, 11 2019.

[106] N. Mubenga, Z. Linkous, and T. Stuart, "A bilevel equalizer for large lithium ion batteries," *Batteries*, vol. 3, p. 39, 12 2017.

[107] G. Zimmer, "Wireless battery management systems highlight industry's drive for higher reliability," 2017.

[108] L. A. Perisoara, I. C. Guran, and D. C. Costache, "A passive battery management system for fast balancing of four lifepo4 cells," in *2018 IEEE 24th International Symposium for Design and Technology in Electronic Packaging*, Oct 2018, pp. 390–393.

[109] D. Freudiger, M. D'Arpino, and M. Canova, "A generalized equivalent circuit model for design exploration of li-ion battery packs using data analytics," *IFAC-PapersOnLine*, vol. 52, no. 5, pp. 568 – 573, 2019, 9th IFAC Symposium on Advances in Automotive Control AAC 2019.

[110] L. F. Costa, F. Hoffmann, G. Buticchi, and M. Liserre, "Comparative analysis of multiple active bridge converters configurations in modular smart transformer," *IEEE Transactions on Industrial Electronics*, vol. 66, no. 1, pp. 191–202, Jan 2019.